STUDY OF QUANTUM PHASE TRANSITIONS AND TOPOLOGICAL PHASES IN CHAINS AND LADDERS.

by

TOPLAL PANDEY

A thesis submitted in partial fulfillment

of the requirements for the degree of

Doctor of Philosophy (PhD) in Material Sciences

Office of Graduate Studies

Laurentian University

Sudbury, Ontario, Canada

THESIS DEFENCE COMMITTEE/COMITÉ DE SOUTENANCE DE THÈSE
Laurentian Université/Université Laurentienne
Office of Graduate Studies/Bureau des études supérieures

Title of Thesis Titre de la thèse	STUDY OF QUANTUM PHASE TRANSITIONS AND TOPOLOGICAL PHASES IN CHAINS AND LADDERS
Name of Candidate Nom du candidat	Pandey, Toplal
Degree Diplôme	Doctor of Philosophy
Department/Program Département/Programme	Materials Science
Date of Defence Date de la soutenance	July 28, 2022

APPROVED/APPROUVÉ

Thesis Examiners/Examinateurs de thèse:

Dr. Gennady Chitov
(Supervisor/Directeur(trice) de thèse)

Dr. Jacques Farine
(Committee member/Membre du comité)

Dr. Ralf Meyer
(Committee member/Membre du comité)

Dr. Zohar Nussinov
(External Examiner/Examinateur externe)

Dr. Kalpdrum Passi
(Internal Examiner/Examinateur interne)

Approved for the Office of Graduate Studies
Approuvé pour le Bureau des études supérieures
Tammy Eger, PhD
Vice-President Research (Office of Graduate Studies)
Vice-rectrice à la recherche (Bureau des études supérieures)
Laurentian University / Université Laurentienne

ACCESSIBILITY CLAUSE AND PERMISSION TO USE

I, **Toplal Pandey**, hereby grant to Laurentian University and/or its agents the non-exclusive license to archive and make accessible my thesis, dissertation, or project report in whole or in part in all forms of media, now or for the duration of my copyright ownership. I retain all other ownership rights to the copyright of the thesis, dissertation or project report. I also reserve the right to use in future works (such as articles or books) all or part of this thesis, dissertation, or project report. I further agree that permission for copying of this thesis in any manner, in whole or in part, for scholarly purposes may be granted by the professor or professors who supervised my thesis work or, in their absence, by the Head of the Department in which my thesis work was done. It is understood that any copying or publication or use of this thesis or parts thereof for financial gain shall not be allowed without my written permission. It is also understood that this copy is being made available in this form by the authority of the copyright owner solely for the purpose of private study and research and may not be copied or reproduced except as permitted by the copyright laws without written authority from the copyright owner.

Abstract

The ground-state phase diagrams and order parameters of low-dimensional quantum models are analyzed. Those models in their spin representation are the dimerized spin-1/2 XY and XYZ chains, and the two-leg ladders with anisotropy and three different dimerization patterns, in the presence of uniform and staggered transverse fields. The analysis is done by using the effective quadratic fermionic Hamiltonian of models, resulting from the Hatree-Fock mean-field approximation. In the fermionic representation, those models are equivalent to the generic Kitaev -Majorana chains/ladders with the proper parametrizations.

An exact solvable model, the XY chain has a rich phase diagram, and its distinct phases are identified by the local and nonlocal (string) order parameters. We have calculated all the local order parameters (spontaneous magnetization) and the nonlocal order parameters within the same systematic framework, along with the winding numbers for all regimes of the phase diagram. By combining the exact and the mean-field methods, the local and string order parameters on the phase diagram of the XYZ chain, are identified and calculated. We found similar qualitative pictures on the phase diagrams of XY and XYZ chains, where the corresponding parameters of the latter model are renormalized by the interaction $\Delta = J_z/J$. For both models, the topological nontrivial phase is shown to have a peculiar oscillating order with the period of a four lattice spacing, not reported before and awaiting for its experimental confirmation. The detailed analysis of patterns of the string order is given. Moreover, the trivial phases of both the cases are investigated by local order parameters (components of spontaneous magnetization).

The special XXZ limit of the model with additional U(1) symmetry is in agreement with the Lieb-Schiltz-Mattis theorem and its extensions, plateaus of magnetization, and some additional conserving quantities. We have shown that within the XYZ chain, where the plateaus are smeared, the robust oscillating string order parameter is continuously connected to its XXZ limit. Also, the nontrivial winding number and zero-energy localized Majorana edge states, as additional attributes of the topological order, are robust in that phase, even off the line of U(1) symmetry.

The phase diagram of the isotropic two-leg ladder is investigated by calculating the field-induced magnetization at each point along the external field. In the phase diagram, the two kind of phases, gapped plateau and gapless Lutinger liquid, (LL) are identified. In the applied uniform field, those models are in agreement with the quantization conditions of the magnetization plateaus. The existence of the mid-plateau in the staggered ladder with columnar field, we report for the first time is an indication of a new spin gapped phase in this type of spin structure. For the staggered and columnar ladder, the alternating field only modifies the phase boundaries of the phase diagram. The ladder with the rung dimerization and columnar field exhibits additional quantum

phase transition by closing and re-opening the zero-plateau and mid-plateau gapped phases with respect to the alternating field.

The Hatree-Fock mean-field Hamiltonian of the ladders with an anisotropy and two dimerization patterns, map onto the sum of two quadratic Majorana Hamiltonians, which are dual to a sum of two (even/odd) XY quantum chains in the alternating transverse fields. The mapping between the effective Hamiltonian of the ladder and the pair of the dual XY chains considerably simplifies calculations of the order parameters, and analyses of the hidden symmetry breaking. The ground state phase diagram of the staggered ladder contains nine phases: four of them are conventional antiferromagnets, while the other five possess the non-local brane orders. Using the dualities and the newly found exact results for the local and string order parameters of the transverse XY chains, we were able to find analytically all the magnetizations and the brane order parameters for the staggered case, as well as the functions of the renormalized couplings of the effective Hamiltonian. The columnar ladder has three ground-state phases, and it does not possess a magnetic long-range order. The brane order parameters for these phases are numerically calculated from the Toeplitz determinants. We expect this study to motivate the search for the real spin-Peierls anisotropic ladder compounds, which can undergo the predicted quantum phase transitions with a gap closure and distinct brane orders.

Acknowledgements

As I am getting ready to leave Laurentian University, I would like to take this opportunity and thank the ones who have helped me a lot during this long journey. First of all, I would like to sincerely thank my supervisor, Dr. Gennady Chitov, for his generous support, guidance and patience throughout the past 11 years, since he was also my master's supervisor. He was teaching me the Advanced Quantum Physics and Statistical Mechanics, and also introduced me to the beautiful world of condensed matter Physics. I owe a lot to Dr. Gennady, his incredible kindness and modest character. He trusted that I would do what I needed to be done, and gave me the encouragement and resources to work effectively. Apart from sharing his knowledge on various topics in condensed matter physics, he granted me much freedom to work on any problems that I found interesting. The door of his office was always open so that I could always stop by to ask questions, share ideas, talk about projects, or even have some causal conversations during the evening, no matter how busy he was.

I would also like to thank the other members of my supervisory committee: Dr. Ralf Meyer and Dr. Jacques Farine for devoting their valuable time. I have benefited a lot from Dr. Ralf with his constructive feedbacks and his informal lectures in both the statistical mechanics and computational simulation. They have given me a broader knowledge of the field. My special thanks goes to Dr. Z. Nussinov, for agreeing to be my external examiner.

I had a big opportunity to discuss about the different aspects of the topological phases of matter with two brilliant scientists during my PhD studies: Curtis Laamanen and Alexander Robillard. Curtis's expertise in the wide range of numerical techniques was just too solid to wear off after finishing my graduate studies. The later years of my studies were greatly nurtured by a discussion with Alexander. He had an excellent intuition about the topological superconductivity, especially the higher-order ones. His qualifications perfectly complemented my understanding of the topological orders. We all spent countless hours of fruitful discussion together, since we were next to each other in the same office. Thank you very much for answering all my naive questions and your encouragements.

My words will always fall short in acknowledging my loving parents, Khadananda and Ishwori, for all of their unconditional support and encouragement throughout my entire life. Thank you both for giving me strength to chase my dreams.

Most importantly, I send my greatest thanks to my wife, Kaushila. She has never stopped supporting my curiosity about physics even when it led me to spend long nights at work. Kaushila, you have played the most important role of all. I will be forever grateful for your love, companionship, endless understanding and encouragement. I would also like to extend my thanks to my dear daughters: Dikshya and Divya, and

my son: Divan, for filling up our time with lots of joys, happiness, and fun. You all have been inspiring me for many years. I am heavily indebted to all of you

My work herein was supported mainly by Department of Physics, Laurentian University Research Fund (LURF), Ontario Graduate Scholarship (OGS), and Queen Elizabeth Science and Technology Grant.

Toplal Pandey

Sudbury

April 2022

Table of Contents

Abstract iii

Acknowledgements v

Table of Contents vii

List of Figures x

Chapter 1. Introduction 1

1.1 Overview . . . 1
1.2 Background . . . 8
1.2.1 Jordan-Wigner transformation . . . 8
1.2.2 Mean-field Approximation . . . 12
1.2.3 Spin duality transformation . . . 14
1.2.4 Local and string order parameters . . . 15
1.2.5 Brane operators and order parameters . . . 17
1.2.6 Topological winding number . . . 18
1.3 Organisation of this thesis . . . 21
1.4 Contributions . . . 24
1.4.1 Publications . . . 24
1.4.2 Presentations . . . 25

Chapter 2. Dimerized XY Chain in Modulated Magnetic Field. 26

2.1 Model . . . 27
2.1.1 Spin and fermionic representation of the model . . . 27
2.1.2 Spectrum . . . 28
2.1.3 Phase diagram . . . 31
2.1.4 Field-induced magnetizations and susceptibility . . . 33
2.2 Order parameters . . . 38
2.2.1 Bogoliubov transformation and Majorana operators . . . 38
2.2.2 Spontaneous magnetization . . . 42
2.2.3 Nonlocal string orders . . . 45
2.2.4 Winding number . . . 51
2.3 Dimerized XY chain . . . 52
2.3.1 Local and string order parameters . . . 52
2.3.2 Topological winding number . . . 58

Chapter 3. Modulated Dimerized XYZ Chain with Magnetic Field 63

3.1 Model 64
3.1.1 The Hamiltonian, spectrum and phase diagram 64
3.1.2 Spin and Majorana averages 70
3.2 Mean-field equations 72
3.3 Results for XYZ chain 76
3.3.1 Induced and spontaneous magnetization 78
3.3.2 Nonlocal string order 80
3.3.3 Winding number 86
3.4 Isotropic chain 87
3.4.1 Noninteracting XX limit ($\Delta = 0$) 87
3.4.2 Interacting XXZ limit ($\Delta \neq 0$) 97

Chapter 4. Dimerized Two-Leg Ladder 108
4.1 Introduction 108
4.2 Model 112
4.2.1 Spin and mean-field Hamiltonian 112
4.2.2 Single particle Hamiltonian and spinor 118
4.3 Isotropic ladder: spectra, phase diagram and induced magnetizations ... 121
4.3.1 Staggered ladder 121
4.3.2 Columnar ladder with columnar field (CC-ladder) 132
4.3.3 Rung-dimerized ladder in columnar field (RC-ladder) 136
4.4 Mean-field theory: technical details 143

Chapter 5. Anisotropic-Dimerized Two-Leg Ladder 151
5.1 The model, mean-field, and single-particle Hamiltonian 152
5.2 Spectra, phase diagram, and dual models 155
5.2.1 Staggered ladder 155
5.2.2 Columnar ladder 159
5.3 Phases and their order parameters 161
5.3.1 Staggered ladder 161
5.3.2 Columnar ladder 166
5.4 Topological numbers 168
5.5 Mean-field theory 170
5.6 Isotropic two-leg ladder 175
5.6.1 Model and mean-field Hamiltonian 175
5.6.2 Spectra and winding number 177
5.6.3 Brane order parameters 181

Chapter 6. Conclusions 188

Appendix A. Mean-field parameters with flux correction υ : 195

Appendix B. Duality of two transverse-field XY chain models and their order parameters **199**

Appendix C. Transverse Ising chain with three-spin interactions **203**

Bibliography **206**

List of Figures

1.1 Illustration of the paths of 1D and 2D JW transformations 9
1.2 Illustration of the diagonal path of 2D JW transformation 12
1.3 Illustration of brane order parameters (2D SOPs) 19

2.1 Phase diagram of dimerized XY chain in h-γ plane 30
2.2 Phase diagram of dimerized XY chain in δ-γ plane 32
2.3 Illustration of induced-magnetizations vs uniform external field 35
2.4 Visualization of the magnetization patterns at different uniform field 36
2.5 Illustration of magnetic susceptibility vs uniform field and anisotropy 37
2.6 Illustration of the SOPs $O_{x,y/e,o}$ along γ axis 47
2.7 Visualization of the $\mathfrak{D}_{zz}$ on topological phase vs lattice points 49
2.8 Illustration of magnetizations $m_{x,y}$ and SOPs $\mathcal{O}_z$ vs h and γ 50
2.9 Phase diagram of dimerized XY chain in δ, γ plane 55

3.1 Phase diagram of dimerized XYZ chain in (γ, h) plane 69
3.2 Mean-field parameters vs external field and γ 75
3.3 Illustration of the radius of topological phase vs interaction strength Δ 78
3.4 Illustration of four induced-magnetization vs external field 79
3.5 Visualization of the $\mathfrak{D}_{zz}$ in topological phase vs lattice points 81
3.6 Illustration of planner magnetizations $m_{x,y}$ and SOPs $\mathcal{O}_{z,i}$ vs h and γ 83
3.7 Visualization of $\mathfrak{D}_{zz}$ vs lattice points at different h_a and δ 85
3.8 Effective single-particle spectrum vs uniform field h 88
3.9 Illustration of complex wave vector k_+ vs uniform field 90
3.10 Illustration of the string correlation function $\mathfrak{D}_{zz}(1,n)$ vs lattice points 98
3.11 Phase diagram of XXZ chain in h-Δ plane 103

4.1 Three dimerization patterns in two-leg ladder 112
4.2 Snake-like path of JWT in two-leg ladder 114
4.3 Phase diagram of the two-leg ladder: SC-ladder 123
4.4 Illustration of dispersion relation vs external field 124
4.5 Illustration of induced-magnetization vs external field 126
4.6 Illustration of known result: induced-magnetization vs applied field 127
4.7 Phase diagram of SS-ladder in (h-δ) plane 129
4.8 Dispersion relation of SS-ladder at different external field 130
4.9 Illustration of induced-magnetization vs external field at different h_a and δ 131
4.10 Phase diagram of CC-ladder in (h-δ) plane 133
4.11 Induced-magnetizations vs external field at different δ and h_a 134
4.12 Induced-magnetization vs external field from known result 136
4.13 Phase diagram of RC-ladder in the (h-δ) plane 138

4.14 Induced-magnetization vs external field from known result 139
4.15 Illustration of induced-magnetization vs external field at different δ 140
4.16 Illustration of induced-magnetizations vs external field at different h_a 141
4.17 Mean-field parameters vs external field for various ladder models 148

5.1 Phase diagram of staggered ladder in (γ,δ) plane 156
5.2 Phase diagram of columnar ladder in (γ,δ) plane 160
5.3 Illustration of order parameters vs γ in staggered ladder 164
5.4 Brane order parameter vs γ in the columnar ladder 168
5.5 Renormalized couplings per unit bare values vs γ 174
5.6 Phase diagram of staggered two-leg ladder in $J_\perp, \delta$ plane 179
5.7 Illustration of Odd BOPs for staggered ladder 183
5.8 Illustration of BOPs $\mathcal{O}_{x,y/e,o}$ vs δ 184

Chapter 1

Introduction

1.1 Overview

According to the Landau theory of phase transitions, phases can be distinguished by the different types of the long-range order, or its absence. The ordering is described by an appropriately chosen local order parameter. In the Landau theory phases are distinct due to their different symmetries, and the continuous phase transition is always related to a spontaneous breaking of system's symmetry [1].

There are quite large numbers of examples of low-dimensional fermionic or spin systems where the states of the matter and their changes can not be classified in terms of apparent symmetry breaking and/or local order parameter, most notably a particular class of gapped systems known as the quantum spin liquids [2–4]. Low-dimensional systems provide a lot of possibilities for realization of various exotic quantum liquid states, where the long-range order is prevented even at a zero temperature. In the low-dimensional quantum magnets, fermions, and topological insulators/superconductors the existence of gapped phases and their transitions between them are not necessarily

accompanied by breaking of some symmetry associated with local observables. See [2, 4–27], and more references therein.

To characterize the phases with hidden nonlocal or topological orders, the concept of the string order parameters (SOPs) introduced by den Nijs and Rommelse is particularly instrumental [28]. The appearance of such nonlocal SOP is accompanied by hidden $\mathbb{Z}_2 \bigotimes \mathbb{Z}_2$ symmetry breaking [4, 24, 29–32]. In the last decade, SOPs were successfully reported to characterize quantum phases with hidden orders in various spin chains and ladders at zero temperature [6, 13, 16, 19, 23, 30, 33, 34] . In recent related works, it has been analytically and numerically analyzed how the Landau formalism can be extended to deal with nonconventional quantum orders [35–38], called topological orders. Technically the key quantities to demonstrate topological phases are nonlocal string operators, string correlation functions and string order parameters [28].

To characterize these states, a concept of topological order was introduced [2] and its definition is a really subtle issue [39]. This order is often associated with the nontrivial topological indices as Pontraygin (Winding), Chern numbers [4, 24, 29] and/or Berry phases [4], which are not reducible to the parameters of the conventional Landau theory. These quantities provide rather complementary description and do not seem to be indispensable [35–38]. Hatsugai and co-workers [40, 41] proposed the quantized Barry phases as a quantum order parameter to probe non-local orders. This scheme was successfully applied e.g., for several quantum spin liquid systems. It turns out that the change of the quantized Barry phase can also diagnose the crossovers between the states which are not separated by gap closing, local symmetry or order changes [42–45].

The important property of SOP is that it can be used for both the quantum and thermal phase transitions. For instance, the SOP can be used for analysis of the thermal transitions into a Berezinskii-Kosterlitz-Thouless-type phase with an algebraic order

[28]. Very importantly, SOP is a proper order parameter in the sense of Landau: for the integrable models, one can calculate exactly the critical indices β and η from the SOP and the string-string correlation function, resp., near the critical point [33] and check explicitly that such β, η along with other critical indices satisfy the standard hyperscaling relations [34–38]. Since the SOP is limiting value of the nonlocal correlation function, its analytical calculation is a difficult task even for exactly solvable models. For example, for the dimerized Heisenberg spin-$\frac{1}{2}$ chain, the calculation is quite simple in the leading Sing-Gordon approximation for the Hamiltonian [33], while taking into account the marginal terms renders the problem that is much more difficult [46], and more work is still needed. The other subtlety is that only for a spin chain and a two-leg ladder, the definition of the SOPs is straightforward.

There is an extensive recent literature on hidden orders in massive phases of the Heisenberg chains and ladders. In particular, the critical properties of the dimerized two and three-leg ladders have been studied in numerical and analytical works [19, 34, 35, 47–56]. Quantum critical lines or even gapless regions in the parameter space adjacent to various massive phases of spin ladders may also be also induced by frustrations, magnetic fields, or four-spin interactions [6, 7].

There has been an opinion expressed in the literature that various low-dimensional fermionic or spin systems with hiddenly ordered phases and transitions between them, defy completely the Landau paradigm. It appears to us that such a claim is too radical, and one can formulate the theory of such transitions consistent with the Landau framework using the nonlocal SOPs [57]. However, the Landau picture needs to be amended since some facets of the topological order quantified by topological indices, Berry phases, are not reducible even to nonlocal SOPs. The major problem is that the current treatment of such systems in most cases is heavily numerical, and the quali-

tative physical picture is obscured. It is really warranted to put more weight first on advancing relatively simple analytical approaches based on the effective (mean-field) models, similar, e.g., to the Kitaev model [22, 23], or the single-particle tight-binding models used for the analyses of the topological insulators and superconductors [24]. Results based on those models clearly indicate that interactions are not an indispensable element of the topological order framework.

In this research, we carry out such program from analyses of the dimerized XY and XYZ chains and the two-leg Heisenberg ladders with uniform and modulated axial magnetic fields. In the ladder, three dimerization patterns such as staggered, columnar and rung dimerization are considered. The first exact solvable model is equivalent to non-interacting Jordan-Wigner fermions. The interacting fermionic terms of chains and ladders are decoupled via the Hatree-Fock mean-field approximation, and the spin models are reduced to effective quadratic fermionic Hamiltonians. An important task addressed in this work is to formalize the technical protocol: In the proposed unifying formalism, the role of the Gingburg-Landau effective action is played by the effective quadratic fermionic Hamiltonian, and it is enhanced to map the generating function in terms of Majorana fermions [37, 38] as a part of the matrix element of the Toeplitz matrix. In the earlier related work, it has been shown that such approximation is quite adequate even quantitatively [34–38, 53, 58].

All the local and nonlocal order parameters calculated from the string correlation function of Majorana fermions evaluated from the limiting value of determinant of the block Toeplitz matrices. For quadratic Hamiltonians, elements of those matrices are found in a closed analytical form as the functions of parameters of the Hamiltonian. In the interacting models such as the dimerized XYZ chain and the two-leg ladder, the renormalized parameters associated with the Majorana fermions in each matrix el-

ement, are calculated in terms of bare parameters of the original Hamiltonian [38, 59]. Those calculations were done self-consistently from the minimization of the free-energy of the model. From those renormalized parameters, field-induced uniform magnetization can be numerically calculated at each point along the axis of the applied field. The number of magnetization plateaus appeared on those magnetization curves for isotropic chains and ladders satisfies necessary quantization condition as derived in [60–62]. The constant magnetization on the plateau region is an indication of gapped phase, while the magnetization gradually increasing on the gapless incommensurate region is called the Luttinger-liquid (LL) phase.

By utilizing duality transformations, we demonstrate that it is possible to map the problem of calculation of nonlocal SOPs in the chains and brane order parameters (BOPs) in the ladders onto the problem of local (Landau) order parameters in the dual representation, where the dual models are given by exactly-solvable Hamiltonians and their order parameters can be calculated exactly. It is then also straightforward to relate appearance of the SOP with the spontaneous symmetry breaking in terms of the dual Hamiltonian. In some cases, the duality can simply map the nonlocal order onto some average of the product of the decoupled local orders e.g., magnetization, and hidden symmetry breaking becomes apparent in terms of the sublattice magnetization(s) on a dual lattice, with one or both of the Ising $\mathbb{Z}_2$ symmetries broken [23, 35–38, 59]. In general manifestations of the hidden symmetry breaking are the least straightforward. In addition, we show that the gapped phases not only have distinct SOPs , but they can also be distinguished by the winding (Pontryagin) number.

In the context of the previously reported difficulties, it is important to gain more insight on SOPs by dealing with nontrivial models rather than the simple models. One of these models we study here, in the guise of the dimerized XY chain with uniform and

modulated transverse fields, has been known for several decades [63]. It is an exactly solvable model, and its spectrum and phase diagram are well known [63, 64]. However, the explicit calculations for the spontaneous magnetization seems to be missing in the literatures. Most importantly, the nature of the order in the topological phase was not clarified, and here we report out findings of its nonlocal order, oscillating with the period of four lattice spacings, and monotonously saturated in the paramagnetic (PM) phase [37]. A similar treatment is done in dimerized XYZ chain with uniform and alternating transverse fields, where its renormalized effective Hamiltonian and spectrum have the same expressions as the noninteracting (XY) model. From the derivation, the only difference we found is that the six bare couplings of free-fermionic Hamiltonian are replaced by the respective renormalized parameters. It is natural to explore to which extend the results of [37] can be generalized for the interacting case $\Delta \neq 0$. The phase diagram of the model is one of the main results of our study. To systematically probe non-local order beyond 1D, one needs to define the brane order parameters [65–72] , and that is the concept we use in the two-leg ladder. To analyse the brane order parameter, the spin Hamiltonian of the two-leg ladder is treated within a Hatree-Fock mean-field approach and mapped onto the quadratic effective fermionic Hamiltonian [59]. The progress in calculation of the brane order parameters is made by using the duality transformations.

The fermionic representation of models XY and XYZ are in the form of the Kitaev chain of Majorana fermions with dimerized hopping and modulated chemical (potential). The latter model has an additional modulated anomalous (superconducting) pairing term in the Hamiltonian. The solvable Kitaev Majorana models with dimerization and spatial modulations of the potential were studied very actively in recent years with the focus on their topological phases with hidden orders and Majorana edge state [36, 73–75], similar models with more general settings were studied in Ref. [76–78].

In the context of our current research interest, the models presented here provide rich phase diagrams, critical properties, when the phase diagrams contain both conventional local and quite peculiar nonlocal orders.

It appears that the notion of the topological order is not understood uniquely in the literature. In connection to the spin chain and ladder, it appears to be associated with the additional U(1) symmetry of the isotropic limit. In this limit, the Lieb-Schultz-Mattis (LSM) theorem [79] and its subsequent generalizations [60–62, 80, 81] predict either gapless incommensurate phase without symmetry breaking or gapped phases with broken $\mathbb{Z}_2 \bigotimes \mathbb{Z}_2$ symmetry, integer fillings, and plateaus of magnetization. The plateaus are sometimes viewed as hallmark of topological order. Our understanding of topological order is not tied up to the continuous U(1) symmetry or related plateaus. The gapped phases with broken (discreet) symmetry are secured by the extension of the LSM theorem for the spin chains without continuous symmetry [62]. Without U(1), the plateaus are smeared, but the robust SOP still exists and is continuously connected to its U(1) limit. Thus we associate topological order with nontrivial SOP or brane order parameter (BOP)[see definition in sec.1.2.5]. Also, the nontrivial winding number and zero-energy localized Majorana edge states, as additional attributes of topological order, are robust in the topological phase even aside from the line of U(1) symmetry, in agreement with analogous exact results [36–38].

These results allow us to stress close similarities between various gapped phases occurring in spin models and topological insulators/superconductors. The latter are of great current interest [4,24,27]. The proposed approach provides a unifying theoretical framework to deal with nonlocal order parameters in such seemingly different systems within the Landau paradigm.

1.2 Background

1.2.1 Jordan-Wigner transformation

The first step of solving the Heisenberg model [see definition (3.1) below] is the fermionization of the model's spin Hamiltonian. In order to map the spin operator onto spinless fermionic operator we start from one dimensional Jordan-Wigner (JW) transformation [79, 82, 83]. It is defined as

$$\sigma_n^\dagger = c_n^\dagger \exp\left[i\pi \sum_{l=1}^{n-1} \hat{n}_l\right] \tag{1.1}$$

and

$$\sigma_n^z = 2c_n^\dagger c_n - 1 \tag{1.2}$$

where $\sigma_n^\pm = \frac{1}{2}(\sigma_n^x \pm i\sigma_n^y)$ and $\hat{n}_l = c_l^\dagger c_l$ is the number operator having the value 0 or 1 and satisfying the following relations [79]:

$$e^{i\pi\hat{n}_n} = e^{-i\pi\hat{n}_n} = 1 - 2c_n^\dagger c_n. \tag{1.3}$$

The fermionic operators $(c_l^\dagger, c_l)$ satisfy standard anticommutation relations:

$$\{c_n, c_m^\dagger\} = \delta_{nm}, \qquad \{c_n, c_m\} = \{c_n^\dagger, c_m^\dagger\} = 0 \tag{1.4}$$

We present schematically the transformation (1.1) as indicated in Fig. 1.1 where the path of JW-transfornation goes through each lattice site exactly once. To obtain the phase of any site say m-site we sum up from the site 1 to $m-1$ keeping in the mind that the summation can not extend to every site except m, that preserves the spin commutation relation. In this research the Heisenberg model only consists of the first-nearest neighbour spin-spin interaction. Using JW transformation (1.1) we map the

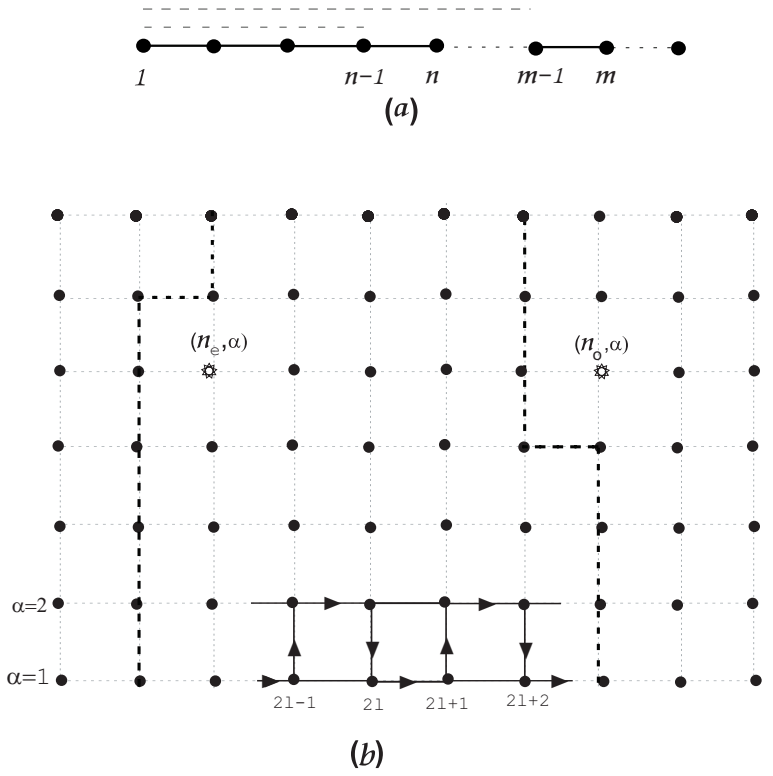

Figure 1.1: Schematics of path for the JW transformation that we employ in the spin (a) chain-see Eq. (1.1). The dashed line crosses only one time through any site at which the phase term is to be calculated. (b) two-leg ladder-see Eqs. (1.8a) and (1.8b). The arrow passes only once through any site at which the phase term calculated.

spin-spin operators of the Hamiltonian onto spinless fermionic form:

$$\sigma_n^\dagger \sigma_{n+1}^- = c_n^\dagger \exp\Big[i\pi \sum_{l=1}^{n-1} \hat{n}_l\Big] \exp\Big[-i\pi \sum_{l=1}^{n} \hat{n}_l\Big] c_{n+1} = c_n^\dagger c_{n+1}, \tag{1.5}$$

$$\sigma_n^- \sigma_{n+1}^\dagger = c_{n+1}^\dagger c_n \tag{1.6}$$

where we have used the Eq. (1.3) and

$$c_n^\dagger e^{\pm i\pi \hat{n}_n} = c_n^\dagger \tag{1.7}$$

(see [84] for details).

Using the concept of 1D JW-transformation and the commutation algebra of the fermionic operators, we obtain the generalization of the JW transformation in the case of two dimensions. 2D JW-transformation is applicable in the presence of the transverse coupling and the problem gets more interesting. To resolve the two dimensional problem we introduce a transformation where the phase at the site (n, α) is now obtained by summing up all the sites at the left of dashed line as depicted in the Fig. 1.1b. Here $n_{e/o}$ represents the site of position along the axis of chain while α represents inter-chain site position. The summations are carried out in different way for the phase taken in (n_e, α) or (n_o, α) site.

There are different ways to introduce this transformation when we depart from a single chain problem to the ladder model [23, 35, 39, 83, 85–88]. We introduce 2D JW transformation:

$$\sigma_\alpha^\dagger(n_o) = c_\alpha^\dagger(n_o) \exp\left[i\pi \sum_{l=1}^{n_o-1} \sum_{d=1}^{M} \hat{n}_d(l) + \sum_{d=1}^{\alpha-1} \hat{n}_d(n_o)\right] \tag{1.8a}$$

$$\sigma_\alpha^\dagger(n_e) = c_\alpha^\dagger(n_e) \exp\left[i\pi \sum_{l=1}^{n_e-1} \sum_{d=1}^{M} \hat{n}_d(l) + \sum_{d=\alpha+1}^{M} \hat{n}_d(n_e)\right]. \tag{1.8b}$$

The phase factor is the number of occupied sites along the defined path shown in the Fig. 1.1b. In particular, for two-leg ladder, $\alpha = 1, 2$ and $M = 2$ then Eqs. (1.8a) and (1.8b) become

$$\sigma_\alpha^\dagger(n_o) = c_\alpha^\dagger(n_o) \exp\left[i\pi \sum_{l=1}^{n_o-1} \sum_{d=1}^{2} \hat{n}_d(l) + \sum_{d=1}^{\alpha-1} \hat{n}_d(n_o)\right] \tag{1.9a}$$

$$\sigma_\alpha^\dagger(n_e) = c_\alpha^\dagger(n_e) \exp\left[i\pi \sum_{l=1}^{n_e-1} \sum_{d=1}^{2} \hat{n}_d(l) + \sum_{d=\alpha+1}^{2} \hat{n}_d(n_e)\right] \tag{1.9b}$$

As doing spin-spin interaction in Eq. (1.5) along the path indicated in the Fig.1.1b, one can map following spin-spin interaction terms onto spinless fermionic operators:

$$\sigma_1^\dagger(2l-1)\sigma_1^-(2l) = c_1^\dagger(2l-1)c_1(2l)e^{-i\hat{\Phi}_1(2l-1)}, \tag{1.10a}$$

$$\sigma_2^\dagger(2l-1)\sigma_2^-(2l) = c_2^\dagger(2l-1)c_2(2l), \tag{1.10b}$$

$$\sigma_2^\dagger(2l)\sigma_1^-(2l) = c_2^\dagger(2l)c_1(2l), \tag{1.10c}$$

$$\sigma_1^\dagger(2l-1)\sigma_2^-(2l-1) = c_1^\dagger(2l-1)c_2(2l-1), \tag{1.10d}$$

$$\sigma_1^\dagger(2l)\sigma_1^-(2l+1) = c_1^\dagger(2l)c_2(2l+1), \tag{1.10e}$$

$$\sigma_2^\dagger(2l)\sigma_2^-(2l+1) = c_2^\dagger(2l)c_2(2l+1)e^{-i\hat{\Phi}_2(2l)}. \tag{1.10f}$$

We write them in the following explicit form:

$$\sigma_\alpha^\dagger(n)\sigma_\alpha^-(n+1) = e^{-i\hat{\Phi}_\alpha(n)}c_\alpha^\dagger(n)c_\alpha(n+1) \tag{1.11}$$

$$\sigma_\alpha^\dagger(n)\sigma_{\alpha+1}^-(n) = c_\alpha^\dagger(n)c_{\alpha+1}(n), \tag{1.12}$$

where we have used the phase term

$$\hat{\Phi}_\alpha(n) = \begin{cases} 0, & \alpha = 1,\ n = 2l \\ 0, & \alpha = 2,\ n = 2l-1 \\ \pi(\hat{n}_2(n) + \hat{n}_2(n+1)), & \alpha = 1,\ n = 2l-1 \\ \pi(\hat{n}_1(n) + \hat{n}_1(n+1)), & \alpha = 2,\ n = 2l \end{cases} \tag{1.13}$$

along the chain and it is the generalized form of the phase term of Eq. (1.7). Those mappings (1.11) and (1.12) and their hermitian conjugates (h.c) are quite useful to fermionize the spin Hamiltonian of the ladder.

For the first time we propose the diagonal path of JW transformation as shown in Fig. 1.2. It is defined as

$$\sigma_n^\dagger = c_n^\dagger \exp\left(i\pi \sum_{\text{path},\ l=1}^{n-1} c_l^\dagger c_l\right) \tag{1.14}$$

with $\sigma_n^z = 2c_n^\dagger c_n - 1$ and $\sigma_n^\pm = \frac{1}{2}(\sigma_n^x \pm i\sigma_n^y)$.

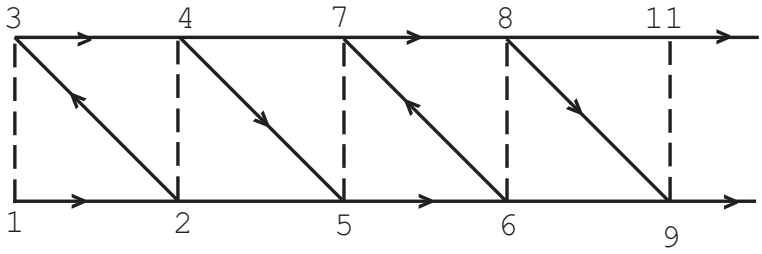

Figure 1.2: Diagonal path of the JW transformation used for the two-leg ladder.

This diagonal JW transformation will be used for the rung-dimerized ladder in chapter 4. Following all the steps described in the snake-like path (see Fig. 1.1b) we obtain two phase terms along the rung and chain

$$\hat{\Phi}(n) = \begin{cases} \pi(\hat{n}_2(n-1), & n = 2l-1 \\ \pi(\hat{n}_1(n+1), & n = 2l \end{cases} \tag{1.15}$$

and

$$\hat{\Phi}_\alpha(n) = \begin{cases} 0, & \alpha = 1,2;\ n = 2l \\ \pi(\hat{n}_2(n-1) + \hat{n}_2(n), & \alpha = 1,\ n = 2l-1 \\ \pi(\hat{n}_1(n+1) + \hat{n}_1(n+2)), & \alpha = 2,\ n = 2l-1 \end{cases} \tag{1.16}$$

respectively.

1.2.2 Mean-field Approximation

The mean-field theory for the quantum spin chains and ladders is in fact the Hatree-Fock approximation for their interacting fermionic terms which appear in the Hamilto-

nian. We use the most general decoupling [89] for the interacting term with a product of two number operators ($\hat{n}_l = c_l^\dagger c_l$):

$$\hat{n}_l\hat{n}_m \approx \hat{n}_l\langle\hat{n}_m\rangle + \hat{n}_m\langle\hat{n}_l\rangle - \langle\hat{n}_l\rangle\langle\hat{n}_m\rangle + \Big(c_l^\dagger c_m\langle c_l c_m^\dagger\rangle - c_l^\dagger c_m^\dagger\langle c_l c_m\rangle\Big) + H.c$$

$$+|\langle c_l c_m^\dagger\rangle|^2 - |\langle c_l c_m\rangle|^2. \tag{1.17}$$

In this work, we only consider next neighbour spin interaction, i.e., $m = l + 1$. Such approximation applied to the Heisenberg chain is known from the literature to be accurate, at least qualitatively, see e.g., [89–94]. We treat the interaction terms of Heisenberg chain via Eq. (1.17):

$$\Big(\hat{n}_n - \frac{1}{2}\Big)\Big(\hat{n}_{n+1} - \frac{1}{2}\Big) = |\mathcal{K}_n|^2 - |P_n|^2 + \frac{1}{4}(m_n + m_{n+1} - m_n m_{n+1})$$

$$-\frac{1}{2}(m_n\hat{n}_{n+1} + m_{n+1}\hat{n}_n) + \mathcal{K}_n c_n^\dagger c_{n+1} - P_n c_n^\dagger c_{n+1}^\dagger + H.c \tag{1.18}$$

where the average terms are

$$\mathcal{K}_n = \langle c_n c_{n+1}^\dagger\rangle \tag{1.19}$$

$$P_n = \langle c_n c_{n+1}\rangle \tag{1.20}$$

$$m_n = \langle 1 - 2c_n^\dagger c_n\rangle \tag{1.21}$$

To deal with interacting terms of the Heisenberg two-leg ladder we introduce one extra label on the fermionic operators of the mean-field Hamiltonian. In doing so one can easily distinguish interacting terms along the chain and along the rung. Following the steps as done in (1.18) we obtain longitudinal decoupling

$$\Big(\hat{n}_\alpha(n) - \frac{1}{2}\Big)\Big(\hat{n}_\alpha(n+1) - \frac{1}{2}\Big) = \mathcal{K}_\alpha(n)c_\alpha^\dagger(n)c_\alpha(n+1) - P_\alpha(n)c_\alpha^\dagger(n)c_\alpha^\dagger(n+1) + H.c$$

$$+|\mathcal{K}_\alpha(n)|^2 - |P_\alpha(n)|^2 - \frac{1}{2}\Big(m_\alpha(n)\hat{n}_\alpha(n+1) + m_\alpha(n+1)\hat{n}_\alpha(n)\Big)$$

$$+\frac{1}{4}\Big(m_\alpha(n) + m_\alpha(n+1) - m_\alpha(n)m_\alpha(n+1)\Big) \tag{1.22}$$

and transverse decoupling

$$\Big(\hat{n}_1(n) - \frac{1}{2}\Big)\Big(\hat{n}_2(n) - \frac{1}{2}\Big) = t_\perp(n)c_1^\dagger(n)c_2(n) + H.c - \frac{1}{2}\Big(m_1(n)\hat{n}_2(n) + m_2(n)\hat{n}_1(n)\Big)$$

$$+\frac{1}{4}\Big(m_1(n) + m_2(n) - m_1(n)m_2(n)\Big) + |t_\perp(n)|^2 \tag{1.23}$$

where the average quantities are

$$\mathcal{K}_\alpha(n) = \langle c_\alpha(n)c_\alpha^\dagger(n+1)\rangle \tag{1.24}$$

$$P_\alpha(n) = \langle c_\alpha(n)c_\alpha(n+1)\rangle \tag{1.25}$$

$$t_\perp(n) = \langle c_1(n)c_2^\dagger(n)\rangle \tag{1.26}$$

$$m_\alpha(n) = \langle 1 - 2c_\alpha^\dagger(n)c_\alpha(n)\rangle \tag{1.27}$$

where α and n are leg and chain indices respectively. Here the parameters $\mathcal{K}_\alpha(n)$, $P_\alpha(n)$ and $t_\perp(n)$ depend on the numbers of chains and legs since dimerizations are considering either along the chain or along the legs.

1.2.3 Spin duality transformation

Spin duality transformation has a remarkable property in the low dimensional quantum system where the spin operators σ of original lattice is translated onto dual spin operators τ's in dual lattice space. In the one-dimensional system their relationships [95] are

$$\sigma_n^x = \tau_{n-1}^x\tau_n^x \tag{1.28}$$

and

$$\sigma_n^y = \prod_{l=1}^{N} \tau_l^x. \tag{1.29}$$

Here τ-s obey the standard algebra (preserve commutation and anti-commutation relations) of Pauli operators, and they reside on the sites of the dual lattice, which can be placed between the sites of the original chain where the operators σ-s reside. N is the number of the original/dual lattice sites. To advance our analysis of spin chains and ladders (to be discussed in next chapters) we use the JW transformations (1.1), (1.8a), (1.8b), and the self-adjoint operators

$$2c_n^\dagger = a_n + ib_n \tag{1.30}$$

with the standard anticommutation relations

$$\{a_n, a_m\} = 2\delta_{nm}, \quad \{b_n, b_m\} = 2\delta_{nm},$$

$$\{a_n, b_m\} = 0. \tag{1.31}$$

Then one can establish the following relations for the inverse JW transformation from the Majorana fermions to the dual spin operators τ (1.28) and (1.29):

$$\sigma_n^x \sigma_{n+1}^x = ib_n a_{n+1} = \tau_{n-1}^x \tau_{n+1}^x \tag{1.32}$$

$$\sigma_n^y \sigma_{n+1}^y = ib_{n+1} a_n = \tau_n^z \tag{1.33}$$

1.2.4 Local and string order parameters

We write the local order parameter [79, 96] of the Heisenberg model as the limit of the spin-spin correlation function in terms of two sublattices, and named as spontaneous

magnetization:

$$m_\alpha^2 = \lim_{n-m\to\infty} \langle \sigma_m^\alpha \sigma_n^\alpha \rangle, \quad \alpha = x, y, z \tag{1.34}$$

In this research we study an asymptotic behaviour spin-spin correlation function and its existence in the different regions of the parametric space of the models.

Now we define the string operators

$$O_n^\alpha = \exp\left[\frac{i\pi}{2} \sum_{k\leftarrow n} \sigma_k^\alpha\right] \tag{1.35}$$

where the summation is carried out along all sites of the string, left from the nth site. In the case of the chain model this is unambiguous and means $k < n$, while for ladders or other models the path of the string must be specified, as we discuss in the following chapter. The string order parameter (SOP) $\mathcal{O}_\alpha$ is determined from the limit $m - n \to \infty$ of the string-string correlation function

$$\left\langle O_m^\alpha O_n^\alpha \right\rangle = (-1)^{m-1} \left\langle \exp\left[\frac{i\pi}{2} \sum_{k=n}^{m-1} \sigma_k^\alpha\right] \right\rangle \tag{1.36}$$

Taking $1 = 1$ and $m = 2l+1$ in (1.36) (note that SOP for odd number of spins vanishes due to symmetry), the SOP is introduced as

$$\mathcal{O}_\alpha^2 = \lim_{l\to\infty} (-1)^l \left\langle \prod_{k=1}^{2l} \sigma_k^\alpha \right\rangle \tag{1.37}$$

In the original proposal by den Nijs and Rommelse [28] and in the subsequent work on the spin chains (see. e.g., [30,33]) the SOP was identified (up to some minor variations) with the limit of the string-string correlation function, which is not convenient, since such SOP has a wrong dimension of square of the order parameter. The definition we use here [97] is more consistent with the standard theory of critical phenomena and is

in line with the definition of the Landau order parameter via a correlation function of local operators. We will show that in the critical region $\mathcal{O}_\alpha \propto |t|^\beta$, where t is a distance from the critical point and the critical index of the order parameter β correctly enters all the scaling relations.

Using the duality transformation (1.28) in equation (1.37) we get

$$\mathcal{O}_x^2 = \lim_{l\to\infty}(-1)^l \langle \tau_0^x \tau_{2l}^x \rangle \tag{1.38}$$

So, the nonlocal SOP defined on the sites of the direct lattice becomes a local order parameter on the dual lattice. This implies that for the phase transitions with nonlocal orders the conventional Landau framework can be recovered via duality.

1.2.5 Brane operators and order parameters

The string operators and order parameters were generalized for two-leg spin ladders [13–16, 98, 99]. However it is more consistent to use the concept of the brane order to go beyond one spatial dimension [59, 65, 67–72].

We define an even brane operator which includes the area (brane) with an integer number of legs:

$$\mathcal{B}_e^i(n) \equiv \prod_{\alpha=1}^{2}\prod_{l=1}^{n} \sigma_\alpha^i(l), \quad i = x, y, z \ , \tag{1.39}$$

and the odd brane operator which includes one "loose" extra spin at the far right end:

$$\mathcal{B}_{o,\alpha}^i(n) \equiv \mathcal{B}_e^i(n-1)\sigma_\alpha^i(n), \quad \alpha = 1, 2. \tag{1.40}$$

We also define the corresponding brane-brane correlation functions which are calculated

in the following: the even-even correlator

$$\langle \mathcal{B}^i_e(m)\mathcal{B}^i_e(n)\rangle \ , \tag{1.41}$$

the mixed correlators

$$\langle \mathcal{B}^i_e(m)\mathcal{B}^i_{o,\alpha}(n)\rangle \ \text{ and } e \leftrightarrow o \ , \tag{1.42}$$

and the odd-odd correlation function

$$\langle \mathcal{B}^i_{o,\alpha}(m)\mathcal{B}^i_{o,\beta}(n)\rangle \ . \tag{1.43}$$

Those brane-brane correlators are schematically depicted in Fig. 1.3. In the following we will also encounter the brane correlation function of the operator

$$\mathcal{B}^z_e(n-1)\sigma^x_1(n)\sigma^y_2(n) \ \text{ and } x \leftrightarrow y \ , \tag{1.44}$$

which is the even z-brane with the x and y spins attached to its far right edge.

The brane order parameters (BOPs) are defined as non-vanishing limits of corresponding brane-brane correlation functions as $m - n \to \infty$.

1.2.6 Topological winding number

In the previous subsection we have presented the local, non-local and brane order parameters to characterize conventional and topological phases in the spin chains and ladders. In addition, the topological phases can be classified by defining the other topological number called winding number or Pontryagin index. It counts the number of loops formed by the renormalized vectors in the topological phases over the Brillouin zone by wrapping the phases about the center of the complex plane. Those renormal-

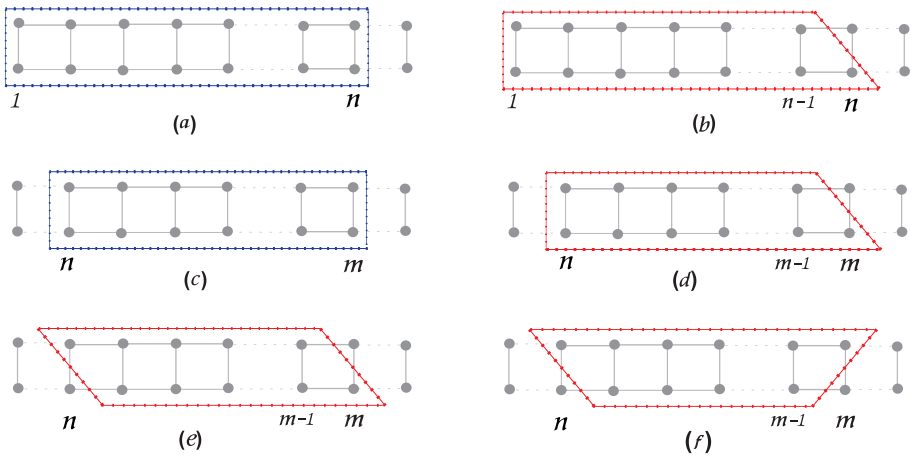

Figure 1.3: Branes and brane-correlation functions: (a) and (b) depict an even/odd brane, resp., for (b) another odd brane may be obtained by reflection with respect to horizontal axis; (c)- even-even brane correlators; (d)-even-odd brane correlator; (e), (f)- odd-odd brane correlators. The odd-even and odd-odd brane correlators can also correspond to other graphs obtained from cases (d-f) by reflections with respect to horizontal/vertical axes.

ized vectors in the complex plane can be found from the spectrum of the model in momentum space.

It has been shown in the recent years that many quantum phase transitions with hidden orders are accompanied by a change of topological numbers [4, 24]. Here we calculate the winding number (or the Pontryagin index) in all regions of the model's phase diagram. Such parameters were calculated recently in similar 1D models, see, e.g., [35, 37, 38, 59, 73, 74, 100–103]. Following the formalism of [104] we rewrite model's Hamiltonian as a Bogoliubov-de Gennes Hamiltonian matrix

$$\mathcal{H}(k) = \begin{pmatrix} \hat{A} & \hat{B} \\ \hat{B}^{\dagger} & -\hat{A} \end{pmatrix} \tag{1.45}$$

By unitary transformation the Hamiltonian (1.45) can be brought to the block

off-diagonal form

$$\mathcal{H}_k = \begin{pmatrix} 0 & \hat{D}(k) \\ \hat{D}^\dagger(k) & 0 \end{pmatrix} \tag{1.46}$$

with operator

$$\hat{D}(k) = \hat{A}(k) + \hat{B}(k) \tag{1.47}$$

which has two eigenvalues $\lambda_\pm$. For the Hamiltonian matrix of this type the winding number is defined as the following integral over the Brillouin zone [104]

$$N_\omega = \frac{1}{2\pi i} \int_{-\pi/2}^{\pi/2} dk [\partial_k \ln \det \hat{D}] \tag{1.48}$$

can be readily calculated for any model as

$$N_\omega = \frac{1}{2\pi i} \arg[\lambda_+(k) + \lambda_-(k)|_{\frac{\pi^+}{2}}^{\frac{\pi^-}{2}} \tag{1.49}$$

Another angle of analysis [59] can be presented upon analytical continuation of the wave numbers on the complex plane: $e^{i2k} = z$. Then the winding number (1.48) becomes

$$N_\omega = \frac{1}{2\pi i} \oint_{|z|=1} dz [\partial_z \ln \det \hat{D}] \tag{1.50}$$

It accounts for the excess of the number of zeros over the number poles (weighted with their degrees of multiplicity) of $\det \hat{D}$ inside the unit circle on the complex plane [59, 105]. In a quantum model the zeros of $\det \hat{D}$ are also zeros of the spectra $E_\pm$ of the model, since $(E_+E_-)^2 = \det \hat{D}\hat{D}^\dagger$. Any change of winding number means that a root crossed the unit circle $|z| = 1$, which signals a quantum phase transition [59, 106]. For the considered models we find

$$\det \hat{D}(z) = f(z)(z - z_+)(z - z_-), \tag{1.51}$$

where $z_{\pm}$ are the roots of the quadratic equation of z derived from the spectrum of the model and $f(z)$ is a function of z consisting with the parameters of the Hamiltonian.

As discussing above one can be viewed N_{ω} as a complementary parameter in characterizing topological gapped phases.

1.3 Organisation of this thesis

This thesis is organized in six chapters as described below:

1. **Chapter 2:** In this chapter, which covers publication (II) and a section of publication (I), we present the ground state properties of the dimerized XY chain with the uniform and the modulated transverse fields. In the section 2.1, we introduce the spin and fermionic representations of the model. We also discuss its spectrum, phase diagram, and the field-induced magnetization. Section 2.2 contains the main results of the model. We present the formalism, the calculation of the spontaneous magnetisation (local order parameter) for the magnetic phase, the string order parameter for the topological phase, and the winding numbers. We analytically discuss dimerized XY chain at zero field ($h = h_a = 0$) in the section 2.3. Using the duality transformation, the SOPs and local order parameters are calculated exactly. We also find the winding numbers for the different phases of the model.

2. **Chapter 3:** Within this chapter that covers publication (III), it additionally contains descriptions of ground state properties of dimerized XYZ chain in the uniform and staggered magnetic fields. In section 3.1, we introduce the analogous fermionic representation of the interacting ($\Delta \neq 0$) model and present spectrum, phase diagram, and some average quantities. Those are building blocks

to be used in the effective Hamiltonian, and in the mean-field equations. Section 3.2 presents the derivation of the mean field equations, renormalized parameters, and the renormalized effective Hamiltonian of the model by using the mean-field (Hartee-Fock) approximation. Section 3.3 contains the results for the XYZ chain. We present the phase diagram, mean-field parameters, spontaneous magnetization, local, nonlocal order parameters, and winding numbers for each phase. Section 3.4 presents the results for the isotropic XXZ limit of the model. Since more analytical work can be done in this limit, more qualitative discussions of the results are presented, including the role of interaction, robustness of the mean-field approximation, and a relation of the reported topological orders to earlier findings of the spontaneous magnetism in this model. The algebraically ordered incommensurate gapless phase for interacting and noninteracting models are analyzed in this section as well.

3. **Chapter 4:** This chapter is about the ground state properties of the dimerized two-leg ladder with modulated transverse magnetic field. In a section 4.2, we introduce the field dependence fermionic effective Hamiltonian with the renormalized parameters, using the mean-field (Hartee-Fock) approximation. In section 4.3, we study the conditions of quantum criticalities and analyze phase diagrams of the isotropic two-leg ladders in three dimerization patterns such as staggered, columnar and rung-dimerization. Using the explicit expression of field-induced magnetization, we plot the magnetization curve versus bare magnetic field. Those calculations were done numerically by determining the renormalized parameters self-consistently from the minimization of the model's free energy. The appearance of magnetization plateaus in the magnetization curve is the peculiar property of the isotropic ladder. The number of gapped plateaus and Luttinger-liquid (LL) gapless phases we found here depend on the type of the ladder we use. In-

terestingly, those results that we found in the different isotropic ladders are in a good agreement with the quantized condition for the magnetization plateaus. In section, 4.4 we apply the technical details of the Hatree-Fock mean-field approximation, which maps the spin Hamiltonian of ladders onto their quadratic effective fermionic Hamiltonians. In all possible cases, thee sets of related mean-field parameters of Hamiltonians are calculated explicitly by determining renormalized parameters from the minimization of their free-energies.

The manuscript based on the results of this chapter is in preparation.

4. **Chapter 5:** In this chapter, which covers the publication (IV) and a part of publication (I), we study the ground state properties of the anisotropic two-leg ladder. In section 5.1, spin Hamiltonian is defined, and the quadratic effective fermionic Hamiltonian is introduced along with its mean-field (renormalized) parameters. Section 5.2 contains most of the formalism on spectra, phase diagram and dual model. Our new findings suggest that there is a possibility of quantum phase transition in columnar ladder with appropriate anisotropic parameter which have interesting potential experimental predictions. Section 5.3 explains most of the formalism of mapping onto the dual space and all results coming from those calculations. The calculation of topological winding numbers for the different phases is given in section. 5.4. The derivation of the quadratic fermionic effective Hamiltonian and details on the mean-field equations are presented in section 5.5. In section 5.6, we present the analogous results of the dimerized two-leg ladder at its isotropic limit $\gamma = 0$.

5. **Chapter 6:** Finally, this chapter summarizes the results obtained and presented in this thesis briefly, and provides some future directions.

6. **Appendix:** In Appendix A, the mean-field parameters are found explicitly from

minimization of the free energy. Those equations take into account the flux correction term v at each plaquette of the lattice, which is a new analytical result. Appendix B contains several new exact results for the order parameters in the XY chain with transverse fields, which are applied to calculate the brane orders. The Appendix C contains details on the order parameter calculation for the quantum Ising chain with the three-spin interaction.

1.4 Contributions

This thesis is mainly based on the following publications and presentations:

1.4.1 Publications

I. *Constructing Landau Framework for Topological Order: Quantum Chains and Ladders*, Gennady Y. Chitov and Toplal Pandey, J.Stat. Mech., 043101 (2017);

This work has been done in collaboration with Prof. Gennady Y. Chitov;

II. *String and Conventional Order Parameters in the Solvable Modulated Quantum Chain*, Gennady Y. Chitov, Toplal Pandey, and P. N. Temonin, Phys. Rev. B **100**, 104428 (2019);

This work has been done in collaboration with Prof. Gennady Y. Chitov and the late Dr. P. N. Timonin from Physics Research Institute at Southern Federal University, Russia;

III. *Phase Diagram and Topological Order in the Modulated XYZ Chain with the Magnetic Field*, Toplal Pandey, and Gennady Y. Chitov, Phys. Rev. B **102**, 054436 (2020);

This work has been done in collaboration with Prof. Gennady Y. Chitov;

IV. *Brane order and quantum magnetism in modulated anisotropic ladders*, Toplal Pandey, and Gennady Y. Chitov, arXiv:2111.09813v1 (2021).

This work, which is under review and has not been published yet, has been done in collaboration with Prof. Gennady Y. Chitov.

1.4.2 Presentations

done by the PhD candidate:

I. *Quantum Phase Transition and Hidden Topological Orders in low-dimensional Magnetics*, CAP congress, Montreal, Canada (2013);

II. *Quantum Phase Transition and Hidden Topological Orders in low-dimensional Magnetics*, CAP congress, Sudbury, Canada (2014);

III. *Constructing Landau Framework for Topological Order: Quantum Chains and Ladders*, International Conference in Physics, Lyon, France (2016);

IV. *String and Local Order Parameters in the Solvable Modulated Quantum Chain*, CAM conference in Physics, Sudbury, Canada (2019);

Chapter 2

Dimerized XY Chain in Modulated Magnetic Field.

In this chapter, we study the exactly solvable anisotropic dimerized XY spin-1/2 chain in the uniform and staggered transverse magnetic fields. In order to solve the model and find such quantities as energy spectrum, ground state energy, and gapped phases etc, we use the JW transformation. The advantage of using such transformation is that it always preserves the spin commutation relations. It maps the spin-1/2 operators onto the non-interacting spinless fermion operators in the model's Hamiltonian. From the spectrum we identify commensurate and incommensurate phases in the phase diagram. We also present field induced magnetisation, spontaneous magnetisation (local order parameter) via Bogoliubov transformation and Majorana operators. In this chapter, we also discuss the formalism to calculate the spontaneous magnetisation for the magnetic phase and string order parameters SOPs (hidden orders), and winding numbers for the different topological phases.

2.1 Model

2.1.1 Spin and fermionic representation of the model

To analyse the various aspects of the conventional Landau and the topological orders we define the model and recapitulate its main results known explicitly and implicitly from the earlier work. The spin Hamiltonian of the model is the dimerized quantum XY chain in the presence of uniform (h) and alternating (h_a) transverse magnetic fields:

$$H = \sum_{n=1}^{N} \frac{J}{4}\{[1+\gamma+\delta(-1)^n]\sigma_n^x\sigma_{n+1}^x + [1-\gamma+\delta(-1)^n]\sigma_n^y\sigma_{n+1}^y\}$$

$$+\frac{1}{2}[h+(-1)^n h_a]\sigma_n^z. \tag{2.1}$$

Here σ are the standard Pauli matrices, J is the nearest-neighbour exchange coupling, and γ and δ are the anisotropy and dimerization parameters, respectively. This exactly solvable model was first introduced and analyzed by Perk,*et al.* [63]. (See also [35,107–110] for related more recent work on the versions of this model.). The standard JW transformation (1.1) [79,111] maps (2.1) onto the free fermionic Hamiltonian

$$H = \sum_{n=1}^{N} \frac{J}{2}\{[1+\delta(-1)^n](c_n^\dagger c_{n+1} + h.c) + \gamma(c_n^\dagger c_{n+1}^\dagger + h.c)\}$$

$$+[h+(-1)^n h_a]\Big(c_n^\dagger c_n - \frac{1}{2}\Big) \tag{2.2}$$

called in recent literature the (modulated) Kitaev chain [112]. In the fermionic representation (2.2) the chain has dimerized hopping and modulated chemical potential. So weather we deal with the modulated XY spin or the Kitaev fermionic chains, is a matter of more convention, especially since the results below will be given in terms of spins or fermions, on the same footing. The fermionic operators c_n in Eq. (2.2) obey the

canonical anticommutation relation, where as spin operators σ_n satisfy commutation algebra of Pauli matrices.

We utilize the duality transformations (1.28) and (1.29) [95, 113]. This transformation maps (2.1) onto the dual spin Hamiltonian

$$H = H_e + H_o + H_{mix} \tag{2.3}$$

where,

$$H_e = \frac{J}{4}\sum_{l=1}^{N/2}(1+\gamma-\delta)\tau_{2l-2}^{x}\tau_{2l}^{x} + (1-\gamma+\delta)\tau_{2l}^{z} \tag{2.4a}$$

$$H_o = \frac{J}{4}\sum_{l=1}^{N/2}(1+\gamma+\delta)\tau_{2l-1}^{x}\tau_{2l+1}^{x} + (1-\gamma-\delta)\tau_{2l-1}^{z} \tag{2.4b}$$

$$H_{mix} = -\frac{i}{2}\sum_{l=1}^{N}[h+(-1)^{n}h_a])\tau_{n-1}^{x}\tau_{n}^{x}\prod_{m=n}^{N}\tau_{m}^{z}(1-\gamma+\delta)\tau_{2l}^{z} \tag{2.4c}$$

which is sum of two one-dimensional ($1D$) transverse Ising models residing on the even and odd sites of the dual lattice, plus the field-induced $\mathbb{Z}_2 \bigotimes \mathbb{Z}_2$ symmetry-breaking term H_{mix} which couples the even and odd sectors of the dual τ Hamiltonian.

2.1.2 Spectrum

The next step to diagonalize the Hamiltonian is to apply the fourier transform for even and odd sites of the chain. We define even and odd transformations as

$$c_{2l}^{\dagger} = \frac{1}{\sqrt{N}}\sum_{k} e^{i(2l)k}c_{e}^{\dagger}(k) \tag{2.5a}$$

$$c_{2l-1}^{\dagger} = \frac{1}{\sqrt{N}}\sum_{k} e^{i(2l-1)k}c_{o}^{\dagger}(k) \tag{2.5b}$$

where k is the wavenumber which is continuous variable and runs over the first Brillouin zone $[-\pi/2, \pi/2]$. For system with more than one species of fermions it is convenient to use the Nambu formalism [114]. After Fourier transformation, the fermionic Hamiltonian (2.2) takes the form of single particle Hamiltonian:

$$H = \frac{1}{2}\sum_{k} \Psi_k^\dagger \mathcal{H}_k \Psi_k \tag{2.6}$$

where the fermions are unified in the spinor

$$\Psi_k^\dagger = \left(c_1^\dagger(k), c_2^\dagger(k), c_1(-k), c_2(-k)\right) \tag{2.7}$$

where we have used $c_{e/o}(k) = \frac{1}{\sqrt{2}}[c_1(k) \pm c_2(k)]$. Thus the JW fermions in the coordinate representation (2.2) becomes

$$c_n^\dagger = \frac{1}{\sqrt{N}}\sum_{\alpha,k} c_\alpha^\dagger(k)(-1)^{(\alpha-1)n} e^{ikn} \tag{2.8}$$

For simplicity, we set the lattice specing a=1 and band index $\alpha = 1, 2$. The 4×4 Hamiltonian matrix (we set $J = 1$ from now on) can be written as

$$\mathcal{H}_k = \begin{pmatrix} \hat{A} & \hat{B} \\ \hat{B}^\dagger & -\hat{A} \end{pmatrix} \tag{2.9}$$

with

$$\hat{A} \equiv \begin{pmatrix} h + \cos k & h_a + i\delta \sin k \\ h_a - i\delta \sin k & h - \cos k \end{pmatrix} \tag{2.10}$$

and

$$\hat{B} \equiv \begin{pmatrix} -i\gamma \sin k & 0 \\ 0 & i\gamma \sin k \end{pmatrix} \tag{2.11}$$

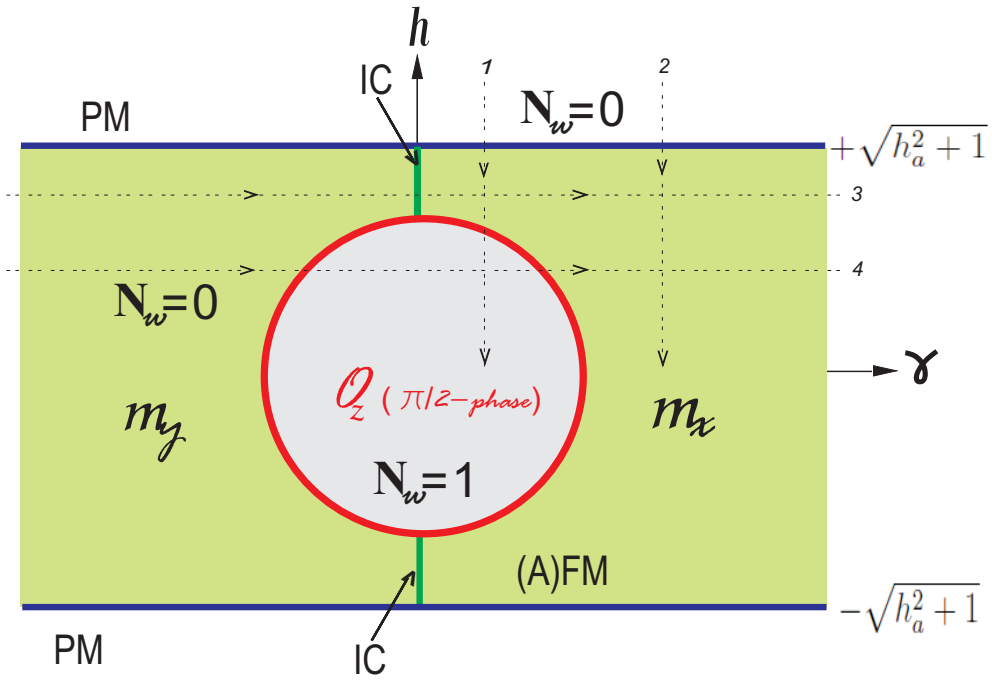

Figure 2.1: Phase diagram of the model in h-γ plane. The model is critical (i) on two infinite lines $h = \pm h_c^{(1)}$ (dark blue, $h_c^{(1)} = \sqrt{h_a^2 + 1}$); (ii) on the circle $h^2 + \gamma^2 = \mathcal{R}^2$ (bold red, radius $\mathcal{R} = \sqrt{h_a^2 + \delta^2}$); and (iii) on two line segments $\sqrt{h_a^2 + \delta^2} \leq |h| \leq \sqrt{h_a^2 + 1}$ at $\gamma = 0$ (bold green). Depending on the sign of the spin coupling J, the local order $m_{x,y}$ can be ferro- or antiferromagnetic. Three phases: disordered paramagnetic (PM), (anti)ferromagnetic, and topological with modulated string order parameter O_z are shown. The four paths (1-4) in the parametric space used for the calculation of magnetisation and string order parameters are indicated by thin dashed lines. The winding numbers N_w calculated in the Subsection 2.2.4 are also shown.

From the explicit expression (2.9), eigenvalues [63] $\pm E_\pm(k)$ are found

$$E_\pm(k) = \sqrt{\mathfrak{C}_2(k) \pm \sqrt{\mathfrak{C}_2^2(k) - \mathfrak{C}_4(k)}}, \tag{2.12}$$

with

$$\mathfrak{C}_2(k) = h^2 + h_a^2 + \cos^2 k + (\delta^2 + \gamma^2) \sin^2 k \tag{2.13}$$

and

$$\mathfrak{C}_4(k) = \Big[h^2 - h_a^2 - \cos^2 k - (\delta^2 - \gamma^2)\sin^2 k\Big]^2 + (\gamma \sin 2k)^2 \tag{2.14}$$

The Hamiltonian (2.6) reduced to the diagonal form

$$H = \sum_{\alpha,k} E_\alpha(k)\Big[\eta_\alpha\dagger(k)\eta_\alpha(k) - \frac{1}{2}\Big] \tag{2.15}$$

where $\eta_\alpha(k)$ is the new set of fermionic operators defined by a unitary transformation on the pair c_n which will be discussed in detail in the next subsection.

2.1.3 Phase diagram

The phase diagram of the model was first introduced by Perk *et.al.* [63]. See also [64] for the recent review. The critical lines where the model becomes gapless, are determined by the condition $\mathfrak{C}_4(k)$=0. Compare Eqs. (2.12) and (2.14) and Fig.2.1. There are three phase boundaries:

(i)At

$$h = \pm\sqrt{h_a^2 + 1}, \qquad \forall\ \gamma, \delta \tag{2.16}$$

the gap vanishes at the center of the Brillouin Zone (BZ) ($k = 0$).

(ii) At the edge of the BZ ($k = \pi/2$) the gap vanishes on the circle

$$h^2 + \gamma^2 = h_a^2 + \delta^2. \tag{2.17}$$

(iii) Two critical line segments at $\gamma = 0$ correspond to the gap vanishing at the incommensurate (IC)wave vector

$$k_c = \pm \arcsin\sqrt{\frac{1 + h_a^2 - h^2}{1 - \delta^2}} \tag{2.18}$$

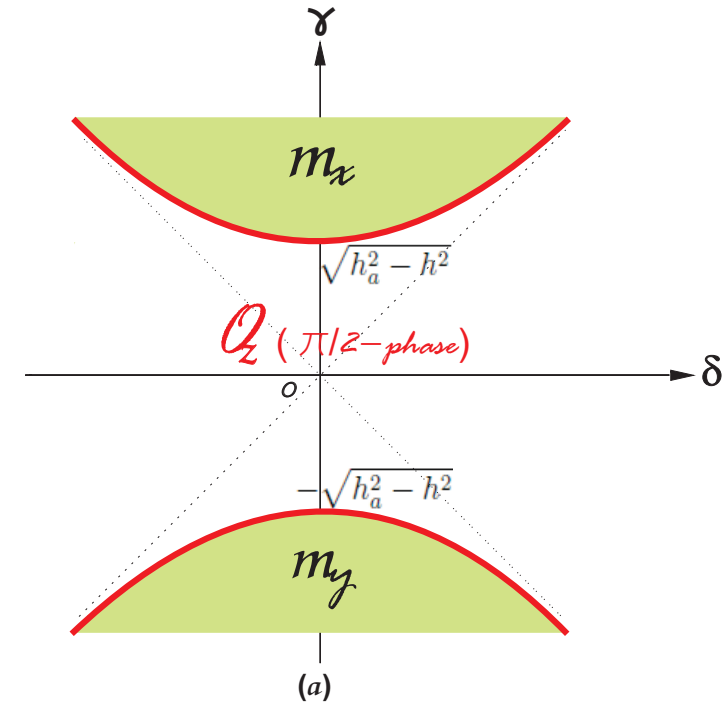

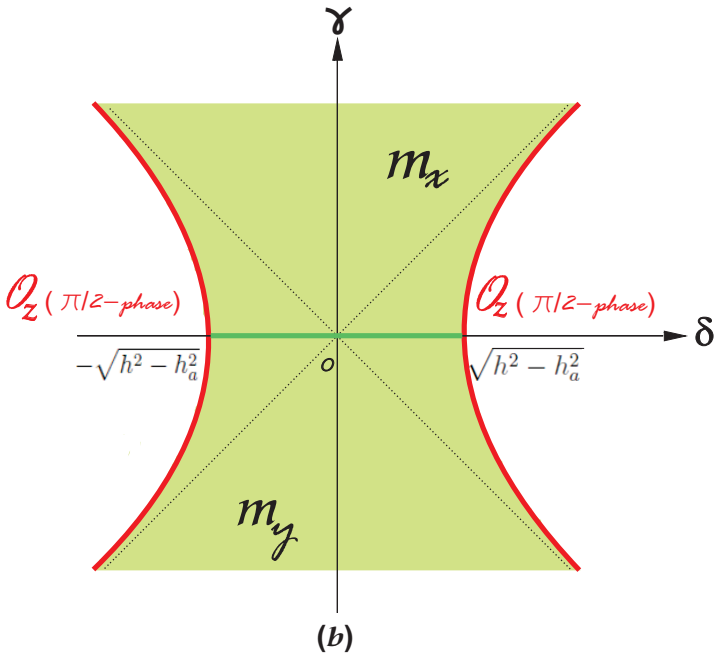

Figure 2.2: The boundaries (bold red) (2.17) between the phases with local order $m_{x,y}$ and the $\pi/2$-modulated topological string order O_z in δ-γ plane for the case of $h < h_a$ (upper figure) and $h > h_a$ (lower figure). The bold green line shown in the lower figure indicates the phase boundary $\gamma = 0$ where the gap vanishes at the IC wave vector (2.18) (compared to Fig. 2.1). The two thin dotted lines $\gamma = \pm\delta$ are the phase boundaries in the limit $h = h_a = 0$, studied in the earlier work [35].

Here, the IC solution exists in the range of parameters:

$$\gamma = 0, \quad |\delta| < 1 \quad \text{and} \quad \sqrt{h_a^2 + \delta^2} \leq |h| \leq \sqrt{h_a^2 + 1} \tag{2.19}$$

The wave vector (2.18) varies continuously from $k_c = 0$ at the intersection of $\gamma = 0$ and $h = \pm\sqrt{h_a^2 + 1}$ to $k_c = \pm\pi/2$ where the critical segments end at the intersections with the circle.

It is useful to plot the phase boundaries (2.17) in the γ-δ plane, especially keeping in mind connection to the earlier work [35]. This phase diagram is shown in Fig. 2.2.

2.1.4 Field-induced magnetizations and susceptibility

Differentiation of the free energy with respect to h and to h_a yield magnetisations

$$m_z = \frac{1}{N}\sum_{n=1}^{N}\langle\sigma_n^z\rangle \tag{2.20a}$$

$$m_z^a = \frac{1}{N}\sum_{n=1}^{N}(-1)^n\langle\sigma_n^z\rangle, \tag{2.20b}$$

respectively [63]. At zero temperature the explicit expressions are

$$m_z = \frac{h}{\pi}\int_0^{\frac{\pi}{2}}\Big[\Big(\frac{1}{E_+}+\frac{1}{E_-}\Big) + \frac{\cos^2 k + |\omega_a|^2}{\sqrt{h^2\cos^2 k + |\omega|^2|\omega_a|^2}}\Big(\frac{1}{E_+}-\frac{1}{E_-}\Big)\Big]dk \tag{2.21}$$

and

$$m_z^a = \frac{h_a}{\pi}\int_0^{\frac{\pi}{2}}\Big[\Big(\frac{1}{E_+}+\frac{1}{E_-}\Big) + \frac{|\omega|^2}{\sqrt{h^2\cos^2 k + |\omega|^2|\omega_a|^2}}\Big(\frac{1}{E_+}-\frac{1}{E_-}\Big)\Big]dk \tag{2.22}$$

where we defined the auxiliary parameters:

$$\omega = h + i\gamma \sin k \quad \text{and} \quad \omega_a = h_a + i\delta \sin k \tag{2.23}$$

The physics becomes more transparent if we introduce two magnetizations on even/odd sublattices $m_z^{e/o}$ as

$$m_z = \frac{1}{2}(m_z^e + m_z^o) \quad \text{and} \quad m_z^a = \frac{1}{2}(m_z^e - m_z^o). \tag{2.24}$$

The differentiation of magnetization with respect to magnetic field h gives the susceptibility [63]

$$\begin{aligned}\chi = \frac{1}{\pi}\int_0^{\frac{\pi}{2}} \Big[&- h^2\Big(\frac{1}{E_+^3} + \frac{1}{E_-^3}\Big)\Big(1 + \Big(\frac{\cos^2 k + |\omega_a|^2}{R}\Big)^2\Big) + \Big(\frac{1}{E_+} + \frac{1}{E_-}\Big) \\ &+\Big(\frac{1}{E_+} - \frac{1}{E_-}\Big)\Big(\frac{\cos^2 k + |\omega_a|^2}{R}\Big)\Big(1 - \frac{h^2}{R^2}(\cos^2 k + |\omega_a|^2)^2\Big) \\ &-2h^2\Big(\frac{\cos^2 k + |\omega_a|^2}{R}\Big)\Big(\frac{1}{E_+^3} - \frac{1}{E_-^3}\Big)\end{aligned} \tag{2.25}$$

where we have used the notation

$$R = \sqrt{h^2 \cos^2 k + |\omega|^2 |\omega_a|^2} \tag{2.26}$$

We plot all four field-induced magnetizations as functions of the uniform component of the magnetic field h in the Fig. 2.3. Two cases need to be distinguished. The first case shown in Fig. 2.3a corresponds to the variation of the field h along the path 1 on the phase diagram in the h-γ plane shown in Fig. 2.1. The path crosses the paramagnetic phase (PM) and ferromagnetic phase (FM) at the boundary $h{=}h_c^{(1)}{=}\sqrt{h_a^2+1}$ and the boundary between the ferromagnetic and topological phases at $h{=}h_c^{(2)}{=}\sqrt{h_a^2+\delta^2-\gamma^2}$.

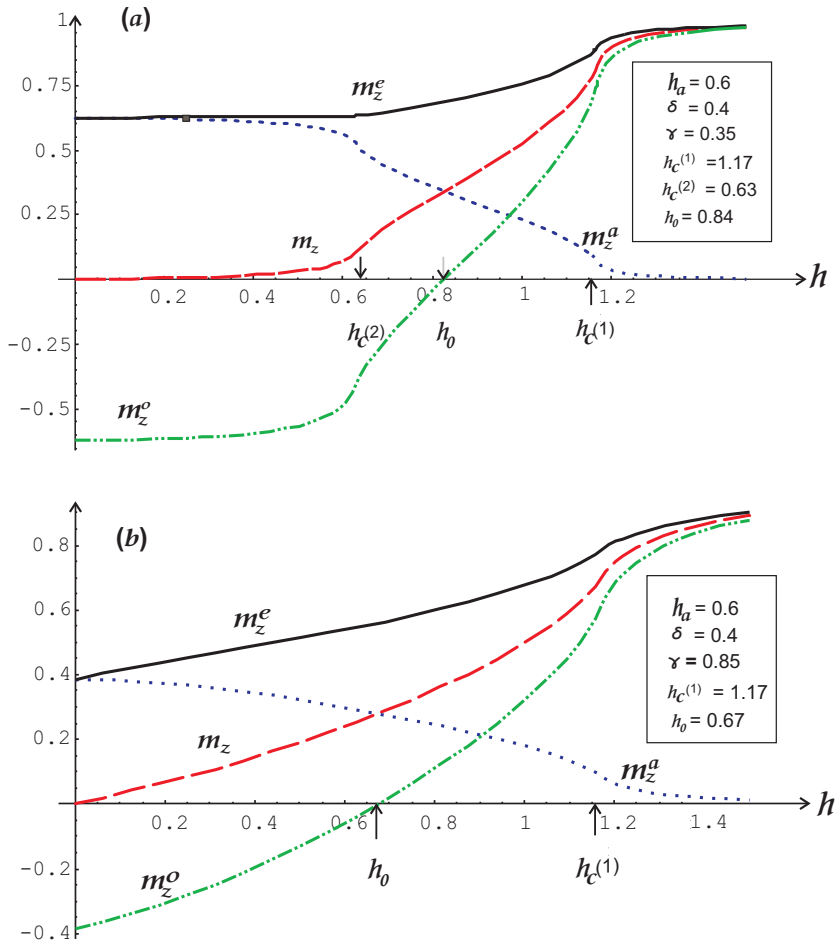

Figure 2.3: Four magnetisations vs uniform magnetic field h at $\delta = 0.4$ and fixed value of the alternated magnetic field $h_a = 0.6$ for two values of γ. At (a) $\gamma = 0.35$ and the field h takes the path 1 shown in the phase diagram Fig. 2.1. It crosses the phase boundaries at $h = h_c^{(1)} = 1.17$ and $h = h_c^{(2)} = 0.63$ where the cusps are noticable. The intermediate point $h_0 = 0.84$ where the odd sublattice magnetization vanishes and the induced magnetic pattern changes from ferrimagnetic to antiferrimagnetic (see Fig. 2.4 is not related to any singularities. The induced order becomes antiferomagnetic at $h = 0$. At (b) the path 2 of the field h (see Fig. 2.1) does not cross the critical circle at $\gamma = 0.85$. The magnetizations demonstrate cusps at the only critical point $h_c^{(1)}$, while at $h < h_c^{(1)}$, including the point $h = h_0 = 0.67$ of the induced pattern switch, the magnetizations are smooth.

The magnetizations have noticeable cusps at these critical points [63].

By using Eq. (2.25) we plot the field-induced susceptibility in Fig. 2.5a. Two logarithmic singularities are obtained at two critical fields $h_c^{(1)}$ and $h_c^{(2)}$. At the intermediate field h_0 (its value is available numerically only) the odd sublattice magnetization vanishes and the induced magnetic pattern changes from ferrimagnetic to antiferrimagnetic (see Fig.2.4). This point is not related to any singularities in the magnetizations or their derivatives.

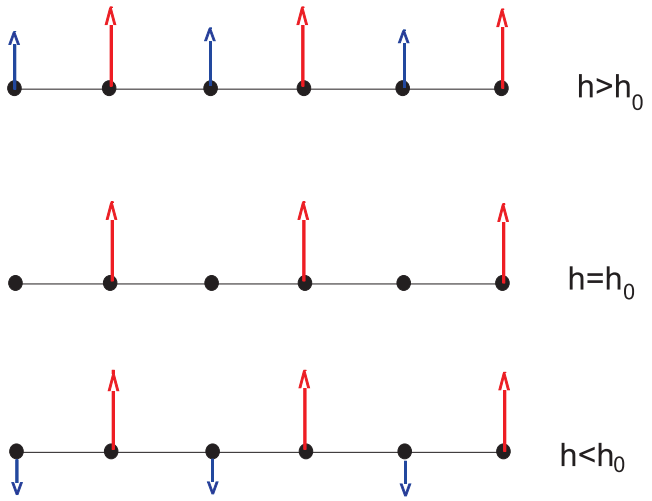

Figure 2.4: Visualization of the field-induced magnetization at different values of uniform external field h as presented in Fig. 2.3. The red/blue spins contribute to the even/odd transverse magnetizations, respectively. The pattern evolves smoothly with h from ferrimagnetic ordering $h > h_0$ to antiferrimagnetic at $h < h_0$ passing through the point $h = h_0$ where the magnetization on the odd sites m_z^o vanishes.

The second case shown in Figs. 2.3b and 2.5b correspond to the path 2 on the phase diagram. It crosses only the PM-FM phase boundary and bypasses the topological phase. The magnetizations demonstrate cusps at the only critical point $h_c^{(1)}$, while at $h < h_c^{(1)}$, including the point h=h_0=0.6758 of the induced pattern switch, the magnetizations. There is only one singularity of susceptibility if it crosses the phase boundary $h_c^{(1)}$ (see Fig. 2.5b for detail).

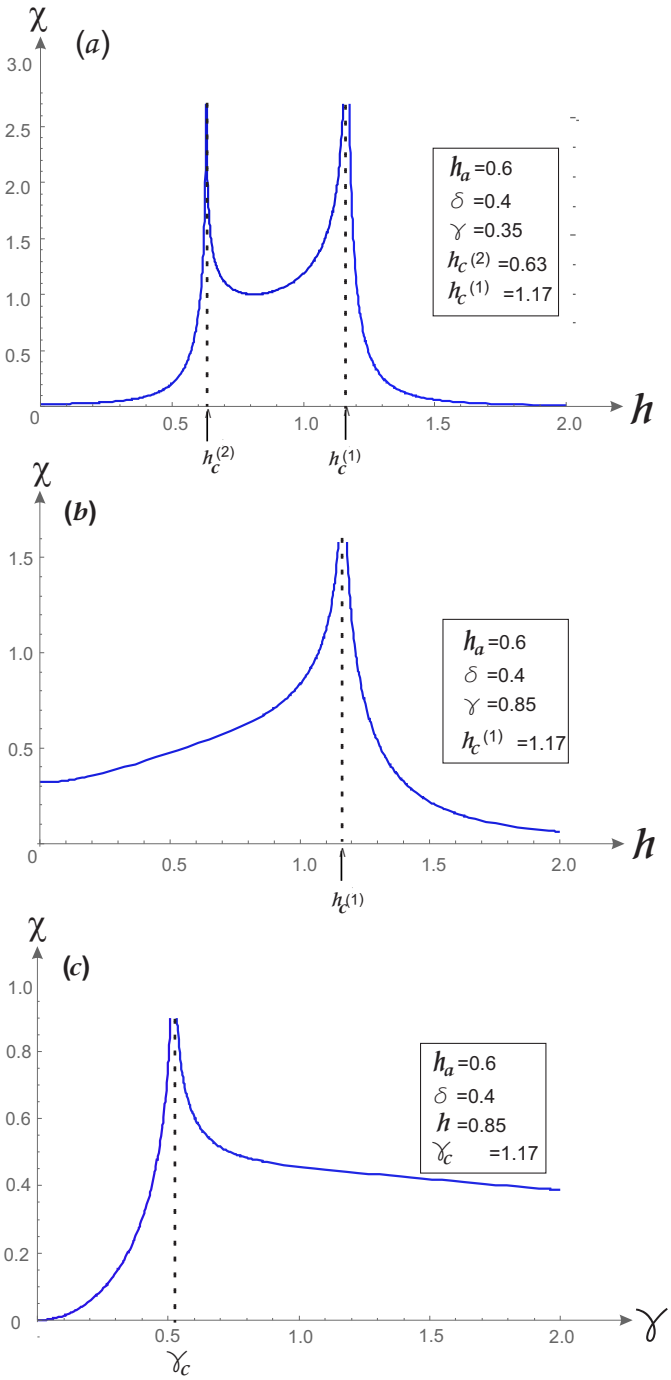

Figure 2.5: Magnetic susceptibility vs uniform magnetic field h at $\delta = 0.4$ and fixed value of alternated magnetic field $h_a = 0.6$ for two values of γ. (a) $\gamma = 0.35$ and the field h takes the path 1 shown in the phase diagram Fig. 2.1 where two singularities appear at $h_c^{(1)} = 1.17$ and $h_c^{(2)} = 0.63$. At (b) the path 2 of the field h (see Fig. 2.1) does not cross the critical circle at $\gamma = 0.85$. The susceptibility demonstrates the divergence at only a critical point $h_c^{(1)}$, and becomes continuous elsewhere. (c) Along the path 3 of the phase diagram (2.1) at $h = 0.3$ the susceptibility becomes singular at $\gamma_c = 0.52$ and continuous elsewhere along γ axis.

We also consider the path 3 of the phase diagram (2.1) where it crosses topological-FM phases at the phase boundary γ_c=$\sqrt{h_a^2+\delta^2-h^2}$; $\gamma \geq 0$. In this case the susceptibility is asymptotic at the γ_c as shown in the Fig. 2.5c. The main conclusions following from the analysis of the field-induced magnetization are: (i) the magnetization cusps translate into corresponding diverging susceptibilities to probe the critical points (phase boundaries); (ii) the vanishing odd sublattice magnetization m_z^o and related change of direction of the odd magnetization at the intermediate field h=h_0 do not constitute a critical point; (iii) the components of transverse magnetization cannot probe the order (or serve to build up a local order parameter) of the phase lying inside the circle shown in Fig. 2.1.

2.2 Order parameters

2.2.1 Bogoliubov transformation and Majorana operators

To diagonalize Hamiltonian (2.6) in terms of new fermionic operators $\eta_\alpha(k)$, we follow the procedure introduced in [79] and utilize the Bogoliubov transformation within the formalism worked out in [109]:

$$c_\alpha(k)=\sum_\beta \Big(\frac{\psi^*_{\beta\alpha}(k)+\phi^*_{\beta\alpha}(k)}{2}\Big)\eta_\beta(k)+\Big(\frac{\psi^*_{\beta\alpha}(k)-\phi^*_{\beta\alpha}(k)}{2}\Big)\eta^\dagger_\beta(-k) \tag{2.27a}$$

$$c^\dagger_\alpha(-k)=\sum_\beta \Big(\frac{\psi^*_{\beta\alpha}(k)+\phi^*_{\beta\alpha}(k)}{2}\Big)\eta^\dagger_\beta(-k)+\Big(\frac{\psi^*_{\beta\alpha}(k)-\phi^*_{\beta\alpha}(k)}{2}\Big)\eta_\beta(k) \tag{2.27b}$$

where $\psi_{\beta\alpha}(k)$ and $\phi_{\beta\alpha}(k)$ are eigen matrices satisfy the conditions:

$$\psi^*_{\beta\alpha}(-k)=\psi_{\beta\alpha}(k) \tag{2.28a}$$

$$\phi^*_{\beta\alpha}(-k) = \phi_{\beta\alpha}(k) \tag{2.28b}$$

It is convenient to introduce the Majorana fermions

$$a_n + ib_n = 2c_n^\dagger \tag{2.29}$$

Using Eqs. (2.8), (2.27), and (2.29) the Majorana fermions can be expressed as

$$a_n = \frac{1}{\sqrt{N}} \sum_{\alpha,\beta,k} \Psi^*_{\beta\alpha}(k)\Big(\eta_\beta(k) + \eta^\dagger_\beta(-k)\Big)(-1)^{(\alpha-1)n} e^{-ikn} \tag{2.30a}$$

$$b_n = \frac{-1}{\sqrt{N}} \sum_{\alpha,\beta,k} \Phi^*_{\beta\alpha}(k)\Big(\eta_\beta(k) - \eta^\dagger_\beta(-k)\Big)(-1)^{(\alpha-1)n} e^{-ikn} \tag{2.30b}$$

The unitary 2×2 matrices $\hat{\Phi}$ and $\hat{\Psi}$

$$\hat{\Phi}^\dagger\hat{\Phi} = \hat{\Psi}^\dagger\hat{\Psi} = \mathbb{I} \tag{2.31}$$

are constructed from the normalized (left) eigenvectors of the operators $(\hat{A}\mp\hat{B})(\hat{A}\pm\hat{B})$ whose eigenvalues are $E^2_\pm$. Explicitly, $\hat{\Phi}$ and $\hat{\Psi}$ solve the following equations:

$$\hat{\Phi}(\hat{A} - \hat{B})(\hat{A} + \hat{B}) = \hat{I}^2_E\hat{\Phi}, \tag{2.32a}$$

$$\hat{\Psi}(\hat{A} + \hat{B})(\hat{A} - \hat{B}) = \hat{I}^2_E\hat{\Psi} \tag{2.32b}$$

where

$$\hat{I}_E = \mathrm{diag}(E_+, E_-) \tag{2.33}$$

Using Eqs. (2.10), (2.11), and (2.32) we find an eigen matrix:

$$\hat{\Phi}(k) = \begin{pmatrix} e^{-i\theta}\beta_+ & \beta_- \\ -\beta_- & e^{i\theta}\beta_+ \end{pmatrix} \tag{2.34}$$

where

$$e^{i\theta} = \frac{\omega\omega_a}{|\omega||\omega_a|} \tag{2.35}$$

and

$$\beta_\pm = \frac{1}{\sqrt{2}}\Big(1 \pm \frac{h\cos k}{R}\Big)^{1/2} \tag{2.36}$$

with

$$R = \sqrt{h^2\cos^2 k + |\omega|^2|\omega_a|^2} \tag{2.37}$$

One can also parametrize $\hat{\Phi}$ in terms of Bogoliubov angle ϑ_B defined as

$$\beta_+ = \cos\vartheta_B, \qquad \beta_- = \sin\vartheta_B \tag{2.38}$$

Once the solution of (2.32a) is found, the solution of (2.32b) can be calculated straightforwardly as

$$\hat{\Psi} = \hat{I}_E^{-1}\hat{\Phi}(\hat{A} - \hat{B}) \tag{2.39}$$

Alternatively, one can first find $\hat{\Psi}$ from (2.32b), and then $\hat{\Phi}$ as $\hat{\Phi} = \hat{I}_E^{-1}\hat{\Psi}(\hat{A} + \hat{B})$. Using the thermodynamic average for the Bogoliubov fermions

$$\langle\eta_\alpha(k)\eta_\beta^\dagger(k')\rangle = \delta_{\alpha\beta}\delta_{kk'}[1 - \eta_\alpha(k)], \tag{2.40a}$$

$$\langle\eta_\alpha^\dagger(k)\eta_\beta(k')\rangle = \delta_{\alpha\beta}\delta_{kk'}, \tag{2.40b}$$

where $\eta_\alpha(k) = [1+\exp(\beta E_\alpha)]^{-1}$ is the Fermi-Dirac distribution function, we can obtain

the field-induced magnetization

$$m_z = \frac{1}{2\pi}\int_{-\pi/2}^{\pi/2} Tr\{\hat{\Phi}^\dagger(k)\hat{\Psi}(k)\}dk, \quad T=0 \tag{2.41}$$

The above formula is equivalent to Eq. (2.21) obtained from differentiation of the partition function. Introducing the matrix

$$\hat{G}(k) = \hat{\Psi}^\dagger(k)\hat{\Phi}(k) \tag{2.42}$$

we find the zero-temperature correlation function of the Majorana operators:

$$\langle ib_n a_m\rangle == \frac{1}{2\pi}\sum_{\alpha,\beta}\int_{-\pi/2}^{\pi/2} G_{\beta\alpha}(k)(-1)^{(\alpha-1)n}(-1)^{(\beta-1)m}e^{-ik(m-n)}dk \tag{2.43}$$

The explicit form of matrix $\hat{G}$ (2.42) is calculated from Eqs. (2.34) and (2.39). One can check that its components satisfy the following relations;

$$G_{21}(k\pm\pi) = G_{12}(k) \tag{2.44a}$$

$$G_{22}(k\pm\pi) = G_{11}(k) \tag{2.44b}$$

Then Eq. (2.43) can be simplified into

$$\langle ib_n a_m\rangle == \frac{1}{2\pi}\int_{-\pi}^{\pi}\{G_{11}(k)+(-1)^n G_{12}(k)\}e^{-ik(m-n)}dk \tag{2.45}$$

where the matrix elements are found to be

$$G_{11}(k) = (\cos k+\omega^*)\Big[\frac{\beta_+^2}{E_+}+\frac{\beta_-^2}{E_-}\Big]+\frac{1}{2}\frac{\omega^*|\omega_a|^2}{R}\Big[\frac{1}{E_+}-\frac{1}{E_-}\Big], \tag{2.46a}$$

$$G_{12}(k) = \omega_a \Big[\frac{\beta_-^2}{E_+} + \frac{\beta_+^2}{E_-}\Big] + (\cos k + \omega^*) e^{i\theta}\beta_+\beta_- \Big[\frac{1}{E_+} - \frac{1}{E_-}\Big] \tag{2.46b}$$

The formulas derived in this subsection provide us with the main results needed for the rest of calculations.

2.2.2 Spontaneous magnetization

We define the spontaneous longitudinal sublattice magnetization as

$$(m_x^e)^2 = \lim_{(m-l)\to\infty} \langle \sigma_{2l}^x \sigma_{2m}^x \rangle \tag{2.47a}$$

$$(m_x^o)^2 = \lim_{(m-l)\to\infty} \langle \sigma_{2l-1}^x \sigma_{2m-1}^x \rangle \tag{2.47b}$$

The spontaneous longitudinal magnetization is the (local) order parameter defined as

$$m_x = \frac{1}{2}(m_x^e + m_x^o). \tag{2.48}$$

We also defined the Majorana string operator:

$$O_x(m) = \prod_{l=1}^{m-1} [ib_l a_{l+1}]. \tag{2.49}$$

By definition $O_x(1) = 1$. For further reference let us remind some useful relations between original spins, Majorana fermions, and the dual spin operators (1.32) and (1.33). Then $O_x(m) = \sigma_l^x \sigma_m^x$. The spin-correlation function can be calculated as the correlation function of the Majorana operators [79]

$$\langle \sigma_L^x \sigma_R^x \rangle = \langle O_x(L) O_x(R) \rangle = \Big\langle \prod_{n=L}^{R-1} [ib_n a_{n+1}] \Big\rangle. \tag{2.50}$$

The latter is given by the determinant

$$\langle \sigma_L^x \sigma_R^x \rangle = \begin{vmatrix} \langle ib_L a_{L+1} \rangle & \langle ib_L a_{L+2} \rangle & ... & \langle ib_L a_R \rangle \\ \langle ib_{L+1} a_{L+1} \rangle & \langle ib_{L+1} a_{L+2} \rangle & ... & \langle ib_{L+1} a_R \rangle \\ . & . & . & \\ . & . & . & \\ . & . & . & \\ \langle ib_{R-1} a_{L+1} \rangle & \langle ib_{R-1} a_{L+2} \rangle & ... & \langle ib_{R-1} a_R \rangle \end{vmatrix} . \tag{2.51}$$

To calculate the quantities of our interest we choose the ends as

$$L = 2, \quad R = 2N \quad \mapsto \quad \text{even quantity}$$

$$L = 1, \quad R = 2N - 1 \quad \mapsto \quad \text{odd quantity} \tag{2.52}$$

In both cases we are dealing with $2(N-1) \times 2(N-1)$ matrices. Note that (2.51) is not the conventional Toeplitz determinant, since the elements of the matrix $\langle ib_n a_m \rangle$ given by Eg. (2.45) do not satisfy the condition $\langle ib_n a_m \rangle = f(m-n)$. It is however possible to represent (2.51) via a block Toeplitz matrix [115, 116]. Let us define

$$G^{\pm}(k) = G_{11}(k) \pm G_{12}(k) \tag{2.53}$$

and its inverse Fourier transform

$$G^{\pm}(l) = \frac{1}{2\pi} \int_{-\pi}^{\pi} G^{\pm}(k) e^{-ikl} dk \tag{2.54}$$

along with the 2×2 matrix

$$\hat{\mathcal{G}}_{e/o}(l) = \begin{pmatrix} G^{\pm}(l) & G^{\pm}(l+1) \\ G^{\mp}(l-1) & G^{\mp}(l) \end{pmatrix} \tag{2.55}$$

Then the sublattice magnetizations $m_x^{e/o}$ can be evaluated as the limit of the determinant of the corresponding block Toeplitz matrix constructed from $(N-1) \times (N-1)$ blocks $\hat{\mathcal{G}}_{e/o}$ of size 2×2:

$$\lim_{N\to\infty} (m_x^{\sharp})^2 \longmapsto \begin{vmatrix} \hat{\mathcal{G}}_{\sharp}(-1) & \hat{\mathcal{G}}_{\sharp}(1) & ... & \hat{\mathcal{G}}_{\sharp}(3-2N) \\ \hat{\mathcal{G}}_{\sharp}(1) & \hat{\mathcal{G}}_{\sharp}(-1) & ... & \hat{\mathcal{G}}_{\sharp}(5-2N) \\ . & . & . & \\ . & . & . & \\ . & . & . & \\ \hat{\mathcal{G}}_{\sharp}(2N-5) & \hat{\mathcal{G}}_{\sharp}(2N-7) & ... & \hat{\mathcal{G}}_{\sharp}(-1) \end{vmatrix}. \tag{2.56}$$

At this point we were unable to derive analytical results for asymptotics of the above block Toeplitz determinants. So we resort to direct numerical calculations for large finite-size matrices. The results for spontaneous magnetization are given in Fig. 2.8. The numerical values of the parameters we present in that figures are stable in the fourth decimal place for the $M \times M$ matrices of sizes $M \gtrsim 30$. In immediate vicinities of the critical points the order parameters are checked to decay smoothly as $M \to \infty$.

We checked that the numerical results obtained from (2.56) agree with two available analytical limits at $h_a = 0$,

$$h_a = 0 \mapsto \quad m_x^e = m_x^o = m_x \tag{2.57}$$

For $\delta = 0$ the result is due to Pfeuty [117]:

$$m_x^2 = \frac{2}{1+\gamma}[\gamma^2(1-h^2)]^{1/4}, \quad h < 1. \tag{2.58}$$

For the $h = 0$ case the order parameter can be obtained by combining the result of Pfeuty and the duality transformations (1.28) and (1.29), yielding [35]

$$m_x^2 = 2\Big[\frac{(\gamma^2-\delta^2)}{[(1+\gamma)^2-\delta^2]}\Big], \quad \delta < \gamma. \tag{2.59}$$

The analytical results (2.58) and (2.59) can be obtained from (2.56) by the brute force calculations utilizing Szego's theorem [118], but those calculations are quite demanding, see next subsection for details.

The Expressions for m_y are obtained along the same lines. Numerical values satisfy useful relation $m_y(-\gamma) = m_x(\gamma)$, see Fig. 2.8.

2.2.3 Nonlocal string orders

Using Majorana string operator (2.49) one can define the even and odd string operators [36]

$$O_{x,e}(m) = \prod_{l=1}^{m}[ib_{2l-1}a_{2l}] = \prod_{n}^{2m}\sigma_n^x, \tag{2.60a}$$

$$O_{x,o}(m) = \prod_{l=1}^{m}[ib_{2l}a_{2l+1}] = \prod_{n=2}^{2m+1}\sigma_n^x. \tag{2.60b}$$

The even/odd SOP's $O_{x,e/o}$ are introduced as

$$O^2_{\diamondsuit,\sharp} = \lim_{(n-m)\to\infty}|\langle O_{\diamondsuit,\sharp}(m)O_{\diamondsuit,\sharp}(n)\rangle|, \tag{2.61}$$

where we used the symbols $\diamondsuit = x, y$ and $\sharp = e, o$.

From Eqs. (2.60a) and (2.60b), Eq. (2.61) can be evaluated as the limit of determinants:

$$\lim_{N\to\infty} O^2_{x,e/o} \longmapsto \begin{vmatrix} G^{\mp}(-1) & G^{\mp}(1) & ... & G^{\mp}(1-2N) \\ G^{\mp}(1) & G^{\mp}(-1) & ... & G^{\mp}(3-2N) \\ . & . & . & \\ . & . & . & \\ . & . & . & \\ G^{\mp}(2N-3) & G^{\mp}(2N-5) & ... & G^{\mp}(-1) \end{vmatrix}. \tag{2.62}$$

Those even and odd SOPs are numerically calculated from the determinant of the ordinary $N \times N$ Toeplitz matrix (2.62).

To probe additional nonlocal orders we utilize another pair of string operators [36]:

$$O_{y,e}(m) = \prod_{l=1}^{m} [-ia_{2l}b_{2l+1}] = \prod_{n=2}^{2m+1} \sigma_n^y, \tag{2.63a}$$

$$O_{y,o}(m) = \prod_{l=1}^{m} [-ia_{2l-1}b_{2l}] = \prod_{n=1}^{2m} \sigma_n^y. \tag{2.63b}$$

The corresponding SOPs are defined similarly to (2.61) and are numerically calculated from the following $N \times N$ Toeplitz determinant:

$$\lim_{N\to\infty} O^2_{y,e/o} \longmapsto \begin{vmatrix} G^{\mp}(1) & G^{\mp}(-1) & ... & G^{\mp}(3-2N) \\ G^{\mp}(3) & G^{\mp}(1) & ... & G^{\mp}(5-2N) \\ . & . & . & \\ . & . & . & \\ . & . & . & \\ G^{\mp}(2N-1) & G^{\mp}(2N-3) & ... & G^{\mp}(1) \end{vmatrix}. \tag{2.64}$$

In the limit of $h = h_a = 0$ the above determinants can be evaluated exactly by the standard technique [118], reproducing the earlier results for nonvanishing $\mathcal{O}_{x,y/e,o}$ obtained form the duality mapping [35]. When $h \neq 0$ and $h_a \neq 0$, we were unable to derive analytical results for asymptotic of these Toeplitz determinants (2.56) and (2.62). In the presence of the field, we plot the behaviours of SOPs $\mathcal{O}_{x,y/e,o}$ in the Fig. 2.6. We numerically calculated from $2N \times 2N$ matrices with $N = 30, 100, 190$. Those parameters we found here represented by solid, dotted, and dashed lines with respect to respective size the matrices. Those numerical results of SOPs $\mathcal{O}_{x,y/e,o}$ shown in Fig. 2.6 are found to die off in the thermodynamical limit $N \to \infty$, and thus those quantities $\mathcal{O}_{x,y/e,o}$ are not proper order parameters in the presence of magnetic field. So, we will further discuss the $\mathcal{O}_{z,\sharp} \sim \mathcal{O}_{x,\sharp}.\mathcal{O}_{y,\sharp}$ In addition to (2.60a), (2.60b), (2.63a),

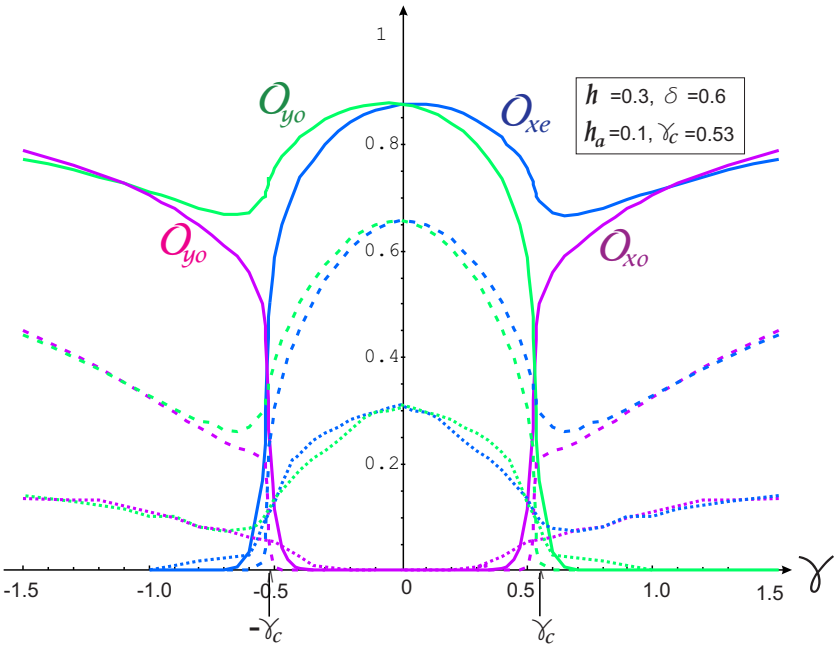

Figure 2.6: SOPs $\mathcal{O}_{x,y/e,o}$ are numerically calculated along γ axis from the $2N \times 2N$ matrices with $N = 30, 100, 190$ at $\delta = 0.6$, $h_a = 0.1$, and $h = 0.3$. Even/odd and x/y components of string order parameters are drawn. Magnitude of order parameters in all phases are not saturated and finally die off in the thermodynamical limit $N \to \infty$.

and (2.63b) we define another string operator

$$O_z(n) = \prod_{l=1}^{n} [ib_l a_l] = \prod_{n=2}^{n} \sigma_l^z, \tag{2.65}$$

and the related string correlation function in the Toeplitz determinant form:

$$\left\langle \prod_{l=1}^{n} [ib_l a_l] \right\rangle = \left\langle \prod_{n=2}^{n} \sigma_l^z \right\rangle = \begin{vmatrix} \langle ib_L a_L \rangle & \langle ib_L a_{L+1} \rangle & ... & \langle ib_L a_R \rangle \\ \langle ib_{L+1} a_L \rangle & \langle ib_{L+1} a_{L+1} \rangle & ... & \langle ib_{L+1} a_R \rangle \\ . & . & . & \\ . & . & . & \\ . & . & . & \\ \langle ib_R a_R \rangle & \langle ib_R a_{L+1} \rangle & ... & \langle ib_R a_R \rangle \end{vmatrix} \tag{2.66}$$

Inside the circle $|h| < h_c^{(2)}$ this string correlation function is found to be oscillating with the period of four lattice spacing, see Fig. 2.7, so we will label it as $\pi/2$ phase to distinguish it from the positive "ferrimagnetic like" string correlation function in the paramagnetic phase $|h| > h_c^{(1)}$.

We will need three parameters to account for the string order:

$$\lim_{R\to\infty} \mathfrak{D}_{zz}(L,R) \equiv \lim_{R\to\infty} \left\langle \prod_{l=1}^{R} [ib_l a_l] \right\rangle \tag{2.67}$$

$$= \begin{cases} (-1)^m O_{z,1}^2, & L = 1, \quad R = 2m, \\ (-1)^m O_{z,2}^2, & L = 2, \quad R = 2m, \\ (-1)^{m+L} O_{z,3}^2, & L = 1, \quad R = 2m+1 \text{ or } L = 2, \quad R = 2m+1. \end{cases} \tag{2.68}$$

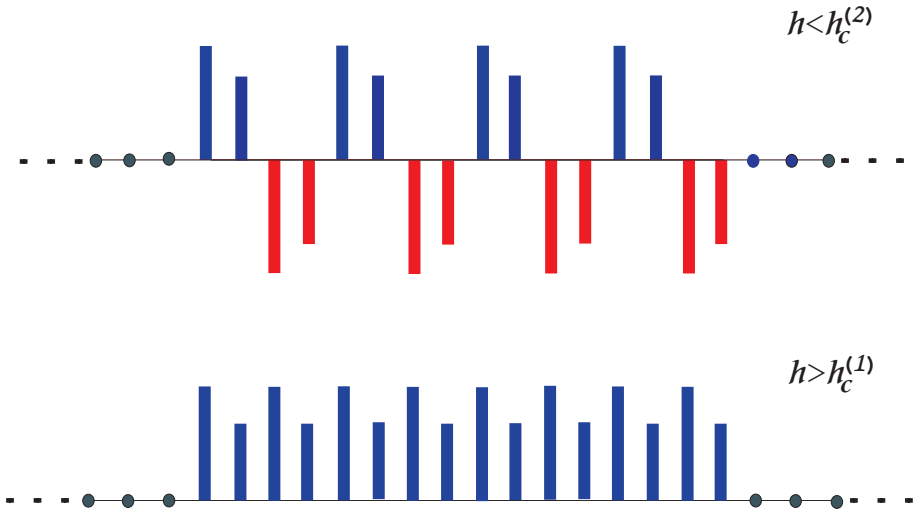

Figure 2.7: Visualization of the modulation of the string order parameter $\mathcal{O}_z$ inside the circle ($|h| < h_c^{(2)}$) on the phase diagram shown in Fig. 2.1 vs "plain" behaviour of O_z in the paramagnetic phase $|h| > h_c^{(1)}$.

The reason for this is that due to the dimerization δ and the staggered field h_a, the value of the string correlation function depends not only on the length of the string, but also on whether its ends L/R are sitting on the even or odd sites of the chain. The explicit matrix form (2.66) with elememts $G^{\pm}(i-j)$ can be written as the block Toeplitz matrix, similar to (2.56). Four-site periodic oscillations of the string correlation function inside the circle indicates periodicity of the orientations of σ_z spins along the string, or, alternatively, the modulation of fermionic density around the half-filling. In the FM phase (see Fig. 2.1) the O_z string correlation function vanishes at large length, while in the paramagnetic phase $|h| > h_c^{(1)}$ it is positive, showing only quite trivial "ferrimagnetic" oscillations synchronized with the staggered field. Qualitatively, it indicates that all σ_z spins in the string are polarized along the field, or, in terms or fermions, the latter have concentration above half-filling. In the limit $h = h_a = 0$ the SOPs will be discussed in section 2.3.

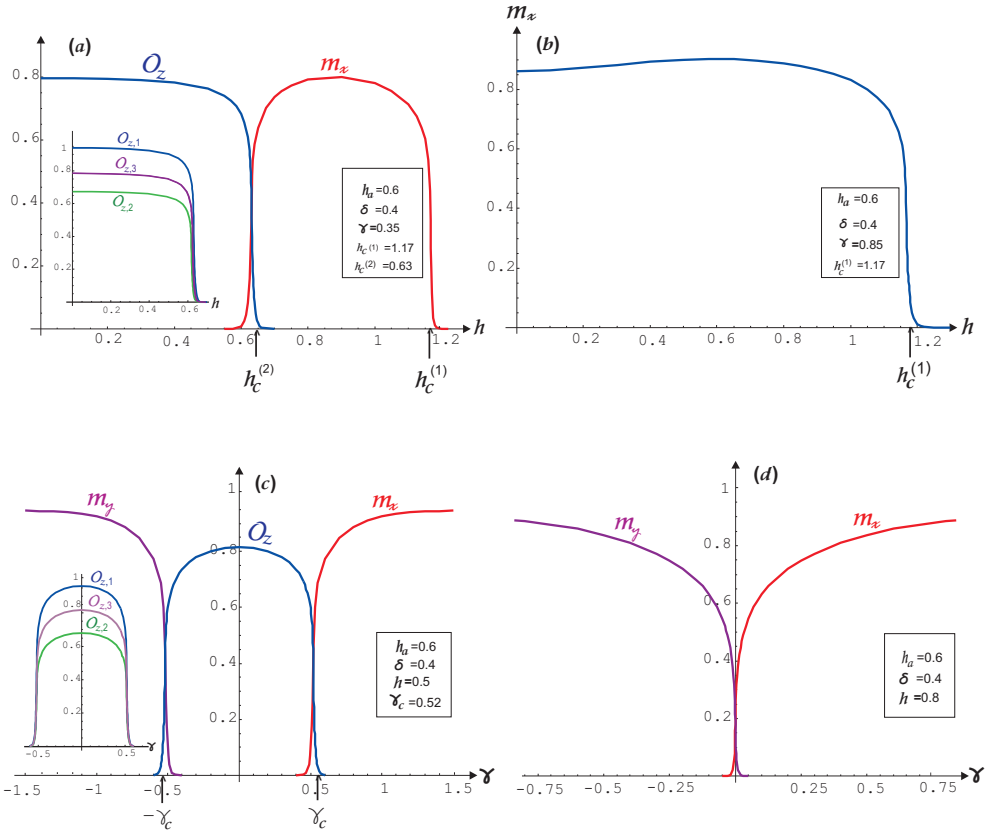

Figure 2.8: Spontaneous magnetization $m_{x,y}$ and modulated string order parameter O_z numerically calculated from $2N \times 2N$ matrices with $N = 70$. (a)-(d) Paths 1-4 on the phase diagram shown in Fig. 2.1. The spontaneous magnetizations are the averaged values of the even/odd componants (2.48) (not shown), while the modulated string order parameter O_z is the average value of the three parameters $O_{z,i}$, shown in the insets. In the phases with local orders $m_{x,y}$ the string order parameters $O_{z,i}$ vanish, while in the disorder phase $h > h_c^{(1)}$ they are nonzero, but physically trivial (not shown). The exact values of the critical parameters $h_c^{(1)}$, $h_c^{(2)}$, and γ_c (shown by arrows) are calculated from Eqs. (2.16) and (2.17). Nonvanishing small tails of the order parameters seen in the immediate vicinities of the critical points are the finite-size effects, checked to die off as $N \to \infty$.

2.2.4 Winding number

It has been shown in the recent years that many quantum phase transitions with hidden orders are accompanied by a change of topological numbers [4, 27]. Here we calculate the winding number (or the Pontryagin index) in all regions of the model's phase diagram. Such parameters were calculated recently in similar 1D models, see, e.g., [35, 73, 74, 100–103].

By a unitary transformation the Hamiltonian (2.9) can be brought to the block off-diagonal form

$$\mathcal{H}_k = \begin{pmatrix} 0 & \hat{D}(k) \\ \hat{D}^\dagger(k) & 0 \end{pmatrix} \tag{2.69}$$

with operator

$$\hat{D}(k) = \hat{A}(k) + \hat{B}(k) \tag{2.70}$$

which has two eigenvalues

$$\lambda_\pm(k) = \pm\frac{1}{\sqrt{2}}\Big[1 + 2h_a^2 + \delta^2 - \gamma^2 + (1 - \delta^2 + \gamma^2)\cos 2k - 2i\gamma \sin 2k\Big]^{1/2}. \tag{2.71}$$

In one spatial dimension the winding number defined as [104]

$$N_\omega = \frac{1}{2\pi i}\int_{BZ} dk Tr[\partial_k \ln \hat{D}] \tag{2.72}$$

can be readily calculated for this model as

$$N_\omega = \frac{1}{2\pi i}\arg[\lambda_+(k) + \lambda_-(k)|_{\frac{\pi^+}{2}}^{\frac{\pi^-}{2}} \tag{2.73}$$

The result for N_ω are given on the ground-state phase diagram in Fig. 2.1. N_ω can be viewed as a complementary parameter characterizing a given phase. The disordered

(PM) phase and the magnetic phases where conventional local order $m_{x,y}$ exists, are topologically trivial, $N_\omega = 0$. The phase inside the circle where modulated nonlocal string order parameter O_z exists, is topologically nontrivial $N_\omega = 1$.

2.3 Dimerized XY chain

When we turn off the magnetic fields ($h = h_a = 0$) in the model (2.1) and restrict ourselves to two relevant perturbations (δ, γ), pertinent to other systems considered in this work, the spectrum (2.12) of the model becomes [107, 108]

$$E_\pm(k) = \sqrt{\cos^2 k + (\delta \pm \gamma)^2 \sin^2 k} \tag{2.74}$$

with the gap

$$\Delta = |\gamma \pm \delta|. \tag{2.75}$$

Now we utilize the nature of order and symmetry changes on the lines of the quantum phase transition $\gamma = \pm\delta$ on the parameter plane (δ, γ). We utilize the duality transformations (1.28) and (1.29) on the Hamiltonian (2.1). It maps onto two even and odd dual Hamiltonaians (2.4a) and (2.4b). In this limit symmetry-breaking Hamiltonain (2.4c) vanishes since it is the function of magnetic fields.

2.3.1 Local and string order parameters

Since the Hamiltonian (2.1) at $h = h_a = 0$ maps onto the sum of two even and odd dual Hamiltonians (2.4a) and (2.4b) via duality transformations (1.28) and (1.29), then order parameter of direct lattice can be translated onto dual lattice. On the dual lattice these Hamiltonians (2.4a) and (2.4b) are equivalent to Quantum Ising Models (QIM). According to the classical results [96, 117] for the 1D Quantum Ising chain with the

Hamiltonian

$$H = \sum_{i=1}^{N} [J\tau_i^x \tau_{i+1}^x + h\tau_i^z], \tag{2.76}$$

the model is disordered at $\lambda \equiv J/h \leq 1$, while the long-range order $m_x \neq 0$ appears at $\lambda > 1$. The order parameter is obtained from the correlation function:

$$\lim_{l\to\infty} \langle \tau_i^x \tau_{i+1}^x \rangle = (-1)^l (1-\lambda^{-2})^{\frac{1}{4}} = (-1)^l m_x^2 \tag{2.77}$$

From the comparision of the Hamiltonians (2.4a), (2.4b), and (2.76) we see that if $\lambda_\sharp > 1$, where

$$\lambda_{e/o} = \frac{1+\gamma \mp \delta}{1-\gamma \pm \delta}, \tag{2.78}$$

then τ^x is ordered on either even or odd dual sublattices. So we should distinguish between the even and odd SOPs defined on the sites of the even and odd dual sublattices, respectively. As one can see, the SOP defined by equation (1.38) is even and we will denote it by $\mathcal{O}_{x,e}$ from now on. To define the odd SOP ($\mathcal{O}_{x,o}$) we can take $m = 2$ and $n = 2l + 1$ in equation (1.36), then $\mathcal{O}_{x,o}$ is given by equation (1.38) where the correlation function on its rhs is now $\langle \tau_1^x \tau_{2l+1}^x \rangle$. Using the above formulas the even and odd SOPs can be calculated exactly:

$$\mathcal{O}_{x,e/o} = \begin{cases} 2^{1/4} \left(\frac{t_\mp}{(1+t_\mp)^2} \right)^{1/8} & t_\mp \geq 0 \\ 0 & t_\mp \leq 0 \end{cases} \tag{2.79}$$

where we denote

$$t_\mp = \gamma \mp \delta \tag{2.80}$$

Let us now calculate the y component of the SOP. The duality transformation (1.28) and (1.29) with interchange $x \leftrightarrow y$ map the Hamiltonian (2.1) again onto a sum of two

even and odd Quantum Ising Model (QIM) Hamiltonians:

$$H_e = \frac{1}{4}\sum_{l=1}^{N/2}(1-\gamma+\delta)\tau_{2l-2}^y\tau_{2l}^y + (1+\gamma-\delta)\tau_{2l}^y \tag{2.81a}$$

$$H_o = \frac{1}{4}\sum_{l=1}^{N/2}(1-\gamma-\delta)\tau_{2l-1}^y\tau_{2l+1}^y + (1+\gamma+\delta)\tau_{2l-1}^y \tag{2.81b}$$

Following the same steps as above we easily find:

$$\mathcal{O}_{y,e/o} = \begin{cases} 0 & t_\mp \geq 0 \\ \mathcal{O}_{x,e/o}(-t_\mp) & t_\mp \leq 0 \end{cases} \tag{2.82}$$

We show the phase diagram of the dimerized XY model in Fig.2.9. The phase boundaries in the Fig. 2.9 are in agreement with parabolic lines of Fig. 2.2 in the limiting case $h = h_a = 0$. Two lines of quantum phase transitions $\gamma = \pm\delta$ divide the parameter plane into four regions denoted by A-D. For each region we indicate nonvanishing order parameters with characterize different phases located there.

The next important step in our analysis is to establish relation between the conventional long-range order with local order parameter(s) and the nonlocal (topological) SOPs. Using the duality transformation (1.28) and decoupling the dual Hamiltonian into the even and odd terms, we find the magnetization m_x of the spins of the original Hamiltonian (2.1) as:

$$m_x^2 = \lim_{l\to\infty}\langle\sigma_1^x\sigma_{2l}^x\rangle = \lim_{l\to\infty}\langle(\tau_0^x\tau_{2l}^x)(\tau_1^x\tau_{2l-1}^x)\rangle \tag{2.83}$$

The y component of the magnatization can be treated in a similar way, so we get

$$m_\alpha = \mathcal{O}_{\alpha,o}\mathcal{O}_{\alpha,e}, \quad \alpha = x, y \tag{2.84}$$

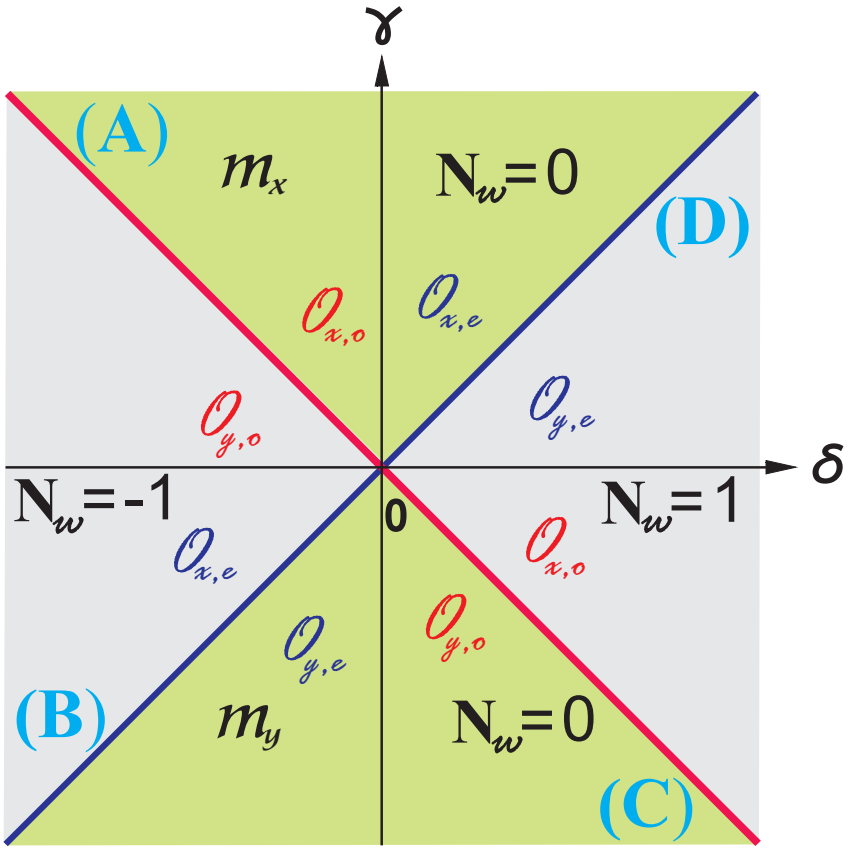

Figure 2.9: Phase diagram of the anisotropic dimerized XY chain. Nonvanishing string and local order parameters, topological winding numbers are shown in four sectors A, B, C, D of the (δ, γ) parametric plane. The violet/red lines $\gamma = \pm\delta$ are the lines of quantum phase transitions (gaplessness).

As we see from the model's phase diagram in Fig. 2.9, the even and odd SOPs are mutually exclusive in the region B and D. Those are the regions without conventional local (Landau) order. The phases in the regions B and D possess only a nonlocal (topological) order which is quantified by the SOP. As we conclude from the duality mapping, the dimerized XY model (2.1) possesses the hidden $\mathbb{Z}_2 \bigotimes \mathbb{Z}_2$ symmetry which was also noticed earlier in various spin chains and ladders [30]. In the present analytically solvable model the origin of such summetry can be easily traced to the $\mathbb{Z}_2$ symmetry of the even and odd Ising models (2.4a) and (2.4b). Nonzero even SOP $\mathcal{O}_{x,e}$

and the odd SOP $\mathcal{O}_{x,o}$ in the sector B and D are due to spontaneous breaking of the $\mathbb{Z}_2$ symmetry in the even (2.4a) or (2.4b) sectors of the dual Hamiltonian respectively. These SOPs signal appearance of the spontaneous "dual" magnetization $\langle\tau_e^x\rangle$ or $\langle\tau_o^x\rangle$. We have to emphasize an important issue: since mappings of the original model (2.1) onto the dual models (2.4a), (2.4b) or (2.81a), (2.81b) are results of the different dual transformations, the analyses in terms of the SOP $\mathcal{O}_x$ or $\mathcal{O}_y$ are complimentary, and the order parameters $\mathcal{O}_x$ and $\mathcal{O}_y$, even if they both are found to be nonzero in some parts of the phase diagram should not be understood as coexistent.

In this case the hyperbolic phase boundaries shown in Fig. 2.2 reduce to two lines $\gamma = \pm\delta$ [35], and nonvanishing SOPs $\mathcal{O}_{z,\sharp}$ are localized inside the cone $\delta^2 > \gamma^2$. When $\delta > 0$ the only surviving component of 4-periodic string correlation function is $\mathcal{O}_{z,1}$. Similarly, when $\delta < 0$ then only a component of string correlation function $\mathcal{O}_{z,2}$ survives. Here the averaging of the even and odd strings decouple, and SOPs $\mathcal{O}_{z,i}$ can be found in a simple form. The values $\mathcal{O}_{x/y,e/o}$ inside the cone $\delta^2 > \gamma^2$ are available [35] yielding

$$\begin{pmatrix} \mathcal{O}_{z,1} \\ \mathcal{O}_{z,2} \end{pmatrix} = \sqrt{2}\Big[\frac{(\delta^2-\gamma^2)}{[(1+\pm\delta)^2-\gamma^2]^2}\Big]^{1/8} \begin{pmatrix} \vartheta(\delta) \\ \vartheta(-\delta) \end{pmatrix} \tag{2.85}$$

We have checked the agreement between the analytical result (2.85) and the numerical evaluation of the determinant (2.66).

We conclude from equations (2.79) and (2.82) (see also Fig. 2.9) that contrary to common belief, the even and odd SOPs can coexist. In the region A of the phase diagram which corresponds to $\gamma^2 > \delta^2, \gamma > 0$ both even and odd SOPs $\mathcal{O}_{x,e/o}$ are nonvanishing, and then, as follows from equation (2.84) the local order (magnetization) $m_x \neq 0$ appears in the original model (2.1). Similarly, when $\gamma^2 > \delta^2, \gamma < 0$ (region C of the phase diagram), the magnetization $m_y \neq 0$. The appearance of the local order, or,

equivalently for this model, the coexistence of the even and odd SOPs are the results of the spontaneous $\mathbb{Z}_2 \bigotimes \mathbb{Z}_2$ symmetry breaking simultaneously in both even and odd sectors of the dual Hamiltonian. From equations (2.79),(2.82), and (2.84) we find the numerical values of the local order parameters:

$$m_x(\gamma) = m_y(-\gamma) = \sqrt{2}\Big(\frac{\gamma^2 - \delta^2}{[(1+\gamma)^2 - \delta^2]^2}\Big)^{1/8} \tag{2.86}$$

In the limit $\delta = 0$ the above equation concides with the result of Barouch and McCoy [96].

Another useful limit of the model (2.1) is $h = h_a = \gamma = 0$ when it becomes a dimerized XX chain. This model does not have local long range order, and its phase diagram can be read from the line $\gamma = 0$ in Fig. 2.9. The topological order in the phase $\delta > 0$ or $\delta < 0$ is characterized by a pair of mutually exclusive SOPs $\mathcal{O}_{\alpha,o}$ and $\mathcal{O}_{\alpha,e}$ (we can choose $\alpha = x$ or $\alpha = y$) seperated by a quantum critical point $\delta = 0$ where all SOPs vanish. From equations (2.79) and (2.82) we find

$$\mathcal{O}_{x,o} = \mathcal{O}_{y,e} = 2^{1/4}\Big(\frac{\delta}{(1+\delta)^2}\Big)^{1/8}, \quad \delta > 0 \tag{2.87}$$

The magnitudes of the SOPs are symmetric with respect to δ and $\mathcal{O}_{x,e}(\delta) = \mathcal{O}_{y,o}(\delta) = \mathcal{O}_{x,o}(-\delta)$ for $\delta < 0$.

If we define the primary order parameter as the one which is nonzero exclusively for a given phase, then we can identify m_x and m_y as the primary order parameters for the magnetized phases residing, respectively, in the sector A and C of the phase diagram. The topological order of the phase B and D is characterized by the pair of the primary (string) parameters $\mathcal{O}_{x,e}$ and $\mathcal{O}_{x,o}$ for the choice (1.28) and (1.29) of the dual transformation. (If we swap $x \leftrightarrow y$, we end up with the dual representation

where the primary order parameters are $\mathcal{O}_{y,e}$ and $\mathcal{O}_{y,o}$.). The overlapped even and odd SOPs: $\mathcal{O}_{x,e}$; $\mathcal{O}_{y,o}$ and $\mathcal{O}_{x,o}$; $\mathcal{O}_{y,e}$ in the region B and D of the phase diagram (see Fig. 2.9) signal the appearance of the z-string order parameters $\mathcal{O}_{z,1}$ and $\mathcal{O}_{z,2}$ respectively. These parameters $\mathcal{O}_{z,1}$ and $\mathcal{O}_{z,2}$ given in (2.85) are found to be oscillating with the period of the four lattice spacing.

From behaviour of the gap (2.75) and the primary order parameter (see (2.79), (2.82), and (2.86), whichever applicable) near the lines $\gamma = \pm\delta$ of the quantum phase transition we find the critical indices of he order parameter $\beta = 1/8$ (see its definition below equation (2.79) and of the correlation lenth $\nu = 1$. (The latter can be read from the gap equation (2.75) since $\xi^{-1} \propto \Delta \propto |t|^{\nu}$). So the critical behaviour of the model on the phase boundaries belongs to the 2D Ising universality class as it must, since the Hamiltonian (2.1) is equivalent to free fermions.

2.3.2 Topological winding number

We also calculate the winding number in all regions of the phase diagram (2.9) of model (2.1) at $h = h_a = 0$. Following same steps as explained in section 2.2.4, we have two eigenvalues

$$\pm\lambda(k) = \pm\sqrt{1 + (\delta^2 - \gamma^2 - 1)\sin^2 k - i\gamma \sin 2k}. \tag{2.88}$$

Note a useful relation between the eigenvalues of operator $\hat{D}(k), \hat{D}^{\dagger}(k)$ (see equation (2.70) for $\hat{D}(k)$ in the limit $h = h_a = 0$) and the spectrum (2.74):

$$E_+(k)E_-(k) = \lambda(k)\lambda^*(k) \tag{2.89}$$

In one spatial dimension the winding number defined as [104]

$$N_\omega^r = \frac{1}{4\pi i}\int_{BZ} dk Tr[\partial_k \ln \hat{D} - \partial_k \ln \hat{D}^\dagger] \tag{2.90}$$

can be readily calculated analytically for this model. We calculate the winding number in all four regions of phase diagram in Fig. 2.9. To make a connection between the definition (2.90) and a more intuitive definition of the winding number let us introduce a two-component unit vector $n(k) = (n_1(k), n_2(k))$ constructed from the spectrum of the model. The eigenvalues (2.74) allow us to define two unit vectors with the components

$$n_1(E_\pm(k)) = \cos k/E_\pm(k) \tag{2.91a}$$

$$n_2(E_\pm(k)) = (\delta \pm \gamma)\sin k/E_\pm(k) \tag{2.91b}$$

which can also be related to Bogoliubov angle $e^{i\theta_k} = n_1(k) + in_2(k)$. (For the definition of θ_k see, e.g., [119]). The winding number is defined as [4, 29]

$$N_\pm = \frac{1}{2\pi}\sum_{i,j=1}^{2}\int_{BZ} dk \varepsilon_{ij} n_i(E_\pm(k)\partial_k n_j(E_\pm(k) \tag{2.92}$$

counts the number of loops wrapped by a unit vector around the origin while the vector spans over the Brillouin zone. One can show that the definition (2.90) yields

$$N_\omega^r = N_- - N_+ = \frac{1}{2}[\mathrm{sign}(\delta - \gamma) - \mathrm{sign}(\delta + \gamma)]. \tag{2.93}$$

The topological number N_ω^r accounts for the 'relative' winding of two normalized eigenvalues of the Hamiltonian. We find the winding number N_ω which adds up the loops

made by each of eigenvectors more convenient for various applications:

$$N_\omega = N_- + N_+ = \frac{1}{2}[\text{sign}(\delta - \gamma) + \text{sign}(\delta + \gamma)]. \tag{2.94}$$

As one check from equations (2.93) or (2.94), both topological numbers change by ± 1 on the phase boundaries $\gamma = \pm\delta$, signalling the phase transition. We choose N_ω as a complimentary topological order parameter characterizing a given phase, since its behaviour is in accord with the standard wisdom: as one can see in Fig. 2.9, $N_\omega = 0$ in the topologically trivial regions where a conventional local order exists.

To summarize

In this chapter, the dimerized XY chain with uniform and modulated transverse fields is studied. In order to solve the model, the fermionization of the spin Hamiltonian was done via the JW transformation. Its fermionic representation is in the form of dimerized Kitaev chain with modulated chemical potential. Using Fourier transform, it is represented as a single particle Hamiltonain with fermions residing on even/odd sites of lattice, unified in the form of spinors. We found four eigenvalues, gap, criticality, and phase boundaries. It has rich phase diagram (see Fig. 2.1) which also includes the incommensurate phase (IC) in its isotropic limit. We calculated the field-induced magnetizations and susceptibilities in the parametric space (see Figs. 2.3 and 2.5).

To deal with conventional (local) and nonlocal (string) orders, we found two eigenvectors $\hat{\Phi}$ and $\hat{\Psi}$ by applying the Bogoliubov transformation to the single particle Hamiltonian. From those eigenvectors, we obtained the explicit expression for the correlation function of Majorana operators at zero temperature. By definition the local and nonlocal orders can be expressed in terms of block Toeplitz matrices with Majorana correlation functions as matrix elements. At this point, we could not derive the analytical results for the asymptotics of the block Toeplitz determinant, so we restore to direct numerical calculations for a large-finite size matrices. The results for spontaneous magnetization $m_{x,y}$ and string order parameters $\mathcal{O}_z$ are plotted in Fig. 2.8. In the topological phase, the string correlation function is found to be oscillating with a period of four lattice spacing. It appears to be vanishing in the FM phase for large length and it quickly saturated in the PM phase (see Fig. 2.7 for detail). We probed additional nonlocal order parameters SOPs $\mathcal{O}_{x,y/e,o}$ in the form of Toeplitz matrices and numerically calculated them in the topological, FM and PM phases. Numerical results showed that all SOPs $\mathcal{O}_{x,y/e,o}$ are not robust at $h \neq 0$ and $h_a \neq 0$ for the matrix size

$N = 30, 100, 190$ as seen in Fig.2.6 and they ultimately die off in the thermodynamical limit $N \to \infty$.

In addition, we have calculated the winding number N_ω in all phases. The disordered PM phase and A(FM) phase with trivial conventional local order parameters are topologically trivial, $N_\omega = 0$, while the phase with the modulated string order has $N_\omega = 1$.

In the zero field limit $h = h_a = 0$, the hyperbolic phase boundaries shown in Fig. 2.2, reduce to two lines $\gamma = \pm\delta$ as in Fig. 2.9. In this limit, by utilizing the duality transformation, the model is mapped onto two 1D QIMs residing separately on even and odd sites of the dual lattice. The SOPs of the original chain are mapped onto the local order parameters of the dual lattice and thus calculated exactly. The phase diagram of the model contains topologically trivial phases where the even and odd SOPs ($\mathcal{O}_{\sharp,e}$,$\mathcal{O}_{\sharp,o}$; $\sharp = x, y$) coexist along with the conventional long-range order (magnetization). There are also topologically nontrivial phases without magnetization, where even or odd SOPs are mutually exclusive. In addition to the exclusiveness of x,y components of SOPs, the oscillating z-component of SOPs ($\mathcal{O}_{z,1}$, $\mathcal{O}_{z,2}$) are obtained from the overlapping of $\mathcal{O}_{x/y,e/o}$, with the period of four lattice spacing.

Chapter 3

Modulated Dimerized XYZ Chain with Magnetic Field

In this chapter, we study the dimerized XYZ antiferromagnetic spin-1/2 chain in the uniform and staggered transverse magnetic fields. In order to solve the model we use standard methods such as the JW transformations and Hatree-Fock (HF) approximation (also called the mean-field approximation). Using such methods the spin Hamiltonian of the chain maps onto the quadratic effective fermionic Hamiltonian. To characterize the different phases of the model's phase diagram we obtain energy gaps, induced magnetization, local (spontaneous magnetization), nonlocal (topological) order parameters and winding numbers. We numerically calculate and illustrate the detailed analysis of patterns of the string order. We calculate the mean field parameters and study the fermionic filling in the interacting and non-interacting chains. Finally, the role of interaction on the phase diagram, and order parameters will be analyzed in the isotropic XXZ model.

3.1 Model

3.1.1 The Hamiltonian, spectrum and phase diagram

In this subsection we define the model and discuss its ground-state properties. The spin Hamiltonian of the dimerized quantum XYZ chain in the presence of uniform (h) and staggered (h_a) axial magnetic field is

$$H=\sum_{n=1}^{N}\frac{J}{4}\Big[(1+(-1)^n\delta)(\sigma_n^x\sigma_{n+1}^x+\sigma_n^y\sigma_{n+1}^y+\Delta\sigma_n^z\sigma_{n+1}^z)$$

$$+(\gamma+(-1)^n\gamma_a)(\sigma_n^x\sigma_{n+1}^x-\sigma_n^y\sigma_{n+1}^y)\Big]+\frac{1}{2}[h+(-1)^n h_a]\sigma_n^z, \tag{3.1}$$

where σ-s are the standard Pauli matrices. The chain has bond alternation with parameter $|\delta|\leq 1$. We also allowed the xy anisotropy γ to be modulated with γ_a. In this model, we consider the antiferromagnetic ($J>0$) model at zero temperature. In the absence of anisotropy ($\gamma=\gamma_a=0$) the model (3.1) becomes XXZ chain. In the case of $\delta=0$ and $\Delta=1$ the model (3.1) is XXX chain, called Heisenberg model.

The model (3.1) is not solvable in general, the exact solutions based on the Bethe ansatz, are available only for some special cases. For the historical references of the isotropic XXX model with zero field, see paper by Yang and Yang [120], for more comprehensive reviews of the available exact results see, e.g., Refs. [111, 118, 121], and for the most recent account of integrability and more references, see Ref. [122]. The standard JW transformation (1.1) maps (3.1) onto the interacting fermionic Hamiltonian

$$H=\sum_{n=1}^{N}\frac{J}{2}(1+\delta(-1)^n)\Big[(c_n^\dagger c_{n+1}+h.c)+2\Delta\Big(c_n^\dagger c_n-\frac{1}{2}\Big)\Big(c_{n+1}^\dagger c_{n+1}-\frac{1}{2}\Big)\Big]$$

$$+\frac{J}{2}(\gamma+(-)^n\gamma_a)(c_n^\dagger c_{n+1}^\dagger+h.c)+(h+(-1)^n h_a)\Big(c_n^\dagger c_n-\frac{1}{2}\Big). \tag{3.2}$$

In the noninteracting limit $\Delta \equiv J_z/J = 0$, the model (3.1) is exactly solvable. The ground state properties of this model were analyzed in chapter 2. The most recent comprehensive analysis of the ground-state phase diagram of the model at $\Delta = \gamma_a = 0$ and its local and nonlocal order parameters are given in Ref. [37]. It turns out that introducing alternation of anisotropy γ_a does not change the results [37] qualitatively, resulting in some minor modifications which we present below. The noninteracting results are used in the subsequent analysis of the case $\Delta \neq 0$. We will always assume $|\gamma_a| < |\gamma|$ and from now on we set $J = 1$. We also modify for further convenience the hopping term of the Hamiltonian (3.2) as

$$1+(-1)^n\delta \mapsto \quad t+(-1)^n\delta. \tag{3.3}$$

In this section we present generalization of results of chapter 2 [37] for $\gamma_a \neq 0$. We set the lattice spacing $a = 1$ and restrict wave numbers to the reduced Brillouin zone (BZ) $k \in [-\pi/2, \pi/2]$. The band index α=1 and 2 serves to map the Fourier-transformed JW fermions from the 2π BZ onto the reduced zone as

$$c(k) = c_1(k).\vartheta(\pi/2-|k|)+c_2(k-\pi).\vartheta(|k|-\pi/2), \tag{3.4}$$

where $\vartheta(x)$ is the Heaviside step function. Then the coordinate representation of the JW fermion reads as

$$c_n = \frac{1}{\sqrt{N}}\sum_{\alpha,k} c_\alpha(k)(-1)^{(\alpha-1)n}e^{ikn}. \tag{3.5}$$

The Hamiltonian (3.2) at $\Delta = 0$ can be written as

$$H = \frac{1}{2}\sum_{k} \Psi_k^{\dagger}\mathcal{H}(k)\Psi_k, \tag{3.6}$$

where the fermions are unified in the spinor

$$\Psi_k^{\dagger} = (c_1^{\dagger}(k), c_2^{\dagger}(k), c_1(-k), c_2(-k)), \tag{3.7}$$

with the 4×4 Hamiltonian matrix

$$\mathcal{H}_k = \begin{pmatrix} \hat{A} & \hat{B} \\ \hat{B}^{\dagger} & -\hat{A} \end{pmatrix} \tag{3.8}$$

where

$$\hat{A} = \begin{pmatrix} h + t\cos k & h_a + i\delta \sin k \\ h_a - i\delta \sin k & h - t\cos k \end{pmatrix} \tag{3.9}$$

and

$$\hat{B} = \begin{pmatrix} -i\gamma \sin k & -\gamma_a \cos k \\ \gamma_a \cos k & i\gamma \sin k \end{pmatrix}. \tag{3.10}$$

The Hamiltonian has four eigenvalues [63] $\pm E_{\pm}$, where

$$E_{\pm}(k) = \sqrt{\mathfrak{C}_2(k) \pm \sqrt{\mathfrak{C}_2^2(k) - \mathfrak{C}_4(k)}} \tag{3.11}$$

with

$$\mathfrak{C}_2(k) = h^2 + h_a^2 + (t^2 + \gamma_a^2)\cos^2 k + (\delta^2 + \gamma^2)\sin^2 k \tag{3.12}$$

and

$$\mathfrak{C}_4(k) = \Big(h^2 - h_a^2 - (t^2 - \gamma_a^2)\cos^2 k - (\delta^2 - \gamma^2)\sin^2 k\Big)^2 + (t\gamma - \delta\gamma_a)^2 \sin^2 2k \tag{3.13}$$

The phase diagram of the model [63] shown in Fig. 3.1, is found from the condition

$$\mathfrak{C}_4(k) = 0, \tag{3.14}$$

for the critical lines, where the model becomes gapless. There are three phase boundaries:

(i) At $\pm h_c^{(1)}$ with

$$h_c^{(1)} = \sqrt{t^2 + h_a^2 - \gamma_a^2}, \quad \forall \gamma, \delta, \tag{3.15}$$

the gap vanishes at the center of BZ ($k = 0$).

(ii) At the edge of the BZ ($k = \pm\pi/2$), the gap vanishes on the circle

$$h^2 + \gamma^2 = h_a^2 + \delta^2, \tag{3.16}$$

which we will associate with the critical field $h_c^{(2)}$.

(iii) Two critical line segments at $\gamma = 0$ ($\gamma_a = 0$) correspond to the gap vanishing at the incommensurate (IC) wave vector

$$k_F = \pm \arcsin Q, \qquad Q = \sqrt{\frac{t^2 + h_a^2 - h^2}{t^2 - \delta^2}}, \tag{3.17}$$

which corresponds to the Fermi momentum ($\hbar = 1$) of the JW fermions. The IC solution exists in the range of parameters $\gamma = \gamma_a = 0$, $|\delta| < 1$, and

$$\sqrt{h_a^2 + \delta^2} \le |h| \le \sqrt{t^2 + h_a^2}. \tag{3.18}$$

The Fermi momentum (3.17) varies continuously from $k_F = 0$ at the intersection of $\gamma = 0$ and $h = \pm\sqrt{t^2 + h_a^2}$, to $k_F = \pi/2$ where the critical segments end at the

intersections with the circle

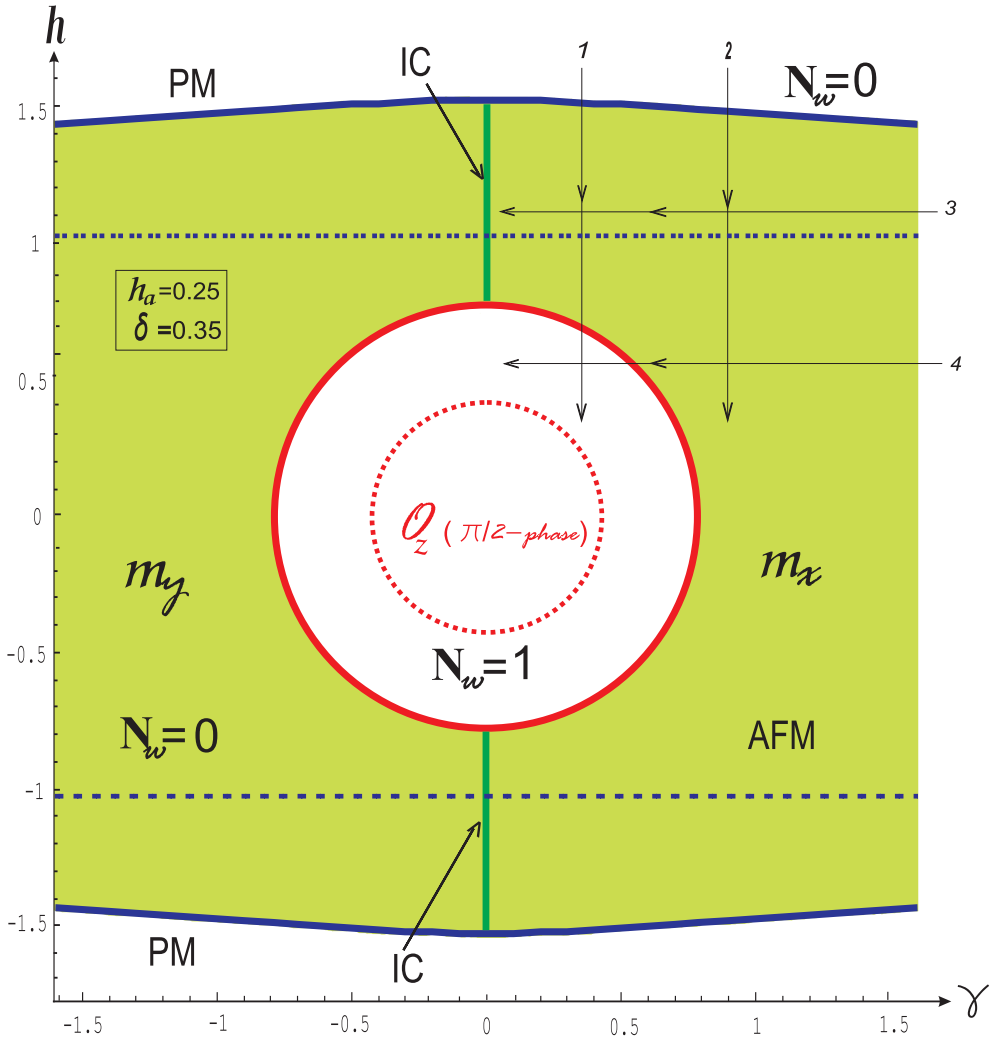

Figure 3.1: Phase diagram of the model in h-γ plane ($\gamma_a = 0$). The model is critical on (i) two infinite lines $h = \pm h_c^{(1)}$ (bold blue); (ii) circle $h^2 + \gamma^2 = \mathcal{R}^2$ (bold red); and (iii) two segments $h_c^{(2)} \leq |h| \leq h_c^{(1)}$ along $\gamma = 0$ (bold green). Three phases are shown: disordered paramagnetic (PM) polarized by the axial field, planar antiferromagnetic (AFM) with local order parameters $m_{x,y}$, and topological $\mathcal{O}_z(\pi/2)$ with oscillating string order. The four paths (1-4) in parametric space are indicated by thin lines. The winding numbers N_ω calculated in Sec.IV are shown. The bold phase boundaries are calculated for interaction $\Delta = 1/2$ while their dashed counterparts correspond to noninteracting case $\Delta = 0$.

3.1.2 Spin and Majorana averages

Differentiation of the free energy with respect to h and to h_a yields two magnetizations

$$m_z = \frac{1}{N}\sum_{n=1}^{N}\langle\sigma_n^z\rangle \tag{3.19}$$

$$m_z^a = \frac{1}{N}\sum_{n=1}^{N}(-1)^n\langle\sigma_n^z\rangle, \tag{3.20}$$

respectively. Their explicit expressions are

$$m_z = \frac{h}{\pi}\int_0^{\frac{\pi}{2}}\Big[\Big(\frac{1}{E_+}+\frac{1}{E_-}\Big)+\frac{t^2\cos^2 k+|\omega_a|^2}{R}\Big(\frac{1}{E_+}-\frac{1}{E_-}\Big)\Big]dk \tag{3.21}$$

and

$$m_z^a = \frac{h_a}{\pi}\int_0^{\frac{\pi}{2}}\Big[\Big(\frac{1}{E_+}+\frac{1}{E_-}\Big)+\frac{|\omega|^2+\gamma_a^2\cos^2 k}{R}\Big(\frac{1}{E_+}-\frac{1}{E_-}\Big)\Big]dk \tag{3.22}$$

We define auxiliary parameters:

$$\omega = h + i\gamma\sin k, \tag{3.23a}$$

$$\omega_a = h_a + i\delta\sin k, \tag{3.23b}$$

$$z = \omega\omega_a - t\gamma_a\cos^2 k, \tag{3.23c}$$

$$c = (ht + h_a\gamma_a)\cos k, \tag{3.23d}$$

$$R = \sqrt{c^2+|z|^2}. \tag{3.23e}$$

The Hamiltonian matrix (3.8) is diagonalized with the help of two unitary 2×2 matrices $\hat{\Phi}$ and $\hat{\Psi}$. We find

$$\hat{\Phi}(k) = \begin{pmatrix} e^{-i\theta}\beta_+ & \beta_- \\ -\beta_- & e^{i\theta}\beta_+ \end{pmatrix}, \tag{3.24}$$

where

$$e^{i\theta} = \frac{z}{|z|} \tag{3.25}$$

and

$$\beta_\pm = \frac{1}{\sqrt{2}}\Big(1 \pm \frac{c}{R}\Big)^{1/2}. \tag{3.26}$$

The second matrix of this Bogoliubov transformation is calculated as

$$\hat{\Psi} = \hat{I}_E^{-1}\hat{\Phi}(\hat{A} - \hat{B}) \tag{3.27}$$

where $\hat{I}_E = \mathrm{diag}(E_+, E_-)$. We introduce the Majorana fermions as

$$a_n + ib_n = 2c_n^\dagger. \tag{3.28}$$

From the matrix

$$\hat{G}(k) = \hat{\Psi}^\dagger(k)\hat{\Phi}(k). \tag{3.29}$$

We find the correlation function of the Majorana operators:

$$\langle ib_n a_m\rangle = \frac{1}{2\pi}\int_{-\pi}^{\pi}\Big(G_{11}(k) + (-1)^n G_{12}(k)\Big)e^{ik(m-n)}dk \tag{3.30}$$

where the matrix elements are:

$$G_{11}(k) = (t\cos k + \omega^*\left\{\frac{\beta_+^2}{E_+} + \frac{\beta_-^2}{E_-}\right\} + (\omega_a - \gamma_a\cos k)e^{-i\theta}\beta_+\beta_-\left\{\frac{1}{E_+} - \frac{1}{E_-}\right\} \tag{3.31a}$$

$$G_{12}(k) = (\omega_a - \gamma_a \cos k) \left\{ \frac{\beta_-^2}{E_+} + \frac{\beta_+^2}{E_-} \right\} + (t \cos k + \omega^*) e^{i\theta} \beta_+ \beta_- \left\{ \frac{1}{E_+} - \frac{1}{E_-} \right\} \quad (3.31b)$$

All the above formulas recover those of the model described in chapter 2 in the limit $t \to 1$ and $\gamma_a \to 0$. The correlation function (3.30) is a building element of Toeplitz determinants [79] used to calculate local order parameters (magnetizations) and nonlocal SOPs. Addition of $\gamma_a \neq 0$ only slightly numerically modifies positions of boundaries on the structure of the phase diagram, the nature of its phases, and order parameters essentially the same as presented in previous chapter and in our work [37], see Fig. 2.1.

3.2 Mean-field equations

The mean-field theory for the XYZ chain is in fact the Hartee-Fock approximation for its interacting fermionic representation (3.2). We use the most general decoupling [89] for the interacting term with a product of two number operators ($\hat{n}_l = c_l^\dagger c_l$) as

$$\hat{n}_l \hat{n}_m \approx \hat{n}_l \langle \hat{n}_m \rangle + \hat{n}_m \langle \hat{n}_l \rangle - \langle \hat{n}_l \rangle \langle \hat{n}_m \rangle + c_l^\dagger c_m \langle c_l c_m^\dagger \rangle + H.c. + |\langle c_l c_m^\dagger \rangle|^2$$

$$+ c_l^\dagger c_m^\dagger \langle c_m c_l \rangle + H.c. - |\langle c_l c_m \rangle|^2. \quad (3.32)$$

Such approximation applied to the Heisenberg chain is known from the literature to be accurate, at least qualitatively, see, e.g., [89, 90, 92–94]. One cannot expect the mean-field approximation to furnish, e.g., correct critical indices to identify the universality class, but predictions of model's phase diagram and order parameters are qualitatively correct. Since 1D is a realm of strong fluctuations, special care needs to be exercised while dealing with the mean-field predictions for phase boundaries (critical points). They need to be cross-checked against available exact results, as we will explain below.

We introduce the following mean-field parameters:

$$\langle c_n c_{n+1}^\dagger \rangle = \mathcal{K} + (-1)^n \delta\eta, \tag{3.33a}$$

$$\langle c_n c_{n+1} \rangle = \mathcal{P} - (-1)^n \delta\eta_p, \tag{3.33b}$$

$$\langle 1 - 2c_n^\dagger c_n \rangle = m_z + (-1)^n m_z^a. \tag{3.33c}$$

Using decoupling (3.32) and parameters (3.33a), (3.33b), and (3.33c) in Eq. (3.2), we obtain the approximate mean-field Hamiltonian

$$H \approx H_{MF} = N\Delta C + \frac{1}{2}\sum_k \psi_k^\dagger \mathcal{H}(k)\psi_k. \tag{3.34}$$

The renormalized Hamiltonian $\mathcal{H}_R(k)$ is given by the same expressions as for the noninteracting case (3.8), (3.9), and (3.10), with the difference that the six bare couplings of the free-fermionic Hamiltonian are replaced by the renormalized parameters as follows:

$$h \mapsto h_R = h - \Delta m_z, \tag{3.35a}$$

$$h_a \mapsto h_{aR} = h_a + \Delta m_z^a, \tag{3.35b}$$

$$t \mapsto t_R = 1 + 2\Delta(\mathcal{K} + \delta^2\eta), \tag{3.35c}$$

$$\delta \mapsto \delta_R = \delta(1 + 2\Delta(\mathcal{K} + \eta)), \tag{3.35d}$$

$$\gamma \mapsto \gamma_R = \gamma - 2\Delta(P - \delta^2\eta_p) \tag{3.35e}$$

$$\gamma_a \mapsto \gamma_{aR} = \gamma_a - 2\Delta\delta(P - \eta_p), \tag{3.35f}$$

and the constant term is

$$C = \mathcal{K}^2 - P^2 - \frac{1}{4}m_z^2 + \frac{1}{4}(m_z^a)^2 + \delta^2(\eta^2 - \eta_P^2 + 2\mathcal{K}\eta + 2P\eta_p). \tag{3.36}$$

Contrary to the model's bare parameters of choice, the renormalized coupling (3.35a)-(3.35f) are to be found from a set of six self-consistent equations obtained from minimization of the free energy. The latter is calculated from the Hartree-Fock Hamiltonian $\mathcal{H}_R(k)$. Using (3.33a), we find equations for the bond average

$$\mathcal{K} = \frac{t_R}{2\pi}\int_0^{2\pi} dk \cos^2 k \Big[\frac{1}{E_+} + \frac{1}{E_-} + \frac{h_R^2 + \gamma_{aR}^2 \cos^2 k}{R}\Big(\frac{1}{E_+} - \frac{1}{E_-}\Big)$$

$$+\frac{\delta_R\gamma_R\gamma_{aR}\sin^2 k}{t_R R}\Big(\frac{1}{E_+} - \frac{1}{E_-}\Big)\Big] \tag{3.37}$$

and for the dimerization susceptibility η

$$\delta\eta = \frac{\delta_R}{2\pi}\int_0^{2\pi} dk \sin^2 k \Big[\frac{1}{E_+} + \frac{1}{E_-} + \frac{|\omega|^2}{R}\Big(\frac{1}{E_+} - \frac{1}{E_-}\Big)$$

$$+\frac{t_R\gamma_R\gamma_{aR}\cos^2 k}{\delta_R R}\Big(\frac{1}{E_+} - \frac{1}{E_-}\Big)\Big]. \tag{3.38}$$

From (3.33b), we obtain equations for the anomalous pairing amplitude

$$P = \frac{\gamma_R}{2\pi}\int_0^{2\pi} dk \sin^2 k \Big[\frac{1}{E_+} + \frac{1}{E_-} + \frac{|\omega_a|^2}{R}\Big(\frac{1}{E_+} - \frac{1}{E_-}\Big)$$

$$+\frac{t_R\delta_R\gamma_{aR}\cos^2 k}{\gamma_R R}\Big(\frac{1}{E_+} - \frac{1}{E_-}\Big)\Big] \tag{3.39}$$

and for the anomalous susceptibility

$$\delta\eta_p = -\frac{\gamma_{aR}}{2\pi}\int_0^{2\pi} dk \cos^2 k \Big[\frac{1}{E_+} + \frac{1}{E_-} + \frac{h_{aR}^2 + t_R^2 \cos^2 k}{R}\Big(\frac{1}{E_+} - \frac{1}{E_-}\Big)$$

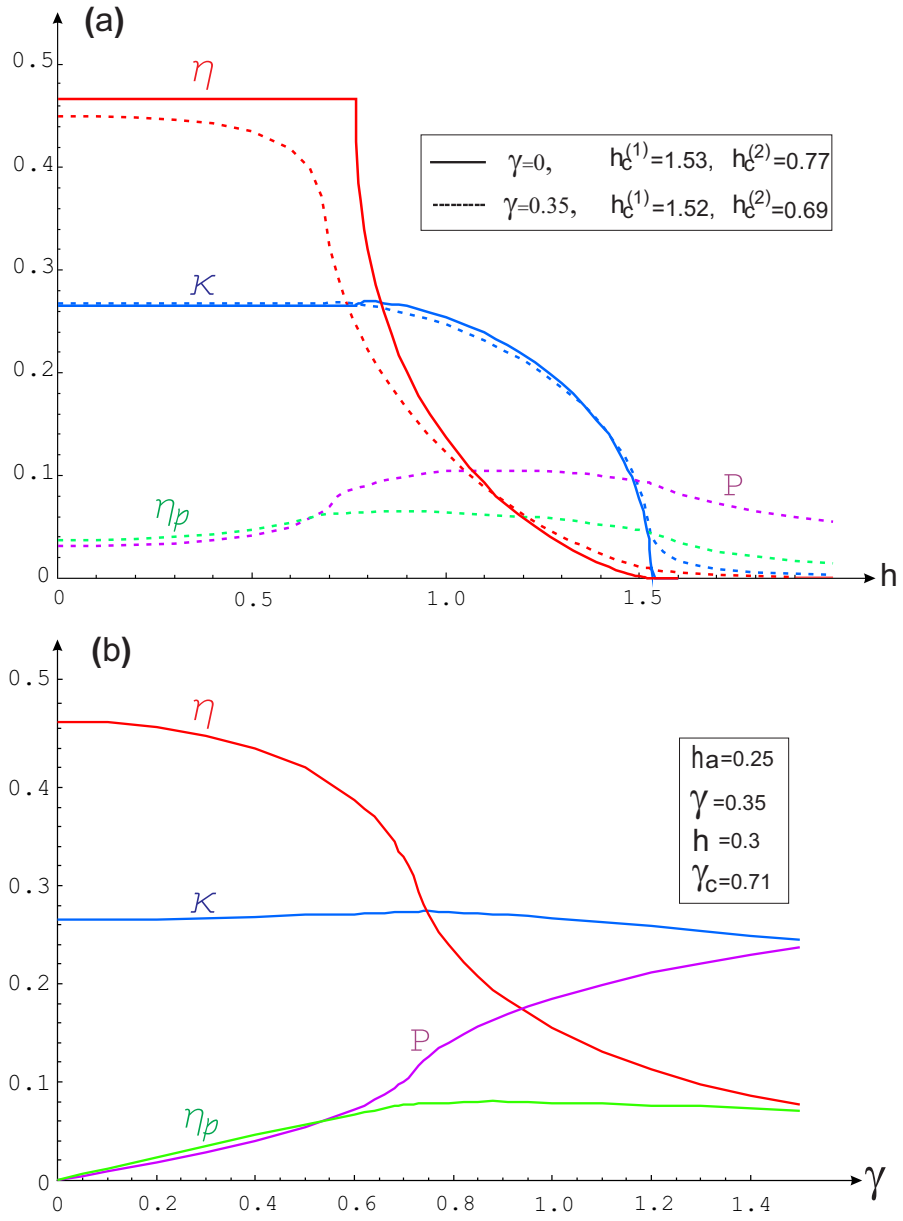

Figure 3.2: Representative behaviour of mean-field parameters (3.37)- (3.40) calculated for interaction $\Delta = 1/2$. (a) shows results along the path 1 on the phase diagram in Fig. 3.1. (b) corresponds to path 3. In addition, (a) presents results along the line $\gamma = 0$.

$$+\frac{t_R\delta_R\gamma_R\sin^2 k}{\gamma_{aR}R}\Big(\frac{1}{E_+}-\frac{1}{E_-}\Big)\Big]. \tag{3.40}$$

The uniform and staggered magnetization (3.33c) satisfy Eqs. (3.21) and (3.22) with their right hand sides written in terms of the renormalized couplings (3.35a)-(3.35f). In the following, we choose the bare coupling $\gamma_a = 0$.

The mean-field parameters (3.35a)-(3.35f) are fundamentally important for calculation of the phase diagram, the local and nonlocal (string order) parameters in different phases. The representative numerical results for these parameters are shown in Fig. 3.2. Note that anomalous average P and η_p are not the true (superconducting) order parameters signalling spontaneous breaking of $U(1)$ symmetry. This symmetry is intrinsically broken by model's anisotropy coupling γ, γ_a. As one can see from Fig. 3.2b, in the symmetry-restoring limit $\gamma, \gamma_a \to 0$, the anomalous average parameter vanish.

3.3 Results for XYZ chain

Before we proceed to explore predictions of the derived mean-field equations, let us first understand qualitatively possible outcomes. The way the mean-field theory is constructed, i.e., by switching to the renormalized couplings (3.37)-(3.40), makes it obvious that the interacting model has the same spectrum as in Eq. (3.11), but with renormalized parameters. Thus we obtain the same phases and their order parameters, conditions for the phase boundaries (gaplessness), etc., as described above for the case $\Delta = 0$, proviso that all bare couplings are renormalized in appropriate formulas. Within present theory, no new phase with a new order parameter, other than presented on the phase diagram in Fig. 3.1, can occur.

Interactions, however, can bring about additional nontrivial solutions of the mean-field equations for the normalized parameters, like, dimerization, anisotropy, uniform

or staggered fields/magnetizations, even when their bare counterparts are zero. That would constitute the case of spontaneous symmetry breaking associated with a phase transition. As one can see from Fig. 3.2b, the anomalous average parameters vanish in the limit $XYZ \to XXZ$. We did not find numerical signs of spontaneous breaking of the $U(1)$ symmetry (superconductivity) at $\Delta \neq 0$. Neither we found spontaneous dimerization when bare $\delta = 0$. This is in agreement with available results for the XYZ and XXZ models [111, 121, 123, 124]. However, it is known from exact results that $\Delta = \pm 1$ are critical points of the antiferro-/ferromagnetic phase transitions in the XXZ model [111, 121]. In the XYZ chain ($\gamma \neq 0$) spontaneous antiferro-/ferromagnetism appears at $|\Delta| > 1$ [123]. To stay on the safe side and to avoid dealing with the interaction-induced magnetism in the results which follow, we will assume the regime of weak interaction $|\Delta| < 1$ in this section. The strongly interacting regime $|\Delta| \gtrsim 1$ is discussed in subsection 3.4.2 for the XXZ chain.

The phase diagram of the model is shown in Fig. 3.1. Overall, the mean-field results in this regime are qualitatively similar to the noninteracting ($\Delta = 0$) case of previous chapter. The PM-AFM boundary (3.16) gets modified by interactions. It is not a straight line anymore. The value for critical field $h_c^{(1)}$ is available only numerically. However, its maximum value reached in the XXZ limit is found exactly from our equations:

$$\gamma = 0: \quad h_c^{(1)} = \Delta + \sqrt{1 + h_a^2} \tag{3.41}$$

in agreement with earlier scaling results [124].

The topological phase with oscillating string order is located inside the circle on the phase diagram in Fig. 3.1. Quite amazingly (in the view of complexity of the six coupled mean-field equations), interactions only change the radius of the circle $\mathcal{R}$,

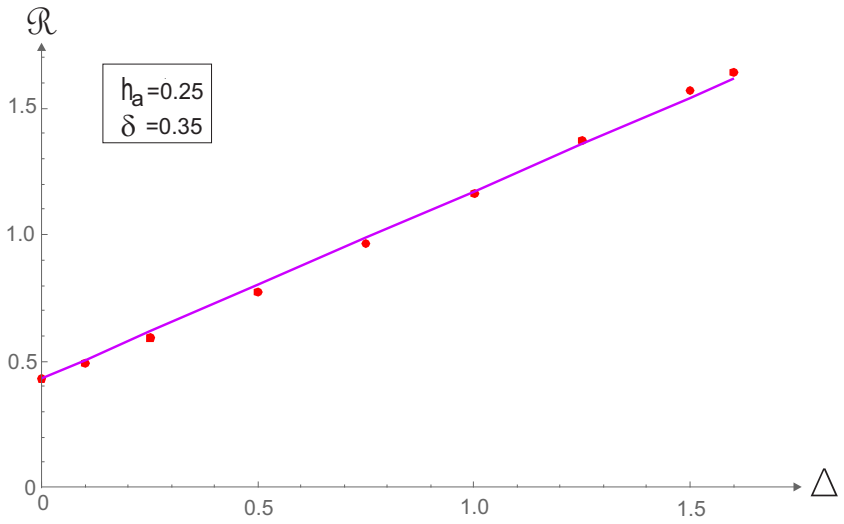

Figure 3.3: Radius of the circle enclosing $\mathcal{O}_z(\pi/2)$ phase in the phase diagram Fig. 3.1 as a function of interaction. The linear fit with the slope $\alpha \approx 0.745$ is shown.

conserving the perfect shape of this phase boundary. Numerically we found

$$\mathcal{R}(\Delta) \approx \mathcal{R}(0) + a\Delta, \tag{3.42}$$

where the radius for the noninteracting case $\mathcal{R}(0) = \sqrt{h_a^2 + \delta^2}$. The linear fit with $a \approx 0.745$, shown in Fig. 3.3, works quite well even at $\Delta \gtrsim 1$.

3.3.1 Induced and spontaneous magnetization

First we present the field-induced magnetizations m_z and m_z^a as functions of the uniform magnetic field h in Fig. 3.4. Their explicit expressions (3.21) and (3.22) are calculated at each point with the renormalized couplings on the right hand sides, determined self-consistently from numerical solution of the mean-field equations given in the previous section.

The plots for the XYZ chain are done for two cases (see Fig. 3.4). The first case

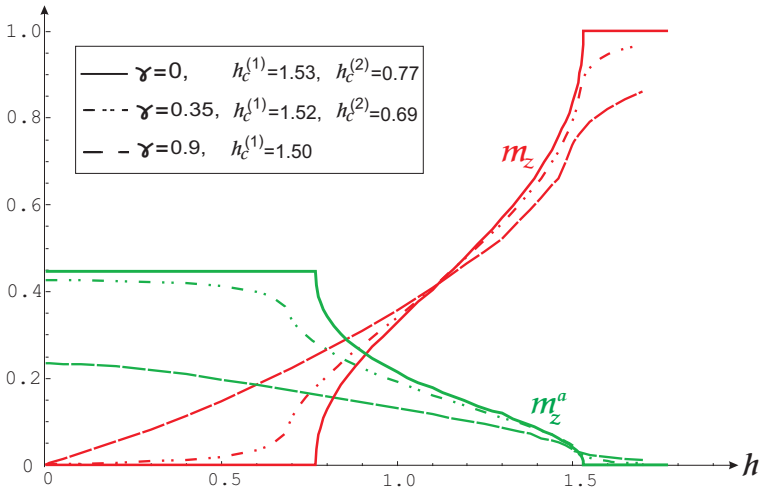

Figure 3.4: Two induced magnetizations m_z (red) and m_z^a (green) vs uniform field h at $\delta = 0.35, h_a = 0.25, \Delta = 0.5$ for different γ. At $\gamma = 0, m_z$ (solid line) demonstrates plateaux in the gapped phases connected by a continuous curve through the gapless IC phase. Similar behaviour is demonstrated by m_z^a. Dashed dotted lines correspond to path 1 shown in phase diagram Fig. 3.1. Dashed lines correspond to the path 2. The magnetizations show noticable cusps at the critical fields $h_c^{(1)}$ (path 2); $h_c^{(1)}$ and $h_c^{(2)}$ (paths $\gamma = 0$ and 1), when the paths cross phase boundaries.

corresponds to the path 1 on the phase diagram in the h-γ plane shown in Fig. 3.1. The path crosses the PM-AFM boundary at $h = h_c^{(1)}$ and the AFM-$\mathcal{O}_z(\pi/2)$ boundary at $h = h_c^{(2)}$. The magnetizations have noticeable cusps at these critical points, which correspond to divergent susceptibilities. In case of the path 2, it crosses only the PM-FM boundary and bypasses the topological phase. The magnetizations demonstrate cusps at the only critical point $h_c^{(1)}$, while at $h < h_c^{(1)}$ they and their derivatives are analytical.

The phase diagram in Fig. 3.1 contains two conventional antiferromagnetic phases with spontaneous planar magnetizations m_x and m_y. The local order parameter m_x is calculated from the limit of the spin-correlation function which is also the correlation

function of the Majorana string operators [79]:

$$\lim_{(R-L)\to\infty}\langle\sigma_L^x\sigma_R^x\rangle = \lim_{R\to\infty}\left\langle\prod_{n=L}^{R-1}[ib_na_{n+1}]\right\rangle \Rightarrow m_x^2. \tag{3.43}$$

As we have shown in chapter 2, this Majorana string correlation function is given by the dererminant of the block Toeplitz matrix constructed from $\frac{1}{2}(R-L)\times\frac{1}{2}(R-L)$ blocks of size 2×2 with the elements given by Eq. (3.30). For explicit expressions of this block Toeplitz matrix we refer the reader to chapter 2. At each point in the parametric space, the elements (3.30) of this matrix are calculated with renormalized couplings determined from the mean-field equations. The results for spontaneous magnetization are given in Fig. 3.6. The numerical values of the parameters we present in that figure are stable in the fourth decimal place for the $M\times M$ matrices of sizes $M\gtrsim 30$. In immediate vicinities of the critical points the order parameters are checked to decay smoothly as $M\to\infty$. The expressions for m_y are obtained along the same lines. Numerical values satisfy useful relation $m_y(-\gamma)=m_x(\gamma)$, verified explicitly.

3.3.2 Nonlocal string order

Now we address the topological phase with nonlocal string order inside the circle in Fig. 3.1, first reported in Ref. [37] for noninteracting case. It turns out that the femionic interaction renormalizes the phase boundary and SOPs, but does not alter the nature of the order in this phase. To qualify this type of order, we use the string operator

$$O_z(n)\equiv\prod_{l=1}^{n}\sigma_l^z=\prod_{l=1}^{n}[ib_la_l] \tag{3.44}$$

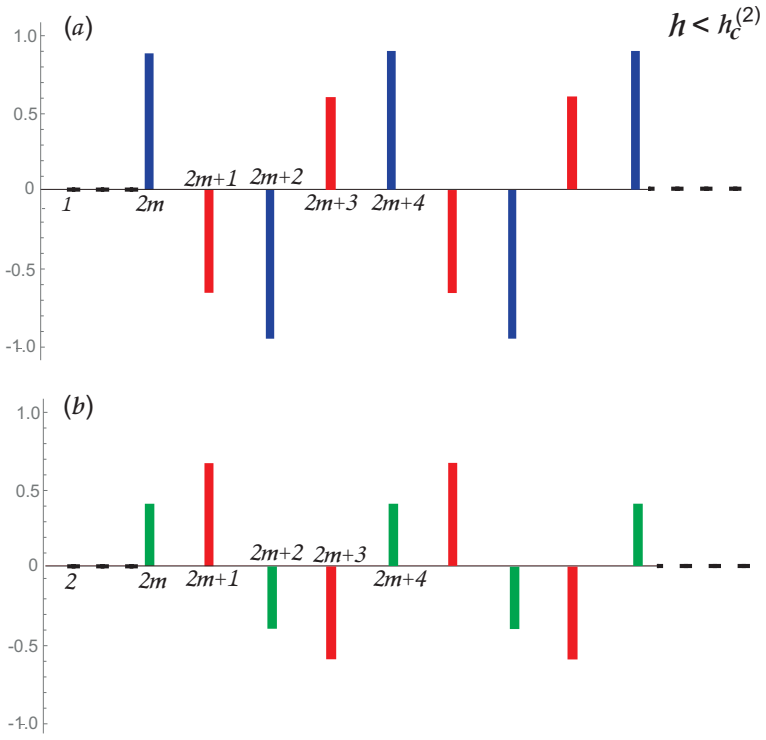

Figure 3.5: Visualization of the oscillating string order inside the circle at the point $h = 0.2$ on path 1 (Fig. 3.1) for $h_a = 0.25, \delta = 0.35, \gamma = 0.35$, and $\Delta = 1/2$. (a) shows $\mathfrak{D}_{zz}(1, N)$ (3.44) with alternating limiting values $\pm\mathcal{O}^2_{z,1}$ (blue) and $\pm\mathcal{O}^2_{z,3}$ (red). (b) shows $\mathfrak{D}_{zz}(2, N)$ with similar parameters $\pm\mathcal{O}^2_{z,2}$ (green) and $\pm\mathcal{O}^2_{z,3}$.

and related string correlation function

$$\mathfrak{D}_{zz}(L, R) = \langle O_z(L-1)O_z(R)\rangle = \left\langle \prod_{l=L}^{R} [ib_l a_l] \right\rangle . \tag{3.45}$$

Following the original proposal by den Nijs and Rommelse [28], the SOP was defined and detected in the subsequent work on the spin chains, see, e.g., Refs. [31, 33, 125]. The SOP was defined (up to some minor variations) as the limit of the string-string correlation function, which is not convenient, since such SOP has a wrong dimension of square of the order parameter. The definition we use, due to Berg *et al.* [97], is more consistent with the standard theory of critical phenomena, and the critical index of

the (string) order parameter β correctly enters all the hyperscaling relations [35]. The correlation function (3.45) is calculated from the determinant of the block Toeplitz matrices, built from elements (3.30). These matrices are given explicitly in previous chapter.

Inside the circle, $\mathfrak{D}_{zz}$ oscillates with the period of four lattice spacings (i.e., *twice the unit cell*), see Fig. 3.5. Doubling of the translational period by the string order is a sign of spontaneous breaking of the hidden $\mathbb{Z}_2 \bigotimes \mathbb{Z}_2$ symmetry. This phase is labeled as $O_z(\pi/2)$ to distinguish it from the plain behaviour of $\mathfrak{D}_{zz}$ in the PM phase. Since $\mathfrak{D}_{zz}(L,R) \neq \mathfrak{D}_{zz}(R-L)$, we need three parameters to account for the string order:

$$\mathfrak{D}_{zz}(L,R) \longrightarrow \lim_{R\to\infty} \begin{cases} (-1)^m O^2_{z,1}, & L=1, \quad R=2m, \\ (-1)^m O^2_{z,2}, & L=2, \quad R=2m, \\ (-1)^{m+L} O^2_{z,3}, & L=1,\ R=2m+1 \text{ or } L=2,\ R=2m+1. \end{cases} \tag{3.46}$$

The ordering patterns (3.46) detected from nondecaying oscillations of the string correlation function for a particular parametric point in the $\mathcal{O}_z(\pi/2)$ phase, are depicted in Fig. 3.5. The magnitudes of the SOPs $\mathcal{O}_{z,i}$ along different paths on the phase diagram Fig. 3.1 are given in Figs. 3.6a and 3.6c. At each point the SOP is calculated with the renormalized couplings determined from the numerical solution of the self-consistent mean-field equations. Similarly to the noninteracting case [37], the other two components of the SOP $\mathcal{O}_x$ and $\mathcal{O}_y$ vanish when $h \neq 0$ and $h_a \neq 0$.

The string correlation function $\mathfrak{D}_{zz}$ in the PM saturated phase is always positive and essentially monotonous. For completeness we plot in Fig. 3.6 the PM SOP defined as $\lim_{R\to\infty} \mathfrak{D}_{zz}(L,R) = \mathcal{O}_z^2$.

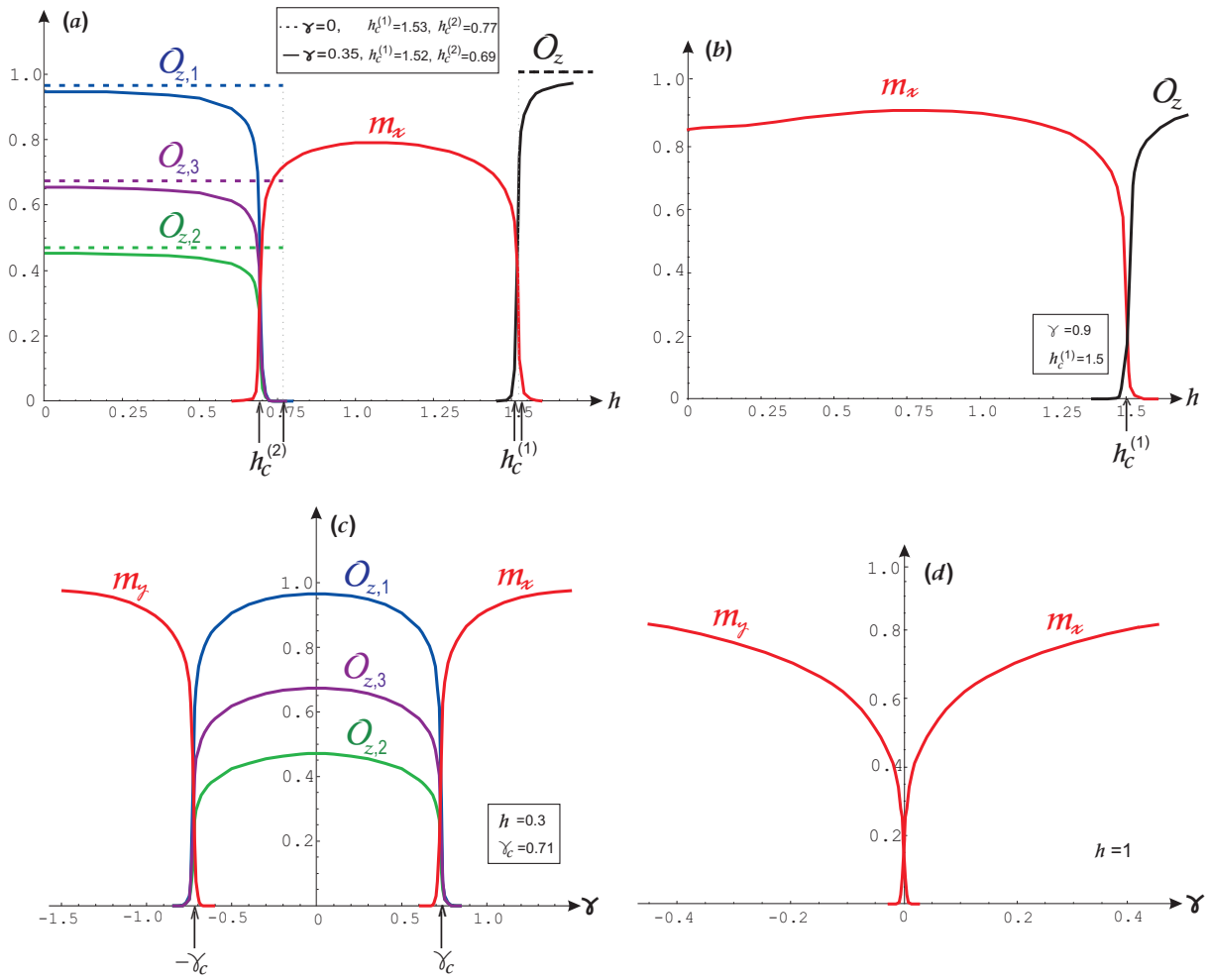

Figure 3.6: Spontaneous planar magnetizations $m_{x,y}$ and modulated order parameters $\mathcal{O}_{z,i}$ numerically calculated from the $2N \times 2N$ matrices with $N = 70$. The panels (a-d) correspond to the path 1-4 on the phase diagram shown in Fig. 3.1 ($h_a = 0.25$ and $\delta = 0.35$). In the AFM phases, $m_{x,y} \neq 0$ and $\mathcal{O}_{z,i} = 0$. In the PM phase $h > h_c^{(1)}, \mathcal{O}_z \neq 0$ and plainly monotonous. The exact values of the parameters seen in the immediate vicinities of the critical points are the finite-size effects, checked to die off as $N \to \infty$. The special case $\gamma = 0$ when all SOPs become step-like functions is shown in (a).

There are interesting limiting cases of the topological string order. Two alternating (bare) parameters of the model, h_a and δ generate the topological phase, see Fig. 3.1. The radius of its boundary $\mathcal{R} = \sqrt{h_{aR}^2 + \delta_R^2}$. We check from the mean-field equations that at $|\Delta| < 1$, $h_{aR} \propto h_a$ and $\delta_R \propto \delta$, i.e., turning off one of those parameters, turns off its renormalized counterpart as well. Although the four lattice spacing periodicity of the string correlation function (3.46) is preserved, its ordering patterns are distinct. There are often physically interesting situation when there is an alternating component of the magnetic field (or modulated chemical potential), when dealing with various versions of the Kitaev-Majorana models (3.2), while the dimerization is absent. Or vice versa, quite often one is dealing with dimerized models with uniform magnetic field (chemical potential). We find for the former case,

$$h_a = 0, \quad \delta \neq 0: \quad \mathcal{O}_{z,1} \neq 0, \quad \mathcal{O}_{z,2} = \mathcal{O}_{z,3} = 0, \tag{3.47}$$

and for the latter,

$$h_a \neq 0, \quad \delta = 0: \quad \mathcal{O}_{z,1} = \mathcal{O}_{z,2} = \mathcal{O}_{z,3}, \tag{3.48}$$

These properties hold for the noninteracting case ($\Delta = 0$) as well as in the presence of interactions ($\Delta \neq 0$). Two cases of the ordering patterns are shown in Fig. 3.7

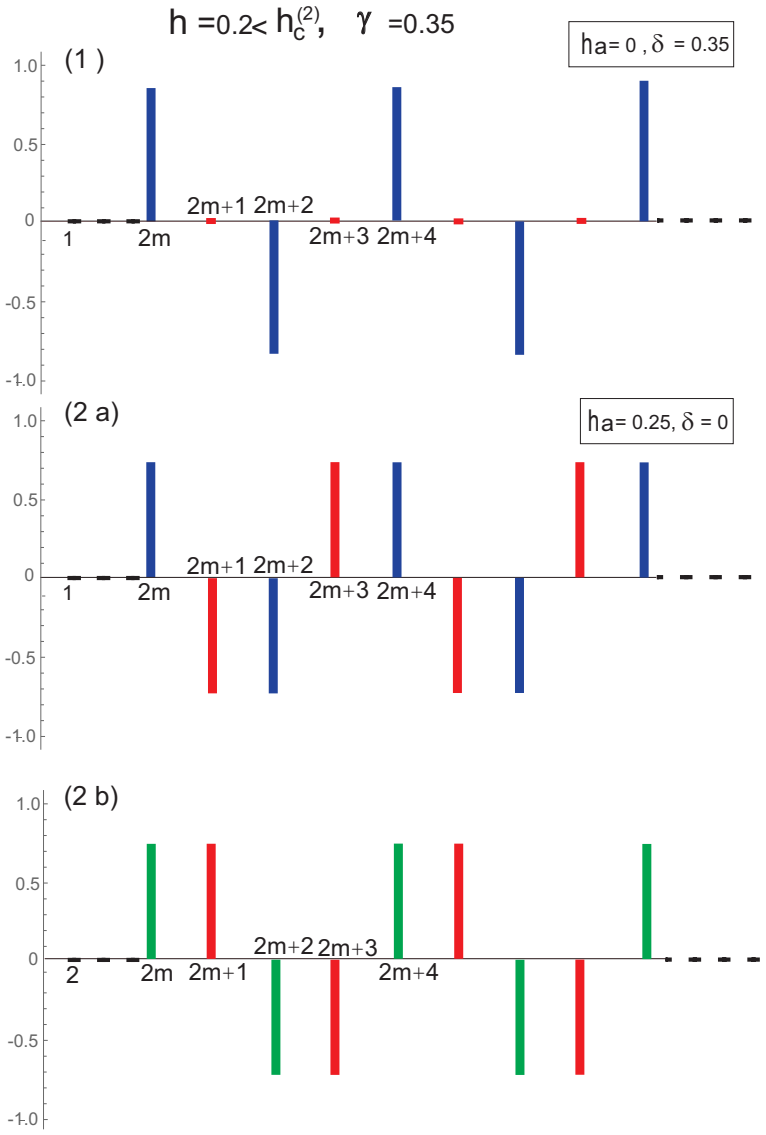

Figure 3.7: Visualization of the oscillating string order inside the circle at the point $h = 0.2$ on path 1 (Fig. 3.1) with $\gamma = 0.35$ and $\Delta = 1/2$ for two special cases. (1) For $h_a = 0$ and $\delta = 0.35$, the string order shown in Fig. 3.5b vanishes, since $\mathcal{O}_{z,2} = \mathcal{O}_{z,3} = 0$, while the order shown in Fig. 3.5a reduces to the pattern (1) above. (2) For $h_a = 0.25$ and $\delta = 0$, $\mathcal{O}_{z,1} = \mathcal{O}_{z,2} = \mathcal{O}_{z,3} \neq 0$, and the patterns shown in Fig. 3.5 become the same, up to a single lattice spacing translation, as shown in (2a) and (2b) above.

Note that the case (3.47) applies for the dimerized isotropic ($\gamma = 0$) Heisenberg chain without magnetic field. In the SU(2) limit $\Delta = 1$, the noninteracting result (2.85) can be improved. The magnitude of the SOP $\mathcal{O}_{z,1}$ was calculated by Hida via bosonization [33], however the oscillating pattern of the string order shown in Fig. 3.7 was not reported before.

To deal with the string order in a more unified and compact way, we introduce a new function

$$\mathfrak{D}^{+}_{zz}(n) = \mathfrak{D}_{zz}(1,n) + \mathfrak{D}_{zz}(2,n) \tag{3.49}$$

From visual inspection of the patterns shown in Figs. 3.5a and 3.5b one can easily check that $\mathfrak{D}^{+}_{zz}(n)$ has its ordering pattern similar to the one shown in Fig.3.7(1), i.e.,

$$\lim_{n\to\infty} \mathfrak{D}^{+}_{zz}(n) = \cos\left(\frac{\pi}{2}n\right)\mathcal{O}^{2}_{z,+}, \tag{3.50}$$

where

$$\mathcal{O}^{2}_{z,+} = \mathcal{O}^{2}_{z,1} + \mathcal{O}^{2}_{z,2}. \tag{3.51}$$

From inspection of Fig. 3.7 one can check as well that the special cases (3.47) and (3.48) can be united under the same pattern of Eq. (3.50).

3.3.3 Winding number

For each phase we also find the winding number. The calculation outlined in Ref. [37], for the quadratic Hamiltonian (3.8), (3.9), and (3.10) leads to the following result:

$$N_{\omega} = \frac{1}{2\pi i}[\ln\lambda_{+}(k) + \ln\lambda_{-}(k)]^{\frac{\pi}{2}}_{-\frac{\pi}{2}} \tag{3.52}$$

where

$$\lambda_{\pm}(k) = h \pm \Big[h_a^2 + (t^2 - \gamma_a^2)\cos^2 k = (\delta^2 - \gamma^2)\sin^2 k$$

$$-i(t\gamma - \delta\gamma_a)\sin 2k \Big]^{1/2} \tag{3.53}$$

are the eigenvalues of $\hat{D}(k) = \hat{A}(k) + \hat{B}(k)$. One can establish an important relation between parameter $\mathfrak{C}_4$ of the Hamiltonian's spectrum, defined by (3.13), and eigenvalues (3.53):

$$\mathfrak{C}_4 = |\lambda_+|^2 |\lambda_-|^2. \tag{3.54}$$

A simple comparison of the condition (3.14) for quantum criticality and Eq. (3.54) leads to the following conclusion: *topological winding number (mod 2) can change only upon crossing gapless phase boundary.* Within the present approach, number N_ω in different phases of interacting model are calculated using Eqs. (3.52) and (3.53) with renormalized couplings. Their values are shown in Fig. 3.1. Only the phase with oscillating string order is topologically nontrivial, $N_\omega = 1$.

3.4 Isotropic chain

In this section, we present the results for isotropic XXZ chain, that is the limit $\gamma = \gamma_a = 0$. It turns out that a considerable progress can be achieved in analytical treatments, making the outcome more transparent for intuitive grasp.

3.4.1 Noninteracting XX limit ($\Delta = 0$)

Most of the formulas of Sec 3.1 for free fermions can be brought to a closed form of standard mathematical functions. The content of this subsection is implicitly present in the earlier work [37], but the XX limit was not specifically analyzed in that paper.

The spectrum (3.11) becomes

$$E_{\pm}(k) = h \pm \xi, \qquad \xi = \sqrt{h_a^2 + t^2 \cos k + \delta^2 \sin^2 k} \tag{3.55}$$

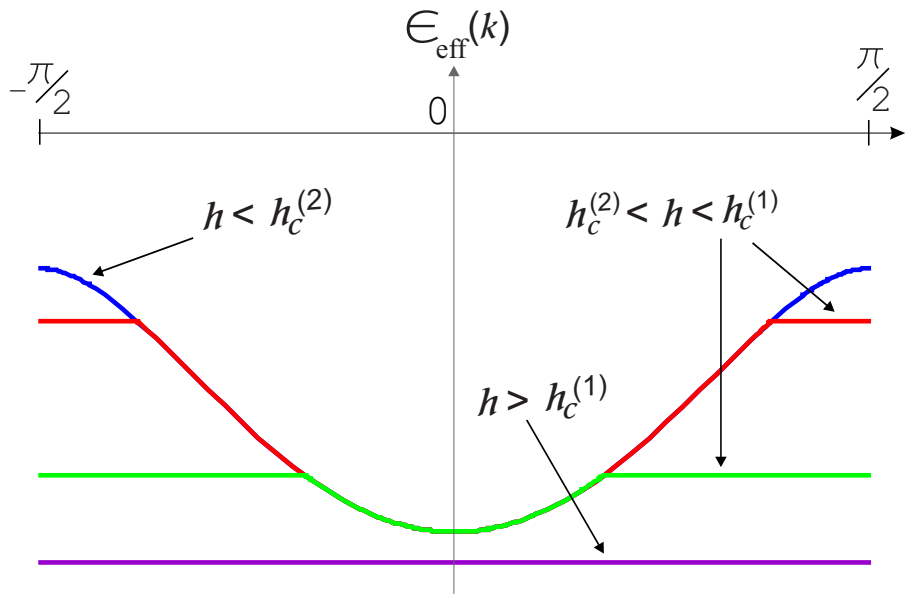

Figure 3.8: The effective single-particle spectrum $\varepsilon_{\rm eff}(k)$ in three phases at different values of the uniform field.

To better understand results of this section, it is convenient to write the ground-state energy per site

$$f = -\frac{1}{2\pi}\int_0^{2\pi} (|E_+| + |E_-|)dk \tag{3.56}$$

as

$$f = \frac{1}{2\pi}\int_{-\pi/2}^{\pi/2} \varepsilon_{\rm eff}(k)dk \tag{3.57}$$

The effective spectrum $\varepsilon_{\rm eff}(k)$ is shown in Fig. 3.8 for three phases. From (3.55) and (3.56), we find the h-independent effective spectrum $\varepsilon_{\rm eff}(k) = -\xi$ in the topological phase ($h < h_c^{(2)}$). In the IC gapless phase ($h_c^{(2)} < h < h_c^{(1)}$), the parabolic spectrum $\varepsilon_{\rm eff} = -\xi$ at $|k| < k_F$ with the Fermi momentum given by Eq. 3.17), becomes a flat

band $\varepsilon_{\text{eff}}(k) = -h$ at $k_F < |k| < \pi/2$. The fermi sea shrinks with the growth of the field, as shown in Fig. 3.8, and in the PM phase ($h > h_c^{(1)}$) the whole band is flat, $\varepsilon_{\text{eff}}(k) = -h$.

Analytically, we find

$$f = \begin{cases} -\frac{1}{2}h, & h > h_c^{(1)} \\ -\frac{1}{\pi}\sqrt{t^2+h_a^2}\mathbf{E}(k_F,\kappa^2) - \frac{1}{2}(1-\frac{2}{\pi}k_F), & h \in [h_c^{(2)}, h_c^{(1)}] \\ \frac{1}{\pi}\sqrt{t^2+h_a^2}\mathbf{E}(\kappa^2), & h < h_c^{(2)} \end{cases} \tag{3.58}$$

Here, $\mathbf{E}$ is the elliptic integral of the second kind, and

$$\kappa^2 = \frac{t^2-\delta^2}{t^2+h_a^2}. \tag{3.59}$$

The uniform magnetization derived from Eq. 3.21

$$m_z = \frac{1}{2} + \frac{1}{\pi}\int_0^{\pi/2} \text{sign}(\text{E}_-)dk \tag{3.60}$$

or obtained directly from differentiation of (3.58), demonstrates two plateaus in the gapped phases, connected by a continuous curve in between:

$$m_z = \begin{cases} 1, & h > h_c^{(1)} \\ 1-\frac{2}{\pi}k_F, & h \in [h_c^{(2)}, h_c^{(1)}] \\ 0, & h < h_c^{(2)} \end{cases} \tag{3.61}$$

The above result is in agreement with the arguments of Ref. [60], the generalizing the Lieb-Schultz-Mattis (LSM) theorem [79] for nonzero field. According to another formulation of the LSM theorem in terms of fermions [61] (cf. Eq. (40)], the plateaus

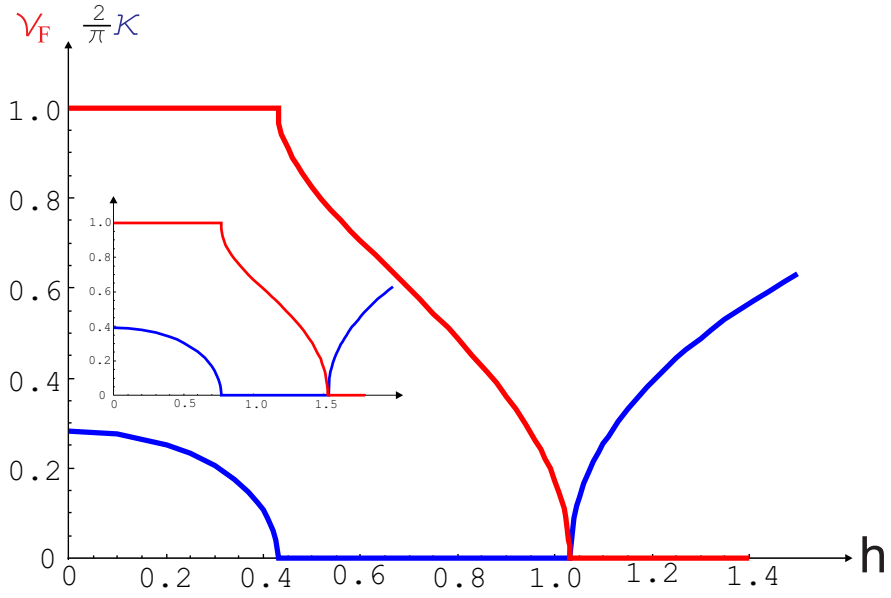

Figure 3.9: Real and imaginary parts of the complex wave vector k_+ giving the values of the fermionic filling per unit cell $\nu_F = 2/\pi k_F$ and inverse correlation length $\xi^{-1} \propto \kappa$ for the three phases. The main plot is done for noninteracting model with $h_a = 0.25$ and $\delta = 0.35$. The inset shows the same parameters for he interacting case with $\Delta = 0.5$..

of magnetization correspond to commensurate rational $(m/N; m, n \in N)$ fermionic fillings per unit cell, and the filling can admit arbitrary real values only in the gapless phase, leading to a smooth evolution of $m_z \in [0, 1]$ at $h \in [h_c^{(2)}, h_c^{(1)}]$.

To unify and generalize the analysis of phases done in Sec. 3.1 and to directly relate it to the LSM theorem [61, 79], we analytically continue the spectrum of the model onto the complex plane $z \in \mathbb{C}$ with $z = e^{ik}$ [111]. In the isotropic limit, the eigenvalues $\lambda_\pm$ defined by Eq. (3.53) become the eigenvalues of the Hamiltonian (3.55), so the condition of the quantum criticality (3.14) with Eq. (3.54) reads

$$|E_+(z)|^2 |E_-(z)|^2 = 0. \tag{3.62}$$

Using Q defined in Eq. (3.17) and extended to $Q \in \mathbb{C}$, we find two roots of (3.62)

$$z_\pm = e^{ik_\pm} = \Lambda_\pm, \quad \text{with } \Lambda_\pm \equiv iQ \pm \sqrt{1-Q^2}, \tag{3.63}$$

The roots $\Lambda_\pm$ encode important information about three phases. (1) In the IC phase $Q \in \mathbb{R}$ and $0 < Q < 1$. The roots are complex conjugate $\Lambda_+ = \Lambda_-^*$ and $|\Lambda_\pm| = 1$. The wave vectors $k_\pm \in \mathbb{R}$ and we can pick $k_+ = k_{_F}$ corresponding to the known solution (3.17). The real wave vector $k_{_F}$ defines the period of oscillations of correlation functions [see Eq. (3.83) below] and controls the (IC) filling (Fermi level) of the parabolic band $\nu_{_\mathrm{F}} = 2/\pi k_{_\mathrm{F}}$, see Figs. 3.8 and 3.9.

(2) In the PM phase $Q = i|Q|$ is imaginary, and it leads to the imaginary $k_\pm = -i \ln \lambda_\pm$, see Fig. 3.9:

$$k_{_F} = \mathrm{Re} k_\pm = 0, \tag{3.64}$$

and

$$\kappa = \mathrm{Im} k_+ = -\ln(\sqrt{1+|Q|^2} - |Q|). \tag{3.65}$$

The nonvanishing imaginary part of the complex root k_+ gives the inverse correlation length [111], and it is responsible for the exponential decay of correlation functions in gapped phases. In the vicinity of the PM transition $h \to h_c^{(1)} + 0 : |Q| \ll 1$, and $\kappa \approx |Q| \propto \left(h - h_c^{(1)}\right)^{1/2}$. The vanishing real part of the root $k_{_F} = 0$ means monotonous behaviour of correlation functions without oscillations.

Note that probing the correlation length in the limit $\gamma \to 0$ is subtle in the PM (polarized) phase. In this case, $m_z = \mathcal{O}_z = 1$ and $m_x = m_y = 0$. Moreover, the correlation functions are featureless, i.e., $\langle \sigma_L^z \sigma_R^z \rangle = 1$ and $\langle \sigma_L^x \sigma_R^x \rangle = \langle \sigma_L^y \sigma_R^y \rangle = 0, \ \ \forall \ L, R$. (These functions were first found by Borouch and McCoy in [96] for the case $h_a = \delta = 0$). The string correlation functions are found to behave in a similar way, i.e., $\mathcal{D}_{zz} = 1$ and

$\mathcal{D}_{xx} = \mathcal{D}_{yy} = 0$ at $\gamma = 0$. As one can find in Table 1.2 of the book by Franchini [111] at $h > 1$ and $\gamma \neq 0 \quad (h_a = \delta = 0)$, the spin correlation function

$$\langle \sigma_1^x \sigma_n^x \rangle \simeq X_D \frac{\Lambda_+^{-n}}{\sqrt{n}} \quad \text{at} \quad n \gg 1, \tag{3.66}$$

where Λ_+ defined as in Eq. (3.63), determines the correlation length and agrees with the $\gamma \to 0$ result (5.90). Vanishing of the correlation function in the above equation is due to prefactor $X_D \to 0$ as $\gamma \to 0$ [111]. No analytical results are available for the spin or string correlation functions in the general case $h_a \neq 0$ and $\delta \neq 0$, but we infer from numerical calculations that those functions have: (i) rapid decreases with distance n; (ii) vanishing amplitudes; (iii) finite gap and thus meaningful definition of the correlation length in the limit $\gamma \to 0$, similar to the equation above. Another way to probe the finite gap (inverse correlation function) at $\gamma = 0$, is to consider nonzero temperature, when one expects temperature correlations to the correlation and/or response functions $\propto \exp(-\mathcal{O}(1)\kappa/T)$.

(3) For the $\mathcal{O}_z(\pi/2)$ phase, it is convenient to use $V \equiv \sqrt{1-Q^2}$. In this phase $V = i|V|$ is imaginary, leading to

$$k_{_F} = \mathrm{Re} k_+ = \frac{\pi}{2}, \tag{3.67}$$

and

$$\kappa = -\mathrm{Im} k_+ = \ln(\sqrt{1+|V|^2} + |V|). \tag{3.68}$$

The real part of the root $k_{_F} = \pi/2$ corresponds to the constant filling $\nu_{_F} = 1$ in this phase and $\pi/2$ oscillations of the string correlation function (3.50). Near transition point $h \to h_c^{(2)} - 0$: $|V| \ll 1$ and $\kappa \approx |V| \propto \left(h_c^{(2)} - h\right)^{1/2}$, in agreement with the expected gap closing.

The above results for real and imaginary parts of the complex roots $k_\pm$ are depicted in Fig. 3.9. In agreement with general arguments [61] and with Fig. 3.9, the magnetization in all three phases can be related to the filling as $m_z = 1 - \nu_{\rm F}$.

Qualitatively, the integer-valued fermionic fillings connected by a continuous curve through the gapless phase of Fig. 3.9, are due to the flat piece of the effective spectrum shown in Fig. 3.8. An interesting topological transition known as fermionic condensation [126] is signalled by appearance of a continuous real filling smoothly connecting between two integer values $(1, 0)$ of the step function predicted by the Landau Fermi-liquid theory. One needs a flat band piece of the single-particle spectrum for such noninteger filling to occur. The flat band and fermionic condensation [127] can model linear-T resistivity in the so-called Planckian metal [128, 129]. These analogies are worth exploring further.

Two complex roots $\Lambda_\pm$ are also the eigenvalues of the transfer matrix which generates the wave function of the zero-energy edge Majorana fermion [36]. Our findings predict that the localized Majorana edge state in the $\mathcal{O}_z(\pi/2)$ phase has the wave function with the inverse penetration depth $\propto \kappa$. The exponential decay of the wave function into the bulk is modulated by $\pi/2$ oscillations. In the IC phase the edge state gets delocalized, since $\kappa = 0$. A more detailed analysis of the Majorana zero-energy edge states is worth pursuing.

The staggered magnetization found from Eq. (3.22) as

$$m_z^a = \frac{h_a}{\pi} \int_0^{\pi/2} \frac{dk}{\xi} (1 - \mathrm{sign}(E_-)) \tag{3.69}$$

leads to

$$m_z^a = \begin{cases} 0, & h > h_c^{(1)} \\ \frac{2h_a}{\pi\sqrt{t^2+h_a^2}}\mathbf{F}(k_{_F},\kappa^2), & h \in [h_c^{(2)}, h_c^{(1)}] \\ \frac{2h_a}{\pi\sqrt{t^2+h_a^2}}\mathbf{K}(\kappa^2), & h < h_c^{(2)} \end{cases} \tag{3.70}$$

Here $\mathbf{K}$ and $\mathbf{F}$ are, respectively, the complete and incomplete elliptic integrals of the first kind.

The bond average and dimerization susceptibility (3.33a) can be also found in a closed form via elliptical functions [130]. Indeed

$$\mathcal{K} = \frac{1}{2\pi}\int_0^{\pi/2} dk \frac{\cos^2 k}{\xi}(1-\mathrm{sign}(E_-)) \tag{3.71}$$

yields

$$\mathcal{K} = \begin{cases} 0, & h > h_c^{(1)} \\ \frac{\sqrt{t^2+h_a^2}}{\pi\sqrt{t^2-\delta^2}}\mathbf{E}(k_{_F},\kappa^2) - (1-\kappa^2)\mathbf{F}(k_{_F},\kappa^2), & h \in [h_c^{(2)}, h_c^{(1)}]. \\ \frac{\sqrt{t^2+h_a^2}}{\pi\sqrt{t^2-\delta^2}}\mathbf{E}(\kappa^2) - (1-\kappa^2)\mathbf{K}(\kappa^2), & h < h_c^{(2)} \end{cases} \tag{3.72}$$

The dimerization susceptibility

$$\eta = \frac{1}{2\pi}\int_0^{\pi/2} dk \frac{\sin^2 k}{\xi}(1-\mathrm{sign}(E_-)) \tag{3.73}$$

is found as

$$\eta = \begin{cases} 0, & h > h_c^{(1)} \\ \frac{\sqrt{t^2+h_a^2}}{\pi\sqrt{t^2-\delta^2}}\mathbf{F}(k_{_F},\kappa^2) - (1-\kappa^2)\mathbf{E}(k_{_F},\kappa^2), & h \in [h_c^{(2)}, h_c^{(1)}]. \\ \frac{\sqrt{t^2+h_a^2}}{\pi\sqrt{t^2-\delta^2}}\mathbf{K}(\kappa^2) - \mathbf{E}(\kappa^2), & h < h_c^{(2)} \end{cases} \tag{3.74}$$

In the isotropic limit, two anomalous parameters (3.33b) breaking the particle number

conservation, $P = \eta_p = 0$ due to $U(1)$ symmetry.

Some additional progress in analytical evaluation of the string correlation function (3.45) can be made for XX chain. The Majorana correlation function (3.30) gets simplified. Introducing

$$G^{\pm}(k) = G_{11}(k) \pm G_{12}(k) \tag{3.75}$$

and

$$g^{\pm} = (t\cos k \pm h_a \pm i\delta \sin k)/\xi, \tag{3.76}$$

we find

$$G^{\pm}(k) = \frac{1}{2}(1 + \mathrm{sign}(E_-)) + \frac{1}{2}(1 - \mathrm{sign}(E_-))g^{\pm}, \tag{3.77}$$

The above equations yields for the gapped phases

$$G^{\pm}(k) = \begin{cases} 1, & h > h_c^{(1)} \\ g^{\pm}, & h < h_c^{(2)} \end{cases} \tag{3.78}$$

and for the gapless IC phase at $h_c^{(2)} < h < h_c^{(1)}$,

$$G^{\pm}(k) = \begin{cases} 1, & k > k_F \\ g^{\pm}, & k < k_F \end{cases} \tag{3.79}$$

At $h > h_c^{(1)}$, the block Toeplitz matrix for evaluation of $\mathfrak{D}_{zz}$ (see previous chapter for its explicit form) becomes just a unit matrix for any choice of L and R in (3.45). So we find the exact result for the SOP:

$$\mathcal{O}_z = 1, \quad h > h_c^{(1)}. \tag{3.80}$$

The above result for the average of strings of σ^z operators (3.44) is in sync with the

existence of plateau of magnetization $m_z = \langle \sigma^z \rangle = 1$.

At $h < h_c^{(2)}$, the SOPs $\mathcal{O}_{z,i}$ form step-like parabolic lines along h, similar to Eqs. (3.70), (3.72), and (3.74) [131]. The values of $\mathcal{O}_{z,i}$ are available via numerical calculations only. However, in case $h_a = 0$ the result (3.49) can be used to find SOP inside the circle along the line $\gamma = 0$:

$$h_a = \gamma = 0, \quad |h| < h_c^{(2)} : \quad \mathcal{O}_{z,1}^2 = 2\frac{\delta^{1/2}}{1+\delta}. \tag{3.81}$$

The model at $\gamma = 0$ with additional U(1) symmetry belongs to a separate universality class with the central charge $c = 1$ [111]. From (3.81) we infer the index of the order parameter $\beta = 1/4$ in the vicinity of the critical point $\delta = 0$. Unfortunately, no progress is made at this point in analytical evaluation of SOPs beyond two special cases (3.49) and (3.81). Two plateaus of m_z have a certain analogy with quantized Hall conductance, proportional to the topological Chern number [132]. In the isotropic limit the eigenvalues $\lambda_\pm$ defined by Eq. (3.53) become the eigenvalues of the Hamiltonian (3.55). In such a case, the winding number (3.52) and magnetization (3.69) are simply related in the gapped phases:

$$m_z = 1 - N_\omega \tag{3.82}$$

The IC gapless phase does not have long-range string order, since all three $\mathcal{O}_{z,i} = 0$ on the right hand side of (3.46). [In the limit $\gamma \to 0$, parameters $\mathcal{O}_{z,i}$ vanish abruptly as $h \to h_c^{(2)} + 0$ and $h \to h_c^{(1)} - 0$, see Fig. 3.6a for visualization]. However the gapless phase is *algebraically ordered*, demonstrating power-law decaying string-string correlation function with the IC oscillations:

$$\mathfrak{D}_{zz}(1,n) = \frac{\mathcal{A}}{\sqrt{n}} \cos(k_F n). \tag{3.83}$$

In the above formula the coefficient $\mathcal{A}$ is nonuniversal, while the critical index of the correlation function $\eta = 1/2$. The latter along with two indicies $\nu = 1$ and $\beta = 1/4$ satisfy all scaling relations. We found a perfect agreement between Eq. (3.83) and direct numerical calculation of the string correlation function. For a particular choice of parameters yielding $k_F = \pi/6$, the results are shown in Fig. 3.10a with $\mathcal{A} = 1/\pi^{1/8} \approx 0.87$.

3.4.2 Interacting XXZ limit ($\Delta \neq 0$)

1. Plateaus, parabolic lines, String order, and Oscillations

To deal with the regime of weak interactions $\Delta \lesssim 1$, we need to replace the bare parameters in the equations of the previous subsection by the renormalized quantities. Having almost all results expressed via standard functions does not rescind the task of extensive numerical calculations, since critical fields $h_c^{(1,2)}$ and renormalized couplings must be found from self-consistent mean-field equations for each point in the four-dimensional space of bare parameters. (Two parameters are eliminated from our analysis, since we found $\gamma_R = \gamma_{aR} = 0$ in the isotropic limit).

As expected [60], the uniform magnetization in the interacting model has two plateaus, as in Eq. (3.61). It is shown in Fig. 3.4. The interaction renormalizes numerical values of critical fields $h_c^{(1,2)}$ and the form of the curve m_z in the IC gapless

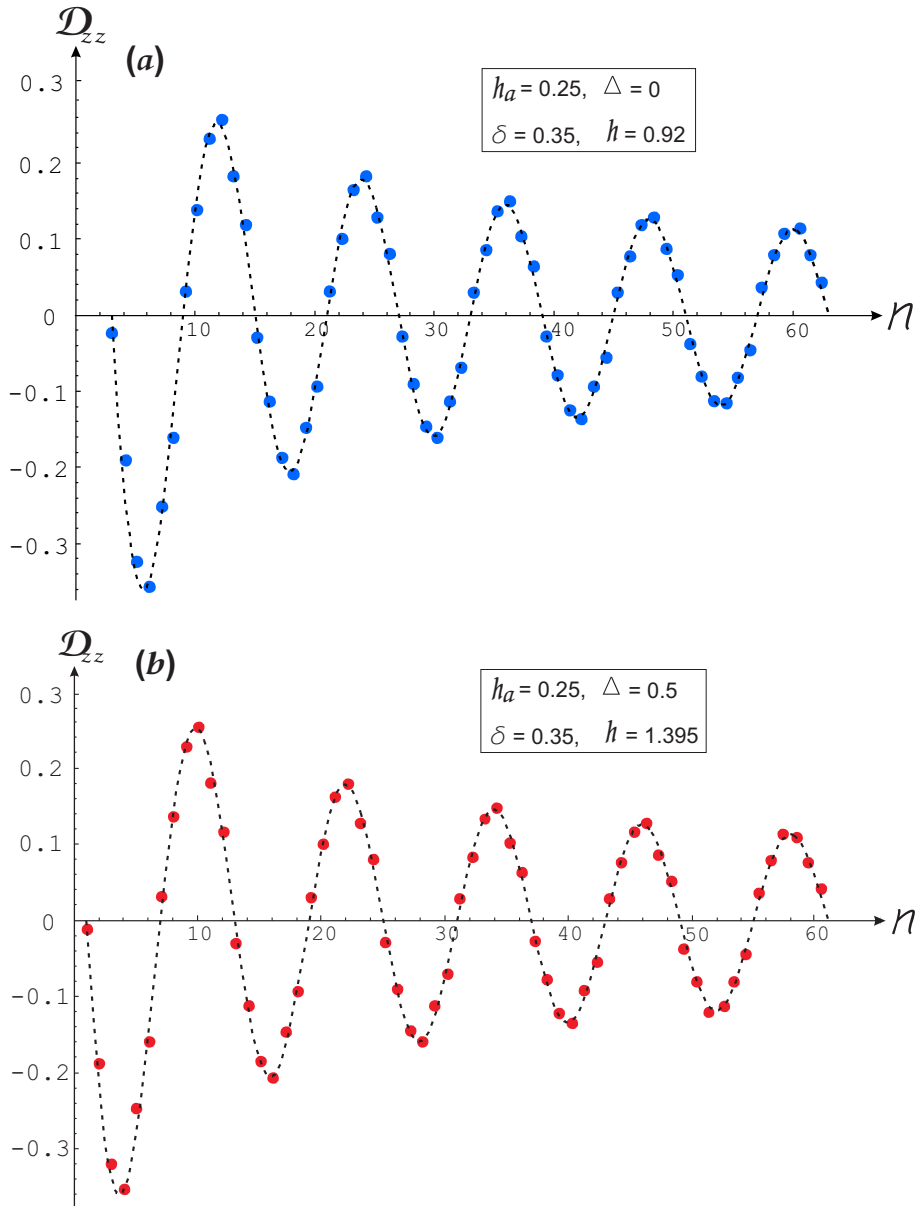

Figure 3.10: Power-law decaying oscillations of the string correlation function $\mathfrak{D}_{zz}(1,n)$ in the gapless IC phase. (a) shows direct numerical results from the Toeplitz determinant (blue dots) for the noninteracting case and the plot of Eq. (3.83) (dashed line). (b) shows direct numerical results for the interacting case when the Toeplitz determinant is calculated with renormalized parameters found from the mean-field equations (red dots) and the plot of Eq. (3.86) (dashed line). In both cases, $\mathcal{A} = 1/\pi^{1/8} \approx 0.87$ and $k_F = \pi/6$.

phase, but not the universal plateau values $m_z = 0, 1$ in two gapped phases. Qualitatively, it means that the interaction does not change the integer-valued filling per unit cell (1 or 0), in agreement with Ref. [61], as one can see in Fig. 3.9. Thus, the present mean-field theory respects the LSM theorem.

The analytical results of the previous subsection allow us to understand how this interesting feature makes it way through the equations. The renormalized effective spectrum has the same form, as shown in Fig. 3.8 for noninteracting case. The bond average $\mathcal{K}$ and dimerization susceptibility η (cf. (3.72) and (3.74)) in the $\mathcal{O}_z(\pi/2)$ phase ($h < h_c^{(2)}$) are h-independent functions of other couplings, see Fig. 3.2(a). In mathematical terms, these functions form *parabolic lines* of zero curvature in the parametric space. Both quantities $\mathcal{K}$ and η vanish in the PM phase ($h > h_c^{(1)}$). The staggered magnetization m_z^a, cf. (3.70) and Fig. 3.4, demonstrates similar behaviour. The ground-state energy f in the $\mathcal{O}_z(\pi/2)$ phase is given by the third expression in (3.58) plus the constant term ΔC where C , determined from Eq. (3.36), is

$$C = \mathcal{K}^2 + \frac{1}{4}(m_z^a)^2 + \delta^2(\eta^2 + 2\mathcal{K}\eta) \tag{3.84}$$

The above term and h-independent effective band ε_{eff} lead to f as an h-independent parabolic line at $h < h_c^{(2)}$ [131], and, consequently, $m_z = 0$. For the PM phase with a totally flat band, we find

$$f = -\frac{1}{4}\Delta - \frac{1}{2}h \tag{3.85}$$

where Eq. (3.35a) with $h_R = h - \Delta$ is used, leading to $m_z = 1$ [133]. So, the plateau $m_z = 1$ is due to: (1) flat band which leads to linear dependence of the ground-state energy on the field; (2) the fact that interaction does not renormalize the slope (-1/2) of this straight line. The relation between the magnetization and the winding number (3.82) holds for the interacting case.

The exact result (3.80) holds for the plateau of the SOP $\mathcal{O}_z$ in PM phase of the interacting model, along with the step-like h-independent behaviour of three parameters $\mathcal{O}_{z,i}$ of the oscillating string long-ranged order, see Figs. 3.6a and 3.5. Since the interaction does not change the wave vector of the oscillating string order $k_F = \pi/2$, cf. Fig. 3.9, one can select a convenient single correlation function (3.50) and to use the SOP $\mathcal{O}_{z,+}$.

It is worth stressing qualitative similarities and distinctions in behaviours of the average quantities entering our equations in two gapped phases: while in the gapped topologically trivial PM phases ($h > h_c^{(1)}$) all quantities m_z, m_z^a, $\mathcal{O}_{z,i}$, $\mathcal{K}$, η are equal to 1 or 0, i.e., they form true plateaus, in the gapped topological phase ($h < h_c^{(2)}$) only the uniform magnetization demonstrates a true (trivial) plateau $m_z = 0$. The other quantities are h-independent functions of other couplings (parabolic lines) [131]. Except for the SOPs, all other quantities are having their values in the gapped phases continuously connected across the IC gapless phase with cusps at two critical points $h_c^{(1)}$ and $h_c^{(2)}$.

The IC gapless phase is the Luttinger liquid (LL) of the JW fermions [134]. The long-range string order of the gapped topological phase ($h < h_c^{(2)}$) is taken over by the algebraic order of the power-law decaying string correlations at $h_c^{(2)} < h < h_c^{(1)}$. We have verified numerically oscillating behaviour of (3.45). It is in agreement with predictions (3.83). In the mean-field approximation, the only effect of interactions on the correlation function is renormalization of k_F and a phase shift. For a comparison with the noninteracting case (3.83) presented in Fig. 3.10a, we chose the model parameters to make the renormalized $k_F = \pi/6$ again. The direct numerical calculations are in

excellent agreement with the analytical expression

$$\mathfrak{D}_{zz}(1,n) = \frac{\mathcal{A}}{\sqrt{n+2}} \cos\Big(\frac{\pi}{6}(n+2)\Big). \tag{3.86}$$

as one can see from Fig. 3.10b. The gapless IC(LL) phase is a counterpart of the floating phase occurring via a BKT thermal phase transition in frustrated 2D Ising models [135, 136].

2. Interaction-driven transtition

The main goals of this subsection is to establish restrictions of the proposed mean-field theory coming from the strength of interactions Δ, and to relate the predicted $\mathcal{O}_z(\pi/2)$-phase to the antiferromagnetic phase known from exact solution. The model of this study is antiferromagnetic, so $\Delta > 0$. Since we are interested to probe effects of the interaction, we turn off other relevant couplings and set $h_a = \delta = 0$.

We analyze the model on the (h, Δ)-plane shown in Fig. 3.11. As known from the exact results [111, 121], the chain without external fields generates spontaneous antiferromagnetism (AFMz) in the axial direction ($m_z^a \neq 0$) at the critical value $\Delta = 1$. At the noninteracting point $\Delta = 0$ the model is in the IC phase at $0 < h < 1$, as we infer from Fig. 3.1 along the line $\gamma = 0$ [the $\mathcal{O}_z(\pi/2)$ circle is absent, since $\mathcal{R}(h_a = \delta = 0) = 0$]. At $h = 1$ the noninteracting model enters the familiar PM phase. The IC-PM phase boundary $h_c^{(1)} = 1 + \Delta$ is a special case of the exact result (3.41). At $\Delta > 1$ the AFMz phase resides inside the V-shaped wedge on the (h, Δ) plane, and at a certain critical field $h = h_c^{(2)}$ the XXZ chain undergoes a phase transition into the IC (LL) phase. This phase boundary, known exactly from the Bethe ansatz, is schematically shown in Fig. 3.11.

The interaction is a marginal perturbation of the free fermionic Hamiltonian. One

can check from the mean-field equations that along with the trivial solution m_z^a, corresponding to the gapless IC state, consistent with the exact results at $\Delta < 1$, those equations admit a nontrivial solution $m_z^a \neq 0$ corresponding to the spontaneously generated antiferromagnetism. The order parameter of this phase is the spontaneous staggered magnetization and it can be found analytically in the regime of weak interaction:

$$m_z^a \approx \frac{2}{\Delta} \exp\Big(-\frac{\pi}{2\Delta}\Big), \quad \Delta \lesssim 1. \tag{3.87}$$

At large $\Delta \gg 1$, the order parameter saturates towards $m_z^a \sim 1$. A nontrivial m_z^a generates via Eq. (3.35b) the spontaneous staggered field $h_{aR} = \Delta m_z^a$.

We have checked that the critical value $\Delta = 1$ and $h = 0$, the mean field predicts the ground-state energy of the AFMz phase $f_{AFMz} = -0.4323$, while for the gapless IC phase $f_{IC} = -0.4196$ with the relative gain of the AFMz phase about 3%. At $\Delta = 1/2$ and $h = 0$, the parameters are $f_{AFMz} = -0.3694$ and $f_{IC} = -0.3690$, with the relative gain $\sim 0.1\%$. At smaller Δ the gain is even smaller, and the two states are virtually degenerate. However an unbiased minimization predicts at $h = 0$ the winning antiferromagnetism all the way to $\Delta = 0$, albeit exponentially weak (3.87). At $\Delta \lesssim 1$, the mean field predicts the AFMz-IC phase boundary

$$h_c^{(2)} \sim h_{aR} \approx 2 \exp\Big(-\frac{\pi}{2\Delta}\Big), \tag{3.88}$$

while at $\Delta \gg 1$ the critical field $h_c^{(2)}$ crosses over towards

$$h_c(2) \propto \Delta. \tag{3.89}$$

The result of numerical mean-field calculations for $h_c^{(2)}$ is shown in Fig. 3.11.

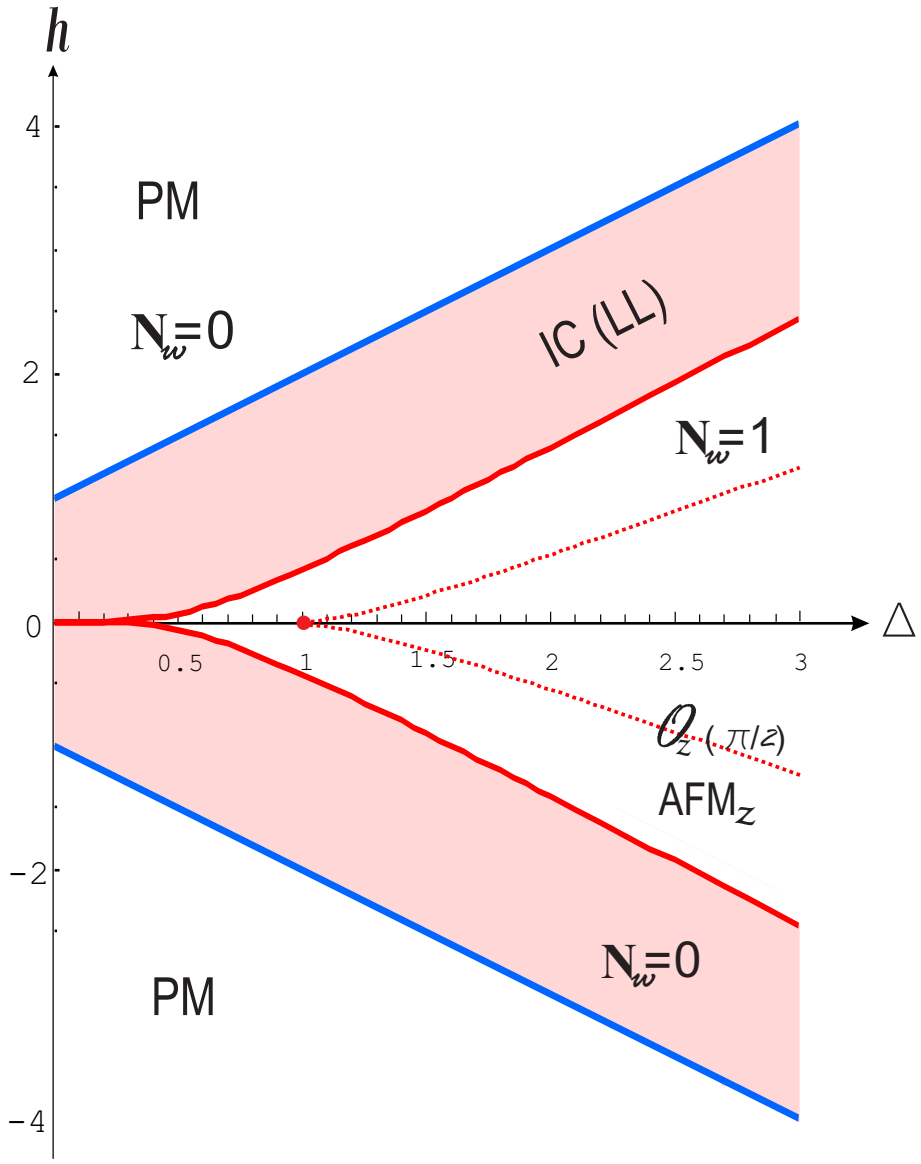

Figure 3.11: Phase diagram of the model with zero bare staggered field and dimerization in $(h,\ \Delta)$ plane. The exact result [111, 121] for the phase boundary between the phase AFMz with spontaneous staggered magnetization and gapless IC (LL) phase, ending at the critical point $(0,\ 1)$, is indicated with red dotted line. The bold red line is the mean-field prediction for this boundary. The mean-field approximation agrees with the exact result for the IC-PM phase boundary, shown in bold blue. The topological winding number N_ω are also shown for each phase.

The AFMz-IC phase transition is of the first order in the mean-field theory, since m_z^a undergoes a jump from zero in the gapless IC phase to a finite value and stays constant for a given Δ in AFMz phase ($h < h_c^{(2)}$). (Note that Δ=const. lines on the (h, Δ) plane are parabolic lines of h-independent parameters, like f, m_z^a, h_{aR}, etc., as explained above). The spontaneous antiferromagnetism with its primary order parameter m_z^a coexists with the four-periodic string order defined in previous sections. The SOPs are introduced by the staggered field $h_{aR} \propto m_z^a$ and are the secondary. The order is of the type (3.48) with patterns shown in panels 2(a) and 2(b) in Fig. 3.7. The string order can be also combined into a single pattern as in Fig. 3.7(1) with the help of the correlation function (3.50). The algebraically ordered gapless IC(LL) phase in Fig. 3.11 is characterized by the power-law decaying correlation functions, similar to the one shown in Fig. 3.10.

So the phase with the interaction-induced antiferromagnetism AFMz on the phase diagram in Fig. 3.11, *per se* is just a special case of the $\mathcal{O}_z(\pi/2)$ phase shown in Fig. 3.1. That is why the second label $\mathcal{O}_z(\pi/2)$ for the magnetic phase is added in Fig. 3.11. However, the transition into the gapless IC phase is quite different in two cases, revealing important distinctions between the two phases. The axial symmetry broken in the interaction-generated AFMz-phase which possesses a sublattice magnetization and doubling of a unit cell, is restored via the first order transition into the IC (LL) phase. The latter, shown in Fig. 3.11, has both the staggered field and magnetization zero, $m_z^a = h_{aR} = 0$. For the case of the field-generated $\mathcal{O}_z(\pi/2)$-IC transition shown in Fig. 3.1, *no symmetry breaking related to sublattice (staggered) magnetization occurs, and the field-induced m_z^a is not the order parameter*. It is continuous across transition and has a cusp only, as one can see in the Fig. 3.4; the gaplessness of the IC phase is a result of subtle interplay of several relevant couplings. In both cases, of the AFMz or $\mathcal{O}_z(\pi/2)$ phases, the uniform magnetization m_z is zero, as shown in Fig. 3.4 ($\gamma = 0$)

at $h < h_c^{(2)}$.

The last comment is in order here to address the validity of the proposed mean-field prediction of the spurious spontaneous antiferromagnetism with $h_a = \delta = 0$ in the range $\Delta < 1$ can undermine our predictions for the phase diagram in Fig. 3.1. The answer is twofold: in the absence of relevant terms $\propto h_a$ or $\propto \delta$ and $h = 0$, the mean-field instability in the region $\Delta < 1$ signals the need of that approximation to be replaced by more sophisticated techniques. In the case when one or more of the mentioned parameters are nonzero, the (exponentially weak) interaction-generated terms do not drive spontaneous magnetization, but rather result in innocuous renormalizations of model's parameters. As an example tested by direct simulations, we can mention the earlier work on coupled dimerized XXX chains ($\Delta = 1$) [35, 53] where two relevant parameters-dimerization and inter-chain coupling are present. The mean-field predictions are shown to be very accurate quantitatively, no spurious phases, in agreement with DMRG or exact diagonalization results, even on the lines of quantum criticality where a mutual cancellation of relevant terms occur.

To summarize

In this chapter, the XYZ spin-1/2 chain with an alternation of the exchange and anisotropy couplings in the presence of uniform and staggered magnetic fields is studied. Using the JW transformation, the model is mapped into the form of interacting Kitaev-Majorana fermionic chain with hopping, superconducting pairing, and modulated chemical potential. The HF (mean-field) approximation is applied to the interacting fermionic Hamiltonian, which is then replaced by the renormalized effective quadratic Hamiltonian. Using the Fourier transform, the renormalized effective quadratic Hamiltonian translates into a renormalized single particle Hamiltonian with spinors consisting of the fermions in the momentum space associated with even/odd

sites of the lattice. The renormalized Hamiltonian is expressed in terms of six renormalized couplings (parameters), which are found from a set of six self-consistent equations obtained from the minimization of free-energy. We found four energy eigenvalues with renormalized parameters, criticality, gaps, and phase boundaries. All calculations for the phase diagram, its boundaries and related quantities were done numerically. The PM-AFM boundary and radius of topological phase gets modified by the interactions (see Fig. 3.1). Like the noninteracting model, it has a rich phase diagram with additional information of the local and nonlocal orders in the different gapped phases.

In order to describe the conventional (Landau) and nonlocal (string) orders, we explicitly expressed two unitary matrices $\hat{\Phi}$ and $\hat{\Psi}$ from the normalized single particle Hamiltonian by applying the Bogoliubov transformation. These matrices allow us to derive analytical expression for the correlation function of two Majorana fermions at zero temperature. By definition, the local and nonlocal order can be expressed in terms of a string correlation function of Majorana fermions. The latter is evaluated as asymptotes of the determinants of the block Toeplitz matrices. In this parametrization of the model, we were not able to derive any analytical results of the asymptotics of the block Toeplitz determinant. With some luck and complex skills, these limits can be found explicitly then one gets an algebraic expressions for the order parameters. Here, we resort to direct numerical calculations for the possible large finite-size matrices.

Combining the above formalism with mean-field approximation, the local and nonlocal order parameters are calculated numerically. The representative numerical results for the above-mentioned parameters are plotted in Fig. 3.6. In this study, we found the circular region with topological phase on the phase diagram in (h, γ) plane with oscillating string order with a period of four lattice spacing, which was not reported before for this model. The detailed analysis of patterns of the string order is given (see

Fig. 3.5 and 3.7 for detail). It vanishes in FM phase at a large distance and it quickly saturates to a constant value in the PM phase.

In the isotropic limit of this model, the plateaus and h-independent parabolic lines were revealed in various quantities, most notable in the uniform axial magnetization. The appearance of the integer-valued and IC fermionic fillings, responsible for qualitatively different behaviour of physical parameters in the gapped and IC gapless phases (see Fig. 3.9 for example), can be qualitatively related to the presence of flat bands in the effective single particle spectrum. Turning on the anomalous coupling $\gamma \neq 0$, rounds the flat band and smears plateaus of magnetization and other step-like parameters. In the IC (LL) phase, the oscillating string correlation function is found to have a power-law, as shown in Fig. 3.10.

Chapter 4

Dimerized Two-Leg Ladder

4.1 Introduction

The elementary excitations of low dimensional quantum systems show remarkable phenomena. Previous results in chapters 2 and 3 showed that the dimerization and anisotropy induce the spin gaps in the spin-1/2 chain [137]. The intriguing properties of spin ladders have been studied extensively in the analytical and numerical studies [5, 85, 86, 137], where the gap and/or massless depend on the number of legs. The effect of dimerization on the spin-1/2 ladders has gained lots of attention. A uniform two leg ladder found to be gapped [5, 137] and it can become gapless at some special cases while introducing dimerization [19, 20, 34, 47, 50, 51]. Critical properties of dimerized ladders are known from analytical and numerical studies: [34,35,51,54,56,99]. The staggered ladder can undergo a continuous quantum phase transition, while the columnar and rung dimerized ladders are always gapped, and do not exhibit any quantum phase transition [53, 56, 138].

Moreover, the field induced quantum phase transition has been studied in recent

years, and the existence of quantized plateaus in the magnetic curve of the spin chains was observed [60, 139]. This unique magnetization curve with the number of plateaus versus applied magnetic field in the generic two-leg ladder has received much more attention from the theoretical and experimental sides [48, 56, 138, 140–143]. For the two-leg ladder with staggered and columnar dimerization patterns, the existence of the magnetization plateaus is confirmed by using the bosonization and direct numerical simulations [48, 49, 140]. Very recently, the magnetization plateau in the columnar ladder was studied numerically in [144]. Azzouz [141] found these magnetization plateaus in isotropic two-leg ladder using the mean-field approach based on the JW transformation.

Like columnar ladder, the rung-dimerized two-leg ladder always induces spin gap and becomes gapless while applying the uniform magnetic field [56]. In this ladder, the magnetization curve and plateaus were reported using various theoretical standard methods such as Green's function, bosonization, and the mean-field approach [56, 138, 142, 145]. More recently similar studies have been done by using numerical techniques such as the Lanczos exact diagonalization, and the quantum Monte-Carlo methods [142, 143].

The magnetization plateau with rational (commensurate) magnetization and a finite excitation gap is only possible if condition

$$P(s-m) = \mathcal{Z}, \tag{4.1}$$

is satisfied. Here P, s, m and $\mathcal{Z}$ are periodicity, spin, constant magnetization [1]*, and*

[1] To be a consistent with previously published works on [35,37,38,59] and previous chapters 2 and 3 of this thesis work we choose the notation of magnetization $m_z = \langle \sigma_z \rangle \equiv 2m$ from now on. Here m is the magnetization written in the quantization condition 4.1

arbitrary integer respectively.

This theorem to be a generalization of the LSM theorem [79] for the case of magnetic field [60, 61, 79, 146, 147]. The necessary quantization condition for appearance of such plateau in generic chains or ladders was derived in [60, 61]. The existence of the number of plateaus of the magnetization curve with finite excitation gap can be determined by using above quantization condition (4.1). The gapless excitation occurs at an incommensurate fermionic filling, which also manifests itself via arbitrary real magnetization.

We call the quantization condition as the ***plateau theorem*** of periodicity from now on. To be more specific, we take an example, i.e, staggered ladder with the columnar magnetic field. In this model, the periodicity and spin are $P = 4$ and $s = \frac{1}{2}$ respectively, then the right side of the Eq (4.1) satisfies the integer values $0, 1, 2$ only if the model contains three magnetization plateau phases at $m = 0, \frac{1}{4}, \frac{1}{2}$. Thus, the model will have the magnetization curve with three magnetization plateaus which we will call 0-plateau phase, half-plateau phase and saturated plateau phase. We drive the conditions for other magnetization plateaus in the following explicit form:

(1) Dimerized chain: P=2, s=$\frac{1}{2}$; $\mathcal{Z}$=0, 1; plateaus at m=0, $\frac{1}{2}$.

(2) Staggered two-leg ladder: P=2, s=$\frac{1}{2}$; $\mathcal{Z}$=0, 1; plateaus at m=0, $\frac{1}{2}$.

(3) Staggered ladder with staggered field: P=2, s=$\frac{1}{2}$; $\mathcal{Z}$=0, 1; plateaus at m=0, $\frac{1}{2}$.

(4): Columnar ladder with columnar field: P=4, s=1/2; $\mathcal{Z}$=0, 1, 2; plateaus at m=0, $\frac{1}{4}$, $\frac{1}{2}$.

(5): Rung-dimerized ladder with columnar field: P=4, s=$\frac{1}{2}$; $\mathcal{Z}$=0, 1, 2;

plateaus at m=0, $\frac{1}{4}$, $\frac{1}{2}$.

In this chapter, we study the quantum phase transitions (QPTs) and the ground state properties of anisotropic dimerized spin-1/2 two-leg ladders in the modulated magnetic field. For the anisotropic two-leg ladder, we consider three possible dimerized patterns: staggered, columnar, and rung. It reveals a very rich structure of the uniform magnetization plateaus at m_z= $0, \frac{1}{2}, 1$, as given by the quantization condition (4.1). To the best of our knowledge, the quantum criticality, phase diagram and induced uniform magnetization of those models with uniform and alternating fields were not addressed in earlier literature in the way we do here. Though we are not sure which type of dimerized ladder can be realized in nature, in the presence of magnetic field, we analyze for all cases the gaps, phase diagrams and magnetization plateaus.

We infer from the earlier works [35, 38, 53, 89], where the mean-field approach was used to solve the chains and ladders, that this method is quite efficient, even qualitatively. Here we apply the Hartee-Fock (HF) approximation to map the interacting fermionic ladder onto a problem of the effective quadratic fermionic Hamiltonian. Before utilizing the HF approximation, we use the JW transformation that maps the spin Hamiltonian onto spinless fermions. Both methods will be utilized to study the ground state properties such as: quantum critical points, phase diagrams, magnetization plateaus, and local and non-local orders, as similarly to what we have done in the previous chapters for the dimerized XY and XYZ chains.

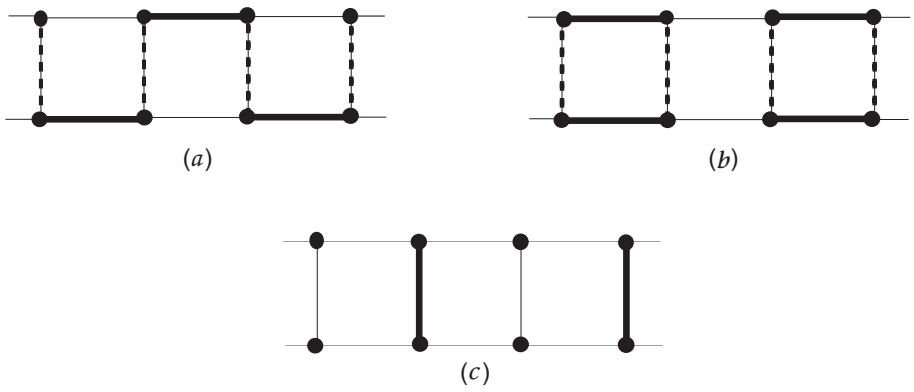

Figure 4.1: Dimerized two-leg ladder. Bold/thin/dashed lines represent the stronter/weaker chain coupling $J(1 \pm \delta)$ and rung coupling $J_\perp(1 \pm \delta_\perp)$, respectively. Dimerization patterns: (a) staggered; (b) columnar; and (c) rung

.

4.2 Model

4.2.1 Spin and mean-field Hamiltonian

The Hamiltonian of the dimerized two-leg ladder in the presence of the uniform (h) and staggered (h_a) magnetic field is

$$H = \sum_{\alpha=1}^{2}\sum_{n=1}^{N}\Big\{J_\alpha(n)\mathbf{S}_\alpha(n)\cdot\mathbf{S}_\alpha(n+1) + h_\alpha(n)S^z_\alpha(n)$$

$$+J\gamma\Big[S^x_\alpha(n)S^x_\alpha(n+1) - S^y_\alpha(n)S^y_\alpha(n+1)\Big]\Big\} + J_\perp\sum_{n=1}^{N}\mathbf{S}_\alpha(n)\cdot\mathbf{S}_{\alpha+1}(n). \qquad (4.2)$$

where spin operators $\mathbf{S} = \frac{1}{2}\boldsymbol{\sigma}$ are defined in terms of the standard Pauli matrices. The ladder has bond alternation with the parameter $|\delta| \leq 1$ either along the chains ($\alpha = 1, 2$) or along the rungs, and the xy anisotropy γ. We consider antiferromagnetic two spin exchange couplings, i.e., $J > 0$, $J_\perp > 0$. In this study, we consider the three possible dimerization patterns: staggered, columnar and rung, shown in Fig. 4.1. The exchange couplings for three dimerization patterns are defined as:

$$J_\alpha(n) = J[1 + (-1)^{n+\alpha}\delta] \quad \text{(staggered)} \tag{4.3a}$$

$$J_\alpha(n) = J[1 + (-1)^{n}\delta] \quad \text{(columnar)} \tag{4.3b}$$

$$J_\perp(n) = J_\perp[1 + (-1)^{n}\delta_\perp] \quad \text{(rung)} \tag{4.3c}$$

with the periodic boundary conditions along the chains.

We also consider two possible modulated magnetic fields:

$$h_\alpha(n) = h + (-1)^{n+\alpha}h_a \qquad \text{(staggered)} \tag{4.4a}$$

$$h_\alpha(n) = h + (-1)^{n}h_a \qquad \text{(columnar)} \tag{4.4b}$$

We map the spin ladder Hamiltonian (4.2) onto it's fermionic representation by using the JW transformation. There are different ways to introduce this transformation when we depart from a single-chain problem to the spin ladder (see, e.g., [23, 83, 86]). Here, we use the snake-like path for the JW transformation (see inset of Fig 1.1b) which is used in [35, 86]. To make a clear picture of the two dimesional JW transformation along the snake-like path for the two leg ladder, we refer two Eqs. (1.8a) and (1.8b). Labelling the sites of the ladder along the path as shown in Fig. 4.2, the JW transformation can be defined as

$$\sigma_n^\dagger = c_n^\dagger \exp\left(i\pi \sum_{\text{path},\ l=1}^{n-1} c_l^\dagger c_l\right) \tag{4.5}$$

with $\sigma_n^z = 2c_n^\dagger c_n - 1$ and $\sigma_n^\pm = \frac{1}{2}(\sigma_n^x \pm i\sigma_n^y)$.

The spin ladder (4.2) will be treated within the mean-field approach [83, 85, 86],

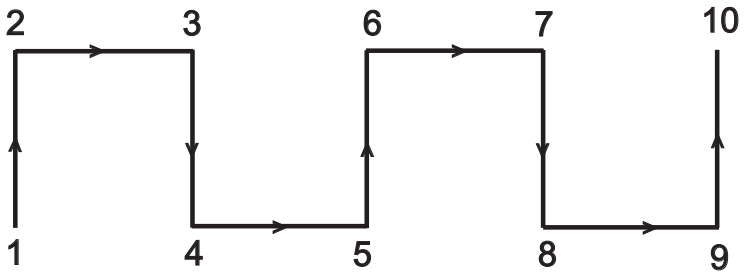

Figure 4.2: Snake-like path of the JW transformation used for the two-leg ladder.

which consists of two steps: first, one maps the spin Hamiltonian onto an interacting model of spinless fermions via a JW transformation (4.5); second, the interaction terms are decoupled via the HF (mean-field) approximation [89]. This mean-field approach is confirmed to be qualitatively and even quantitatively adequate for an analysis of similar dimerized ladders [35, 53, 58]. Taking the technical details to section 4.4, the spin Hamiltonian (4.2) is reduced to the quadratic effective fermionic Hamiltonian:

$$H \approx H_{MF} = \frac{1}{2}\sum_{n=1}^{N}\sum_{\alpha=1}^{2}\Big((-1)^{n+\alpha-1}+\upsilon\Big)\Big\{J_{\alpha R}(n)c_{\alpha}^{\dagger}(n)c_{\alpha}(n+1)$$

$$+\Gamma_{\alpha R}(n)c_{\alpha}^{\dagger}(n)c_{\alpha}^{\dagger}(n+1)+h.c.\Big\}+2h_{\alpha R}(n)c_{\alpha}^{\dagger}(n)c_{\alpha}(n)$$

$$+\frac{1}{2}\sum_{n=1}^{N}J_{\perp R}(n)c_{1}^{\dagger}(n)c_{2}(n)+h.c+2N\Big(C-\frac{h_{R}}{2}\Big) \tag{4.6}$$

where we have introduced the renormalized couplings:

$$J_{\alpha R}(n)=\begin{cases} J[t_{R}+(-1)^{n+\alpha}\delta_{R}], & \text{staggered} \\ J[t_{R}+(-1)^{n}\delta_{R}], & \text{columnar} \\ J(1+2\mathcal{K}), & \text{rung,} \end{cases} \tag{4.7}$$

$$\Gamma_{\alpha R}(n) = \begin{cases} J[\gamma_R + (-1)^{n+\alpha}\gamma_{aR}], & \text{staggered} \\ J[\gamma_R + (-1)^{n}\gamma_{aR}], & \text{columnar} \\ J(\gamma - 2P), & \text{rung,} \end{cases} \tag{4.8}$$

$$J_{\perp R}(n) = \begin{cases} J_\perp(1 + 2t_\perp), & \text{stag/col} \\ J_\perp(t_{\perp R} + (-1)^n \delta_{\perp R}), & \text{rung,} \end{cases} \tag{4.9}$$

$$h_{\alpha R}(n) = \begin{cases} h_R + (-1)^{n+\alpha} h_{aR}, & \text{staggered field} \\ h_R + (-1)^{n} h_{aR}, & \text{columnar field,} \end{cases} \tag{4.10}$$

along with the following renormalized model's parameters.

A. Staggered/columnar patterns:

$$h_R = h - m_z\Big(1 + \frac{J_\perp}{2}\Big), \tag{4.11}$$

$$h_{aR} = h_a + m_z^a\Big(1 \pm \frac{J_\perp}{2}\Big), \tag{4.12}$$

$$t_R = 1 + 2(\mathcal{K} + \delta^2\eta), \tag{4.13}$$

$$\delta_R = \delta\Big(1 + 2(\mathcal{K} + \eta)\Big), \tag{4.14}$$

$$\gamma_R = \gamma - 2(P - \delta^2\eta_p), \tag{4.15}$$

$$\gamma_{aR} = -2\delta(P - \eta_p) \tag{4.16}$$

$$t_{\perp R} = 1 + 2t_\perp. \tag{4.17}$$

B. Rung dimerized pattern:

$$h_R = h - m_z\Big(1 + \frac{J_\perp}{2}\Big) - \frac{J_\perp}{2}\delta m_z^a, \tag{4.18}$$

$$h_{aR} = h_a - m_z^a\Big(1 - \frac{J_\perp}{2}\Big) - \frac{J_\perp}{2}\delta m_z, \tag{4.19}$$

$$t_R = 1 + 2\mathcal{K}, \tag{4.20}$$

$$\gamma_R = \gamma - 2P, \tag{4.21}$$

$$\delta_{\perp R} = \delta_\perp\Big(1 + 2(t_\perp + \eta_\perp)\Big), \tag{4.22}$$

$$t_{\perp R} = 1 + 2(t_\perp + \delta_\perp^2\eta_\perp). \tag{4.23}$$

Here υ denotes the flux correction term per plaquette which is explained in section 4.4. The constant terms with the flux correction term are given in Appendix A. For the minimization of the energy, we use the following final form for the constants in the three dimerization patterns and two transverse fields:

$$C^{ss} = \mathcal{K}^2 - P^2 + \delta^2(\eta^2 - \eta_p^2) + 2\delta^2(\mathcal{K}\eta + P\eta_p) + \frac{1}{2}J_\perp t_\perp^2$$

$$-\frac{1}{4}(m_z^2 - m_{z,a}^2)\Big(1 + \frac{J_\perp}{2}\Big) \tag{4.24}$$

$$C^{sc} = \mathcal{K}^2 - P^2 + \delta^2(\eta^2 - \eta_p^2) + 2\delta^2(\mathcal{K}\eta + P\eta_p) + \frac{1}{2}J_\perp t_\perp^2$$

$$-\frac{1}{4}m_z^2\Big(1 + \frac{J_\perp}{2}\Big) + \frac{1}{4}m_{z,a}^2\Big(1 - \frac{J_\perp}{2}\Big) \tag{4.25}$$

$$C^{cc} = (1 + \upsilon^2)\Big(\mathcal{K}^2 - P^2 + \delta^2(\eta^2 - \eta_p^2) + 2\delta^2(\mathcal{K}\eta + P\eta_p)\Big)$$

$$-\frac{1}{4}m_z^2\Big(1 + \frac{J_\perp}{2}\Big) + \frac{1}{4}m_{z,a}^2\Big(1 - \frac{J_\perp}{2}\Big) + \frac{1}{2}J_\perp t_\perp^2 \tag{4.26}$$

$$C^{rc} = \mathcal{K}^2 - P^2 - \frac{1}{4}m_z^2\Big(1 + \frac{J_\perp}{2}\Big) + \frac{1}{4}m_{z,a}^2\Big(1 - \frac{J_\perp}{2}\Big)$$

$$+\frac{1}{4}J_\perp\delta m_z m_{z,a} + \frac{1}{2}J_\perp\Big(t_\perp^2 + \delta_\perp^2\eta_\perp^2 + 2\delta_\perp^2\eta_\perp t_\perp\Big) \tag{4.27}$$

The definitions and the self-consistent equations for the mean-field parameters entering above relations are given in section 4.4. There, we also present formulas and numerical results for the mean-field parameters and renormalized couplings, and their relations to the bare parameters of the microscopic Hamiltonian. In the following, we will be working with the effective Hamiltonian (4.6), and for the notational simplicity we drop the subscript $_R$ in its parameters from now on, keeping in mind that we deal with the renormalized parameters (4.11)- (4.23). We also express dimensional quantities in units of J from now. Note that (4.6) can also be viewed as a tight-binding Hamiltonian of the modulated Kitaev ladder [148]. In the fermionic representation, the staggered/columanr ladder has dimerized hopping along chains, modulated chemical potential, and superconducting pairing, while the rung dimerized ladder fermionizes into the Kitaev ladder with the dimerized hopping along legs and modulated chemical potential. Thus, whether we deal with the modulated spin ladder or the Kitaev fermionic ladders, it is a mere of convention, specially since the results below will be given in the terms of spins of fermions, on the same footing.

In terms of Majorana operators,

$$2c_{\alpha}^{\dagger}(n) = a_{\alpha}(n) + ib_{\alpha}(n), \tag{4.28}$$

the mean-field effective Hamiltonian (4.6) yields

$$H_{MF} = 2NC + \frac{i}{4}\sum_{n,\alpha}^{N}\Big[\Big((-1)^{n+\alpha-1}+\upsilon\Big)\Big\{\Big(J_{\alpha R}(n)+\Gamma_{\alpha R}(n)\Big)\times$$

$$b_{\alpha}(n)a_{\alpha}(n+1) + \Big(J_{\alpha R}(n)-\Gamma_{\alpha R}(n)\Big)b_{\alpha}(n+1)a_{\alpha}(n)\Big\}$$

$$+2h_{\alpha R}(n)b_{\alpha}(n)a_{\alpha}(n)\Big] + \frac{i}{4}\sum_{n} J_{\perp R}(n)\Big(b_1(n)a_2(n)+b_2(n)a_1(n)\Big) \tag{4.29}$$

4.2.2 Single particle Hamiltonian and spinor

To further simplify the effective Hamiltonian (4.6) and to get rid of its factor $(-1)^n$, we use canonical transformation

$$c_\alpha(n) \mapsto e^{i\phi_n} c_\alpha(n), \tag{4.30}$$

in the real space where we utilize $\phi_{n+1} = \phi_n + \pi n$ ($\phi_1 = 0$). It is convenient to introduce two distinct fermions residing on even/odd sites by $c_\alpha(e/o)$ in the place of $c_\alpha(n)$, since the dimerization (δ or $\delta_\perp$) splits all sites of the ladder in even and odd sectors. Using the Fourier transform $c^\dagger_\alpha(n) = \frac{1}{\sqrt{N}} \sum_k c^\dagger_\alpha(k) e^{ikn}$, we rewrite the Hamiltonian as

$$H = 2NC + \frac{1}{2} \sum_k \Psi^\dagger_k \mathcal{H}(k) \Psi_k \tag{4.31}$$

where even and odd sectors of fermions are unified in the spinor

$$\Psi^\dagger_k = \Big(c^\dagger_{1,e}(k), c^\dagger_{1,o}(k), c^\dagger_{2,e}(k), c^\dagger_{2,o}(k), c_{1,e}(-k), c_{1,o}(-k), c_{2,e}(-k), c_{2,o}(-k) \Big) \tag{4.32}$$

with the wave numbers restricted to the reduced Brillouin zone BZ $k \in [-\pi/2, \pi/2]$, and we set the lattice spacing $a = 1$. The 8×8 Hamiltonian matrix $\mathcal{H}(k)$ can be written as

$$\mathcal{H}(k) = \begin{pmatrix} \hat{A} & \hat{B} \\ \hat{B}^\dagger & -\hat{A} \end{pmatrix} \tag{4.33}$$

The explicit form of the effective Hamiltonian (4.31) depends on the three dimerization patterns with two kinds of the modulated transverse fields as defined in Eqs. (4.3a), (4.3b), (4.3c), (4.4a) and (4.4b). Here, the matrix elements of the operator $\hat{A}$ depend on dimerization patterns and modulated fields, which will be accounted by extra labels (s,c,r) and (s,c) for dimerization and field respectively. The operator $\hat{B}$ is the same for

all phases. As shown below, it is because $\hat{B}$ contains only the anisotropic parameters γ and γ_a. The explicit form of the 4×4 matrix $\hat{A}$ for the staggered pattern in the staggered field is

$$\hat{A}_{ss} = \begin{pmatrix} h - h_a & \hat{U} & \frac{1}{2}J_\perp & 0 \\ \hat{U}^* & h + h_a & 0 & \frac{1}{2}J_\perp \\ \frac{1}{2}J_\perp & 0 & h + h_a & -\hat{U}^* \\ 0 & \frac{1}{2}J_\perp & -\hat{U} & h - h_a \end{pmatrix}, \tag{4.34}$$

where

$$\hat{U} \equiv (t - \upsilon\delta)\cos k + i(\delta - \upsilon t)\sin k. \tag{4.35}$$

For the staggered pattern in columnar field

$$\hat{A}_{sc} = \begin{pmatrix} h + h_a & \hat{U} & \frac{1}{2}J_\perp & 0 \\ \hat{U}^* & h - h_a & 0 & \frac{1}{2}J_\perp \\ \frac{1}{2}J_\perp & 0 & h + h_a & -\hat{U}^* \\ 0 & \frac{1}{2}J_\perp & -\hat{U} & h - h_a \end{pmatrix}. \tag{4.36}$$

For the columnar pattern in columnar field, the matrix $\hat{A}$ is found as

$$\hat{A}_{cc} = \begin{pmatrix} h + h_a & \hat{W}^* & \frac{1}{2}J_\perp & 0 \\ \hat{W} & h - h_a & 0 & \frac{1}{2}J_\perp \\ \frac{1}{2}J_\perp & 0 & h + h_a & -\hat{U}^* \\ 0 & \frac{1}{2}J_\perp & -\hat{U} & h - h_a \end{pmatrix}, \tag{4.37}$$

where

$$\hat{W} \equiv (t + \upsilon\delta)\cos k + i(\delta + \upsilon t)\sin k. \tag{4.38}$$

For the rung dimerized pattern with the columnar field (we will study the rung dimerized ladder in hte presence of columnar field only), we use the diagonal path of JW

transformation (see Fig. 4.2 and Eqs. (1.15) and (1.16) in chapter 1 for detail). Now, we set the matrix $\hat{A}$ for this pattern

$$\hat{A}_{rc} = \begin{pmatrix} h+h_a & t\cos k & \frac{1}{2}J_\perp^+(m_+ +1) & 0 \\ t\cos k & h-h_a & 0 & \frac{1}{2}J_\perp^-(m_- -1) \\ \frac{1}{2}J_\perp^+(m_+ +1) & 0 & h+h_a & t\cos k \\ 0 & \frac{1}{2}J_\perp^-(m_- -1) & t\cos k & h-h_a \end{pmatrix}, \tag{4.39}$$

where we introduced the notations

$$J_\perp^\pm = J_\perp(t_\perp \pm \delta_\perp) \quad \text{and} \quad m_\pm = m_z \pm m_{z,a}. \tag{4.40}$$

The 4×4 matrix $\hat{B}$ is same for all dimerization patterns and it reads

$$\hat{B} = \begin{pmatrix} 0 & -V & 0 & 0 \\ V^* & 0 & 0 & 0 \\ 0 & 0 & 0 & -V \\ 0 & 0 & V^* & 0 \end{pmatrix}. \tag{4.41}$$

where

$$V \equiv (\gamma_a - \upsilon\gamma)\cos k + i(\gamma - \upsilon\gamma_a)\sin k \tag{4.42}$$

The staggered anisotropy γ_a is absent in the bare Hamiltonian, but it could be induced by the mean-field equations. The actual values are found to be very small in the interesting range of parameters. In this our study, we turn off the terms related to anisotropy, i.e., $\gamma = \gamma_a = 0$ in the Hamiltonian matrix (4.33).

To analyze quantum phase transitions, phases of the phase diagram, and magnetization plateaus, we obtain eight eigenvalues $\pm E_{\pm\pm}(k)$ of the Hamiltonian matrix

(4.33). We only use four positive branches $E_{\pm\pm}(k)$ and calculate those quantities for the different models in the following sections.

4.3 Isotropic ladder: spectra, phase diagram and induced magnetizations

In this section, we analyze the energy eigenvalues, phase diagrams, and uniform induced magnetizations of the two-leg ladder in three dimerization patterns and two modulated magnetic fields. These quantities will be investigated with respect to renormalized (effective) parameters. Those renormalized parameters we use, can be calculated from the self-consistent equations given by minimization of the free energy. We present the mean-field parameters of ladders in section 4.4. More importantly, we are able to obtain the magnetization curves in all phases of the phase diagram as functions of the bare magnetic field h. The structure of the magnetization plateaus in the gapped phases agree with the quantization condition (4.1). We explain the detail of those calculations in the following subsections.

4.3.1 Staggered ladder

In this subsection, we consider the staggered two-leg ladder either with staggered or with columnar magnetic field. Using Eqs. (4.33), (4.34), and (4.36), we investigate the magnetization curve within the induced phase boundaries of the phase diagram. Those calculations will be done separately in cases of the staggered and columnar fields. Based on the quantization condition (4.1), we expect three magnetization plateaus at $m_z = 0, \frac{1}{2}, 1$ in the case of columnar field, while the staggered field should only contain two plateaus at $m_z = 0, 1$.

A. Staggered ladder with the columnar field (SC-ladder)

Taking the staggered ladder without anisotropy $\gamma = \gamma_a = 0$, $\hat{B} = 0$ and the effective Hamiltonian (4.31) is given by 4×4 matrix (4.36). We diagonalize (4.36) and find four energy eigenvalues:

$$E^{sc}_{\pm\pm}(k) = h \pm \sqrt{(t - \upsilon\delta)^2 \cos^2 k + \left(\sqrt{h_a^2 + (\delta - \upsilon t)^2 \sin^2 k} \pm \frac{J_\perp}{2}\right)^2}. \tag{4.43}$$

From the equations for eigenvalues (4.43), one can easily see that the flux correction υ only changes the magnitude of hopping and dimerization parameters. To make the analytical and numerical calculation simple, we drop the correction term i.e., $\upsilon = 0$. Then Eq. (4.43) becomes

$$E^{sc}_{\pm\pm}(k) = h \pm \sqrt{t^2 \cos^2 k + \left(\sqrt{h_a^2 + \delta^2 \sin^2 k} \pm \frac{J_\perp}{2}\right)^2} = h \pm \xi_\pm \tag{4.44}$$

From Eq. (4.44) we infer that the model is gapped in general, however the corresponding gaps

$$\Delta_{1/3} = \left| h - \sqrt{t^2 + \left(h_a \pm \frac{J_\perp}{2}\right)^2} \right| \tag{4.45}$$

at the center ($k = 0$), and

$$\Delta_{2/4} = \left| h - \left(\sqrt{h_a^2 + \delta^2} \pm \frac{J_\perp}{2}\right) \right| \tag{4.46}$$

at edge ($k = \pi/2$) of the Brillouin zone vanish on the lines of the quantum critical transitions shown in Fig. 4.3. So, there are four phase boundaries:

(i) At

$$h_c^{(1/3)} = \sqrt{t^2 + \left(h_a \pm \frac{J_\perp}{2}\right)^2}, \tag{4.47}$$

where the gap vanishes at the center of BZ ($k = 0$).

(ii) At edge of BZ ($k = \pi/2$) the gap vanishes at

$$h_c^{(2/4)} = \sqrt{h_a^2 + \delta^2} \pm \frac{J_\perp}{2} \tag{4.48}$$

From the spectra (4.44), we plot the phase diagrams 4.3 in (δ,h) parametric plane. This ground-state phase diagram 4.3 consists of the following five distinct phases:

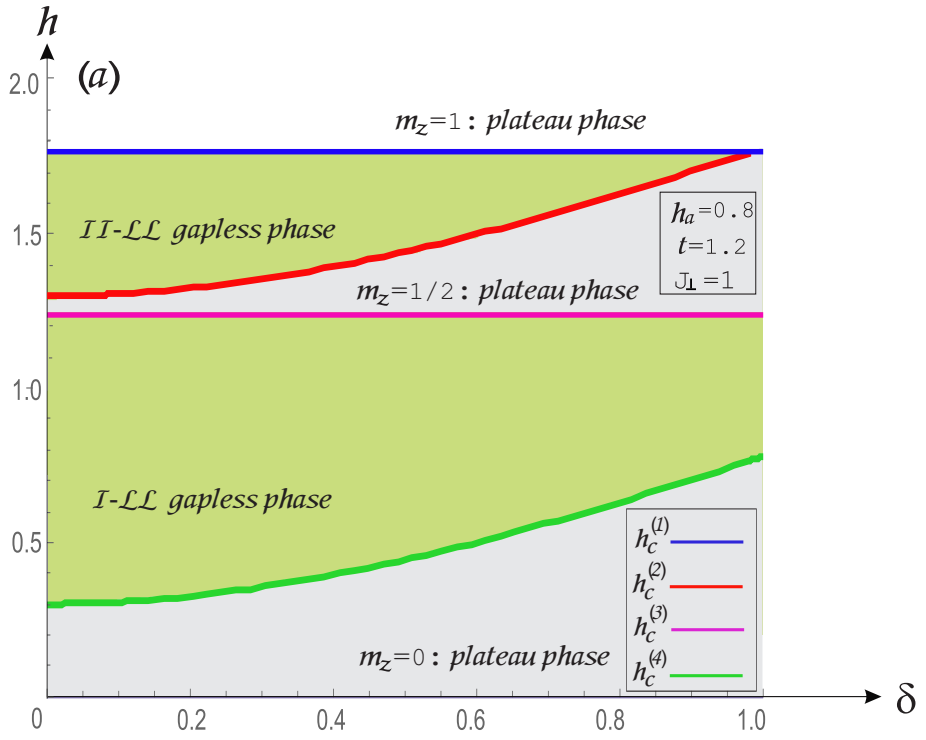

Figure 4.3: Phase diagram of the staggered ladder in (δ,h) parametric plane: All bold coloured lines are lines of the quantum phase transitions separating five phases.

(I) zero plateau gapped phase in the region $h < h_c^{(4)}$,

(II) the first LL gapless phase in the region $h_c^{(4)} < h < h_c^{(3)}$,

(III) the mid-plateau gapped phase in the region $h_c^{(3)} < h < h_c^{(2)}$,

(IV) the second LL gapless phase in the region $h_c^{(2)} < h < h_c^{(1)}$, and

(V) the saturated plateau gapped phase in the region $h > h_c^{(1)}$.

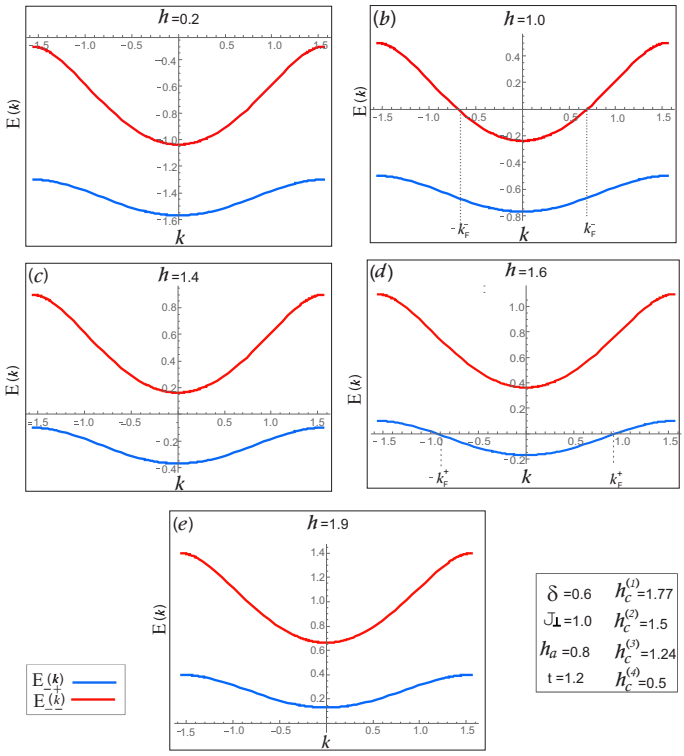

Figure 4.4: Single particle dispersion relations at (a) zero-plateau gapped phase, (b) I-LL gapless phase, (c) mid-plateau gapped phase, (d) II-LL gapless phase and (e) saturated gapped phase.

To better understand of the distinct phases of the phase diagram, the two branches $E_{-+}(k)$ and $E_{--}(k)$ are plotted in Fig. 4.4 for different values of the magnetic field corresponding to the different phases shown in Fig. 4.3. With the values of model's parameters shown in Fig. 4.4, the ground-state of the ladder is in the zero-plateau gapped phase at $h < h_c^{(4)} = 0.5$, where both branches are empty (see Fig. 4.4a). By increasing the magnetic field, energies of both branches start to increase. At the critical field $h_c^{(4)} = 0.5$, the branch $E_{--}(k)$ starts to fill in and the filling gradually

increases with increasing the magnetic field from $h = 0.5$ up to $h < h_c^{(3)} = 1.24$. This corresponds to the first LL gapless phase (see Fig. 4.4b), where two Fermi points $\pm k_F^-$ are shown on the $E_{--}(k)$ branch. At the critical field $h = h_c^{(3)} = 1.24$, two Fermi points merge as $\pm k_F^- = 0$, and the branch $E_{--}(k)$ becomes completely filled. With further increase of the magnetic field, the ladder is brought to the mid-plateau region $h_c^{(3)} < h < h_c^{(2)} = 1.5$, where energies of both branches increase (see Fig. 4.4c), but the spectrum is gapped. At $h > h_c^{(2)} = 1.5$, where the branch $E_{-+}(k)$ starts to fill in. It contains two Fermi points $\pm k_F^+$. This is the second LL gapless region at $h_c^{(2)} < h < h_c^{(1)} = 1.77$ (see Fig. 4.4d). Finally at the critical field $h = h_c^{(1)} = 1.77$, the branch $E_{-+}(k)$ becomes completely filled and two Fermi points merge at the center of the Brillouin zone $\pm k_F^+ = 0$. In the saturated plateau gapped phase $h > h_c^{(1)}$, both branches are completely filled and the filling is saturated (see Fig. 4.4e).

The induced magnetization per site $m_z = \frac{1}{2N}\sum_{n=1}^{2N}\langle\sigma_n^z\rangle$ can be calculated by differentiating the free-energy of the model with respect to h. After minimization of the free-energy, its explicit expression is

$$m_z = \frac{1}{2} + \frac{1}{2\pi}\int_0^{\pi/2}\Big\{\text{sign}(E_{-+}) + \text{sign}(E_{--})\Big\}dk \tag{4.49}$$

Now, we present the field-induced magnetization m_z as a function of the uniform magnetic field h in Fig. 4.5. Those magnetization curves are shown in Fig.4.5a and 4.5b at different values of h_a and dimerization δ respectively. The uniform magnetization is calculated at each point with the renormalized couplings on the right-hand side of Eq. (4.49), determined self-consistently from the numerical solution of the mean-field equations given in section 4.4. Qualitatively, the structure of the magnetization plateaus can be understood from residual filling of the $E_{-\pm}$ bands explained above. As clearly seen in Fig. 4.5a, the magnetization remains zero (zero-plateau) in the low

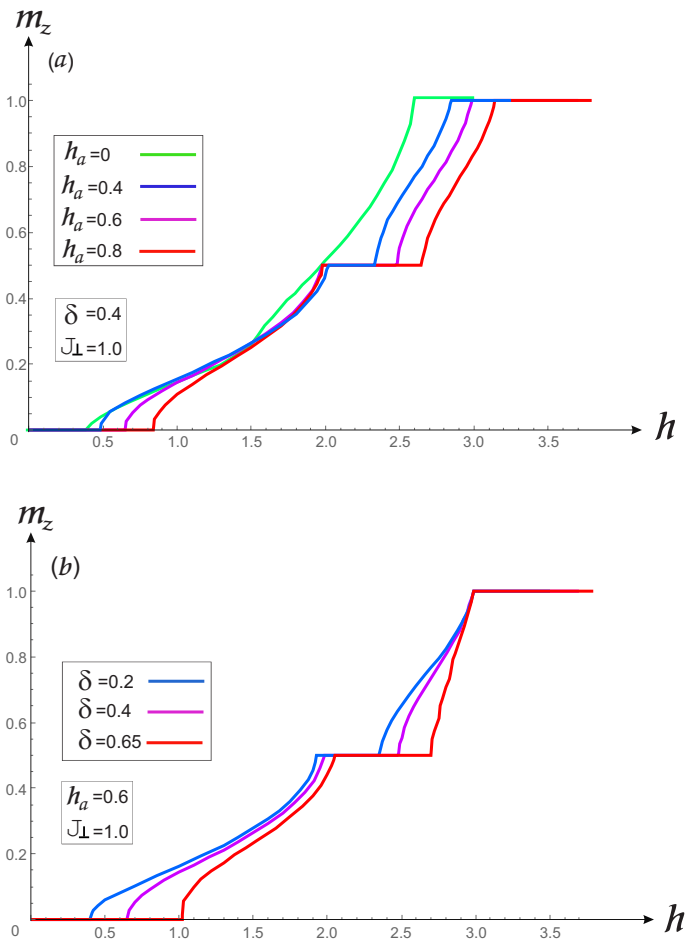

Figure 4.5: Uniform induced magnetization m_z vs uniform magnetic field at different values of (a) alternating field h_a, and (b) dimerization δ.

external field h up to the forth critical field $h_c^{(4)}$, which depends on the strength of the alternating field h_a keeping the other parameters ($J_\perp$, δ) the same. By further increase of the magnetic field, the magnetization starts to increase and undergoes a quantum phase transition to the first LL gapless phase, followed by another transition into the mid-plateau ($m_z = 1/2$) gapped phase, located between the third and second quantum critical fields. The width of the mid-plateau depends on the strength of the alternating field h_a. The existence of the mid-plateau state reported here for the first time is an indication of the appearance of a new spin gapped phase in this type of ladder. If

there is no alternating field i.e., $h_a = 0$, the mid-plateau is not allowed by the plateau theorem, in agreement with the earlier result [48]. The ladder then contains only one LL gapless phase (see green curve in Fig. 4.5a). In Fig. 4.6, we present our mean-field results for $h_c^{(4)}$ and $h_c^{(1)}$ shown by red arrows in comparison to the numerical results of Ref. [48]. The plateau-gapped and LL-gapless phases we found from the mean-field approach are in good agreement with the numerical results. As we increase alternating field h_a, the second LL-gapless phase starts to appear with mid-plateau. In other words, the alternating field h_a splits the LL-phase into two LL phases by creating a mid-plateau in between them. Finally, the magnetization reaches its saturation value at first critical field $h_c^{(1)}$, see Fig. 4.5a.

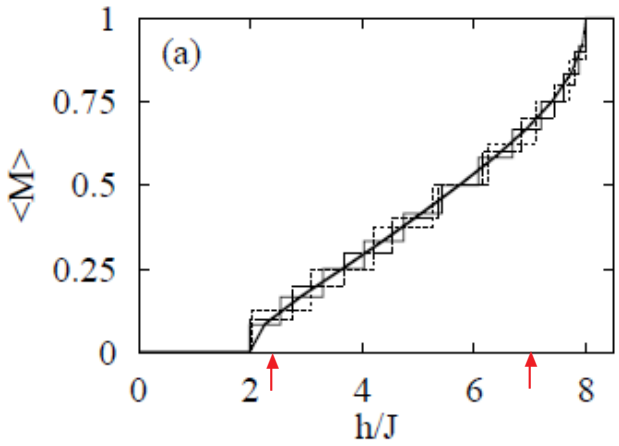

Figure 4.6: Numerical results for magnetization of the staggered dimerized ladder for $\delta = 0.5$ and $J_\perp = 1$ taken from the Ref. [48]. The mean-field approximation results for $h_c^{(4)}$ and $h_c^{(1)}$ are shown by red arrows.

Fig. 4.5b represents the field dependence of magnetization with different dimerization parameter δ. It is shown that the width of the zero-plateau and mid-plateau phases increases with the strength of dimerization, while other parameters are kept the same. In the first and second LL gapless phases, the magnetization increases smoothly. Interestingly, one can notice that all magnetization curves merge into the same point

corresponding to the same value of the first critical field $h_c^{(1)}$, where magnetization gets into its saturated value $m_z = 1$.

B. Staggered ladder with staggered field (SS-ladder)

In this case four eigenvalues of the 4×4 matrix (4.34) are

$$E^{ss}_{\pm\pm}(k) = h \pm \sqrt{h_a^2 + (t - \upsilon\delta)^2 \cos^2 k + \Big((\delta - \upsilon t)\sin k \pm \frac{J_\perp}{2}\Big)^2}. \tag{4.50}$$

From (4.50), one can easily see that the flux correction term υ just changes the magnitude of the hopping and dimerization parameters and no new features are brought about by $\upsilon \neq 0$. To make the analytical and numerical calculation simpler, we drop the correction $\upsilon = 0$. In order to make the above eigenvalues symmetric with respect to k, we use the shift $k \mapsto k + \pi/2$ in the branches $E_{-+}(k)$ and $E_{--}(k)$. Using the relation $E_{-+}(k) \leftrightarrow E_{--}(k-\pi)$ between two branches, we combine four branches (4.50) in the more compact form

$$E^{ss}_{\pm}(k) = h \pm \sqrt{h_a^2 + t^2 \sin^2 k + \Big(\delta \cos k - \frac{J_\perp}{2}\Big)^2} = h \pm \xi. \tag{4.51}$$

The wavenumbers of superimposed branches (4.51) run within the double Brillouin zone $k \in [-\pi, \pi]$. From Eq. (4.51) we infer that the model is gapped in general, however the gaps

$$\Delta_1 = \Big| h - \sqrt{h_a^2 + t^2 + \frac{1}{4}J_\perp^2} \Big| \tag{4.52}$$

at $k = \pi/2$ of the Brillouin zone $k \in [-\pi, \pi]$ and

$$\Delta_4 = \Big| h - \sqrt{h_a^2 + \Big(\delta - \frac{J_\perp}{2}\Big)^2} \Big| \tag{4.53}$$

at center of BZ $k = 0$, vanish on the lines of the quantum critical transitions shown in Fig. 4.7. So, there are two phase boundaries:

(i) At

$$h_c^{(1)} = \sqrt{h_a^2 + t^2 + \frac{1}{4}J_\perp^2}, \tag{4.54}$$

where the gap vanishes at $k = \pi/2$ and

(ii) At $k = 0$ the gap vanishes at

$$h_c^{(4)} = \sqrt{h_a^2 + \left(\delta - \frac{J_\perp}{2}\right)^2}. \tag{4.55}$$

From Eq. (4.51) we illustrate the ground-state phase diagram 4.7 in the (h,δ) para-

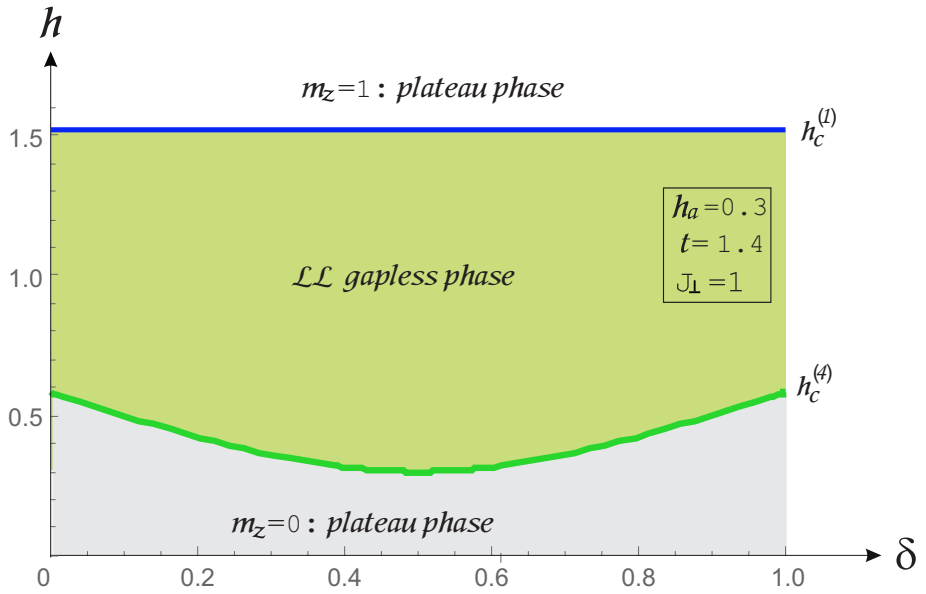

Figure 4.7: Phase diagram of staggered ladder in staggered field in the h-δ parametric plane. The model is critical on (i) $h = h_c^{(4}$ (red); (ii) $h = h_c^{(1)}$ (blue). Three phases are shown: $m_z = 0$: plateau phase, LL-gapless phase, and $m_z = 1$: saturated phase.

metric plane. It is shown that there are only three distinct phases: the zero-plateau gapped phase in the region $h \leq h_c^{(4)}$, the LL gapless phase in the region $h_c^{(4)} < h < h_c^{(1)}$,

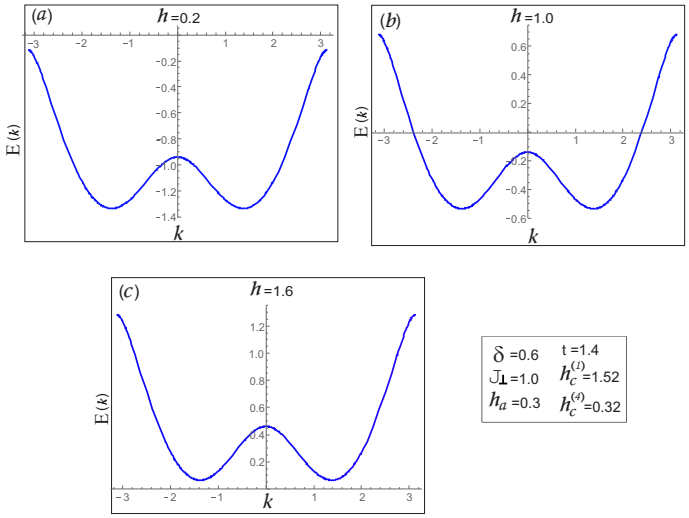

Figure 4.8: Single particle dispersion relations in the (a) zero-plateau gapped phase, (b) LL-gapless phase, and (c) saturated gapped phase.

and the saturated gapped phase in the region $h \geq h_c^{(1)}$. To make the quantum phases more visual, we plot the branch $E_-(k)$ (see Fig. 4.8) for different values of the external field within the Brillouin zone $k \in [-\pi, \pi]$, and analyze the variation of the branches and the filling in the different phases of the phase diagram. For the detailed discussion, we refer to Fig. 4.4 and its description. Comparing Figs. 4.4 and 4.8, one can easily understand why the mid-plateau does not occur in the SS-ladder.

In order to investigate induced magnetization m_z, we rewrite its expression (4.49) in the explicit form

$$m_z = \frac{1}{2} + \frac{1}{2\pi} \int_0^\pi \text{sign}(E_-) dk \tag{4.56}$$

and numerically calculate at each point with the renormalized couplings, which are determined from the self-consistent equations. We plot the field-induced magnetization as a function of the uniform component of the magnetic field h in Fig. 4.9. Those curves are schematically drawn in Figs. 4.9a and 4.9b for the different values of alternating field h_a and dimerization δ respectively. In the low field range $h < h_c^{(4)}$, the uniform

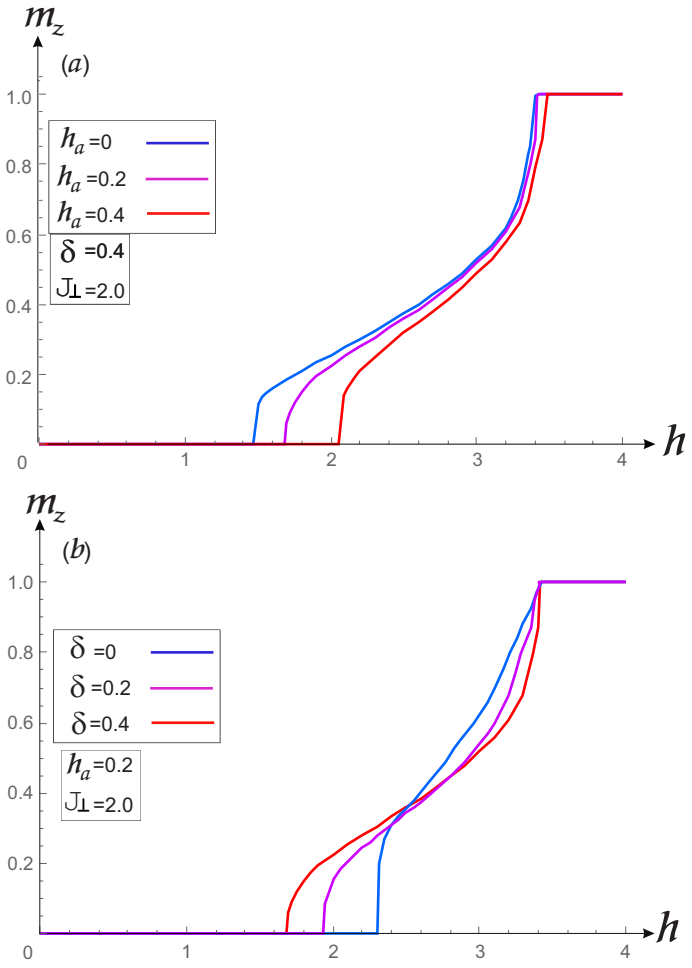

Figure 4.9: Schematic plot of the uniform induced magnetization m_z as a function of uniform magnetic field h for different values of (a) alternating field h_a, and (b) dimerization δ.

magnetization remains zero at zero-plateau gapped phase. In the Fig. 4.9b, the width of the zero-plateau phase decreases with the strength of dimerization δ, while the other parameters are kept fixed. As soon as the field h exceeds $h_c^{(4)}$, the magnetization increases gradually until it reaches the critical point, where its saturated value is $m_z = 1$. In Fig. 4.9b, the magnetization is shown for different dimerizations δ. From Fig. 4.9a we infer the effect of the alternating field h_a on the magnetization: it only affects the magnitude of two critical fields $h_c^{(4)}$ and $h_c^{(1)}$ (phase boundaries), but there is no significant effect in creating new phases.

4.3.2 Columnar ladder with columnar field (CC-ladder)

In this case the 4×4 matrix (4.37) has four energy eigenvalues

$$E^{cc}_{\pm\pm}(k) = h \pm \Big\{ h_a^2 + \frac{1}{4}J_\perp^2 + (t^2 + \upsilon^2\delta^2)\cos^2 k + (\delta^2 + \upsilon^2 t^2)\sin^2 k$$

$$\pm 2\sqrt{\frac{1}{4}h_a^2 J_\perp^2 + \upsilon^2\Big\{\delta^2 t^2 + \frac{1}{4}J_\perp^2(t^2\sin^2 k + \delta^2\cos^2 k)\Big\}}\Big\}^{1/2}. \tag{4.57}$$

From Eq. (4.57) we plot the quantum phase diagram in Fig. 4.10. This phase diagram consists of four phase boundaries:

(i) At

$$h_c^{(2/4)} = \sqrt{h_a^2 + \frac{1}{4}J_\perp^2 + \delta^2 + \upsilon^2 t^2 \pm 2\sqrt{\frac{1}{4}h_a^2 J_\perp^2 + \upsilon^2 t^2\Big(\delta^2 + \frac{1}{4}J_\perp^2\Big)}} \tag{4.58}$$

where the gap vanishes at edge of BZ ($k = \pi/2$).

(ii) At the center of BZ ($k = 0$) the model is quantum critical at

$$h_c^{(1/3)} = \sqrt{h_a^2 + \frac{1}{4}J_\perp^2 + t^2 + \upsilon^2\delta^2 \pm 2\sqrt{\frac{1}{4}h_a^2 J_\perp^2 + \upsilon^2\delta^2\Big(t^2 + \frac{1}{4}J_\perp^2\Big)}}. \tag{4.59}$$

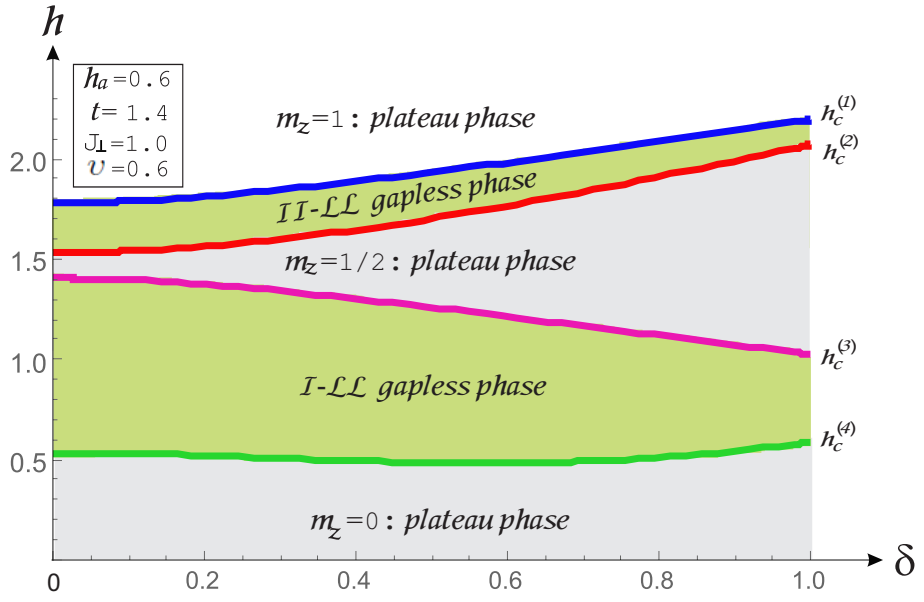

Figure 4.10: Phase diagram of columnar two-leg ladder in the (h-δ) parametric plane. All bold coloured lines are lines of quantum phase transitions separating five phases.

The phase diagram in Fig. 4.10 contains five quantum phases distinguished by four phase boundaries (4.58) and (4.59). They are: the 0-plateau gapped phase, first LL gapless phase, mid-plateau gapped phase, second LL gapless phase, and saturated gapped phase. As we drop the flux correction $\upsilon = 0$, the mid-plateau phase does not occur in this ladder at zero staggered field ($h_a = 0$) since the phase diagram only contains two phase boundaries h_c^1 and h_c^4. To make the qualitative agreement with the numerical results [48, 144], the flux correction term needs to be considered.

To qualitatively understand the five distinct quantum phases we can analyse the

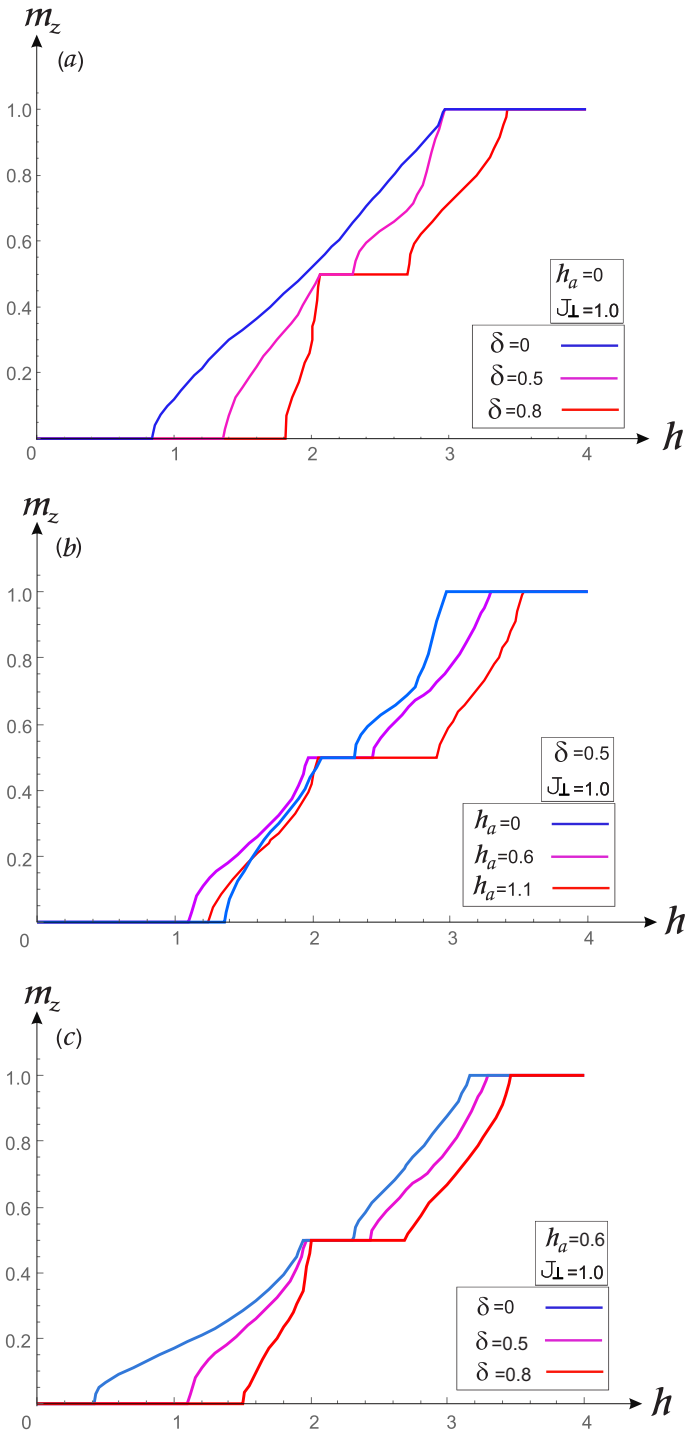

Figure 4.11: Uniform induced magnetization m_z vs uniform magnetic field h for different values of (a) dimerization δ at $h_a = 0$ (b) alternating field h_a at $\delta = 0.5$, and (c) dimerization δ at $h_a = 0.6$.

variation of spectra and the fermionic filling on two branches $E_{-+}(k)$ and $E_{--}(k)$ within the Brillouin zone $(-\pi/2,\pi/2)$ for the different values of the external magnetic field. As we increase the external field h from $h = 0$ to $h > h_c^{(1)}$, one can check that the spectra $E_{-+}(k)$ and $E_{--}(k)$ evolve similarly to what was discussed above and plotted in Fig. 4.4, with similar physical behaviour.

In addition to the dispersion relations, the nature of the different quantum phases can be clarified from the study of the induced magnetization. Now, we can use the explicit expression for the magnetization (4.49). Fig. 4.11 presents the plot of the magnetization versus the uniform magnetic field for different values of the alternating field h_a and dimerization parameter δ. Here we numerically calculate the induced magnetization at each point by using renormalized couplings which are determined self-consistently from the mean-field equations given in the section 4.4.

Three sets of magnetization curves are plotted in case of the columnar ladder with columnar field. Fig. 4.11c represents the magnetization versus applied field for $h_a = 0.6$ at different values of dimerization. In this Fig. 4.11c, five distinct phases are observed even without dimerization $\delta = 0$. It explains that the width of mid-plateau depends on the δ and h_a, while the width of the zero-plateau phase is determined by the difference of the dimerization and rung coupling $J_\perp$. Another advantage of the present mean-field approach is that, in case of $h_a = 0$ (see Fig. 4.11a), it yields the magnetization plateaus, and the LL gapless phases in agreement with the numerical results [144] shown in Fig. 4.12. In case $h_a = 0$, the width of the mid-plateau phase is determined by the value of dimerization δ. If $\delta = 0$, the middle plateau does not occur in this model, in agreement with the plateau theorem and the numerical results of Kariyado and Hatsugai [144]. We calculate the critical fields shown by red and green arrows in Fig. 4.12 for $\delta = 0.5$ and $\delta = 0$. As one can see from Fig. 4.12, our mean-field results for the magnetization

is in good qualitative agreement with the numerical data. However, the calculated values for the critical fields are about $20-30$ percent apart from the numerical results, which is expected for a mean field approach.

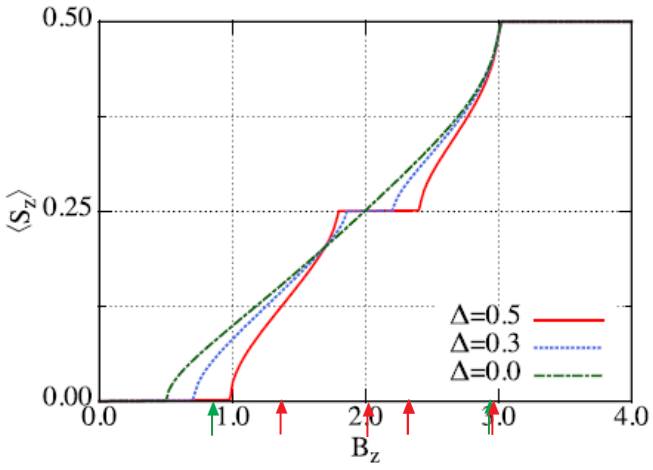

Figure 4.12: Numerical results for the magnetization of the columnar dimerized ladder for $\delta = 0, 0.5$ and $J_\perp = 1$ taken from the Ref. [144] where Δ is the dimerization parameter. The present mean-field results for $h_c^{(2/4)}$ and $h_c^{(1/3)}$ are shown by green/red arrows for $\delta = 0/0.5$.

In the following, we study the effect of external magnetic field on the induced magnetization for the different values of alternating magnetic field h_a, see Fig. 4.11b. In the 0-plateau region, the magnetizations are zero, and QCPs are seen at the boundaries of the first LL gapless phase. By further increasing the field, the ladder undergoes transition into the mid-plateau gapped phase. The width of the mid-plateau increases with the alternating field h_a.

4.3.3 Rung-dimerized ladder in columnar field (RC-ladder)

In this subsection, we study the ground state properties of a rung-dimerized ladder with the columnar field. The general plateau theorem predicts the phase diagram with three plateaus (0, $\frac{1}{2}$,1) of the magnetization. Using Eqs. (4.33) and (4.39), we obtain

four energy eigenvalues,

$$E^{rc}_{\pm\pm}(k) = h \pm \frac{J_\perp}{2}\Big\{\delta_\perp(1+m_{z,a}) + m_z t_\perp\Big\}$$
$$\pm\sqrt{t^2\cos^2 k + \Big\{h_a \pm \frac{J_\perp}{2}\Big(\delta_\perp m_z + t_\perp(1+m_{z,a})\Big)\Big\}^2} \tag{4.60}$$

Two magnetizations m_z and $m_{z,a}$ appear separately in Eq. (4.60) where the flux correction term for this model is $m_z \pm m_{z,a}$. These two quantities change only the magnitude of the dimerization and rung hopping parameters. From analysis of Eq. (4.60) it is clear that corrections does not change the result qualitatively, resulting in some minor modifications of phase boundaries. Then, the (4.60) becomes in the following simplified form:

$$E^{rc}_{\pm\pm}(k) = h \pm \frac{J_\perp}{2}\delta_\perp \pm \sqrt{t^2\cos^2 k + \Big(h_a \pm \frac{J_\perp}{2}t_\perp\Big)^2} \tag{4.61}$$

From the spectrum (4.61), we find the ground-state phase diagram of the rung dimerized ladder in (h, δ) the parametric plane shown in Fig. 4.13. It contains five distinct phases: 0-plateau gapped phase, I-LL gapless phase, mid-plateau gapped phase, II-LL gapless phase and saturated gapped phase. These four phase boundaries are:

(i) At

$$h_c^{(1/3)} = \sqrt{t^2 + \Big(h_a \pm \frac{J_\perp}{2}t_\perp\Big)^2} \mp \frac{J_\perp}{2}\delta_\perp, \tag{4.62}$$

the gap vanishes at the centre of the BZ ($k = 0$).

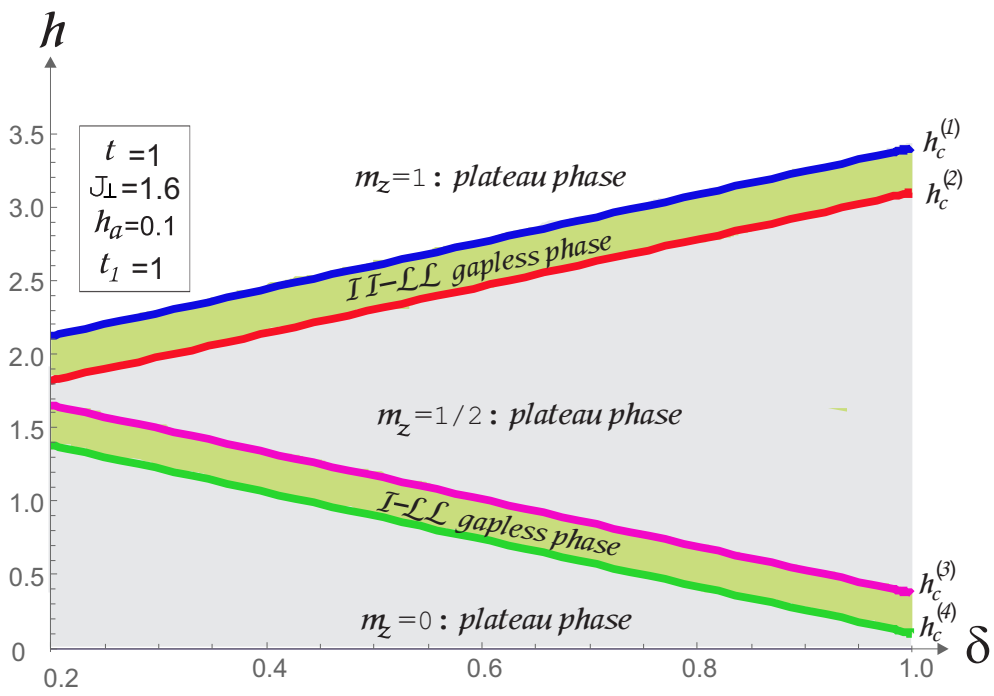

Figure 4.13: Phase diagram of rung-dimerized ladder in the (h,δ) parametric plane. All bold coloured lines are lines of quantum phase transitions separating five distinct phases.

(ii) At the edge of the BZ ($k = \pi/2$) the model becomes gapless at

$$h_c^{(2/4)} = h_a \pm \frac{J_\perp}{2}(t_\perp - \delta_\perp). \tag{4.63}$$

The ground state phase diagram of this model was investigated analytically and numerically [56, 138, 142, 143, 145] without alternating magnetic field ($h_a = 0$). We are not aware of the studies for the case $h_a \neq 0$. In Fig. 4.14, we present numerical results of Ref. [143] for the magnetization at $h_a = 0$. The calculation of the critical fields are done for the same parameters of ladder Hamiltonian via the mean-field approximation.

For a qualitative understanding of the phase transition in this case and structure

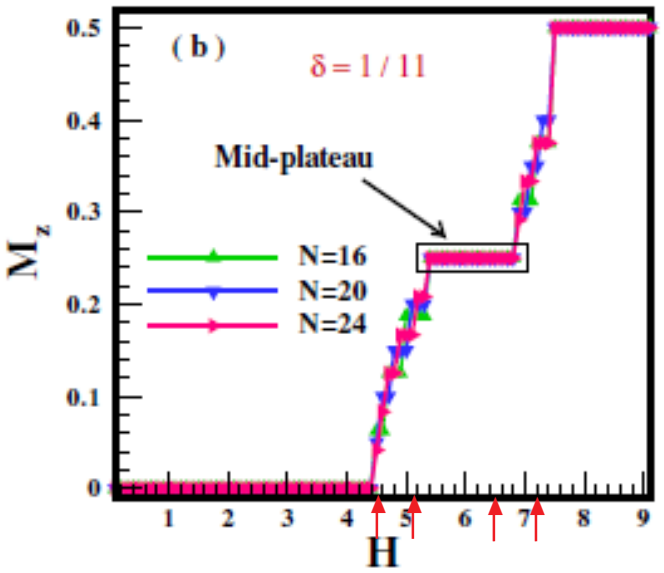

Figure 4.14: Numerical results for magnetization of the rung dimerized ladder for $\delta = 1/11$, $h_a = 0$ and $J_\perp = 11/4$ adapted from Ref. [143]. The mean-field results for $h_c^{(2/4)}$ and $h_c^{(1/3)}$ are shown by red arrows.

of the gapped and gapless phases, we can analyse the branches $E_\pm(k)$ with magnetic field. The results are similar to those discussed above in the context of Fig. 4.4.

In order to characterize different phases of the phase diagram via the induced magnetization process with respect to applied uniform magnetic field h, we write its explicit expression:

$$m_z = \frac{1}{2\pi}\int_0^{\pi/2}\Big\{\mathrm{sign}(E_{++}) + \mathrm{sign}(E_{+-}) + \mathrm{sign}(E_{-+}) + \mathrm{sign}(E_{--})\Big\}dk. \qquad (4.64)$$

The induced magnetization (4.64) is calculated numerically. Those calculations were done with the renormalized couplings, determined self-consistently from the mean-field equations. Fig. 4.15 presents the field-induced magnetization m_z as a function of the uniform magnetic field at different dimerization δ and alternating magnetic field h_a. Fig. 4.14 presents the ground-state magnetization vs external field calculated via exact

diagonalization at $h_a = 0$ in Ref. [143] along with our mean-field results for the critical fields $h_c^{(2/4)}$ and $h_c^{(1/3)}$, shown by red arrows. The gapped plateau and the LL gapless phases, found from our mean-field approach, are in agreement with their numerical results. However, our values of the critical fields are about $20 - 30\%$ apart from their numerical values. In this case, the mid-plateau phase only depends on the strength of dimerization δ (see blue curve in Fig. 4.16a for reference). In case $\delta = 0$, no mid-plateau phase occurs as reported in [56, 141, 143, 144].

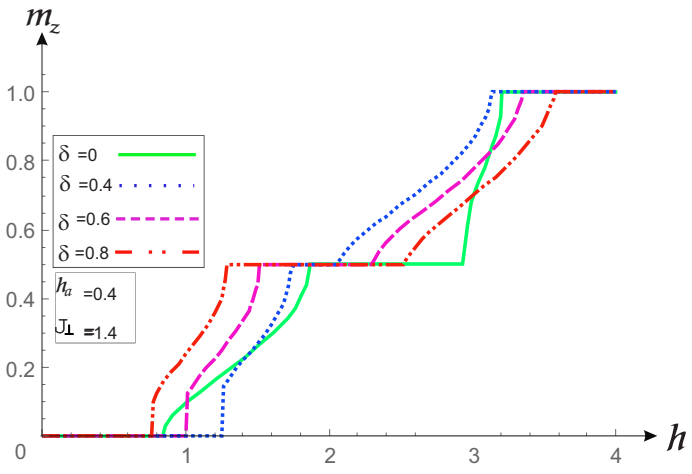

Figure 4.15: Uniform induced magnetization m_z vs uniform magnetic field h at different values of dimerization. It demonstrates three plateaus $m_z = 0, \frac{1}{2}, 1$ in three gapped phases, and they are connected by two continuous curves corresponding to two LL gapless phases.

A. Effect of alternating field on magnetization curve:

In this subsection, we study the effect of alternating field on the magnetization and the ground state phase diagram. At the weak alternating field h_a, the model is symmetric with respect to the applied fields h and h_a, and the system obeys the condition (4.1) of the plateau theorem for magnetization. In Fig. 4.15, we plot the magnetization for $h_a = 0.4$ and $J_\perp = 1.4$ at different value of δ and one can see that

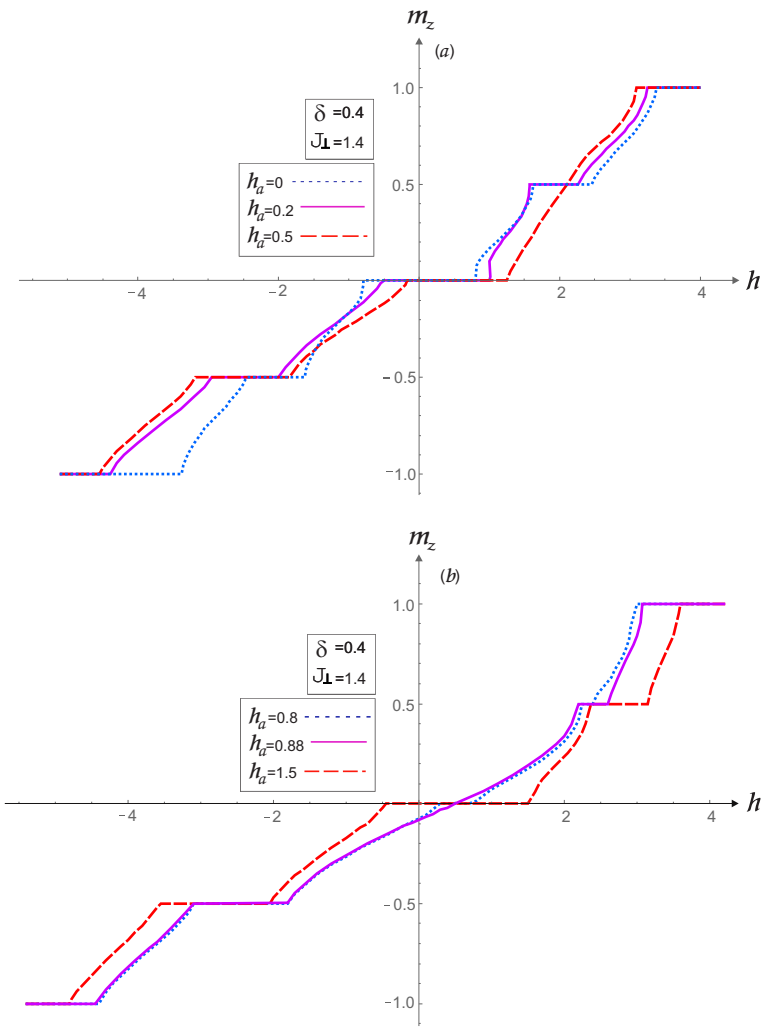

Figure 4.16: Uniform induced magnetization m_z vs uniform magnetic field at (a) different $h_a \leq h_{a,c}^{(1)}$, and (b) different $h_a > h_{a,c}^{(2)}$. They demonstrate either two or three plateaus-gapped phases, depending on the applied alternating field applied h_a.

h_a not only modifies the phase boundaries, but can also create the mid-plateau phase even when $\delta = 0$. This property of h_a was discussed in the previous subsections in the limit of $\delta = 0$ for staggered and columnar ladders.

Upon further increase of h_a, we find interesting physics of the rung-dimerized ladder. This case of dimerization is sensitive to the sign of h_a since the spectra (4.61) depend on h_a not on h_a^2 as in other cases. That is why we also include the induced magnetizations m_z curves along the negative magnetic field h at different values of h_a (see Fig. 4.16). As we carefully checked for negative value of h_a, the antisymmetric magnetization curves are observed with Fig. 4.16. At $h_a = h_{a,c}^{(1)} = 0.47$, the mid-plateau phase disappears and starts to re-appear from $h_a = h_{a,c}^{(2)} = 0.77$. This kind of closing and re-opening of the gapped phase with respect to alternating field h_a constitutes another quantum phase transition. Those numerical calculations of the magnetization and alternating field are done by determining renormalized parameters self-consistently from the mean-field equations. On the other hand, one can obtain explicit condition

$$\left| h_a - \frac{J_\perp}{2} t_\perp \right| + J_\perp \delta_\perp \leq \sqrt{\left(h_a + \frac{J_\perp}{2} t_\perp \right)^2 + t^2} \tag{4.65}$$

for vanishing the mid-plateau in the phase diagram. We can find this condition from the critical fields (4.62) and (4.63), expressing in terms of the renormalized parameters.

As we see in Fig. 4.16a, the ground-state of the system is in the mid-plateau state is in the lower alternating field. Further increasing the field h_a, the width of the mid-plateau region starts to decrease and it vanishes at the critical field of $h_a = h_{a,c}^{(1)}$. As we increase the field $h_{a,c}^{(1)} \geq h_a \geq h_{a,c}^{(2)}$, the quantum phase transition is observed by re-appearing the mid-plateau region (see blue curve of Fig. 4.16b). As soon as the field increases from field $h_a > h_{a,c}^{(2)}$, the zero-plateau phase vanishes and the mid-plateau phase increases with the values of h_a. By increasing the field (4.16b: red curve), the

system re-gains the zero-plateau gapped phase. In fact, at this critical field, the system possesses a quantum phase transition by re-opening the zero-plateau gapped phase. In the mid-plateau and zero-plateau regions, anomalous behaviours are seen at different critical fields. Based on our knowledge nothing is described as such peculiar property of this model in the presence of alternating field h_a. Beyond this critical field, the magnetization curve always contains five phases in phase diagram.

4.4 Mean-field theory: technical details

We fermionize the spin ladder Hamiltonian (4.2) using the JW transformation (4.5). There are different ways to introduce this transformation when we depart from a single chain problem to the spin ladder (see, e.g., [23, 39, 83]). We use the snake-like JW transformation path discussed in Chapter 1, which yields the following fermionic Hamiltonian:

$$H = \frac{1}{2}\sum_{n,\alpha}\Big[e^{i\hat{\Phi}_\alpha(n)}\Big\{J_\alpha(n)c^\dagger_\alpha(n)c_\alpha(n+1) + J\gamma c^\dagger_\alpha(n)c^\dagger_\alpha(n+1)\Big\} + h.c.$$

$$+2J_\alpha(n)\Big(\hat{n}_\alpha(n)-\frac{1}{2}\Big)\Big(\hat{n}_\alpha(n+1)-\frac{1}{2}\Big) + 2h_\alpha(n)\Big(\hat{n}_\alpha(n)-\frac{1}{2}\Big)\Big]$$

$$+\frac{1}{2}\sum_n J_\perp(n)\Big\{c^\dagger_1(n)c_2(n) + h.c. + 2\Big(\hat{n}_1(n)-\frac{1}{2}\Big)\Big(\hat{n}_2(n)-\frac{1}{2}\Big)\Big\}. \tag{4.66}$$

The interacting fermionic term in (4.66) is decoupled (see detail in chapter 1) by using the standard decoupling [89] for the product of the two number operators ($\hat{n}_\alpha(l) = c^\dagger_\alpha(l)c_\alpha(l)$. The decoupled mean-field Hamiltonian reads

$$H = 2NC + \frac{1}{2}\sum_{n,\alpha}\Big\{J_\alpha(n)\Big[e^{i\hat{\Phi}_\alpha(n)} + 2\langle c_\alpha(n)c^\dagger_\alpha(n+1)\rangle\Big]c^\dagger_\alpha(n)c_\alpha(n+1)$$

$$+J\gamma\Big[e^{i\hat{\Phi}_\alpha(n)}-2\langle c_\alpha(n)c_\alpha(n+1)\rangle\Big]c^\dagger_\alpha(n)c^\dagger_\alpha(n+1)+h.c.$$

$$-J_\alpha(n)\Big[(1-2\langle c^\dagger_\alpha(n+1)c_\alpha(n+1)\rangle)c^\dagger_\alpha(n)c_\alpha(n)$$

$$+(1-2\langle c^\dagger_\alpha(n)c_\alpha(n)\rangle)c^\dagger_\alpha(n+1)c_\alpha(n+1)\Big]+2h_\alpha(n)c^\dagger_\alpha(n)c_\alpha(n)\Big\}$$

$$+\frac{1}{2}\sum_n J_\perp(n)\Big\{[1+2\langle c_1(n)c^\dagger_2(n)\rangle]c^\dagger_1(n)c_2(n)+h.c.$$

$$-(1-2\langle c^\dagger_1(n)c_1(n)\rangle)c^\dagger_2(n)c_2(n)-(1-2\langle c^\dagger_2(n)c_2(n)\rangle)c^\dagger_1(n)c_1(n)\Big\} \tag{4.67}$$

The phase operator $\hat{\Phi}_\alpha(n)$ entering in Eq. (5.65) is obtained from the path of JW transformation shown in Fig. 1.1 and explicitly written in Eq. (1.13). This phase operator $\hat{\Phi}_\alpha(n)$ is treated as a quantized quantity $\hat{\Phi}_\alpha(n)$. Then according to the Lieb theorem [149] the ground-state of the ladder is in π-flux phase [147], which results to $e^{i\hat{\Phi}_\alpha(n)}\approx(-1)^{n+\alpha-1}$. Once we introduce transverse magnetic field (4.4a) or (4.4b), the induced magnetisation (4.68) shifts the band away from the half filling and the flux is changed. We introduce the field induced magnetizations

$$\langle 1-2c^\dagger_\alpha(n)c_\alpha(n)\rangle=\begin{cases} m_z+(-1)^{n+\alpha}m_{z,a}, & \text{(staggered)} \\ m_z+(-1)^n m_{z,a} & \text{(columnar)}\end{cases}. \tag{4.68}$$

with respect to the staggered and columnar fields respectively. To make the correction to the flux per plaquette, we replace the phase factor (1.13) in Eq. (4.67) by its average value:

$$\langle e^{i\hat{\Phi}_\alpha(n)}\rangle=\langle e^{i\pi\hat{n}_\alpha(n)}e^{i\pi\hat{n}_\alpha(n+1)}\rangle\equiv\langle(1-2\hat{n}_\alpha(n))(1-2\hat{n}_\alpha(n+1))\rangle \tag{4.69}$$

Using (4.68) the flux correction (4.69) reads

$$\langle e^{i\hat{\Phi}_\alpha(n)}\rangle \equiv m_z^2 - m_{z,a}^2 \tag{4.70}$$

To simplify the calculation, we use the notation $\langle e^{i\hat{\Phi}_\alpha(n)}\rangle = \upsilon$ from now on, and imposing all requirements on the Hamiltonian (4.67) amounts to the approximation $e^{i\hat{\Phi}_\alpha(n)} \approx [(-1)^{n+\alpha-1} + \upsilon]$,

$$e^{i\hat{\Phi}_\alpha(n)} + 2\langle c_\alpha(n)c_\alpha^\dagger(n+1)\rangle = [(-1)^{n+\alpha-1} + \upsilon](1 + 2t_\alpha(n)) \tag{4.71}$$

$$e^{i\hat{\Phi}_\alpha(n)} - 2\langle c_\alpha(n)c_\alpha(n+1)\rangle = [(-1)^{n+\alpha-1} + \upsilon](1 - 2P_\alpha(n)), \tag{4.72}$$

where we introduced the mean field averaged parameters

$$t_\alpha(n) = \begin{cases} \mathcal{K} + (-1)^{n+\alpha}\delta\eta, & \text{(staggered)} \\ \mathcal{K} + (-1)^n\delta\eta, & \text{(columnar)} \\ \mathcal{K}, & \text{(rung)} \end{cases} \tag{4.73}$$

$$P_\alpha(n) = \begin{cases} P - (-1)^{n+\alpha}\delta\eta_p, & \text{(staggered)} \\ P - (-1)^n\delta\eta_p, & \text{(columnar)} \\ P, & \text{(rung)} \end{cases}, \tag{4.74}$$

$$t_\perp(n) = \langle c_1(n)c_2^\dagger(n)\rangle = \begin{cases} t_\perp, & \text{(stagg/col)} \\ t_\perp + (-1)^n\delta_\perp\eta_\perp, & \text{(rung).} \end{cases} \tag{4.75}$$

The renormalized couplings (4.11) - (4.23) are to be found from the sets of self-consistent equations obtained from the minimization of the free energy for three dimerization patterns. We present the equations for the case $\gamma = \gamma_R = \gamma_a = 0$. The sets of

the mean-field equations are quite different for three dimerization patterns, and they are given in Appendix A. Based on the condition of plateau theorem for the magnetization, we rewrite the mean-field parameters and calculate them numerically (see. Fig.4.17).

(1) Staggered pattern with staggered field (SS-ladder):

$$m_{z,a} = \frac{h_{aR}}{2\pi}\int_0^{\pi}\frac{1}{\xi}(1-\mathrm{sign}(E_{-+}))dk \tag{4.76}$$

$$\mathcal{K} = \frac{t_R}{4\pi}\int_0^{\pi}\frac{\sin^2 k}{\xi}(1-\mathrm{sign}(E_{-+}))dk \tag{4.77}$$

$$\delta\eta = \frac{1}{4\pi}\int_0^{\pi}\frac{\sin k}{\xi}\Big(\delta_R\sin k+\frac{J_{\perp R}}{2}\Big)(1-\mathrm{sign}(E_{-+}))dk \tag{4.78}$$

$$t_\perp = \frac{1}{4\pi}\int_0^{\pi}\frac{1}{\xi}\Big(\delta_R\sin k+\frac{J_{\perp R}}{2}\Big)(1-\mathrm{sign}(E_{-+}))dk \tag{4.79}$$

(2) Staggered pattern with columnar field (SC-ladder):

$$m_{z,a} = \frac{h_{aR}}{2\pi}\int_0^{\pi/2}\Big[\Big(1+\frac{J_{\perp R}}{2R}\Big)\frac{(1-\mathrm{sign}(E_{-+}))}{\xi_+}+\Big(1-\frac{J_{\perp R}}{2R}\Big)\frac{(1-\mathrm{sign}(E_{--}))}{\xi_-}\Big]dk \tag{4.80}$$

$$\mathcal{K} = \frac{t_R}{4\pi}\int_0^{\pi/2}\cos^2 k\Big[\frac{1}{\xi_+}(1-\mathrm{sign}(E_{-+}))+\frac{1}{\xi_-}(1-\mathrm{sign}(E_{--}))\Big]dk \tag{4.81}$$

$$\delta\eta = \frac{\delta_R}{4\pi}\int_0^{\pi/2}\sin^2 k\Big[\frac{1}{\xi_+}\Big(1+\frac{J_{\perp R}}{2R}\Big)(1-\mathrm{sign}(E_{-+}))$$
$$\frac{1}{\xi_-}\Big(1-\frac{J_{\perp R}}{2R}\Big)(1-\mathrm{sign}(E_{--}))\Big]dk \tag{4.82}$$

$$t_\perp = \frac{1}{4\pi}\int_0^{\pi/2}\Big[\Big(R+\frac{J_{\perp R}}{2}\Big)\frac{(1-\mathrm{sign}(E_{-+}))}{\xi_+}-\Big(R-\frac{J_{\perp R}}{2}\Big)\frac{(1-\mathrm{sign}(E_{--}))}{\xi_-}\Big]dk \tag{4.83}$$

where we have used

$$R = \sqrt{h_{aR}^2+\delta_R^2\sin^2 k} \tag{4.84}$$

(3) Columnar pattern with columnar field (CC-ladder):

$$m_{z,a} = \frac{h_{aR}}{2\pi}\int_0^{\pi/2}\Big\{\Big(1+\frac{J_{\perp R}^2}{4R}\Big)\frac{1-\mathrm{sign}E_{-+}}{\xi_+}+\Big(1-\frac{J_{\perp R}^2}{4R}\Big)\frac{1-\mathrm{sign}E_{--}}{\xi_+}\Big\}dk \tag{4.85}$$

$$\mathcal{K} = \frac{1}{4\pi(1+\upsilon^2)}\int_0^{\pi/2}\Big[\Big\{t_R(\cos^2 k+\upsilon^2\sin^2 k)+\upsilon^2\frac{t_R}{R}\Big(\delta_R^2+\frac{J_{\perp R}^2}{4}\sin^2 k\Big)\Big\}$$
$$\times\frac{(1-\mathrm{sign}E_{-+})}{\xi_+}+\Big\{t_R(\cos^2 k+\upsilon^2\sin^2 k) \tag{4.86}$$
$$-\upsilon^2\frac{t_R}{R}\Big(\delta_R^2+\frac{J_{\perp R}^2}{4}\sin^2 k\Big)\Big\}\frac{(1-\mathrm{sign}E_{--})}{\xi_-}\Big]dk \tag{4.87}$$

$$\delta\eta = \frac{1}{4\pi(1+\upsilon^2)}\int_0^{\pi/2}\Big[\Big\{\delta_R(\sin^2 k+\upsilon^2\cos^2 k)+\upsilon^2\frac{\delta_R}{R}\Big(t_R^2+\frac{J_{\perp R}^2}{4}\cos^2 k\Big)\Big\}$$
$$\times\frac{(1-\mathrm{sign}E_{-+})}{\xi_+}+\Big\{\delta_R(\sin^2 k+\upsilon^2\cos^2 k)$$
$$-\upsilon^2\frac{\delta_R}{R}\Big(t_R^2+\frac{J_{\perp R}^2}{4}\cos^2 k\Big)\Big\}\frac{(1-\mathrm{sign}E_{--})}{\xi_-}\Big]dk \tag{4.88}$$

$$t_\perp = \frac{J_{\perp R}}{8\pi}\int_0^{\pi/2}\Big[\Big\{1+\frac{1}{R}\Big(h_{aR}^2+\upsilon^2(t_R^2\sin^2 k+\delta_R^2\cos^2 k)\Big)\Big\}\frac{(1-\mathrm{sign}E_{-+})}{\xi_+}$$
$$\Big\{1-\frac{1}{R}\Big(h_{aR}^2+\upsilon^2(t_R^2\sin^2 k+\delta_R^2\cos^2 k)\Big)\Big\}\frac{(1-\mathrm{sign}E_{--})}{\xi_+}\Big]dk \tag{4.89}$$

where we have used

$$R = \sqrt{\frac{1}{4}h_{aR}^2J_{\perp R}^2+\upsilon^2\Big\{t_R^2\delta_R^2+\frac{1}{4}J_{\perp R}^2(t_R^2\sin^2 k+\delta_R^2\cos^2 k)\Big\}} \tag{4.90}$$

(4) Rung dimerization pattern with columnar field (RC-ladder):

$$m_{z,a} = \frac{1}{2\pi}\int_0^{\pi/2}\Big[\Big(h_{aR}+\frac{J_\perp}{2}t_{\perp R}\Big)\frac{(1-\mathrm{sign}(E_{-+}))}{\xi_+}$$
$$+\Big(h_{aR}-\frac{J_\perp}{2}t_{\perp R}\Big)\frac{(1-\mathrm{sign}(E_{--}))}{\xi_-}\Big]dk \tag{4.91}$$

$$\mathcal{K} = \frac{t_R}{4\pi}\int_0^{\pi/2} \cos^2 k\Big[\frac{(1-\text{sign}(E_{-+}))}{\xi_+} + \frac{(1-\text{sign}(E_{--}))}{\xi_-}\Big]dk \tag{4.92}$$

$$t_\perp = \frac{1}{2\pi}\int_0^{\pi/2} \Big[\Big(h_{aR} + \frac{J_\perp}{2}t_{\perp R}\Big)\frac{(1-\text{sign}(E_{-+}))}{\xi_+}$$

$$-\Big(h_{aR} - \frac{J_\perp}{2}t_{\perp R}\Big)\frac{(1-\text{sign}(E_{--}))}{\xi_-}\Big]dk \tag{4.93}$$

$$\delta_\perp\eta_\perp = \frac{1}{4\pi}\int_0^{\pi/2}\Big[\text{sign}(E_{-+}) - \text{sign}(E_{--})\Big]dk. \tag{4.94}$$

From the numerical solutions of the above mean-field equations (4.76)-(4.94) of various

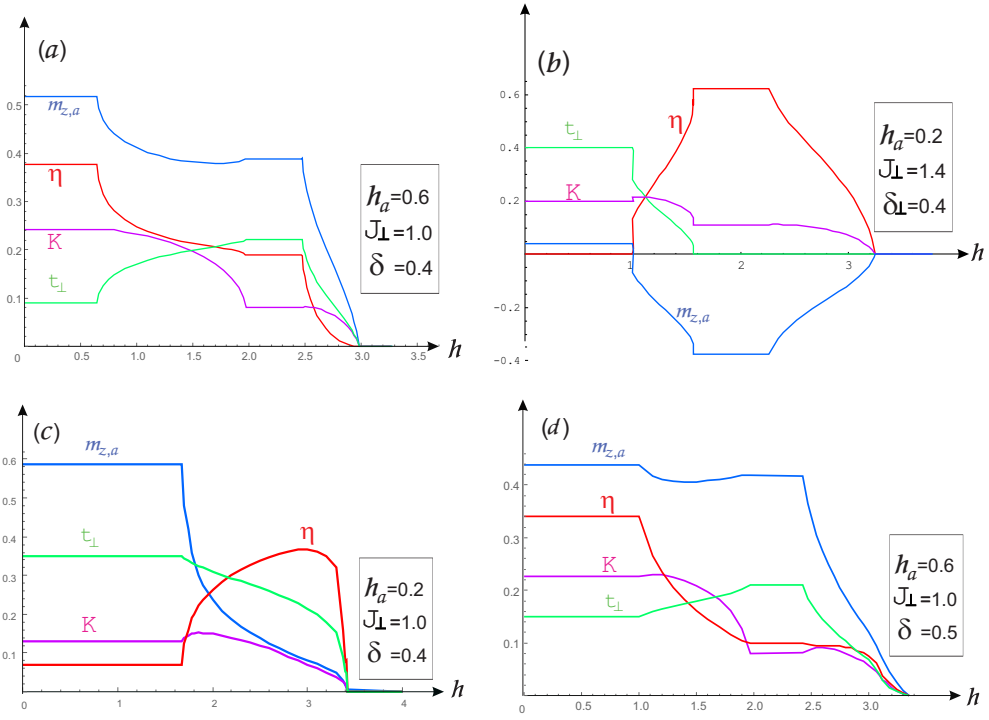

Figure 4.17: Representative behavior of mean-field parameters (4.76)-(4.94) calculated for given parameters in the (a) SC-ladder, (b) RC-ladder, (c) SS-ladder, and (d) CC-ladder.

dimerization patterns and evaluation of the renormalized couplings, we find that the renormalized and bare values differ by the factor of unity. It is important to distinguish between those four sets of couplings for making comparison i.e., phase boundaries, gap

values, etc, with numerical simulations. However, to study the qualitative physical properties of the phases, and the phase transition between them, it is quite convenient to present results directly in terms of the renormalized parameters, as it is mostly done in this thesis. The sets of the mean-field parameters of various models are presented with respect to the external magnetic field h, are presented in Fig. 4.17. In the limit $h = h_a = 0$ these above equations agree with those we use for the dimerized two-leg ladder in chapter. 5.

To summarize

In this chapter, the two-leg spin-1/2 ladders with two fields and three dimerization patterns are analyzed at zero temperature. After the fermionization of the spin Hamiltonian by using JW transformation, the spin ladder maps onto the ladder of interacting spinless fermions. The latter are treated within the Hartee-Fock mean-field approximation, which allows us to obtain effective quadratic Hamiltonians. Their renormalized parameters are related to the bare coupling as defined as the mean-field equations. In zero fields $h = h_a = 0$, the effective mean-field Hamiltonian recovers MF Hamiltonian obtained in [35]. The mean-field renormalized parameters are numerically calculated from the sets of self-consistent equations found from minimization of the free energy.

The ground-state phase diagram and the critical fields follow straightforwardly from the solution of zeros of spectra of the effective fermionic Hamiltonian in the parametric space for each of the four dimerization patterns: SC, SS, CC, RC. The SC, CC, and RC ladders have rich phase diagrams, and they consist of four critical fields with five distinct phases: 0-plateau gapped phase, I-LL gapless phase, mid-plateau gapped phase, II-LL gapless phase, and saturated gapped phase. In case of SS ladder, the ground-state phase diagram has only three phases with two critical fields and no mid-plateau gapped phase occurs.

By using the single particle dispersion relation, eigenvalues of the effective Hamiltonian, the quantum phases and critical fields were studied. The field-induced uniform magnetization m_z is calculated for each value of the external field h with the renormalized couplings determined self-consistently from the numerical solutions of mean-field equations given in section 4.4. The quantum phases of the four cases (SC, SS, CC, RC) are quite distinct and can be classified by hte plateaus of magnetization in the external field. As expected from the requirements of the plateau theorem (4.1), three magnetization plateaus m_z=0; $\frac{1}{2}$; 1 were found in SC, CC, and RC ladders, while the SS-ladder demonstrates only two magnetization plateaus m_z=0,1. To take into account the contribution of the magnetic field, we extended the requirement of the flux theorem [149] and introduced the flux correction term υ. In most of the cases this correction leads to numerical changes only, while for CC-ladder it is indispensable to reproduce the qualitatively correct results which agree with the plateau theorem.

The columnar field h_a brings new qualitative physical results in the staggered ladder. The existence of the mid-plateau state reported for the first time, is an indication of appearance of a new spin gapped phase in this type of model. In CC and RC ladders the columnar field h_a only modifies the phase boundaries of the phase diagram. In the RC ladder two new quantum phase transitions are predicted for mid-plateau and zero-plateau gapped phases.

Chapter 5

Anisotropic-Dimerized Two-Leg Ladder

In this chapter, we study the quantum phase transition (QPTs), and ground-state properties of a more general spin-1/2 two-leg ladder than discussed in chapter 4. We consider anisotropic dimerized ladder ($\gamma \neq 0$, $\delta \neq 0$), while we turn off the uniform and staggered magnetic field $h = h_a = 0$. As we show in this chapter, in these ladder models the quantum phase transitions occur for both types of dimerization patterns: staggered and columnar. These spin ladders are mapped onto spinless fermionic ladders by a judiciously choosen JW transformation along with HF approximation, which are equivalent to the Kitaev-Majorana fermionic ladders.

To make the study of the quantum phase transitions and the phase diagram more effective, we relabel the ladder fermionic operators of effective mean-field Hamiltonian onto chain operators along the snake-path. The local (Landau) orders and the non-local brane order parameters (BOPs) are obtained from two sectors of dual Hamil-

tonians, which are decoupled by using the spin duality-transformations of the effective Hamiltonian. All local and BOPs are found analytically for the ladder with staggered dimerization, while the columnar ladder needs to be treated numerically in dealing with the Toeplitz determinants.

In order to analyse the qualitative picture of physical properties of phases, transition between them, local and non-local orders, it is convenient to present analytical results directly in terms of renormalized couplings. Those renormalized parameters at each point in the γ axis are determined self-consistently by calculating the mean-field parameters of mean-field equations.

5.1 The model, mean-field, and single-particle Hamiltonian

In order to analyse various aspects of the conventional Landau and topological order, we propose a modulated dimerized spin-1/2 two-leg ladder. The spin Hamiltonian of anisotropic two-leg ladder is

$$H = \sum_{\alpha=1}^{2}\sum_{n=1}^{N}\Big\{J_\alpha(n)\mathbf{S}_\alpha(n)\cdot\mathbf{S}_\alpha(n+1) + J\gamma\Big[S^x_\alpha(n)S^x_\alpha(n+1) - S^y_\alpha(n)S^y_\alpha(n+1)\Big]\Big\} + J_\perp\sum_{n=1}^{N}\mathbf{S}_\alpha(n)\cdot\mathbf{S}_{\alpha+1}(n). \tag{5.1}$$

The intrinsic dimerization and anisotropy are assumed along the chains only, with the rung coupling $J_\perp$ taken as a constant. All the spin exchange couplings are antiferromagnetic. The two possible dimerization patterns shown in Fig. 4.1a and 4.1b are defined in Eqs. (4.3a) and (4.3b).

As explained in chapter 4, the spin ladder (5.1) will be treated within the HF

approximation along with the JW transformation. Relegating the technical details to section 5.5, the spin model is reduced to the quadratic effective fermionic Hamiltonian

$$H_{MF} = \frac{1}{2}\sum_{n,\alpha}(-1)^{n+\alpha-1}\Big(J_{\alpha R}(n)c^{\dagger}_{\alpha}(n)c_{\alpha}(n+1) + \Gamma_{R}(n)c^{\dagger}_{\alpha}(n)c^{\dagger}_{\alpha}(n+1) + h.c.\Big)$$

$$+\frac{1}{2}\sum_{n} J_{\perp R}(n)\Big(c^{\dagger}_{1}(n)c_{2}(n) + h.c.\Big) + 2NC. \tag{5.2}$$

We have introduced the renormalized couplings (4.7), (4.8), and

$$J_{\perp R} = J_{\perp}(1 + 2t_{\perp}), \tag{5.3}$$

along with the renormalized model's parameters (4.13)- (4.16). The constant term is

$$C = \mathcal{K}^2 - P^2 + \delta^2(\eta^2 - \eta_p^2) + 2\delta^2(\mathcal{K}\eta + P\eta_p) + \frac{1}{2}J_{\perp}t_{\perp}^2 \tag{5.4}$$

The definitions and the self-consistent equations for the mean-field parameters entering above relations are given in section 5.5. There, we also present formulas and numerical results for the mean-field parameters and renormalized couplings, and their relations to the bare parameters of the microscopic Hamiltonian. In the following, we will be working with the effective Hamiltonian (5.2) and we use notations, canonical transformations, and Fourier transform as done in chapter 4. Thus, we rewrite the Hamiltonian (5.2):

$$H = 2NC + \frac{1}{2}\sum_{k}\Psi^{\dagger}_{k}\mathcal{H}(k)\Psi_{k}, \tag{5.5}$$

where even and odd sectors of fermions are unified in the spinor

$$\Psi^{\dagger}_{k} = \Big(c^{\dagger}_{1,e}(k), c^{\dagger}_{1,o}(k), c^{\dagger}_{2,e}(k), c^{\dagger}_{2,o}(k), c_{1,e}(-k), c_{1,o}(-k), c_{2,e}(-k), c_{2,o}(-k)\Big), \tag{5.6}$$

with the wave numbers restricted to the reduced Brillouin zone BZ $k \in [-\pi/2, \pi/2]$ and we set the lattice spacing $a = 1$. The 8×8 Hamiltonian matrix $\mathcal{H}(k)$ reads

$$\mathcal{H}(k) = \begin{pmatrix} \hat{\mathbb{A}} & \hat{\mathbb{B}} \\ \hat{\mathbb{B}}^\dagger & -\hat{\mathbb{A}} \end{pmatrix}. \tag{5.7}$$

The explicit form of the 4×4 matrix $\hat{\mathbb{A}}$ depends on the dimerization pattern. For the staggered case

$$\hat{\mathbb{A}}_s = \begin{pmatrix} \hat{U}^T & \frac{1}{2} J_\perp \mathbb{I} \\ \frac{1}{2} J_\perp \mathbb{I} & -\hat{U} \end{pmatrix}, \tag{5.8}$$

where

$$\hat{U} = \begin{pmatrix} 0 & t \cos k + i\delta \sin k \\ t \cos k - i\delta \sin k & 0 \end{pmatrix}. \tag{5.9}$$

For the columnar pattern

$$\hat{\mathbb{A}}_c = \begin{pmatrix} \hat{U} & \frac{1}{2} J_\perp \mathbb{I} \\ \frac{1}{2} J_\perp \mathbb{I} & -\hat{U} \end{pmatrix}. \tag{5.10}$$

The 4×4 matrix $\hat{\mathbb{B}}$ is the same for both dimerization patterns and it reads

$$\hat{\mathbb{B}} = \begin{pmatrix} \hat{V} & 0 \\ 0 & -\hat{V}^T \end{pmatrix}, \tag{5.11}$$

where

$$\hat{V} = \begin{pmatrix} 0 & \gamma_a \cos k - i\gamma \sin k \\ -\gamma_a \cos k - i\gamma \sin k & 0 \end{pmatrix}. \tag{5.12}$$

The staggered anisotropy γ_a is absent in the bare Hamiltonian, but it could be induced by the mean-field equations. The actual values found from the mean-field equations are very small in the interesting range of the parameters, so γ_a will be discarded in the final results.

5.2 Spectra, phase diagram, and dual models

5.2.1 Staggered ladder

The 8×8 Hamiltonian matrix (5.7) (see Eqs. (5.8) and (5.11)) has eight eigenvalues $\pm E_{\pm\pm}(k)$, where

$$E_{\pm\pm}(k) = \sqrt{(\gamma_a \pm t)^2 \cos^2 k + \left((\gamma \pm \delta)\sin k \pm \frac{J_\perp}{2}\right)^2} \,. \tag{5.13}$$

From Eq. (5.13), we infer that the model is gapped in general, however the gap

$$\Delta = \left|\gamma \pm \delta \pm \frac{J_\perp}{2}\right| \tag{5.14}$$

at the edge of Brillouin zone $k = \pi/2$, vanishes on the lines of quantum critical transitions shown in Fig. 5.1:

$$\gamma = \pm\left|\delta \pm \frac{J_\perp}{2}\right| \,, \tag{5.15}$$

when three relevant perturbations $\delta, \gamma, J_\perp$ cancel, rendering the model gapless. The phase diagram of the isotropic ($\gamma = 0$) dimerized ladder and quantum phase transitions, accompanied by non-local order parameters in this model, were actively studied in the literature [19, 34, 35, 47, 48, 51, 53, 54, 99, 150]. The anisotropy ($\gamma \neq 0$) renders model's phase diagram richer: phases with non-local (brane) orders are found along with conventional antiferromagnetic phases. To the best of our knowledge, these results were not reported before.

To understand the nature of different phases of the phase diagram in Fig. 5.1, it is convenient to relabel the ladder fermionic operators of the effective mean-field

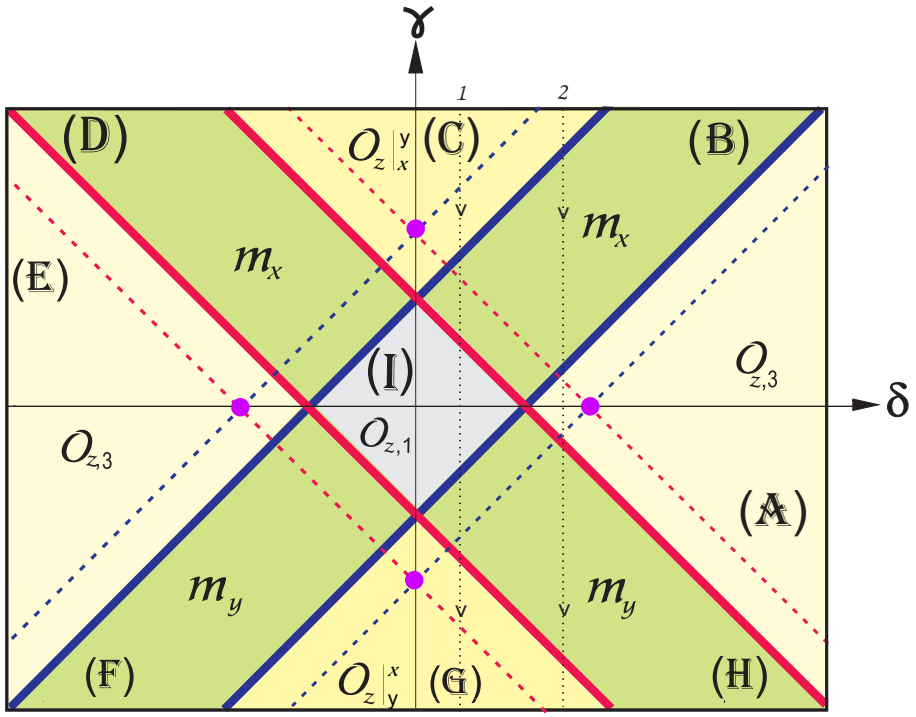

Figure 5.1: Phase diagram of the anisotropic staggered two-leg ladder. Non-vanishing brane and local order parameters are shown in nine regions from A to I of the (δ, γ) parametric plane. The voilet/red lines $\gamma = \pm(\delta \pm \frac{J_\perp}{2J})$ are the lines of quantum phase transitions (gaplessness)

.

Hamiltonian (5.2) according to the snake-like path shown in Fig. 4.2. This yields

$$H_{MF} = \frac{1}{2}\sum_{l=1}^{N}\Big\{ -(t-\delta)c^\dagger_{2l-1}c_{2l+2} + (t+\delta)c^\dagger_{2l}c_{2l+1}$$

$$+\gamma(-c^\dagger_{2l-1}c^\dagger_{2l+2} + c^\dagger_{2l}c^\dagger_{2l+1}) + J_\perp c^\dagger_{2l-1}c_{2l}\Big\} + h.c. \tag{5.16}$$

In terms of the Majorana operators [37, 151],

$$2c^\dagger_{2n} = a_{2n} + ib_{2n-1} \tag{5.17}$$

Hamiltonian (5.16) maps onto a sum of two decoupled quadratic Majorana Hamiltoni-

ans (Kitaev-Majorana chains) defined on the even and odd sites of the snake-like chain shown in Fig. 4.2:

$$H_{MF} = H_o + H_e \tag{5.18}$$

where

$$H_o = \frac{i}{4}\sum_{l=1}^{N}\Big\{-(t-\gamma-\delta)b_{2l+1}a_{2l-1} + (t+\gamma+\delta)b_{2l-1}a_{2l+1} + J_\perp b_{2l-1}a_{2l-1}\Big\}. \tag{5.19}$$

$$H_e = \frac{i}{4}\sum_{l=1}^{N}\Big\{-(t+\gamma-\delta)b_{2l-2}a_{2l+2} + (t-\gamma+\delta)b_{2l}a_{2l} + J_\perp b_{2l-2}a_{2l}\Big\}. \tag{5.20}$$

To advance our analysis, we make an inverse JW transformation of the above Hamiltonians from the Majorana operators to new dual spins represented by the Pauli matrices $\tilde{\tau}$. Using the path of Fig. 4.2, to relabel the original ladder spins σ, the sequence of the transformations from the original spins to Majoranas and then to dual spins reads

$$\sigma_n^x\sigma_{n+1}^x = ib_{n-1}a_{n+1} = \tilde{\tau}_{n-1}^x\tilde{\tau}_{n+1}^x \tag{5.21}$$

$$\sigma_n^y\sigma_{n+1}^y = ib_n a_n = \tilde{\tau}_n^z. \tag{5.22}$$

The dual spins $\tilde{\tau}$ obey the standard algebra of the Pauli operators, and they reside on the sites of the dual lattice, which can be placed between the sites of the original lattice. Then the odd and even Hamiltonians (5.19) and (5.20) become

$$H_o = \frac{1}{4}\sum_{l=1}^{N}\Big\{(t+\gamma+\delta)\tilde{\tau}_{2l-1}^x\tilde{\tau}_{2l+1}^x - (t-\gamma-\delta)\tilde{\tau}_{2l-1}^y\tilde{\tau}_{2l+1}^y + J_\perp\tilde{\tau}_{2l-1}^z\Big\} \tag{5.23}$$

$$H_e = \frac{1}{4}\sum_{l=1}^{N}\Big\{(t+\gamma-\delta)\tilde{\tau}_{2l-2}^x\tilde{\tau}_{2l}^z\tilde{\tau}_{2l+2}^x + J_\perp\tilde{\tau}_{2l-2}^x\tilde{\tau}_{2l}^x + (t-\gamma+\delta)\tilde{\tau}_{2l}^z\Big\}. \tag{5.24}$$

Making use of the canonical transformation

$$\tau^x_{2l-1} = \tilde{\tau}^x_{2l-1}, \tag{5.25a}$$

$$\tau^y_{2l-1} = (-1)^l \tilde{\tau}^y_{2l-1}, \tag{5.25b}$$

$$\tau^z_{2l-1} = (-1)^l \tilde{\tau}^z_{2l-1}, \tag{5.25c}$$

we bring the odd sector of the effective Hamiltonian to the form of the XY chain in a staggered transverse field:

$$H_o = \frac{1}{4}\sum_{l=1}^{N} \big\{(t+\gamma+\delta)\tau^x_{2l-1}\tau^x_{2l+1} + (t-\gamma-\delta)\tau^y_{2l-1}\tau^y_{2l+1} + (-1)^l J_\perp \tau^z_{2l-1}\big\}. \tag{5.26}$$

To simplify the even sector of the Hamiltonian, we follow the same steps as above, and then perform an additional dual transformation to $\tilde{\mu}$-spins defined as:

$$\tilde{\tau}^x_{2l-2}\tilde{\tau}^x_{2l} = \tilde{\mu}^z_{2l-2} \tag{5.27a}$$

$$\tilde{\tau}^z_{2l} = \tilde{\mu}^y_{2l-2}\tilde{\mu}^y_{2l}, \tag{5.27b}$$

followed by the canonical transformation analogous to (5.25a)-(5.25c). As a result, we obtain the even Hamiltonian in a convenient form of the XY chain:

$$H_e = \frac{1}{4}\sum_{l=1}^{N} \big\{(t+\gamma-\delta)\mu^x_{2l-2}\mu^x_{2l} + (t-\gamma+\delta)\mu^y_{2l-2}\mu^y_{2l} + (-1)^l J_\perp \mu^z_{2l-2}\big\}. \tag{5.28}$$

5.2.2 Columnar ladder

We diagonalize the 8×8 Hamiltonian matrix (5.7), (5.10), (5.11)) and find four two-fold degenerate eigenvalues $\pm E_{\pm}(k)$, where

$$E_{\pm}(k) = \sqrt{(\gamma_a \pm t)^2 \cos^2 k + \left(\sqrt{\delta^2 \sin^2 k + \frac{1}{4}J_{\perp}^2} \pm \gamma \sin k\right)^2}. \tag{5.29}$$

The spectrum (5.29) has the gap

$$\Delta = \left|\gamma \pm \sqrt{\delta^2 + \frac{1}{4}J_{\perp}^2}\right| \tag{5.30}$$

at the edge of the Brillouin zone $k = \pi/2$, which vanishes when

$$\gamma^2 = \delta^2 + \frac{1}{4}J_{\perp}^2. \tag{5.31}$$

These curves of quantum criticality (phase boundaries) are plotted in Fig. 5.2. Anisotropy ($\gamma \neq 0$) brings some new physics contrary to the "plain vanilla" case of the isotropic ($\gamma = 0$) columnar-dimerized ladder, which is always gapped and locked in the same phase [34, 35, 53].

Using relabelling according to the path in Fig. 4.2, and transformations explained in detail in the previous subsection, the effective mean-field Hamiltonian (5.2) for the columnar pattern is mapped onto a sum (5.18) of two decoupled even and odd quadratic Majorana Hamiltonians (Kitaev chains) with

$$H_o = \frac{1}{4}\sum_{l=1}^{N}\left\{(t-(-1)^l\delta-\gamma)b_{2l+1}a_{2l-1} + (t-(-1)^l\delta+\gamma)b_{2l-1}a_{2l+1} + J_{\perp}b_{2l-1}a_{2l-1}\right\} \tag{5.32}$$

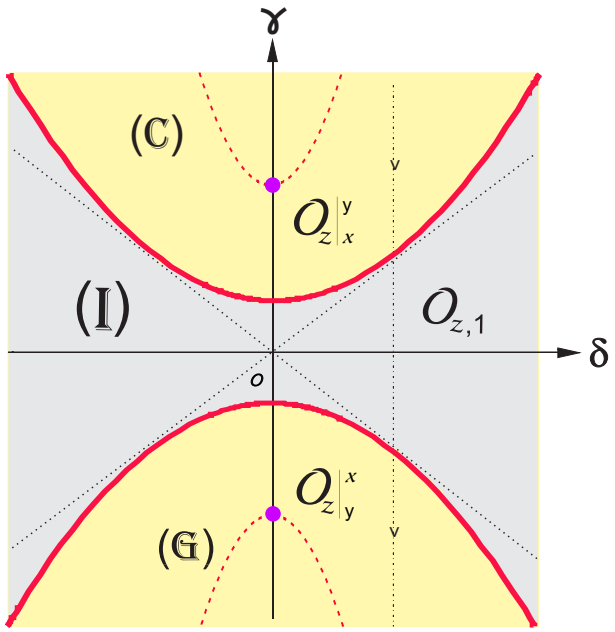

Figure 5.2: Phase diagram of the anisotropic columnar two-leg ladder. Non-vanishing brane and local order parameters, topological winding numbers are shown in three sectors C, G, and I on the (δ, γ) parametric plane. The bold red lines $\gamma = \pm\sqrt{\delta^2 + \frac{1}{4}J_\perp^2}$ are the lines of quantum phase transitions.

$$H_e = \frac{1}{4}\sum_{l=1}^{N}\left\{(t-(-1)^l\delta+\gamma)b_{2l-2}a_{2l+2} + (t-(-1)^l\delta-\gamma)b_{2l}a_{2l} + J_\perp b_{2l-2}a_{2l}\right\}. \quad (5.33)$$

In their turn, the Majorana Hamiltonians can be transformed to the dual spins, as defined above, yielding two equivalent decoupled dimerized XY chains in the staggered transverse fields:

$$H_o = \frac{1}{4}\sum_{l=1}^{N}\left\{(t-(-1)^l\delta+\gamma)\tau_{2l-1}^x\tau_{2l+1}^x + (t-(-1)^l\delta-\gamma)\tau_{2l-1}^y\tau_{2l+1}^y + (-1)^l J_\perp\tau_{2l-1}^z\right\} \quad (5.34)$$

$$H_e = \frac{1}{4}\sum_{l=1}^{N}\left\{(t-(-1)^l\delta+\gamma)\mu_{2l-2}^x\mu_{2l}^x + (t-(-1)^l\delta-\gamma)\mu_{2l-2}^y\mu_{2l}^y + (-1)^l J_\perp\mu_{2l-2}^z\right\}. \quad (5.35)$$

5.3 Phases and their order parameters

5.3.1 Staggered ladder

In the previous section, we worked out the mean-field approximation for the staggered ladder to map its Hamiltonian onto a sum of two decoupled dual XY chains (5.26) and (5.28). The phase boundaries (5.15) shown in Fig. 5.1 are deduced from the fermionic spectrum (5.13). Fig. 5.1 can now be more easily reproduced from superimposing on the (δ, γ) plane the phase diagrams of the even and odd XY chains (5.26,5.28). The information on phases and order parameters of such chains is given in Appendix B. The dual order parameters (expressed via τ and μ operators) for each of the nine regions (A-I) indicated in Fig. 5.1, are presented in Table 5.1. From Hamiltonians (5.26) and (5.28) we easily establish the symmetry of the staggered ladder:

$$\delta \;\; \mapsto \;\; -\delta : \text{ even} \leftrightarrow \text{odd}, \; \tau \leftrightarrow \mu \tag{5.36}$$

$$\gamma \;\; \mapsto \;\; -\gamma : \text{ even} \leftrightarrow \text{odd}, \; \tau \leftrightarrow \mu, \; x \leftrightarrow y \; . \tag{5.37}$$

After relabelling ladder's sites according to the path shown in Fig. 4.2, the brane operators introduced in the chapter 1 can be represented via string operators defined along a given path (say $\mathcal{P}$) as

$$O_i(n) \equiv \prod_{l \leq n, l \in \mathcal{P}} \sigma_l^i, \quad i = x, y, z. \tag{5.38}$$

We also introduce a short-hand notation for the product of two sting operators

$$D_{ii}(L, R) \equiv O_i(L-1) O_i(R) = \prod_{l=L}^{R} \sigma_l^i, \tag{5.39}$$

Table 5.1: Order parameters in terms of dual and original spins for nine regions of the phase diagram of the staggered ladder shown in Fig. 5.1.

Region	τ order (odd sector)	μ order (even sector)	σ order	N_w
A	$\langle\tau_x\rangle$	$\langle\mu_y\rangle$	$\mathcal{O}_{z,3}$	0
B	$\langle\tau_x\rangle$	$\mathcal{O}_{z,\mu}$	m_x	-1
C	$\langle\tau_x\rangle$	$\langle\mu_x\rangle$	$\mathcal{O}_z\vert_x^y$	-2
D	$\mathcal{O}_{z,\tau}$	$\langle\mu_x\rangle$	m_x	-1
E	$\langle\tau_y\rangle$	$\langle\mu_x\rangle$	$\mathcal{O}_{z,3}$	0
F	$\langle\tau_y\rangle$	$\mathcal{O}_{z,\mu}$	m_y	1
G	$\langle\tau_y\rangle$	$\langle\mu_y\rangle$	$\mathcal{O}_z\vert_y^x$	2
H	$\mathcal{O}_{z,\tau}$	$\langle\mu_y\rangle$	m_y	1
I	$\mathcal{O}_{z,\tau}$	$\mathcal{O}_{z,\mu}$	$\mathcal{O}_{z,1}$	0

such that its average yields the string-string correlation function

$$\mathfrak{D}_{ii}(L,R) \equiv \langle D_{ii}(L,R)\rangle \ . \tag{5.40}$$

Now we will find explicitly the order parameters in four regions (A,B,C,I) of the phase diagram in Fig. 5.1, while the rest of the phases can be done using the symmetry (5.36) and (5.37), without calculations.

Region (A): The dual magnetizations are found using (B.11):

$$\langle\tau_1^x\tau_{2N+1}^x\rangle \underset{N\to\infty}{\longmapsto} \langle\tau_x\rangle^2 = \frac{2\sqrt{t}}{t+\gamma+\delta}\Big[(\gamma+\delta)^2 - \frac{J_\perp^2}{4}\Big]^{1/4} \tag{5.41}$$

$$\langle\mu_0^y\mu_{2N}^y\rangle \underset{N\to\infty}{\longmapsto} \langle\mu_y\rangle^2 = \frac{2\sqrt{t}}{t+|\gamma-\delta|}\Big[(\gamma-\delta)^2 - \frac{J_\perp^2}{4}\Big]^{1/4} \tag{5.42}$$

Using the duality transformations (5.21,5.22,5.27a,5.27b) we can relate the two-point correlators of the dual spins to the string-string correlations functions of the spins σ

as:

$$\tau_1^x \tau_{2N+1}^x = D_{xx}(2, 2N+1), \tag{5.43}$$

$$\mu_0^y \mu_{2N}^y = D_{yy}(2, 2N+1), \tag{5.44}$$

resulting in the z-string order parameter in this region of the phase diagram

$$\begin{aligned} \langle \tau_1^x \tau_{2N+1}^x \mu_0^y \mu_{2N}^y \rangle &= (-1)^N \mathfrak{D}_{zz}(2, 2N+1) \longrightarrow \pm \mathcal{O}_{z,3}^2 \\ \mathcal{O}_{z,3} &= \langle \tau_x \rangle \langle \mu_y \rangle \ . \end{aligned} \tag{5.45}$$

Note that the above string correlator is equivalent to the odd-odd z-brane correlation function (1.43): $\mathfrak{D}_{zz} \leftrightarrows \langle \mathcal{B}_{o,\alpha}^z \mathcal{B}_{o,\beta}^z \rangle$, so $\mathcal{O}_{z,3}$ defined by Eqs. (5.45,5.41,5.42) is an exact value of the brane order parameter. It is plotted in Fig. 5.3(b) along the path (2) shown in Fig. 5.1.

Region (B): The dual order parameter of z-components of μ strings residing in the even sector, is easily obtained from Eq. (B.15):

$$\Big\langle \prod_{l=1}^{N} \mu_{2l}^z \Big\rangle \underset{N\to\infty}{\longmapsto} \mathcal{O}_{z,\mu}^2 = \Big[\frac{J_\perp^2/4 - (\gamma-\delta)^2}{J_\perp^2/4 - (\gamma-\delta)^2 + t^2} \Big]^{1/4} \tag{5.46}$$

The duality (5.21,5.22,5.27a,5.27b) yields

$$\prod_{l=0}^{N} \mu_{2l}^z = D_{xx}(1, 2N+2)) \ , \tag{5.47}$$

so the overlapping dual orders amount to a conventional antiferromagnetic order of the

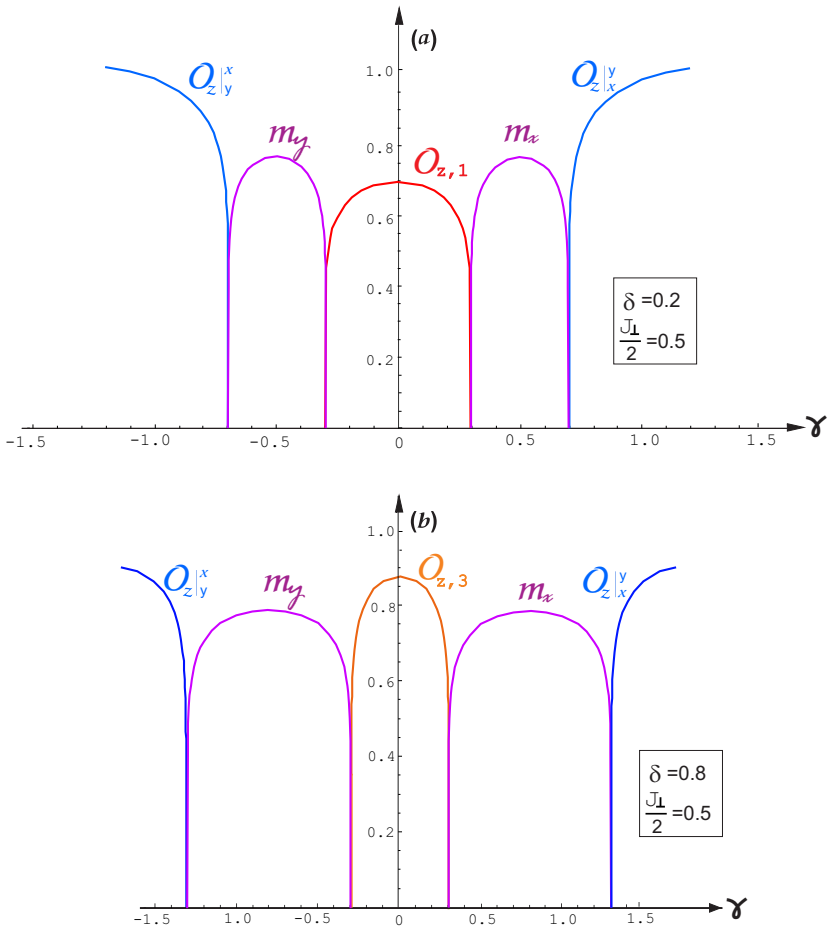

Figure 5.3: Order parameters of the staggered ladder along two paths indicated in Fig. 5.1. (a): $\delta = 0.2$ (path 1); (b): $\delta = 0.8$ (path 2); $t = 1$ in both cases

.

original spins σ in this phase:

$$\langle \tau_1^x \tau_{2N+1}^x \prod_{l=0}^{N} \mu_{2l}^z \rangle = \langle \sigma_1^x \sigma_{2N+2}^x \rangle \longrightarrow \pm m_x^2 \ , \tag{5.48}$$

where the explicit formula for magnetization $m_x = \langle \tau_x \rangle \mathcal{O}_{z,\mu}$ is given by Eqs. (5.41,5.46).

Region (C): The dual magnetization is readily found in this case as:

$$\langle \mu_0^x \mu_{2N}^x \rangle \underset{N\to\infty}{\longmapsto} \langle \mu_x \rangle^2 = \frac{2\sqrt{t}}{t+\gamma-\delta}\big[(\gamma-\delta)^2 - \frac{J_\perp^2}{4}\big]^{1/4} \tag{5.49}$$

We use the duality transformations to find

$$\mu_0^x \mu_{2N}^x = \sigma_1^x \sigma_2^x D_{yy}(2, 2N+1)\sigma_{2N+1}^x \sigma_{2N+2}^x \ , \tag{5.50}$$

and then we define the order parameter of this phase from the limit of the overlapping dual correlators as

$$\begin{aligned} \langle \tau_1^x \tau_{2N+1}^x \mu_0^x \mu_{2N}^x \rangle &= (-1)^N \langle \sigma_1^x \sigma_2^y D_{zz}(3, 2N) \sigma_{2N+1}^y \sigma_{2N+2}^x \rangle \\ &\longrightarrow \pm \big(\mathcal{O}_z|_x^y\big)^2 \ , \\ \mathcal{O}_z|_x^y &= \langle \tau_x \rangle \langle \mu_x \rangle \ . \end{aligned} \tag{5.51}$$

Such quite tricky order parameter $\mathcal{O}_z|_x^y$ is obtained from the limit of the correlation function of two z-stings which both have σ^y and σ^x spins attached to their right ends. Those strings with attachments are the chain representations of the brane operators with edge attachments defined by (1.44). Curiously enough, such tricky order parameter is given by a simple analytical expression from Eqs. (5.41,5.49).

Region (I): We use Eq. (B.15) from appendix to calculate the dual τ^z-string order parameter:

$$\Big\langle \prod_{l=1}^{N} \tau_{2l-1}^z \Big\rangle \underset{N\to\infty}{\longmapsto} \mathcal{O}_{z,\tau}^2 = \Big[\frac{J_\perp^2/4 - (\gamma+\delta)^2}{J_\perp^2/4 - (\gamma+\delta)^2 + t^2}\Big]^{1/4} \tag{5.52}$$

and the duality transformations to get

$$\prod_{l=1}^{N+1} \tau^z_{2l-1} = D_{yy}(1, 2N+2) \ . \tag{5.53}$$

The order parameter for this phase is found then as

$$\begin{aligned} \left\langle \prod_{l=1}^{N+1} \tau^z_{2l-1} \mu^z_{2l-2} \right\rangle &= (-1)^{N+1} \mathfrak{D}_{zz}(1, 2N+2) \longrightarrow \pm \mathcal{O}^2_{z,1} \\ \mathcal{O}_{z,1} &= \mathcal{O}_{z,\tau} \mathcal{O}_{z,\mu} \ . \end{aligned} \tag{5.54}$$

Thus all order parameters for each phase of the phase diagram of the staggered ladder are found analytically as closed expressions in terms of the (*renormalized*) couplings of the model. To visualize the results of this subsection, the local and non-local (brane) order parameters are plotted in Fig. 5.3 (a,b) along two paths shown in Fig. 5.1. Note that in the limit $J \perp\!\!\!\rightarrow 0$ the antiferromagmetic phases shown in Fig. 5.1 vanish, although single chains are known to be antiferromagnetically orderd in the regions (C) and (G) [35]. This proves that the brane order parameters probe the long-range order in both directions: along the chains and along the rungs.

5.3.2 Columnar ladder

The effective Hamiltonian of the columnar ladder is mapped onto two equivalent dimerized XY chains in a staggered transverse field (5.34,5.35). Contrary to the previous case, the columnar ladder has identical spectra in the even and odd sectors, resulting in the two-fold degeneracy of the eigenvalues of the Hamiltonisan (5.29). As a consequence, the phase diagram of this case is simpler, since there are no regions in the parametric space where different orders in the even and odd sectors overlap, resulting in larger variety of phases in Fig. 5.1. The phase diagram of the staggered ladder

consists of only three phases of the chain (5.34) (or (5.35)), where the same even/odd order parameters coexist, see Fig. 5.2.

The region (I) of the phase diagram in Fig. 5.2 has its the counterpart on the phase diagram of the staggered ladder, discussed above in detail. The string order parameter of this phase is:

$$\mathcal{O}_{z,1} = \mathcal{O}_{z,\tau}\mathcal{O}_{z,\mu} = \mathcal{O}^2_{z,\tau} \tag{5.55}$$

The order in the phase (C) is the brane parameter with the edge spin attachments:

$$\mathcal{O}_z|^y_x = \langle\tau_x\rangle\langle\mu_x\rangle = \langle\tau_x\rangle^2 \ , \tag{5.56}$$

and for the phase (G) parameters are obtained from $x \leftrightarrows y$. The equivalent even and odd sectors of the dual Hamiltonian lead not only to the degeneracy of the spectrum, but also, as one can see from (5.55,5.56), to the change of the universality class of the lines continuous phase transitions in the columnar ladder (bold red lines in Fig. 5.2). In the effective free-fermionic approximation used in this paper, the order parameters of all phases of the staggered ladder have the critical index $\beta = 1/8$ (2D Ising universality class), while for the order parameters (5.55,5.56) of the columnar ladder $\beta = 1/4$.

For the dual chains (5.34,5.35) with dimerization no analytical results for the magnetization or the oscillating string order parameter are available. The parameters $\langle\tau_x\rangle$ and $\mathcal{O}_{z,\tau}$ are calculated numerically from the Toeplitz determinants, using the results for the generating functions and the Toeplitz matrices given in [37]. The order parameters of the columnar ladder calculated from the Toeplitz matrices of the size 140×140 are plotted in Fig. 5.4. The calculations are done along the path indicated in Fig. 5.2.

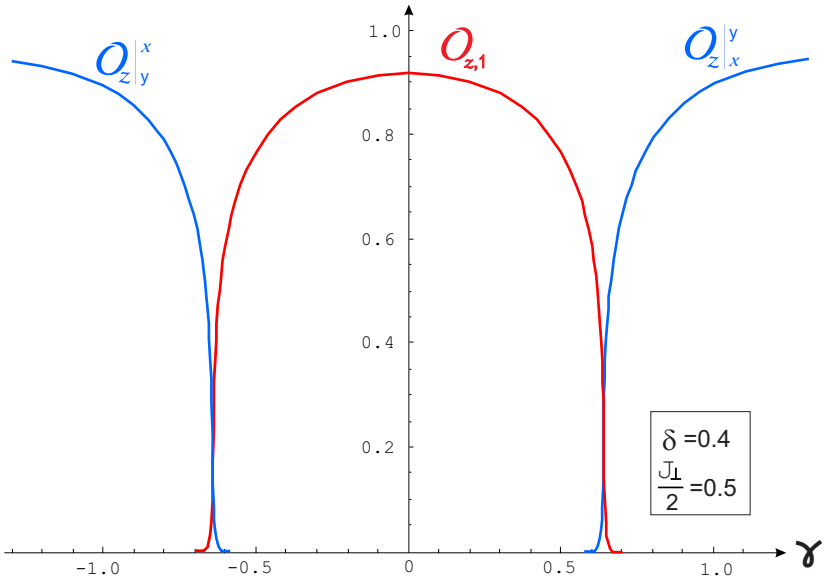

Figure 5.4: Brane order parameters in the columnar ladder along the path indicated in Fig. 5.2. The tails seen near the critical points are finite-size effects: the results are obtained numerically from 140×140 Toeplitz matrices.

.

5.4 Topological numbers

After mapping of the effective fermionic Hamiltonian of the staggered (columnar) ladder onto the pair of decoupled XY chains (5.26,5.28) and (5.34,5.35), respectively, the calculation of the winding numbers can be done using the earlier results for the XY chain in transverse field [37]. In particular, the four eigenvalues $E_{\pm\pm}(k)$ (5.13) of the 8×8 Hamiltonian matrix (5.7) of the staggered ladder, correspond to the two pairs of eigenvalues of the anisotropic even and odd XY chains with the anisotropy parameters

$$\gamma_{o/e} = \gamma \pm \delta \tag{5.57}$$

and the alternating transverse field $J_\perp/2$. The degenerate spectrum $\pm E_\pm(k)$ (5.29) of the 8×8 Hamiltonian matrix of the columnar ladder corresponds to the eigenvalues of

the two equal dimerized XY chain with the alternating field $J_\perp/2$.

The fermionic representation of the even/odd sector of the staggered Hamiltonian yields a 4×4 matrix analogous to (5.7) with 2×2 blocks:

$$\hat{A} \equiv \begin{pmatrix} t\cos k & J_\perp/2 \\ J_\perp/2 & -t\cos k \end{pmatrix} , \tag{5.58}$$

and

$$\hat{B}_\sharp \equiv \begin{pmatrix} -i\gamma_\sharp \sin k & 0 \\ 0 & i\gamma_\sharp \sin k \end{pmatrix} , \quad \sharp = e, o. \tag{5.59}$$

For the Hamiltonian of this type the winding number is defined as the following integral over the Brillouin zone [104, 152]:

$$N_{w,\sharp} = \frac{1}{2\pi i} \int_{-\pi/2}^{\pi/2} dk [\partial_k \ln \det \hat{D}_\sharp] , \tag{5.60}$$

where $\hat{D}_\sharp(k) \equiv \hat{A}(k) + \hat{B}_\sharp(k)$. To avoid ambiguities related to the definition of the phase of $\det \hat{D}_\sharp(k)$ at the ends of the Brillouin zone [37], one needs to check whether the path of $\det \hat{D}_\sharp(k)$ on the complex plane encloses the origin during the integration. The latter happens if $\det \hat{D}_\sharp(\pm\pi/2)$ and $\det \hat{D}_\sharp(0)$ have different signs. The winding number for the ladder is found as

$$N_w = N_{w,e} + N_{w,o} , \tag{5.61}$$

and its values for each phase are given in Table 5.1 for the staggered dimerization.

Another angle of analysis can be presented upon analytical continuation of the wave numbers on the complex plane: $e^{i2k} = z$. Then the winding number (5.60) becomes

the logarithmic residue of $\det\hat{D}_\sharp$:

$$N_{w,\sharp} = \oint_{|z|=1} \frac{dz}{2\pi i} \partial_z \ln \det \hat{D}_\sharp \ . \tag{5.62}$$

It accounts for the excess of the number of zeros over the number of poles (weighted with their degrees of multiplicity) of $\det\hat{D}_\sharp$ inside the unit circle on the complex plane [105]. The zeros of $\det\hat{D}$ are also zeros of the spectra $E_\pm$ of the XY chain, since $(E_+E_-)^2 = \det\hat{D}\hat{D}^\dagger$. Any change of winding number means that a root (roots) crossed the unit circle $|z| = 1$, which signals a quantum phase transition [106, 153]. Foe the Hamiltonians (5.26,5.28) we find

$$\det\hat{D}_\sharp(z) = -\frac{(1-\gamma_\sharp)^2}{4z}(z-z_+)(z-z_-) \ , \tag{5.63}$$

where $z_\pm$ are the roots of the quadratic equation

$$(1-\gamma_\sharp)^2 z^2 + 2(1-\gamma_\sharp^2 + J_\perp^2/2)z + (1+\gamma_\sharp)^2 = 0. \tag{5.64}$$

For the columnar ladder the contribution to the winding number (5.61) from the even and odd sectors (5.34,5.35) trivially doubles. The 2×2 matrices $\hat{A}$ and $\hat{B}$ are given in [37] with $h_a = J_\perp/2$. A calculation similar to the one above, yields the winding numbers for the three phases of the columnar ladder shown in Fig. 5.2, equal to their counterparts of the staggered ladder given in Table 5.1.

5.5 Mean-field theory

We fermionize the spin ladder Hamiltonian (5.1) using the JW transformation. There are different ways to introduce this transformation when we depart from a single-

chain problem to spin ladder (see, e.g., [23, 65, 83, 85]. We use the snake-like JW transformation path discussed in chapter 4 (see Fig. 4.2) and proved to be convenient to deal with the two-leg ladder. This transformation yields the following fermionic Hamiltonian:

$$H = \frac{1}{2}\sum_{n,\alpha}\Big\{e^{i\hat{\Phi}_\alpha(n)}\Big(J_\alpha(n)c^\dagger_\alpha(n)c_\alpha(n+1) + \frac{J\gamma}{2}c^\dagger_\alpha(n)c^\dagger_\alpha(n+1)\Big)$$

$$+2J_\alpha(n)\Big(\hat{n}_\alpha(n)-\frac{1}{2}\Big)\Big(\hat{n}_\alpha(n+1)-\frac{1}{2}\Big)\Big\} + \frac{1}{2}\sum_n\Big\{J_\perp(n)c^\dagger_1(n)c_2(n)$$

$$+2J_\perp(n)\Big(\hat{n}_1(n)-\frac{1}{2}\Big)\Big(\hat{n}_2(n)-\frac{1}{2}\Big)\Big\} + h.c. \tag{5.65}$$

The phase operators $\hat{\Phi}_\alpha(n)$ appearing in Eq. 5.65 are explicitly given in (1.13).

We treat the interacting terms in (5.65) via standard mean-field decouplings (1.22) and (1.23). The decoupled Hamiltonian reads

$$H_{MF} = 2NC + \frac{1}{2}\sum_{n,\alpha}\Big\{J_\alpha(n)\Big[e^{i\hat{\Phi}_\alpha(n)} + 2\langle c_\alpha(n)c^\dagger_\alpha(n+1)\rangle\Big]c^\dagger_\alpha(n)c_\alpha(n+1)$$

$$+J\gamma\Big[e^{i\hat{\Phi}_\alpha(n)} - 2\langle c_\alpha(n)c_\alpha(n+1)\rangle\Big]c^\dagger_\alpha(n)c^\dagger_\alpha(n+1)\Big\}$$

$$+\frac{1}{2}J_\perp\sum_n[1+2t_\perp]c^\dagger_1(n)c_2(n) + h.c. \tag{5.66}$$

According to the Lieb theorem [149] the ground state of a quadratic fermionic Hamiltonian on a bipartite lattice at half-filling is the π-flux phase. Imposing this requirement on the approximate Hamiltonian (5.66) amounts to the approximation $e^{i\hat{\Phi}_\alpha(n)} \approx$

$(-1)^{n+\alpha-1}$, thus

$$e^{i\hat{\Phi}_\alpha(n)} + 2\langle c_\alpha(n) c_\alpha^\dagger(n+1)\rangle = (-1)^{n+\alpha-1}(1+2t_\alpha(n)) \ , \tag{5.67}$$

$$e^{i\hat{\Phi}_\alpha(n)} - 2\langle c_\alpha(n) c_\alpha(n+1)\rangle = (-1)^{n+\alpha-1}(1-2P_\alpha(n)) \ , \tag{5.68}$$

where we used the mean-field averaged parameters (4.73), (4.74) and (4.75) for two dimerization patterns: staggered and columnar.

The renormalized couplings (4.13)-(4.17) are to be found from the set of self-consistent equations obtained from minimization of the free-energy. We present the equations for the case $\gamma_a = \gamma_{aR} = 0$.

The sets of the mean-field equations are different for two dimerization patterns.

(1) Staggered dimerization:

Minimization of the ground-state energy evaluated from the spectrum (5.13) yields the bond average

$$\mathcal{K} = \frac{t_R}{4\pi}\int_0^{\pi/2} dk \cos^2 k \Big\{ \frac{1}{E_{++}} + \frac{1}{E_{+-}} + \frac{1}{E_{-+}} + \frac{1}{E_{--}} \Big\} \tag{5.69}$$

and the dimerization susceptibility η

$$\delta\eta = \frac{1}{4\pi}\int_0^{\pi/2} dk \sin^2 k \Big\{ \delta_R \Big(\frac{1}{E_{++}} + \frac{1}{E_{+-}} + \frac{1}{E_{-+}} + \frac{1}{E_{--}} \Big) + \gamma_R \Big(\frac{1}{E_{++}} + \frac{1}{E_{+-}} - \frac{1}{E_{-+}} - \frac{1}{E_{--}} \Big)$$
$$+ \frac{J_{\perp R}}{2\sin k} \Big(\frac{1}{E_{++}} - \frac{1}{E_{+-}} - \frac{1}{E_{-+}} + \frac{1}{E_{--}} \Big) \Big\}. \tag{5.70}$$

The anomalous pairing amplitude is found as

$$P=\frac{1}{4\pi}\int_0^{\pi/2}dk\sin^2 k\Big\{\gamma_R\Big(\frac{1}{E_{++}}+\frac{1}{E_{+-}}+\frac{1}{E_{-+}}+\frac{1}{E_{--}}\Big)+\delta_R\Big(\frac{1}{E_{++}}+\frac{1}{E_{+-}}-\frac{1}{E_{-+}}-\frac{1}{E_{--}}\Big)$$
$$+\frac{J_{\perp R}}{2\sin k}\Big(\frac{1}{E_{++}}-\frac{1}{E_{+-}}+\frac{1}{E_{-+}}-\frac{1}{E_{--}}\Big)\Big\},\tag{5.71}$$

and the transverse bond parameter is:

$$t_\perp=\frac{1}{4\pi}\int_0^{\pi/2}dk\Big\{\frac{1}{2}J_{\perp R}\Big(\frac{1}{E_{++}}+\frac{1}{E_{+-}}+\frac{1}{E_{-+}}+\frac{1}{E_{--}}\Big)+\delta_R\sin k\Big(\frac{1}{E_{++}}-\frac{1}{E_{+-}}-\frac{1}{E_{-+}}+\frac{1}{E_{--}}\Big)$$
$$+\gamma_R\sin k\Big(\frac{1}{E_{++}}-\frac{1}{E_{+-}}+\frac{1}{E_{-+}}-\frac{1}{E_{--}}\Big)\Big\}.\tag{5.72}$$

(2) Columnar dimerization:

Minimization of the ground-state energy with the spectrum (5.29) yields the following set of the mean-field equations:

$$\mathcal{K}=\frac{t_R}{2\pi}\int_0^{\pi/2}dk\cos^2 k\Big\{\frac{1}{E_+}+\frac{1}{E_-}\Big\}\tag{5.73}$$

$$\delta\eta=\frac{\delta_R}{2\pi}\int_0^{\pi/2}dk\sin^2 k\Big\{\Big(\frac{1}{E_+}+\frac{1}{E_-}\Big)+\frac{\gamma_R\sin k}{R}\Big(\frac{1}{E_+}-\frac{1}{E_-}\Big)\Big\}\tag{5.74}$$

$$P=\frac{1}{2\pi}\int_0^{\pi/2}dk\sin^2 k\Big\{\gamma_R\Big(\frac{1}{E_+}+\frac{1}{E_-}\Big)+\frac{R}{\sin k}\Big(\frac{1}{E_+}-\frac{1}{E_-}\Big)\Big\}\tag{5.75}$$

$$t_\perp=\frac{J_{\perp R}}{4\pi}\int_0^{\pi/2}dk\Big\{\Big(\frac{1}{E_+}+\frac{1}{E_-}\Big)+\frac{\gamma_R\sin k}{R}\Big(\frac{1}{E_+}-\frac{1}{E_-}\Big)\Big\}.\tag{5.76}$$

where $R\equiv\sqrt{\delta_R^2\sin^2 k+\frac{1}{4}J_{\perp R}^2}$. In the limit $J_\perp=0$ the above equations agree with those we used for the XYZ chain [38].

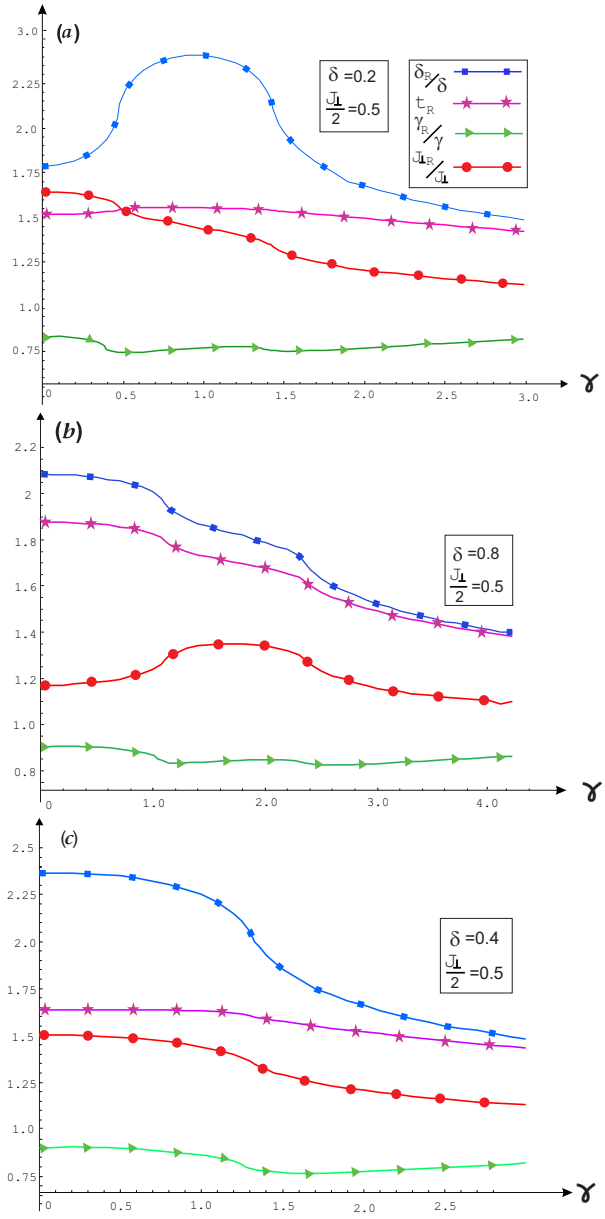

Figure 5.5: The ratios of the renormalized couplings with respect to their bare values calculated from the mean-field equations. The parameters are calculated along two paths of constant δ for the staggered ladder (a,b) and one path of constant δ for the columnar ladder (c). The paths resemble those shown in Figs. 5.1 and 5.2, but taken on the plane of bare parameters (δ, γ).

From numerical solution of the above mean-field equations and evaluation of the renormalized couplings (4.13)-(4.17), we find that the renormalized and the bare values differ by a factor of order of unity. It is important to distinguish these two sets of couplings for making quantitative comparisons of, e.g., phase boundaries, gap values, etc, with the numerical simulations. However to study the qualitative physical properties of the phases, transitions between them, the local and non-local order parameters these phases possess, it is convenient to present results directly in terms of the renormalized parameters, as it is done in this chapter. The ratios of the renormalized and bare parameters of the model calculated for several cases are presented in Fig. 5.5.

5.6 Isotropic two-leg ladder

In this section, we present the results of the isotropic two-leg ladder with intrinsic dimerization ($\gamma = 0, \delta \neq 0$). In this model, most of the analytical methods such as: two dimensional JW transformation, HF approximation, and spin duality transformation of previous section can be used to analyze the local and non-local (topological) phases of the phase diagram. The isotropic limit ($\gamma = 0$) of dimerized ladder has been actively studied analytically and numerically [19–21, 34, 47, 48, 50–56], so the results of this section in particular serve to show the proposed mean-field theory is consistent with available numerical results.

5.6.1 Model and mean-field Hamiltonian

We write the spin Hamiltonian

$$H = \sum_{\alpha=1}^{2} \sum_{n=1}^{N} J_\alpha(n) \mathbf{S}_\alpha(n) \cdot \mathbf{S}_\alpha(n+1) + J_\perp \sum_{n=1}^{N} \mathbf{S}_\alpha(n) \cdot \mathbf{S}_{\alpha+1}(n). \tag{5.77}$$

with two dimerization patterns (4.3a) and (4.3b) , where the dimerization only consider along the chains $\alpha = 1, 2$ [35].

Critical properties of dimerized ladders are known from analytical and numerical studies: [19, 34, 47, 48, 50, 51, 53, 54, 99] the staggered ladder undergo a continuous quantum phase transition and is gapless on the line of quantum criticality, while the columnar ladder is always gapped and does not correspond any transition. We also infer from [34, 35, 53] that the mean-field approximation for this model is quite adequate even quantitatively. So we apply this approach to map the spin ladder model onto a problem of effective quadratic fermionic Hamiltonian. The latter will be utilized to study analytically the critical properties of two dimerizations, calculation of SOPs and topological numbers, similarly what we have done before for exactly solvable chains and ladders.

We map the spin Hamiltonian (5.77) onto spinless fermions via JW transformation (4.5) taking along the snake-like path as shown in Fig. 4.2. The phase term appearing on the fermionic Hamiltonian is determined by the path of JW transformation and it is exactly same as (1.13). On the other hand, the interacting fermionic terms in the Hamiltonian are decouples by applying more generalized HF approximation [89]. We will approximately treat the phase as a good quantum number. This quantum validity of this approximation was confirmed in earlier related work [35, 53, 58, 83]. Then according to the Lieb theorem [149] the ground state of quadratic Hamiltonian is in the π-flux phase [147]. Thus the mean-field effective Hamiltonian reads

$$H_{MF} = 2NC + \frac{1}{2}\Big\{ \sum_{n,\alpha} (-1)^{n+\alpha-1} J_{\alpha R}(n) c^{\dagger}_{\alpha}(n) c_{\alpha}(n+1)$$

$$+ \sum_{n} J_{\perp R}(n) c^{\dagger}_{1}(n) c_{2}(n) \Big\} + h.c. \tag{5.78}$$

where we have used renormalized couplings (4.7) and (4.9) along with the renormalized model's parameters (4.13) and (4.14). The constant term is

$$C = \mathcal{K}^2 + \delta^2\eta(\eta + 2\mathcal{K}) + \frac{1}{2}J_\perp t_\perp^2 \tag{5.79}$$

The renormalization parameters t_R and δ_R are to be determined self-consistently from the minimization of the mean-field Hamiltonian (5.78). In fact those parameters were calculated in the previous section by determining the mean-field parameters at each points from the self-consistent equations. This mean-field Hamiltonian provides essentially the same results for the ground state quantities such as energies, eigenvalues, gaps, renormalized parameters and the phase diagram for the both staggered and columnar ladders [35] with some minor numerical differences. Thus, in the following these renormalized terms are treated as bare model parameters of the effective Hamiltonian (5.78).

5.6.2 Spectra and winding number

1. Staggered ladder

To further simplify the effective Hamiltonian (5.78) one can perform a canonical transformation mapping (4.30). Introducing instead of c_α two distinct fermions residing on the even/odd sites $c_{\alpha,e/o}$ and Fourier transforming, we rewrite the Hamiltonian as

$$H_{MF} = 2NC + \frac{1}{2}\sum_k \Psi_k^\dagger \mathcal{H}(k)\Psi_k \tag{5.80}$$

where even/odd sectors of fermions are unified in the spinor

$$\Psi_k^\dagger = (c_{1,e}^\dagger(k), c_{1,o}^\dagger(k), c_{2,e}^\dagger(k), c_{2,o}^\dagger(k)), \tag{5.81}$$

and 4×4 Hamiltonian matrix $\mathcal{H}(k)$ of the staggered phase

$$\mathcal{H}(k) = \begin{pmatrix} \hat{U}^T & \frac{1}{2}J_\perp \mathbb{I} \\ \frac{1}{2}J_\perp \mathbb{I} & -\hat{U} \end{pmatrix}, \tag{5.82}$$

with

$$\hat{U} = \begin{pmatrix} 0 & t\cos k + i\delta \sin k \\ t\cos k - i\delta \sin k & 0 \end{pmatrix}. \tag{5.83}$$

Here the wavenumbers restricts to the Brillouin zone $k \in [-\pi/2, \pi/2]$. This Hamiltonian (5.80) has four eigenvalues $\pm E_\pm(k)$ where

$$E_\pm(k) = \sqrt{t^2 \cos^2 k + \left(\delta \sin k \pm \frac{J_\perp}{2}\right)^2}. \tag{5.84}$$

The spectrum has the gap

$$\Delta = \left|\delta \pm \frac{J_\perp}{2}\right|. \tag{5.85}$$

Similar to the XY chain, two relevant perturbations cancel on the lines of quantum critical transition

$$\frac{J_\perp}{2} = \pm\delta, \tag{5.86}$$

where the staggered two-leg ladder becomes gapless. (A more refined mean-field treatment of this model's phase diagram and comparison to numerical results can be found in [53]. The present version of the mean field numerical results has very accurate phase diagram [51].) From comparison of the eigenvalues of the ladder's effective Hamiltonian (5.84) and those of the XY chain in the alternating transverse field (see Eq.(6) of Ref. [35]), we can infer the equivalence between the spectra of those models, and even match corresponding parameters: $\frac{1}{2}J_\perp \leftrightarrow h$, and $\delta \leftrightarrow \gamma$.

To calculate the topological winding number N_ω in different phases of the staggered

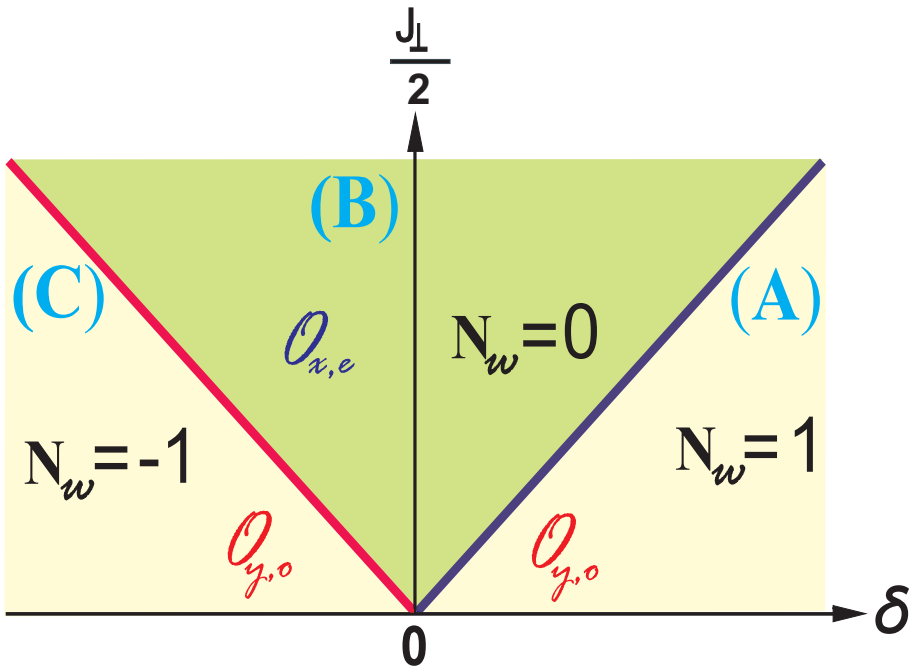

Figure 5.6: Phase diagram of the staggered two-leg ladder in the parametric plane $(J_\perp, \delta)$. The violet/red lines $J_\perp/2 = \pm\delta$ are the lines of quantum phase transitions (gaplessness) separating two phases (B) and (A,C) characterized by their distinct SOPs and winding numbers.

ladder we use a unitary transformation to bring the Hamiltonian matrix $\mathcal{H}(k)$ of Eq. (5.5) to the block diagonal form

$$\mathcal{H}(k) = \begin{pmatrix} \hat{\mathfrak{h}}_+(k) & 0 \\ 0 & \hat{\mathfrak{h}}_-(k) \end{pmatrix} \tag{5.87}$$

familiar from the context of topological insulators and superconductors [24, 27], where $\hat{\mathfrak{h}}_-(k) = \hat{\mathfrak{h}}_+^*(-k)$. Explicitly the operators $\hat{\mathfrak{h}}_\pm(k)$ are

$$\hat{\mathfrak{h}}_\pm(k) = t\cos k\sigma_1 - \Big(\delta \sin k \pm \frac{1}{2}J_\perp\Big)\sigma_2, \tag{5.88}$$

and their eigenvalues are given by Eq. (5.84). Using eigenvalues (5.84) to yield the

unit vector (2.91a) and (2.91b), we get from the definition (2.92)

$$N_{\pm} = \frac{1}{2\pi} \int_{-\pi/2}^{\pi/2} dk \frac{\delta \pm \kappa \sin k}{\cos^2 k + (\delta \sin k \pm \kappa)^2}, \tag{5.89}$$

where we denote

$$\kappa = \frac{J_{\perp}}{2}. \tag{5.90}$$

One can check that $N_+ = N_-$. The result for the winding number N_ω can be cast in a simple form

$$N_\omega = N_+ + N_- = \frac{1}{2}[\mathrm{sign}(\delta - \kappa) + \mathrm{sign}(\delta + \kappa)] \tag{5.91}$$

We have shown the winding numbers for each phase on the phase diagram of the staggered ladder in Fig. 5.6. (Recall that we analyze the ladder with antiferromagnetic couplings.) The complimentary order parameter N_ω changes by $\Delta N_\omega = \pm 1$ on the phase boundaries $\kappa = \pm\delta$. The sectors (A) and (C) correspond to the same topologically nontrivial phase.

2. Columnar Ladder

In the columnar ladder the explicit form of the 4×4 Hamiltonian matrix $\mathcal{H}(k)$ is

$$\mathcal{H}(k) = \begin{pmatrix} \hat{U} & \frac{1}{2} J_{\perp} \mathbb{I} \\ \frac{1}{2} J_{\perp} \mathbb{I} & -\hat{U} \end{pmatrix}, \tag{5.92}$$

and it has two fold degenerate eigenvalues $\pm E(k)$ where

$$E(k) = \sqrt{t^2 \cos^2 k + \delta^2 \sin^2 k + \frac{1}{4} J_{\perp}^2}. \tag{5.93}$$

Contrary to the staggered case, the columnar ladder is always gapped with the gap

$$\Delta = \sqrt{\delta^2 + \frac{1}{4}J_\perp^2}, \tag{5.94}$$

and no phase transition occurs on the whole plane (δ, κ). As in the case of staggered dimerization, from the Ref. [35] (i.e., see Eq. (6)) and Eq. (5.93) we can establish equivalence between the spectra of the effective Hamiltonian of the columnar ladder and the dimerized XY model in the alternating transverse field: $\frac{1}{2}J_\perp \leftrightarrow h$; $\delta \leftrightarrow \delta$.

The columnar phase is trivial not only in the sense that it is always gapped and noncritical, it is also trivial topologically, since no integer winding number can be assigned to this phase. Indeed, if we identify the opposite ends of the Brillouin zone, then the wavenumber k is defined in the space equivalent to the one-dimensional sphere $\mathcal{S}^1$. This is also the space spanned by the two-component unit vector (2.91a) and (2.91b) of the staggered phase. The nontrivial winding number for that phase corresponds to the homotopy group $\pi_1(\mathcal{S}^1) = \mathbb{Z}$. As one can see from (5.93) the analogous unit vector is three-components in the columnar phase, and it spans the space $\mathcal{S}^2$. The corresponding homotopy group is trivial $\pi_1(\mathcal{S}^2) = 0$ and no integer winding number exists, since any closed loop on the sphere $\mathcal{S}^2$ can be shrunk [154].

5.6.3 Brane order parameters

In order to analytically calculate the BOPs, we relabel the fermionic operator of effective Hamiltonian (5.78) along the snake path shown in the Fig. 4.2. In the following we find two types of BOPs, i.e., even/odd as definde in (1.39) and (1.40) (see Fig. 1.3 for detail). By using the relation of Majorana operators (5.17) and transformations (5.21) and (5.22) in the previous section, the effective mean-field Hamiltonian (5.78) for the staggered pattern is mapped onto a sum of two decoupled even and odd dual

Hamiltonians.

$$H = H_e + H_o$$

$$H_e = \frac{1}{4}\sum_{l=1}^{N}[J_\perp \tau_{2l-2}^x \tau_{2l}^x + (t-\delta)\tau_{2l-2}^x \tau_{2l}^z \tau_{2l+2}^x + (t+\delta)\tau_{2l}^Z] \tag{5.95}$$

$$H_o = \frac{1}{4}\sum_{l=1}^{N}[(t+\delta)\tau_{2l-1}^x \tau_{2l+1}^x - (t-\delta)\tau_{2l-1}^y \tau_{2l+1}^y + J_\perp \tau_{2l-1}^Z]. \tag{5.96}$$

The QIM with the three spin interactions (5.95) in the even sector of the Hamiltonian is discussed in the appendix C. The odd sector (5.96) is the XY model in the transverse field with the anisotropy parameter $\gamma = 1/\delta$. From the Hamiltonian (5.96) we easily establish the symmetry $x \leftrightarrow y$; $\delta \mapsto -\delta$.

In our earlier work [34,35] we took the definition of the SOP for ladders which was proposed by Kim and coworkers [16] and used also in other works [19]. In this paper the ladder SOP renamed as BOP and it is calculated via the brane-brane correlation function as defined in chapter 1. The even and odd BOPs defined below have a clear connection to the even/odd sectors (5.95) and (5.96) of the Hamiltonian.

To calculate the first BOP, we define the string operator (5.38) along the path shown in Fig. 4.2. In so doing, we obtain the even BOP:

$$\mathcal{O}_{x,e}^2 = \lim_{N\to\infty}(-1)^N \Big\langle \prod_{k=1}^{2N} \sigma_k^x \Big\rangle = \langle \tau_0^x \tau_{2N}^x \rangle. \tag{5.97}$$

Note that the string chosen allows to incorporate in principle all spins of the ladder in the calculation of $\mathcal{O}_{x,e}$. Let us now choose another string for the operator (5.38) shown in Fig. 5.7. In such case, we obtain the odd BOP:

$$\mathcal{O}_{x,o}^2 = \lim_{N\to\infty}(-1)^{N-1} \Big\langle \prod_{k=2}^{2N-1} \sigma_k^x \Big\rangle = \langle \tau_1^x \tau_{2N-1}^x \rangle \tag{5.98}$$

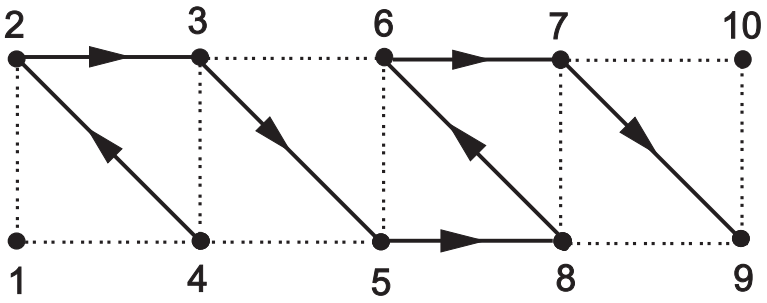

Figure 5.7: String used to define the odd BOP for the two-leg ladder.

We calculated the order parameter of the three-spin Ising chain (C.1) in appendix C. Using the results presented there we obtain:

$$\mathcal{O}_{x,e} = \begin{cases} \left[\frac{J_\perp^2/4-\delta^2}{t^2+J_\perp^2/4-\delta^2}\right]^{1/8} & |J_\perp/2\delta| \geq 1 \\ 0 & |J_\perp/2\delta| < 1 \end{cases} \tag{5.99}$$

The odd BOP can be calculated from the results of Barouch and McCoy [96]

$$\mathcal{O}_{x,O} = \begin{cases} 0 & |J_\perp/2\delta| > 1 \\ t^{1/4}\sqrt{\frac{2}{t+\delta}}[\delta^2 - J_\perp^2/4]^{1/8} & |J_\perp/2\delta| \leq 1. \end{cases} \tag{5.100}$$

To make the behavior of the even and odd BOPs more visible, we present BOPs $O_{x,e}$, $O_{y,e}$ and $O_{y,o}$ as functions of dimerization parameter δ in Fig. 5.8. Their explicit expressions (5.99) and (5.100) are calculated at each point in the dimerization axis and plot them accordingly.

In agreement with earlier results [16, 19, 34, 35, 84] we find that the even and odd BOPs are mutually exclusive (see Fig. 5.8 for detail: $\mathcal{O}_{x,o/e}$ are mutually exclusive in positive δ axis and both are simultaneously vanishing at δ_c). They detect hidden $\mathbb{Z}_2 \bigotimes \mathbb{Z}_2$ symmetry breaking [30] and ordering in the even or odd sectors of the dual Hamiltonian. Note that contrary to its even counterpart, the string for the odd BOP misses two sites at the opposite ends of the ladder. The order probed by $\mathcal{O}_{x,o}$ is

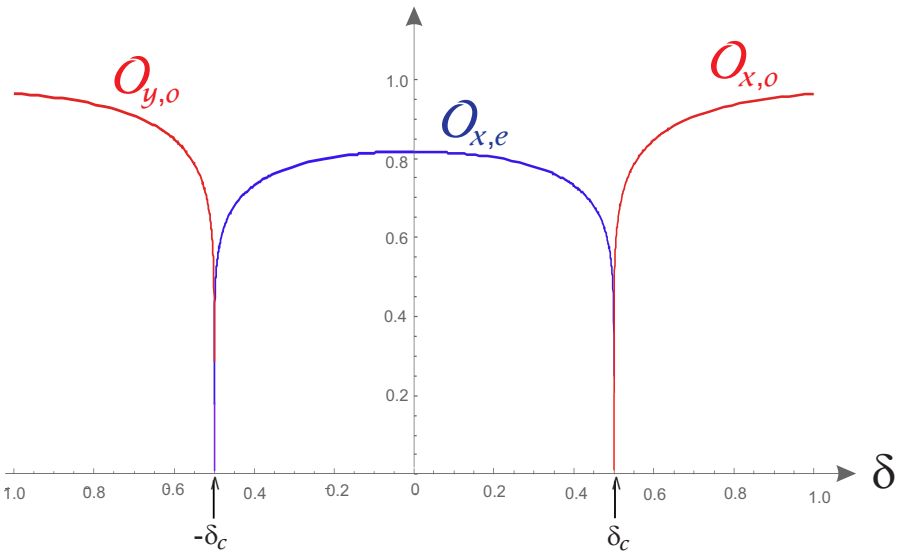

Figure 5.8: BOPs $\mathcal{O}_{x,y/e,o}$ analytically calculated from Eqs. (5.99) and (5.100) on the phase diagram shown in Fig. 5.6. These are calculated along δ axis at $J_\perp/2 = 0.5$

topologically nontrivial, since it corresponds to nonzero winding numbers. According to conventional wisdom [24], there are zero Majorana modes at the ladder's ends in this phase. We indicate the order parameters on the phase diagram of the staggered ladder in Fig. 5.6. From the behaviour of the gap (5.85) and SOPs (5.99) and (5.100) near the lines of the phase transitions $\kappa = \pm\delta$ we find the critical indicies $\nu = 1$ and $\beta = 1/8$ of the 2D Ising universality class, but now their values are the artifact of the effective free-fermionic approximation.

Analysis of the columnar phase is done similarly. The sites of the columnar ladder are labelled along the JW transformatio path in Fig. 4.2. The Majorana representation of the columnar Hamiltonian (5.2) can be mapped via transformations (1.28) and (1.29) onto dual spins. Again the dual Hamiltonian spilts into even and odd sectors $H^{col} = H_o^{col} + H_e^{col}$, where the odd term is the Hamiltonian of the dimerized $XX(\gamma = 0)$ chain in the alternating field (see. Eq. (1) of Ref. [35]), while the even term corresponds to its dual model which is the Ising chain in the alternating transverse field with the

three-spin interactions. Since these models are always gapped (see Eq. (5.94)) and do not undergo any phase transitions, we will not discuss the properties of the columnar phase in more detail.

Note a very remarkable property of the effective Hamiltonian (5.2): for both dimerization patterns it decouples into the reciprocally dual even and odd sectors $H^{st/col} = H_o^{st/col} = H_e^{st/col}$, i.e., these Hamiltonians map onto each other $H_o^{st/col} \rightleftharpoons H_e^{st/col}$ under the duality transforamtion (1.28) and (1.29).

To summarize

In this chapter, spin-1/2 two-leg ladders with anisotropy and two dimerization patterns are analyzed at a zero temperature. After the fermionization is done via the JW transformation, the spin model becomes equivalent to the ladder of the interacting spinless fermions. The interacting fermionic model is treated within the HF mean-field approximation, which allows us to obtain quadratic effective fermionic Hamiltonian. Its renormalized parameters are related to the bare couplings of the microscopic Hamiltonian. (Some examples of the numerical solutions are given in Appendix. A). In the isotropic limit $\gamma = 0$, the effective mean-field Hamiltonian recovers the MF Hamiltonian obtained in [35]. This effective mean-field Hamiltonian is further transformed into the sum of the two decoupled Majorana Hamiltonians, which is in their turn are mapped via an inverse JW transformations onto a sum of two even/odd XY quantum chains in the alternating fields, even without anisotropy. The decoupled Hamiltonians $H_{e,o}(H = H_e + H_o)$ commute, so the averaging in the even and odd sectors factorizes.

The ground state phase diagram of the ladder follows straightforwardly from the solutions of zeros from the eigenvalues of the effective fermionic Hamiltonian in the parametric space for each of the two dimerization patterns. The same results are

obtained with more physical insight from the mapping of the ladder onto a couple of dual spin chains. The analysis is based on our understanding of the spectrum and the ground-state phase diagram of the XY chain in the alternating transverse field: the diagram consists of two conventional magnetic phases, and a phase with a non-local oscillating string order. The phase diagram of the staggered ladder then follows from the superposition of the orders in the dual even/odd XY chains. In the case of the columnar dimerization, the two dual XY chains are equivalent, so the columnar ladder has an extra degeneracy of the spectrum, universality class, and a less rich phase diagram which coincides with that of a single dual (even or odd)chain. On the other hand, the isotropic staggered ladder mapped onto two dual exactly solvable models: XY chain with the uniform transverse field and the Ising chain with the tree-spin interaction.

The ground-state phase diagram of the staggered ladder consists of nine phases, four of them are really distinct, while the other five can be obtained from the symmetries of the model. The dual order parameters are worked out back to the order parameters of the original spin ladder. The staggered ladder possesses four phases with conventional antiferromagnetism ($m_{x,y} = 0$), three phases with z-brane orders, and two phases where the order parameters are z-branes with the pair of spins σ^x, σ^y attached to the edge. Since we were able to find the exact results for the local and string order parameters in the XY chain with alternating field (see appendix B), all the magnetizations and the brane order parameters for the staggered ladder are found analytically as a function of the renormalized couplings of the effective mean-field Hamiltonian. The isotropic staggered ladder only has four phases in a positive plane where two (even/odd) mutually exclusive brane-order parameters are detected.

In the case of columnar phase, the ground-state phase diagram does not possess

magnetic long range order since it only demonstrates the brane order. The order parameters of the three columnar phases are presented in table 5.1 and have their counterparts among the brane-order phases of the staggered ladder. Since the effective Hamiltonian of the columnar ladder maps onto two equivalent XY chains with alternating field and dimerization, no analytical results are available for the order parameters in the latter case. The brane parameters of the columnar ladder are calculated numerically from the Toeplitz determinants. The isotropic columnar ladder does not contain any order parameters since it is always gapped.

The calculation of the topological winding number N_ω is straightforward after the effective Hamiltonian is mapped onto the even and odd XY chains. It was done for all phases and also for both the dimerization patterns. An interesting conclusion is reached when N_ω is written as a logarithmic residue on the complex wave number plane: a change of winding number can only happen when a root (or roots) of a zero energy crosses the unit circle $|z| = 1$ on the complex plane. The latter is the condition for the quantum phase transition [106, 153]. In this sense, the winding number is a complementary parameter to characterize the different gapped phases.

Chapter 6

Conclusions

The phase diagram and the order parameters of modulated anisotropic spin-1/2 XY and XYZ chains, and the two-leg ladders in the presence of the uniform and staggered magnetic fields were analyzed. The main motivation of this work was to further advance the framework incorporating nonlocal order into an extended Landau paradigm. For a large class of quantum spin or fermionic problems we are interested to deal with, the effective Ginzburg-Landau Hamiltonian is a quadratic fermionic Hamiltonian. In general, such Hamiltonians are already the results from some of the mean-field approximation [34, 35, 38, 53], but there is a considerable number of interesting physical problems where they are microscopic Hamiltonians of the models.

We started our analysis from the noninteracting fermionic model. The XY chain is a dimerized Kitaev chain with a modulated chemical potential, which was initially introduced and studied [63] as a dimerized XY chain in the uniform and staggered transverse fields. The model has rich phase diagram (see Fig. 2.1) which contains three possible local order parameters (components of magnetization) and non-local

string order parameters. All the possible phases and conditions of phase boundaries are found from the zeros of the spectrum.

We need to stress once again that there is no insurmountable difference between the local and nonlocal (string) order parameters. Using judiciously chosen duality transformations, we show that a SOP can be identified as a local order parameter from some of the dual Hamiltonian. Sometimes (example: zero field), this can help to easily calculate the SOP in the dual framework, sometimes (example: nonzero field) not. However, it is important to understand the principle. For the general case when all model parameters are nonzero, we were able to define the duality transformations reducing the SOPs to local "dual" orders, but it did not always result in technical simplifications in the calculations of SOPs.

The local and non-local order parameters are expressed via the string correlation function of the Majorana fermions, where the Bogoliubov transformation allows us to express those two-point Mojarana correlation functions. The latter are calculated as asymptotes of determinant of the block Toeplitz matrices. The calculated magnetizations $m_{x,y}$ (local-order parameters) smoothly vanish at the corresponding phase boundaries via the second order phase transitions. We have established the nature of order in the topological phase lying inside the circle in Fig. 2.1. In this phase, the string order appears to be oscillating with a period of four lattice spacing, which was not reported before for this model. In some cases, the asymptote of determinant of Toeplitz matrices can be found explicitly [118], and then one will proceed to get the algebraic expression of the order parameters. For the general case, we have not been able to do so. The generalization of Szego's theorem for the block Toeplitz matrices appeared to be a quite challenging mathematical problem [115, 116]. However, this is a simple numerical calculation, and they are successfully done in our work for chains

and ladders.

In the zero field limit i.e., $h = h_a = 0$, the model's fermionic Hamiltonian is mapped by a duality transformation onto 1D QIMs, residing separately on even and odd sites of the dual lattice. As follows from the duality mapping, the dimerized XY model possesses the hidden $\mathbb{Z}_2 \bigotimes \mathbb{Z}_2$ symmetry, and nonzero SOPs are due to the spontaneous breaking of the $\mathbb{Z}_2$ symmetry in the even and odd sectors of the dual Hamiltonian. In this limit, the hyperbolic phase boundaries shown in Fig. 2.2 reduce to two lines $\gamma = \pm\delta$ as plotted in Fig. 2.9. This phase diagram contains topologically trivial phases where the even and odd SOPs are coexist along with the conventional long-range order (magnetization). There are also topologically nontrivial phases without a conventional order, where only even and odd nonlocal SOPs exist.

The extended Landau framework we developed is shown to work well for the several exactly solvable models. We used it also for dimerized XYZ spin-1/2 chain with the uniform and staggered transverse magnetic fields. The model is treated within Hartee-Fock approximation. This quadratic effective fermionic Hamiltonian expressed in terms of six renormalized couplings dressed by the interaction. Those renormalized couplings were calculated self-consistently from the minimization of the energy.

The main result obtained for the XYZ spin chain is shown in Fig. 3.1, and its local and string order parameters. The representative numerical results for the latter are plotted in Fig. 3.6. As discussed in the non-interacting model, the topological phase consists of an oscillating string order with the period of four lattice spacing. A detailed analysis of the patterns of this string order was given.

The U(1)-symmetric XXZ limit of the model was given a special consideration. It was demonstrated that the present approach respects the LSM theorem and its

implications. In particular, plateaus and h-independent parabolic lines were revealed in various physical quantities, most notable, in the uniform axial magnetization, in accordance with the general arguments [60, 61, 131]. The appearance of the integer-valued and IC fermionic fillings, responsible for qualitatively different behaviour of the physical parameters in the gapped and gapless phases, can be qualitatively related to the presence of flat band in the effective single particle spectrum. Turning on the anomalous U(1)-symmetry breaking coupling $\gamma \neq 0$, rounds the flat band and smears plateaus of magnetization and other step-like parameters. The IC (LL) gapless phase with the algebraic order of the power-law decaying correlations, is unstable versus any $\gamma \neq 0$, transforming into gapped phases with spontaneous planar magnetization ($m_{x,y}$, depending on the sign of γ). The topological order, which we associate with oscillating SOP, evolves continuously (albeit not smoothly) through the $\gamma = 0$ line inside the circle on the (h, γ) plane, without gap closing, vanishing order parameters, or changing topological winding number.

To further advance the extended Landau formalism in an interacting ploblem, we studied the two-leg spin-1/2 ladders. The fermionization of ladders was done via the 2D JW transformation. These two-leg ladders with anisotropy and three patterns of dimerization were analyzed in the presence of the uniform and staggered transverse fields. In the fermionic representation, the staggered/columnar ladders are equivalent to Kitaev ladders with dimerized hopping along the chains, modulated chemical potential and superconducting pairing, while the rung dimerized ladder fermionizes onto the Kitaev ladder with dimerized hopping along the legs and the modulated chemical potential. Interacting fermionic models were treated with the HF mean-field approximation, which allows us to obtain an effective quadratic fermionic Hamiltonian. Its renormalized couplings are related to the bare couplings of the microscopic Hamiltonian.

The ground-state phase diagrams of the isotropic ladders are found in the (h,δ) parametric plane for each of the three dimerization patterns with the proper modulated magnetic fields. The ladders with three dimerization patterns in columnar field contain five distinct phases, three of them are plateaus gapped phases, while the other two possess LL gapless phases. In case of a staggered ladder with the staggered field, the phase diagram only contains the three phases: 0-plateau gapped, LL-gapless and saturated gapped phases. The field-induced magnetization is calculated at each value of the magnetic field with renormalized couplings. Those calculations and plots were done separately for SC, SS, CC, and RC ladders. Our results agree with the plateau theorem (4.1) for the magnetization and earlier results [60, 61] for the special case of zero staggered field. To make the qualitative agreement with those numerical results, we proposed the generalization of Lieb theorem and incorporated flux correction to our equations.

Addition of $h_a \neq 0$ for SS and CC ladders only modifies the positions of the phase boundaries. The existence of the mid-plateau gapped state for the SC-ladder is an indication of appearance of the new spin gapped phase. More interesting physical phenomena is observed in the RC-ladder, where another phase transition occur by closing and re-opening of the 0-plateau and mid-plateau gapped phases as increasing h_a. The representative numerical results for this case are plotted in Fig. 4.16.

More progress in analytical calculations was achieved in the zero field limit $h = h_a = 0$, when the effective mean-field Hamiltonian can be mapped via inverse JW and duality transformations onto a sum of two even/odd XY quantum chains in the alternating transverse fields.

To explore the physical nature of the quantum phases predicted to occur in the anisotropic spin ladder, we introduced and calculated the corresponding brane order

parameters. The duality between the effective mean-field Hamiltonian of the ladders and their pair of decoupled XY chains allowed us to calculate the brane order parameter as a product of the two independent order parameters in the even/odd XY chains and relate those brane orders (hidden) to the symmetry breaking in dual spin chains. The order parameters for all the phases are collected in Table 5.1.

The staggered ladder possesses four phases with conventional antiferromagnetism ($m_{x,y} \neq 0$), three phases with the z-brane order, and two phases where the order parameters are z-branes with the pair of spins σ^x, σ^y attached to the edge. Since we were able to find the new exact results for the local and string order parameters in the XY chain with an alternating field (see appindix B), all the magnetizations and the brane order parameters for the staggered ladder are found analytically as functions of the renormalized couplings of the effective mean-field Hamiltonian. The ground-state phase diagram of the columnar ladder does not possess magnetic long-ranged order, and only demonstrates the brane order. No analytical results are available for the order parameters in this ladder. The brane order parameters of the columnar ladder are calculated numerically from the Toeplitz determinants.

In the isotropic limit $\gamma = 0$, we find the two mutually exclusive (even and odd) SOPs for staggered ladder, where one of the SOPs probe topologically trivial phase, while the other corresponds to the topologically nontrivial phase. The columnar is not very interesting, since it is always gapped and does not undergo phase transitions.

In this work, we have also calculated topological winding number N_ω for all phases of the above discussed models. An interesting conclusion is reached when N_ω is written as a logarithmic residue on the complex wave number plane: a change of a winding number can only happen when a root (or roots) of the zero energy crosses the unit circle $|z| = 1$ on the complex plane. The latter is the condition for the quantum

phase transition [106, 153]. In this sense, the winding number is a complementary parameter and it does not provide additional information which is not encoded in the complex roots of the model's spectra, or in its Lee-Yang zeros, when the temperature is finite [153].

Appendix A

Mean-field parameters with flux correction υ :

The following four sets of mean-field parameters are found from the minimization of energy of sets of isotropic two-leg ladder discussed in chapter 4. We explicitly present those equations

(1) Staggered pattern with staggered field (SS-ladder):

$$m_{z,a} = \frac{h_{aR}}{2\pi}\int_0^\pi \frac{1}{\xi}(1-\mathrm{sign}(E_{-+}))dk \tag{A.1}$$

$$\mathcal{K} = \frac{1}{4\pi(1-\upsilon^2)^2}\int_0^\pi \frac{1}{\xi}\Big\{(1-\upsilon^2)(t_{_R}-\upsilon\delta_{_R})\cos^2 k$$
$$+\upsilon\sin k\Big((\delta_{_R}-\upsilon t_{_R})\sin k+\frac{J_{\perp R}}{2}\Big)\Big\}(1-\mathrm{sign}(E_{-+}))dk \tag{A.2}$$

$$\eta = \frac{1}{4\pi\delta(1-\upsilon^2)^2}\int_0^\pi \frac{1}{\xi}\Big\{\upsilon(1-\upsilon^2)(t_{_R}-\upsilon\delta_{_R})\cos^2 k$$
$$+\sin k\Big((\delta_{_R}-\upsilon t_{_R})\sin k+\frac{J_{\perp R}}{2}\Big)\Big\}(1-\mathrm{sign}(E_{-+}))dk \tag{A.3}$$

$$t_\perp = \frac{1}{4\pi}\int_0^\pi \frac{1}{\xi}\Big((\delta_{_R}-\upsilon t_{_R})\sin k+\frac{J_{\perp R}}{2}\Big)(1-\mathrm{sign}(E_{-+}))dk \tag{A.4}$$

(2) Staggered pattern with columnar field (SC-ladder):

$$m_{z,a} = \frac{h_{aR}}{2\pi}\int_0^{\pi/2}\Big[\Big(1+\frac{J_{\perp R}}{2R}\Big)\frac{(1-\mathrm{sign}(E_{-+}))}{\xi_+}+\Big(1-\frac{J_{\perp R}}{2R}\Big)\frac{(1-\mathrm{sign}(E_{--}))}{\xi_-}\Big]dk \tag{A.5}$$

$$t_\perp = \frac{1}{4\pi}\int_0^{\pi/2}\Big[\Big(R+\frac{J_{\perp R}}{2}\Big)\frac{(1-\mathrm{sign}(E_{-+}))}{\xi_+} - \Big(R-\frac{J_{\perp R}}{2}\Big)\frac{(1-\mathrm{sign}(E_{--}))}{\xi_-}\Big]dk \quad \text{(A.6)}$$

$$\mathcal{K} = \frac{t_R}{4\pi(1-\upsilon^2)}\int_0^{\pi/2}\Big[\Big\{(t_R-\upsilon\delta_R)\cos^2 k + \upsilon(\delta_R-\upsilon t_R) \times\Big(1+\frac{J_{\perp R}}{2R}\Big)\sin^2 k\Big\}\frac{1}{\xi_+}(1-\mathrm{sign}(E_{-+})) + \Big\{(t_R-\upsilon\delta_R)\cos^2 k + \upsilon(\delta_R-\upsilon t_R)\Big(1-\frac{J_{\perp R}}{2R}\Big)\sin^2 k\Big\}\frac{1}{\xi_+}(1-\mathrm{sign}(E_{--}))\Big]dk \quad \text{(A.7)}$$

$$\delta\eta = \frac{t_R}{4\pi(1-\upsilon^2)}\int_0^{\pi/2}\Big[\Big\{\upsilon(t_R-\upsilon\delta_R)\cos^2 k + (\delta_R-\upsilon t_R) \times\Big(1+\frac{J_{\perp R}}{2R}\Big)\sin^2 k\Big\}\frac{1}{\xi_+}(1-\mathrm{sign}(E_{-+})) + \Big\{\upsilon(t_R-\upsilon\delta_R)\cos^2 k + (\delta_R-\upsilon t_R)\Big(1-\frac{J_{\perp R}}{2R}\Big)\sin^2 k\Big\}\frac{1}{\xi_+}(1-\mathrm{sign}(E_{--}))\Big]dk \quad \text{(A.8)}$$

where we have used

$$R = \sqrt{h_{aR}^2 + (\delta_R - \upsilon t_R)^2\sin^2 k} \quad \text{(A.9)}$$

(3) Columnar pattern with columnar field (CC-ladder):

$$m_{z,a} = \frac{h_{aR}}{2\pi}\int_0^{\pi/2}\Big\{\Big(1+\frac{J_{\perp R}^2}{4R}\Big)\frac{1-\mathrm{sign}E_{-+}}{\xi_+} + \Big(1-\frac{J_{\perp R}^2}{4R}\Big)\frac{1-\mathrm{sign}E_{--}}{\xi_+}\Big\}dk \quad \text{(A.10)}$$

$$\mathcal{K} = \frac{t_R}{4\pi(1+\upsilon^2)}\int_0^{\pi/2}\Big[\Big\{t_R(\cos^2 k+\upsilon^2\sin^2 k) + \upsilon^2\frac{t_R}{R}\Big(\delta_R^2+\frac{J_{\perp R}^2}{4}\sin^2 k\Big)\Big\} \times\frac{(1-\mathrm{sign}E_{-+})}{\xi_+} + \Big\{t_R(\cos^2 k+\upsilon^2\sin^2 k) \quad \text{(A.11)}$$

$$-\upsilon^2\frac{t_R}{R}\Big(\delta_R^2+\frac{J_{\perp R}^2}{4}\sin^2 k\Big)\Big\}\frac{(1-\mathrm{sign}E_{--})}{\xi_-}\Big]dk \quad \text{(A.12)}$$

$$\delta\eta = \frac{t_R}{4\pi(1+\upsilon^2)}\int_0^{\pi/2}\Big[\Big\{\delta_R(\sin^2 k+\upsilon^2\cos^2 k) + \upsilon^2\frac{\delta_R}{R}\Big(t_R^2+\frac{J_{\perp R}^2}{4}\cos^2 k\Big)\Big\} \times\frac{(1-\mathrm{sign}E_{-+})}{\xi_+} + \Big\{\delta_R(\sin^2 k+\upsilon^2\cos^2 k)$$

$$-\upsilon^2\frac{\delta_R}{R}\Big(t_R^2+\frac{J_{\perp R}^2}{4}\cos^2 k\Big)\Big\}\frac{(1-\mathrm{sign}E_{--})}{\xi_-}\Big]dk \quad \text{(A.13)}$$

$$t_\perp = \frac{J_{\perp R}}{8\pi}\int_0^{\pi/2}\Big[\Big\{1+\frac{1}{R}\Big(h_{aR}^2+\upsilon^2(t_R^2\sin^2 k+\delta_R^2\cos^2 k)\Big)\Big\}\frac{(1-\mathrm{sign}E_{-+})}{\xi_+}$$
$$\Big\{1-\frac{1}{R}\Big(h_{aR}^2+\upsilon^2(t_R^2\sin^2 k+\delta_R^2\cos^2 k)\Big)\Big\}\frac{(1-\mathrm{sign}E_{--})}{\xi_+}\Big]dk \tag{A.14}$$

where we have used

$$R=\sqrt{\frac{1}{4}h_{aR}^2J_{\perp R}^2+\upsilon^2\Big\{t_R^2\delta_R^2+\frac{1}{4}J_{\perp R}^2(t_R^2\sin^2 k+\delta_R^2\cos^2 k)\Big\}} \tag{A.15}$$

(4) Rung dimerization pattern with columnar field (RC-ladder):

$$m_{z,a}=\frac{1}{2\pi}\int_0^{\pi/2}\Big[\Big\{h_{aR}+\frac{J_\perp}{2}\Big(m_z\delta_{\perp R}+t_{\perp R}(1+m_{z,a})\Big)\Big\}\frac{(1-\mathrm{sign}E_{-+})}{\xi_+}$$
$$+\Big\{h_{aR}-\frac{J_\perp}{2}\Big(m_z\delta_{\perp R}+t_{\perp R}(1+m_{z,a})\Big)\Big\}\frac{(1-\mathrm{sign}E_{--})}{\xi_-}\Big]dk \tag{A.16}$$

$$t_\perp=\frac{1}{4\pi((1+m_{z,a})^2-m_z^2)}\int_0^{\pi/2}\Big[(1+m_{z,a})\Big\{h_{aR}+\frac{J_\perp}{2}\Big(t_{\perp R}(1+m_{z,a})+\delta_{\perp R}m_z\Big)\Big\}$$
$$\times\frac{(1-\mathrm{sign}E_{-+})}{\xi_+}-(1+m_{z,a})\Big\{h_{aR}-\frac{J_\perp}{2}\Big(t_{\perp R}(1+m_{z,a})+\delta_{\perp R}m_z\Big)\Big\}$$
$$\times\frac{(1-\mathrm{sign}E_{--})}{\xi_-}-m_z(\mathrm{sign}E_{-+}-\mathrm{sign}E_{--})\Big]dk \tag{A.17}$$

$$\delta_\perp\eta_\perp=\frac{1}{4\pi((1+m_{z,a})^2-m_z^2)}\int_0^{\pi/2}\Big[-m_z\Big\{h_{aR}+\frac{J_\perp}{2}\Big(t_{\perp R}(1+m_{z,a})+\delta_{\perp R}m_z\Big)\Big\}$$
$$\times\frac{(1-\mathrm{sign}E_{-+})}{\xi_+}+m_z\Big\{h_{aR}-\frac{J_\perp}{2}\Big(t_{\perp R}(1+m_{z,a})+\delta_{\perp R}m_z\Big)\Big\}$$
$$\times\frac{(1-\mathrm{sign}E_{--})}{\xi_-}+(1+m_{z,a})(\mathrm{sign}E_{-+}-\mathrm{sign}E_{--})\Big]dk \tag{A.18}$$

$$\mathcal{K}=\frac{t_R}{4\pi}\int_0^{\pi/2}\cos^2 k\Big\{\frac{(1-\mathrm{sign}E_{-+})}{\xi_+}+\frac{(1-\mathrm{sign}E_{--})}{\xi_-}\Big\}dk \tag{A.19}$$

We present the full version of the constants appeared in the mean-field Hamiltonian (4.6) in three dimerization patterns with two types of magnetic fields:

$$C^{ss}=\Big(1+(\upsilon)^2\Big)\Big(\mathcal{K}^2-P^2+\delta^2(\eta^2-\eta_p^2)+2\delta^2(\mathcal{K}\eta+P\eta_p)\Big)$$
$$-2\delta(\upsilon)\Big(\mathcal{K}^2-P^2+\delta^2(\eta^2-\eta_p^2)+2(\mathcal{K}\eta+P\eta_p)\Big)$$

$$-\frac{1}{4}(m_z^2 - m_{z,a}^2)\Big(1+\frac{J_\perp}{2}\Big) + \frac{1}{2}J_\perp t_\perp^2 \tag{A.20}$$

$$\begin{aligned} C^{sc} = &\Big(1+(\upsilon)^2\Big)\Big(\mathcal{K}^2 - P^2 + \delta^2(\eta^2-\eta_p^2) + 2\delta^2(\mathcal{K}\eta + P\eta_p)\Big) \\ &-2\delta(\upsilon)\Big(\mathcal{K}^2 - P^2 + \delta^2(\eta^2-\eta_p^2) + 2(\mathcal{K}\eta + P\eta_p)\Big) \\ &-\frac{1}{4}m_z^2\Big(1+\frac{J_\perp}{2}\Big) + \frac{1}{4}m_{z,a}^2\Big(1-\frac{J_\perp}{2}\Big) + \frac{1}{2}J_\perp t_\perp^2 \end{aligned} \tag{A.21}$$

$$\begin{aligned} C^{cc} = &\Big(1+(\upsilon)^2\Big)\Big(\mathcal{K}^2 - P^2 + \delta^2(\eta^2-\eta_p^2) + 2\delta^2(\mathcal{K}\eta + P\eta_p)\Big) \\ &-\frac{1}{4}m_z^2\Big(1+\frac{J_\perp}{2}\Big) + \frac{1}{4}m_{z,a}^2\Big(1-\frac{J_\perp}{2}\Big) + \frac{1}{2}J_\perp t_\perp^2 \end{aligned} \tag{A.22}$$

$$\begin{aligned} C^{rc} = &\mathcal{K}^2 - P^2 - \frac{1}{4}m_z^2\Big(1+\frac{J_\perp}{2}\Big) + \frac{1}{4}m_{z,a}^2\Big(1-\frac{J_\perp}{2}\Big) + \frac{1}{2}J_\perp\delta m_z m_{z,a} \\ &+\frac{1}{2}J_\perp\Big(m_z^2 + (1+m_{z,a})^2\Big)\Big(t_\perp^2 + \delta_\perp^2\eta_\perp^2 + 2\delta_\perp^2\eta_\perp t_\perp\Big) \\ &+J_\perp m_z(1+m_{z,a})\delta_\perp\Big(t_\perp^2 + \delta_\perp^2\eta_\perp^2 + 2\eta_\perp t_\perp\Big) \end{aligned} \tag{A.23}$$

Appendix B

Duality of two transverse-field XY chain models and their order parameters

In this appendix, we will present the canonical transformations to map the spin-1/2 XY chain with a uniform transverse field onto the chain in a stagggered field. This mapping is used to get analytical results for the order parameters.

First, we find explicit expressions for the longitudinal magnetizations $m_{x,y}$ in the chain with a staggered field. It is an interesting and useful result, since a brut force calculation of such parameters in a chain with two lattice-space periodicity, amounts to evaluation of limiting values of the determinants of 2×2-block Toeplitz matrices [37]. The latter problem seems to be a quite hopeless for analytical calculations [115, 116, 155], but it is well amenable via mapping onto the chain with a uniform field, as shown below.

Second, we calculate for the first time the string order parameter in a closed form for the XY chain in a uniform transverse field. Using the mapping we get the explicit formulas for the oscillating string order parameter in the topological phase of the staggered model, bypassing a problem of block Toeplitz matrices.

Since the effective mean-field Hamiltonian of the two leg ladder maps onto a sum of two XY chains in the alternating field, as shown in the main text of the chapter 5, the results of this appendix allow us to find analytical expressions for the brane order parameters of the staggered ladder.

The Hamiltonian of the XY chain in uniform transverse field is defind as:

$$H = \sum_{n=1}^{N} \frac{J}{4} \Big\{ (1+\gamma)\sigma_n^x \sigma_{n+1}^x + (1-\gamma)\sigma_n^y \sigma_{n+1}^y \Big\} + \frac{h}{2}\sigma_n^z \tag{B.1}$$

In this appendix we return to the use of dimensional units and restore the exchange coupling J. The properties of this model (B.1) are well known [96, 111]. Its spectrum is

$$E(k) = J\sqrt{\Big(\frac{h}{J} - \cos k\Big)^2 + \gamma^2 \sin^2 k} \tag{B.2}$$

with $k \in [-\pi/2, \pi/2]$. In the range $|h/J| < 1$ the model is anti-ferromagnetically ($J > 0$) ordered: $\langle \sigma^x_L \sigma^x_{L+n} \rangle \to \pm m_x^2$ as $n \to \infty$, with the spontaneous longitudinal magnetization

$$m_x^2 = \frac{2}{1+\gamma}\Big\{\gamma^2\Big(1 - \Big(\frac{h}{J}\Big)^2\Big)\Big\}^{1/4}, \tag{B.3}$$

when $\gamma > 0$. At $\gamma < 0$ the order changes: $m_x \leftrightarrow m_y$. In the polarized phase $|h/J| > 1$ (the phase diagram is symmetric with respect to the sign change of the field) only induced magnetization m_z is present. However one can notice [37, 38] appearance of a continuous monotonous z-string order parameter $\mathcal{O}_z$ defined from the limit of the string-string correlator

$$\mathfrak{D}_{zz}(L, R) \equiv \lim_{(R-L)\to\infty} \Big\langle \prod_{n=L}^{R} \sigma^z_n \Big\rangle \longrightarrow \mathcal{O}_z^2 \tag{B.4}$$

To find $\mathcal{O}_z$ we apply the standard techniques to calculate Toeplitz determinants using the Szego's theorem [118]. The result is expressed via two roots $\lambda_\pm$ of the model's spectra on the complex momentum plane:

$$\mathcal{O}_z^2 = \Big[\frac{(1-\lambda_-^2)(\lambda_+^2 - 1)}{(\lambda_+ - \lambda_-)^2}\Big]^{1/4}, \tag{B.5}$$

where

$$\lambda_\pm = \frac{h/J \pm \sqrt{(h/J)^2 + \gamma^2 - 1}}{1+\gamma}, \tag{B.6}$$

yielding

$$\mathcal{O}_z^2 = \Big[\frac{(h/J)^2 - 1}{(h/J)^2 + \gamma^2 - 1}\Big]^{1/4} \tag{B.7}$$

This z-string parameter, known also (up to irrelevant pre-factors) as the parity string order parameter [68, 97, 156], vanishes at the boundary of the polarized phase with the correct critical index of the order parameter, i.e., $\mathcal{O}_z \propto (h/J - 1)^{1/8}$. In the isotropic limit $\gamma = 0$ it becomes a plateau $\mathcal{O}_z = 1$ with a discontinuity of the phase boundary [37, 38], similar to the plateau of induced magnetization m_x.

With the canonical transformations 5.25a-5.25c where $\tau \Leftrightarrow \sigma$, we can map the

chain (B.1) onto the XY chain with staggered magnetic field:

$$H = \sum_{n=1}^{N} \frac{\tilde{J}}{4}\Big\{(1+\tilde{\gamma})\tilde{\sigma}_n^x\tilde{\sigma}_{n+1}^x + (1-\tilde{\gamma})\tilde{\sigma}_n^y\tilde{\sigma}_{n+1}^y\Big\} + \frac{1}{2}(-1)^n\tilde{h}_a\tilde{\sigma}_n^z \tag{B.8}$$

where the corresponding parameters of two Hamiltonians are related as:

$$\begin{aligned} \tilde{J} &\to J\gamma, \\ \tilde{\gamma} &\to \frac{1}{\gamma}, \\ \tilde{h}_a &\to \frac{h}{J\gamma}. \end{aligned} \tag{B.9}$$

The dimerized XY chain with uniform and staggered fields was studied recently [37] in great detail, so we can easily recover some key properties of the model (B.8) as a simpler special case. The spectrum of the fermionized Hamiltonian (B.8) has two eigenvalues

$$\tilde{E}(k) = \tilde{J}\sqrt{\Big(\frac{\tilde{h}_a}{\tilde{J}} \pm \tilde{\gamma}\sin k\Big)^2 + \cos^2 k} \tag{B.10}$$

where the wavenumbers lie in the reduced Brillouin zone $k \in [-\pi/2, \pi/2]$. Using the correspondence (B.9), wavenumber shifts by $\pm\pi/2$, and the Brillouin zone unfolding, one can establish the equivalence between the spectra (B.2) and (B.10), as well as an equal number of eigenmodes in two spectra.

The model (B.8) has two different phases:

1: At $\tilde{h}_a/\tilde{J} < \tilde{\gamma}$ it has a local magnetic order $\tilde{m}_x$. Since $\sigma_n^x = \tilde{\sigma}_n^x$ and according to (B.9): $\tilde{h}_a/\tilde{J} < \tilde{\gamma} \longleftrightarrow h/J < 1$, the phase $\tilde{m}_x \neq 0$ of (B.8) corresponds to the phase $m_x \neq 0$ of (B.1). From (B.3) and (B.9) we can calculate the magnetic order parameter in the staggered model:

$$\tilde{m}_x^2 = \frac{2}{1+\tilde{\gamma}}\Big\{\gamma^2 - (\tilde{h}_a/\tilde{J})^2\Big\}^{1/4} \quad \text{at} \quad \tilde{\gamma} > \tilde{h}_a/\tilde{J}. \tag{B.11}$$

The magnetization $\tilde{m}_y$ at $\tilde{\gamma} < -\tilde{h}_a/\tilde{J}$ can be calculated from the symmetry $\tilde{m}_y(-\tilde{\gamma}) = \tilde{m}_y(\tilde{\gamma})$.

2: In the region $-\tilde{h}_a/\tilde{J} < \tilde{\gamma} < \tilde{h}_a/\tilde{J}$ the magnetization disappears, and non-local order detected by non-vanishing oscillations of the string-string correlation function $\mathfrak{D}_{zz}$ with a period of four lattice spacing is found from numerical calculations [37].

This oscillating string order is parameterized as follows [37]:

$$\mathfrak{D}_{zz}(L,R) \xrightarrow[R\to\infty]{} \begin{cases} (-1)^m \mathcal{O}_{z,1}^2 \ , & L=1,\ R=2m \\ (-1)^m \mathcal{O}_{z,2}^2 \ , & L=2,\ R=2m \\ (-1)^{m+L} \mathcal{O}_{z,3}^2 \ , & L=1,\ R=2m+1 \text{ or } L=2,\ R=2m+1 \end{cases} \tag{B.12}$$

In a special case of zero dimerization in the Hamiltonian (B.8) under consideration, the string correlator oscillates with a constant amplitude $\mathcal{O}_{z,1} = \mathcal{O}_{z,2} = \mathcal{O}_{z,3}$ following the pattern $(++--)$ [37].

One can easily check that the region with the oscillating string order of the staggered model (B.8) corresponds to the polarized phase of the uniform chain (B.1) at $|h/J| > 1$. The uniform string order parameter (B.4) in that case is dual to the oscillating string parameters of the staggered model. Indeed, since $\tilde{\sigma}_n^z = (-1)^n \sigma_n^z$ we can easily establish relation between string correlators in two models:

$$\tilde{\mathfrak{D}}_{zz}(L,R) = (-1)^s \mathfrak{D}_{zz}(L,R) \ , \tag{B.13}$$

where $s \equiv (R+L)(R-L+1)/2$. Taking $L=1$ we find the oscillating string order as:

$$\tilde{\mathfrak{D}}_{zz}(1,R) \xrightarrow[R\to\infty]{} \begin{cases} (-1)^m \mathcal{O}_z^2 \ , & R=2m \\ (-1)^{m+1} \mathcal{O}_z^2 \ , & R=2m+1 \end{cases} \tag{B.14}$$

with

$$\mathcal{O}_z^2 = \Big[\frac{(\tilde{h}_a/\tilde{J})^2 - \tilde{\gamma}^2}{(\tilde{h}_a/\tilde{J})^2 - \tilde{\gamma}^2 + 1} \Big]^{1/4} \text{ at } \ -\tilde{h}_a/\tilde{J} < \tilde{\gamma} < \tilde{h}_a/\tilde{J} \ . \tag{B.15}$$

Appendix C

Transverse Ising chain with three-spin interactions

The Hamiltonian of the Ising chain in transverse field with three-spin interaction is defined as:

$$H = \sum_{i=1}^{N} (J\sigma_i^x \sigma_{i+1}^x + J_3 \sigma_{i-1}^x \sigma_i^z \sigma_{i+1}^x = h\sigma_i^z) \tag{C.1}$$

The duality transformations (1.28) and (1.29) map the above Hamiltonian onto the anisotropic XY chain in transverse magnetic field [157]. Most of basic properties of the model (C.1) were analysed in [158] and later in [35, 101, 159]. The Jordan-Wigner transformation of (C.1) yields the free fermionic model (up to an unimportant constant term not showing here):

$$H = \sum_k 2A(k) c_k^\dagger c_k - iB(k)(c_k^\dagger c_{-k}^\dagger + c_k c_{-k}) \tag{C.2}$$

where

$$A(k) = h + J\cos k - J_3 \cos 2k \tag{C.3}$$

$$B(k) = J\sin k - J_3 \sin 2k, \tag{C.4}$$

and $c_k^\dagger, c_k$ are the respective fourier transforms of the lattice fermion operators $c_i^\dagger, c_i$. The Bogoliubov transformation

$$\eta_k = \cos\Theta_k c_k - i\sin\Theta_k c_{-k}^\dagger \tag{C.5}$$

where the Bogoliubov angle Θ_k defined as $\tan 2\Theta_k = B(k)/A(k)$, diagonalizes the Hamiltonian. The spectrum of the quasiparticles $\eta_k, \eta_k^\dagger$ is

$$E(k) = \sqrt{A(k)^2 + B(k)^2}$$

$$= \sqrt{h^2 + J^2 + J_3^2 + 2J(h - J_3)\cos k - 2hJ_3 \cos 2k}. \tag{C.6}$$

The model is gapless along the lines of quantum criticality $h = J_3 \pm J$, and for the transverse fields within the range

$$J_3 - J < h < J_3 + J \tag{C.7}$$

the model manifests the local long-range order [158] (magnetization) $m_x \neq 0$. Our goal is to calculate the order parameter m_x. We will use the classical approaches [79,96,160]. More modern treatments and references can be found, e.g. in [118,119]. The fermionic correlation function

$$G_{l-m} = i\langle b_l a_m \rangle \tag{C.8}$$

is defined in terms of the site Majorana operators (2.29). It can be calculated as the Fourier transform

$$G_n = \int_0^{2\pi} \frac{d\varphi}{2\pi} e^{in\varphi} G(\varphi) \tag{C.9}$$

of the generating function

$$G(\varphi) = \sqrt{\frac{A(\varphi) + iB(\varphi)}{A(\varphi) - iB(\varphi)}} = \sqrt{\frac{(e^{i\varphi} - \alpha_+)(e^{i\varphi} - \alpha_-)}{(e^{-i\varphi} - \alpha_+)(e^{-i\varphi} - \alpha_-)}} \tag{C.10}$$

where

$$\alpha_\pm = \frac{J \pm \sqrt{J^2 + 4hJ_3}}{2J_3} \tag{C.11}$$

The spin-spin correlation function $\langle \sigma_1^x \sigma_{N+1}^x \rangle$ is given by the $N \times N$ Toeplitz determinant [79]:

$$\langle \sigma_1^x \sigma_{N+1}^x \rangle = \begin{vmatrix} G_{-1} & G_{-2} & ... & G_{-N} \\ . & . & ... & . \\ . & . & ... & . \\ . & . & ... & . \\ G_{N-2} & G_{N-1} & ... & G_{-1} \end{vmatrix} \tag{C.12}$$

Note that the singular points of $G(\varphi)$ satisfy $\alpha_+\alpha_- = -h/J_3$, and within the magnetically ordered range (C.7) the first root is bound $-1 < \alpha_- < 0$, thus for $J_3/h < 1$ the inequality $0 < \alpha_+^{-1} < 1$ for the second root holds. The generating function can be written as $G(\varphi) = e^{i\varphi}\tilde{G}(\varphi)$ with

$$\tilde{G}(\varphi) = \sqrt{\frac{(e^{-i\varphi} - \alpha_+^{-1})(e^{i\varphi} - \alpha_-)}{(e^{i\varphi} - \alpha_+^{-1})(e^{-i\varphi} - \alpha_-)}} \tag{C.13}$$

Then

$$G_n = \int_0^{2\pi} \frac{d\varphi}{2\pi} e^{i(n+1)\varphi} \tilde{G}(\varphi) = \tilde{G}_{n+1}, \tag{C.14}$$

and the determinant (C.12) can be written in terms of $\tilde{G}_n$:

$$D_N = \begin{vmatrix} \tilde{G}_0 & ... & \tilde{G}_{-N+1} \\ . & ... & . \\ . & ... & . \\ \tilde{G}_{N-1} & ... & \tilde{G}_0 \end{vmatrix} = \tilde{D}_N \tag{C.15}$$

Since zeros/singularities of the generating function $\tilde{G}(\varphi)\{|\alpha_+^{-1}|, |\alpha_-|\} < 1$ lie inside the unit circle $z = e^{i\varphi}$ on the complex plane, the conditions for Szego's theorem are satisfied [118], and it can be applied for calculation of the limit $N \to \infty$ of the Toeplitz determinant $\tilde{D}_N$. The latter result is well known and reads: [118].

$$\lim_{N\to\infty} \tilde{D}_N = \Big[\frac{(1-\alpha_+^{-2})(1-\alpha_-^2)}{(1-\alpha_-/\alpha_+)^2}\Big]^{1/4}. \tag{C.16}$$

Combining all formulae together, we obtain the sought result:

$$m_x^2 = \lim_{N\to\infty} \langle \sigma_1^x \sigma_{N+1}^x \rangle = \Big[\frac{J^2 - (J_3 - h)^2}{J^2 + 4hJ_3}\Big]^{1/4} \tag{C.17}$$

The above formula for magnetization is analytic in the whole locally ordered range (C.7) across the line $h = J_3$. The validity of the formula for the order parameter (C.17) was checked by direct numerical calculation of the determinant (C.12) using *Mathematica*.

Bibliography

[1] L. D. Landau and E. M Lifshitz, *Statistical Physics Part 1 (Course of Theoretical Physics vol. 5)* 3rd edn (Oxford, London: Butterworth-Heinemann) (1980).

[2] X. G. Wen, *Quantum Field Theory of Many-Body Systems* (New York: Oxford) (2004).

[3] P. A. Lee, N. Nagaosa and X. G. Wen, Rev. Mod. Phys. **78** 17 (2006).

[4] E. Fradkin, *Field Theories of Condensed Matter Physics* 2nd edn (New York: Cambridge University Press) (2013).

[5] E. Dagotto and T. M. Rice, *Science* **271** 618 (1996); E. Dagotto, Rep. Prog. Phys. **62** 1525 (1999).

[6] A. Lavarélo, G. Roux and N. Laflorencie, Phys. Rev. B **84** 144407 (2011).

[7] Y. J. Wang, F. H. L. Essler, M. Fabrizio and A. A. Nersesyan, Phys. Rev. B **66** 024412 (2002).

[8] V. Gritsev, B. Normand and D. Baeriswyl, Phys. Rev. B **69** 094431 (2004).

[9] O. A. Starykh and L. Balents, Phys. Rev. Lett. **93** 127202 (2004).

[10] M. Sato, Phys. Rev. B **76** 054427 (2007).

[11] G. H. Liu, H. L. Wang and G. S. Tian, Phys. Rev. B **77** 214418 (2008).

[12] T. Hikihara and O. A. Starykh, Phys. Rev. B **81** 064432 (2010).

[13] H. Watanabe, Phys. Rev. B **52** 12508 (1995).

[14] Y. Nishiyama, N. Hatano and M. Suzuki, J. Phys. Soc. Japan **64** 1967 (1995).

[15] D. G. Shelton, A. A. Nersesyan and A.M. Tsvelik, Phys. Rev. B **53** 8521 (1996).

[16] E. H. Kim, G. Fath, J. Solyom and D. J. Scalapino, Phys. Rev. B **62** 14965 (2000).

[17] G. Fath, O. Legeza and J. Solyom, Phys. Rev. B **63** 134403 (2001).

[18] E. H. Kim, O. Legeza and J. Solyom, Phys. Rev. B **77** 205121 (2008).

[19] M. A. Martin-Delgado, R. Shankar and G. Sierra, Phys. Rev. Lett. **77** 3443 (1996).

[20] M. A. Martin-Delgado, J. Dukelsky and G. Sierra, Phys. Lett. A **250** 430 (1998).

[21] J. Almeida, M. A. Martin-Delgado and G. Sierra, Phys. Rev. B **76** 184428 (2007); Phys. Rev. B **77** 094415 (2008); J. Phys. A: Math. Theor. **41** 485301 (2008).

[22] A. Kitaev, Ann. Phys. **321** 2 (2006).

[23] X. Y. Feng, G. M. Ghang and T. Xiang, Phys. Rev. Lett. **98** 087204 (2007).

[24] X. L. Qi and S. C. Zhang, Rev. Mod. Phys. **83** 1057 (2011).

[25] M. Z. Hasan and C. L. Kane, Rev. Mod. Phys. **82** 3045 (2010).

[26] M. Fruchart and D. Carpentier, C. R. Phys. **14** 779 (2013).

[27] B. A. Bernevig and T. L. Hughes, *Topological Insulators and Topological Superconductors* (Princeton University Press, Princeton) (2013).

[28] M. den Nijs and K. Rommelse, Phys. Rev. B **40** 4709 (1989).

[29] G. E. Volovik, *The Universe in a Helium Droplet* (Oxford: Clarendon) (2003).

[30] M. Oshikawa, Journal of Physics: Condensed Matter **4** 7469 (1992).

[31] T. Kennedy and H. Tasaki, Phys. Rev. B **45** 304 (1992).

[32] M. Kohmoto and H. Tasaki, Phys. Rev. B **46** 3486 (1992).

[33] K. Hida, Phys. Rev. B **45** 2207 (1992); **46** 8268 (1992).

[34] S. J. Gibson, R. Meyer, and G. Y. Chitov, Phys. Rev. B **83** 104423 (2011).

[35] G. Y. Chitov, T. Pandey, J. Stat. Mech.: Theory Exp 043101 (2017).

[36] G. Y. Chitov, Phys. Rev. B **97** 085131 (2018).

[37] G. Y. Chitov, T. Pandey, and P. N. Timonin, Phys. Rev. B **100** 104428 (2019).

[38] T. Pandey and G. Chitov, Phys. Rev. B **102** 054436 (2020).

[39] Z. Nussinov and G. Ortiz, Proc. Natl Acad. Sci. USA **106** 16944 (2009); Ann. Phys. **324** 977 (2009).

[40] Y. Hatsugai, J. Phys. Soc. **75** 123601 (2006).

[41] T. Hirano, H. Katsura and Y. Hatsugai, Phys. Rev. B **77** 094431 (2008).

[42] M. Arikawa, I. Maruyama and Y. Hatsugai, Phys. Rev. B **82** 073105 (2010).

[43] I. Maruyama, T. Hirano and Y. Hatsugai, Phys. Rev. B **79** 115107 (2009).

[44] M. Ezawa, Y. Tanaka and N. Nagaosa, Sci. Rep. **3** 2790 (2013).

[45] N. Chepiga, F. Michaud and F. Mila, Phys. Rev. B **88** 184418 (2013).

[46] M. Bortz, J. Sato and M. Shiroishi, J. Phys. A: Math. Theor. **40** 4253 (2007).

[47] V. N. Kotov, J. Oitmaa and Z. Weihong, Phys. Rev. B **59** 11377 (1999).

[48] D. C. Cabra, M. D. Grynberg, Phys. Rev. Lett **82** 1768 (1999).

[49] D. C. Cabra, M. D. Grynberg, Phys. Rev. B **62** 337 (2000).

[50] Y. J. Wang and A. A. Nersesyan, Nucl. Phys. B **583** 671 (2000).

[51] K. Okamoto, Phys. Rev. B **67** 212408 (2003).

[52] M. Nakamura, T. Yamamoto and K. Ide, J. Phys. Soc. Japan **72** 1022 (2003).

[53] G. Y. Chitov, B. W. Ramakko, and M. Azzouz, Phys. Rev. B **77** 224433 (2008).

[54] J. Chen, K. L. Yao, L. J. Ding, Physica A **391** 2306 (2012).

[55] Y. J. Xu, H. Zhao, Y. G. Chen and Y.H. Yan, Eur. Phys. J. B. **85** 393 (2012).

[56] R. X. Li, S. L. Wang, K. L. Yao, and H. H. Fu, Phys. Lett. A **377** 2422 (2013).

[57] H. D. Chen and J. Hu, Phys. Rev. B **76** 193101 (2007).

[58] M. Azzouz, K. Shahin and G. Y. Chitov, Phys. Rev. B **76** 132410 (2007).

[59] T. Pandey, and G. Chitov, arXiv:2111.09813v1 (2021).

[60] M. Oshikawa, M. Yamanaka, and I. Affleck, Phys. Rev. Lett.**78** 1984 (1997).

[61] M. Oshikawa, Phys. Rev. Lett. **84** 1535 (2000).

[62] Y. Ogata and H. Tasaki, Commun. Math. Phys. **372** 951 (2019).

[63] J. Perk, H. Capel, M.Zuilhof, and T. Siskens, Physica A **81** 319 (1975).

[64] A. Dutta, G. Aeppli, B. K. Chakrabarti, U. Divakaran, T. F. Rosenbaum, and D. Sen, *Quantum Phase Transitions in Transverse Field Spin Models: From Statistical Physics to Quantum Information* (Cambridge University Press, New Delhi) (2015).

[65] H. D. Chen and Z. Nussinov, J. Phys. A: Math. Theor. **41** 075001 (2008).

[66] E. Cobanera, G. Ortiz, and Z. Nussinov, Phys. Rev. B **87** 041105 (R) (2013).

[67] D. Pérez-García, M. M. Wolf, M. Sanz, F. Verstraete, and J. I. Cirac, Phys. Rev. Lett. **100** 167202 (2008).

[68] S. P. Rath, W. Simeth, M. Endres, and W. Zwerger, Annals of Physics **334** 256 (2013).

[69] Y. Bahri and A. Vishwanath, Phys. Rev. B **89** 155135 (2014).

[70] C. Degli Esposti Boschi, A. Montorsi, and M. Roncaglia, Phys. Rev. B **94** 085119 (2016).

[71] S. Fazzini, F. Becca, and A. Montorsi, Phys. Rev. Lett. **118** 157602 (2017).

[72] S. Fazzini and A. Montorsi, Applied Sciences **9**, 10.3390/app9040784 (2019).

[73] R. Wakatsuki, M. Ezawa, Y. Tanaka, and N. Nagaosa, Phys. Rev. B **90** 014505 (2014).

[74] M. Ezawa, Phys. Rev B **96** 121105 (R) (2017).

[75] J. J. Miao, H. K. Jin, F. C. Zhang, and Y. Zhou, Phys. Rev. Lett. **118** 267701 (2017).

[76] E. Sela, A. Altland, and A. Rosch, Phys. Rev. B **84** 085114 (2011).

[77] H. Katsura, D. Schuricht, and M. Takahashi, Phys. Rev. B **92** 115137 (2015).

[78] K. Kawabata, R. Kobayashi, N. Wu, and H. Katsura, Phys. Rev. B **95** 195140 (2017).

[79] E.H. Lieb, T. Schultz, and D. Mattis, Ann. Phys. (NY) **16** 407 (1961).

[80] K. Nomura, J. Morishige, and T. Isoyama, J. Phys. A: Math. Theor **48** 375001 (2015)

[81] T. Isoyama and K. Nomura, Prog. Theor. Exp. Phys. **2017** 103101 (2017).

[82] P. Jordan and E. Wigner, Z Phys. **47** 631 (1928).

[83] M. Azzouz, Phy. Rev. B **48** 6136 (1993).

[84] T. Pandey *MS Thesis Laurentian University* (2014).

[85] M. Azzouz, L. Chen and S. Moukouri, Phys. Rev. B **50** 6233 (1994).

[86] X. Dai and Z. Su, Phys. Rev. B **57** 964 (1998).

[87] H. Hori and S. Yamamoto, J. Phys. Soc. **73** 549 (2004).

[88] T. S. Nunner and T. Kopp, Phys. Rev. B **69** 104419 (2004).

[89] G. Gómez-Santos, Phys. Rev. Lett. **63** 790 (1989).

[90] D. V. Dmitriev, V. Y. Krivnov, A. A. Ovchinnikov, and A. Langari, J. Exp. Theor. Phys. **95** 538 (2002).

[91] D. V. Dmitriev, V. Y. Krivnov, A. A. Ovchinnikov, Phys. Rev. B **65** 172409 (2002).

[92] J. S. Caux, F. H. L. Essler, and U. Löw, Phys. Rev. B **68** 134431 (2003).

[93] R. Hagemans, J. S. Caux, and U. Löw, Phys. Rev. B **71** 014437 (2005).

[94] T. Yamamoto, M. Asano, and C. Ishii, J. Phys. Soc. Jpn. **69** 3965 (2000).

[95] E. Fradkin and L.Susskind, Phys. Rev. D **17** 2637 (1978).

[96] E. Barouch and B. M. McCoy, Phys. Rev. A **3** 786 (1971).

[97] E. Berg, E. G. Dalla Torre, T. Giamarchi, and E. Altman, Phys. Rev. B **77** 245119 (2008).

[98] S. R. White, Phys. Rev. B **53** 52 (1996).

[99] M. Nakamura, Physica B: Condensed matter **329-333** 1000 (2003).

[100] N. Wu, Phys. Lett. A **376** 3530 (2012).

[101] Y. Niu, S. B. Chung, C. H. Hsu, I. Mandal, S. Raghu, and S. Chakravarty, Phys. Rev. B **85** 035110 (2012).

[102] Q. B. Zeng, S. Chen, and R. Lü, Phys. Rev. B **94** 125408 (2016).

[103] Y. Wang, J. J. Miao, H. K. Jin, and S. Chen, Phys. Rev. B **96** 205428 (2017).

[104] A. P. Schnyder and S. Ryu, Phys. Rev. B **84** 060504 (2011).

[105] E. Whittaker and G. Watson, *A Course of Modern Analysis*,2nd ed. (Cambridge University Press, Cambridge) (1915).

[106] R. Verresen, N. G. Jones, and F. Pollmann, Phys. Rev. Lett. **120** 057001 (2018).

[107] F. Ye, G. H. Ding, and B. W. Xu, *Commun. Theor. Phys.* **37** 492 (2002).

[108] F. Ye, and B. W. Xu, *Commun. Theor. Phys.* **39** 487 (2003).

[109] J. P. de Lima, L. L.Goncalves, and T. F. A. Alves, Phys. Rev. B **75** 214406 (2007).

[110] U. Divakaran, A. Dutta, and D. Sen, Phys. Rev. B **78** 144301 (2008).

[111] F. Franchini, *An introduction to Integrable Techniques for One-Dimensional Quantum Systems*, Lecture notes in Physics Vol. 940 (Springer, Heidelberg) (2017).

[112] A. Y. Kitaev, Usp. Fiz. Nauk (Suppl.) **44** 131 (2001).

[113] H. W. Capel and J. H. H. Perk, Physica A **87** 211 (1977).

[114] J. R. Schrieffer, *Theory of Superconductivity* (W. A. Benjamin, New York) (1964).

[115] H. Widom, Adv. Math. **21** 1 (1976).

[116] E. Basor, J. Dubail, T. Emig, and R. Santachiara, J. Stat. Phys. **174** 28 (2019).

[117] P. Pfeuty, Ann. Phys. (NY) **57** 79 (1970).

[118] B. M. McCoy, *Advanced Statistical Mechanics* (Oxford University Press, New York) (2010).

[119] F. Franchini and A. G. Abanov, J. Phys. A: Math. Gen. **38** 5069 (2005).

[120] C. N. Yang and C. P. Yang, Phys. Rev. **147** 303 (1966); **150** 321 (1966); **150** 327 (1966); **151** 258 (1966).

[121] M. Takahashi, *Thermodynamics of One-Dimensional Solvable Models* (Cambridge University Press, New York) (1999).

[122] N. Shiraishi, EPL (Europhysics Letters) **128** 17002 (2019).

[123] M. P. M. den Nijs, Phys. Rev. B **23** 6111 (1981).

[124] F. C. Alcaraz and A. L. Malvezzi, J. Phys. A: Math. Gen. **28** 1521 (1995).

[125] Y. Hatsugai and M. Kohmoto, Phys. Rev. B **44** 11789 (1991).

[126] V. A. Khodel, and V. R. Shaginyan, JETP Lett. **51** 553 (1990).

[127] G. E. Volovik, J. Exp. Theor. Phys. Lett. **110** 352 (2019).

[128] V. R. Shaginyan, M. Y. Amusia, A. Z. Msezane, V. A. Stephanovich, G. S. Japaridze, and S. A. Artamonov, J. Exp. Theor. Phys. Lett. **110** 290 (2019).

[129] A. A. Patel and S. Sachdev, Phys. Rev. Lett. **123** 066601 (2019).

[130] G. Y. Chitov and C. Gros, Phys. Rev. B **69** 104423 (2004).

[131] H. Watanabe, Phys. Rev. B **98** 155137 (2018).

[132] Q. Niu, D. J. Thouless, and Y. S. Wu, Phys. Rev. B **31** 3372 (1985).

[133] R. B. Griffiths, Phys. Rev. **133**, A 768 (1964).

[134] A. Luther and I. Peschel, Phys. Rev. B **12** 3908 (1975).

[135] J. Villain and P. Bak, J. Phys. France **42** 657 (1981); P. Bak, Rep. Prog. Phys. **45** 587 (1982).

[136] G. Y. Chitov and C. Gros, Low Temp. Phys. **31** 722 (2005); A. Kalz and G. Y. Chitov, Phys. Rev. B **88** 014415 (2013).

[137] T. Giamarchi, *Quantum Physics in One Dimension*, International Series of Monographs on Physics (Clarendon Press, Oxford) (2004).

[138] G. I. Japaridze, and E. Pogosyan, J. Phys. Condens. Matter, **18** 9297-9306 (2006).

[139] K. Totsuka, Phys. Lett. A **228** 103 (1997).

[140] A. Langari and M. A. Martin-Delgado, Phys. Rev. B **62** 11725 (2000).

[141] M. Azzouz, Phy. Rev. B **74** 174422 (2006).

[142] J. Jahangiri, F. Amiri, and S. Mahdavifar, Journal of Magnetism and Magnetic Materials, **439** 22-29 (2017).

[143] F. Shafieinejad, J. Hasanzadeh, and S. Mahadavifar, Journal of Superconductivity and Novel Magnetism, **32** 3285-3851 (2019).

[144] T. Kariyado and Y. Hatsugai, Phys. Rev. B **72** 094433 (2015).

[145] G. I. Japaridze and S. Mahdavifar, European Physical Journal, B **68** 59-66 (2009).

[146] D. C. Cabra, A. Honecker, and P. Pujol, Phys. Rev. Lett. **79** 5126 (1997); Phys. Rev. B **58** 6241 (1998).

[147] I. Affleck and J. B. Marston, Phy. Rev. B **37** 3774 (1988).

[148] A. Maiellaro, F. Romeo, and R. Citro, Eur. Phys. J. Spec. Top. **227** 1397-1404 (2018).

[149] E. H. Lieb, Phys. Rev. Lett **73** 2158 (1994).

[150] A. A. Nersesyan, Phys. Rev. B **102** 045108 (2020).

[151] J. L. Latorre, E. Rico, and G. Vidal, arXiv: 0304098v4 (2004).

[152] A. P. Schnyder, S. Ryu, A. Furusaki, and A. W. W. Ludwig, Phys. Rev. B **78** 195125 (2008).

[153] P. N. Timonin and G. Y. Chitov, Phys. Rev. B **104** 045106 (2021).

[154] M. Nakahara *Geometry, Topology and Physics* 2nd edn (New York: Taylor and Francis) (2003)

[155] P. Deift, A. Its, and I. Krasovsky, *Communications on Pure and Applied Mathematics*, **66** 1360 (2013).

[156] A. Montorsi and M. Roncaglia, Phys. Rev. Lett. **109** 236404 (2012).

[157] I. Peschel, J. Stat. Mech. P 12005 (2004).

[158] A. Kopp and S. Chakravarty, Nat. Phys. **1** 53 (2005).

[159] U. Divakaran and A. Dutta, J. Stat. Mech. P 11001 (2007).

[160] T. T. Wu, Phys. Rev. **149** 380 (1966)